HIGH RESOLUTION NEUTRON SPECTROMETER DEVELOPMENT AND 14 MEV NEUTRON SCATTERING BY Bi

Thesis

Submitted by

JAVAD RAHIGHI, B.Sc., M.Sc.

for the degree of

DOCTOR OF PHILOSOPHY

Department of Physics,

University of Edinburgh

FEBRUARY, 1985.

TO MY PARENTS

C O N T E N T S

C O N T E N T S (Contd.)

C O N T E N T S (Contd.)

C O N T E N T S (Contd.)

ABSTRACT

A high resolution fast neutron time of flight spectrometer has been designed and constructed with its associated control units and electronics, for the purpose of measuring 14 MeV differential elastic and inelastic cross sections with good accuracy, in order to provide a test of nuclear models currently used to describe these phenomena.

The experimental facility provides the capability of measuring scattering cross sections of a few mb/sr to a good accuracy over the angular range from 20 to 160°.

Source neutrons are provided by the $^{3}H(d,n)^{4}_{2}He$ reaction. Scattered neutrons are detected in a massively shielded NE224 liquid scintillator detector located 12-13 metres from the scattering sample. A very large volume ($\approx$ 8 litres) neutron detector has been designed and developed to achieve high energy resolution and high detection efficiency.

The elastic and inelastic cross sections of neutrons to ten excited states of up to 7.9 MeV excitation energy of ^{209}Bi have been measured. Absolute cross sections are obtained by normalizing to n - C scattering.

Monte Carlo simulation has been used to correct for finite source and sample effects.

Spherical and deformed optical model calculations have been used to interpret the elastic and inelastic scattering data.

CHAPTER I

INTRODUCTION

1.1 Nuclear Reactions

One of the most basic interactions in nuclear structure and reaction studies is that between a nucleon and a nucleus. Making the assumption that the nucleon-nucleus interaction can be described as a two body interaction, it is the shell model potential which generates nuclear single particle states for structure studies, while for reactions it is the interaction between an incident particle and target nucleus.

The nucleus-nucleus interaction may be determined either theoretically by summing the constituent nucleon-nucleon interactions, known through nucleon-nucleon scattering and studies of the deuteron or phenomenologically by seeing which interaction gives the best fit to the available experimental data. The former approach encounters serious mathematical difficulties if realistic calculations are attempted and the latter results in ambiguities by failing to produce uniquely valued results, that is, it is possible to find several different potentials that give equally good fits to the experimental data. Thus the purely phenomenological approach to the determination of the nucleon-nucleus interaction, is inadequate. It needs to be supplemented by a more basic calculation of the interaction from the constituent nucleon-nucleon interactions. At present the best results are probably to be found by a combination of the microscopic and phenomenological analyses

of experimental data. This work will concentrate very heavily on the experimental methods for collecting data and the phenomenological approach for analyses of the data.

Measurements of differential cross-sections both elastic and inelastic, integrated cross-section and polarisation provide valuable information about the nature of the nucleon-nucleus interaction mechanism. A nucleon incident on the target nucleus may undergo one of the various types of reaction. The relative probabilities of these reactions depend on the structure of the nucleus and on how easily the particle can get in and out of the nucleus, that is on the energy of the incident particle. As the energy of the incident particle increases more reactions become possible. Two extremes have been recognised when a nucleon-nucleus collision occurs and both are of importance for the understanding of the nuclear reaction phenomena. The nucleon and nucleus may combine to form a highly excited compound system. This compound nucleus stays together sufficiently long for its excitation energy to be shared more or less uniformly by all its constituent nucleons. Then by chance, sufficient energy is localised on one nucleon, or one group of nucleons, for it to escape and in this way the compound nucleus decays.

At the other extreme, the incident particle and the target nucleus may make just glancing contact and immediately separate without the formation of an intermediate compound nucleus, thus it is called a direct reaction.

Many reactions proceed through both modes, Fig. 1.1. One essential feature distinguishing the two types of reaction, direct and compound, is the time required for each. The compound reaction is slow, the direct reaction is fast. The direct reaction takes place within the time it takes for the particle to

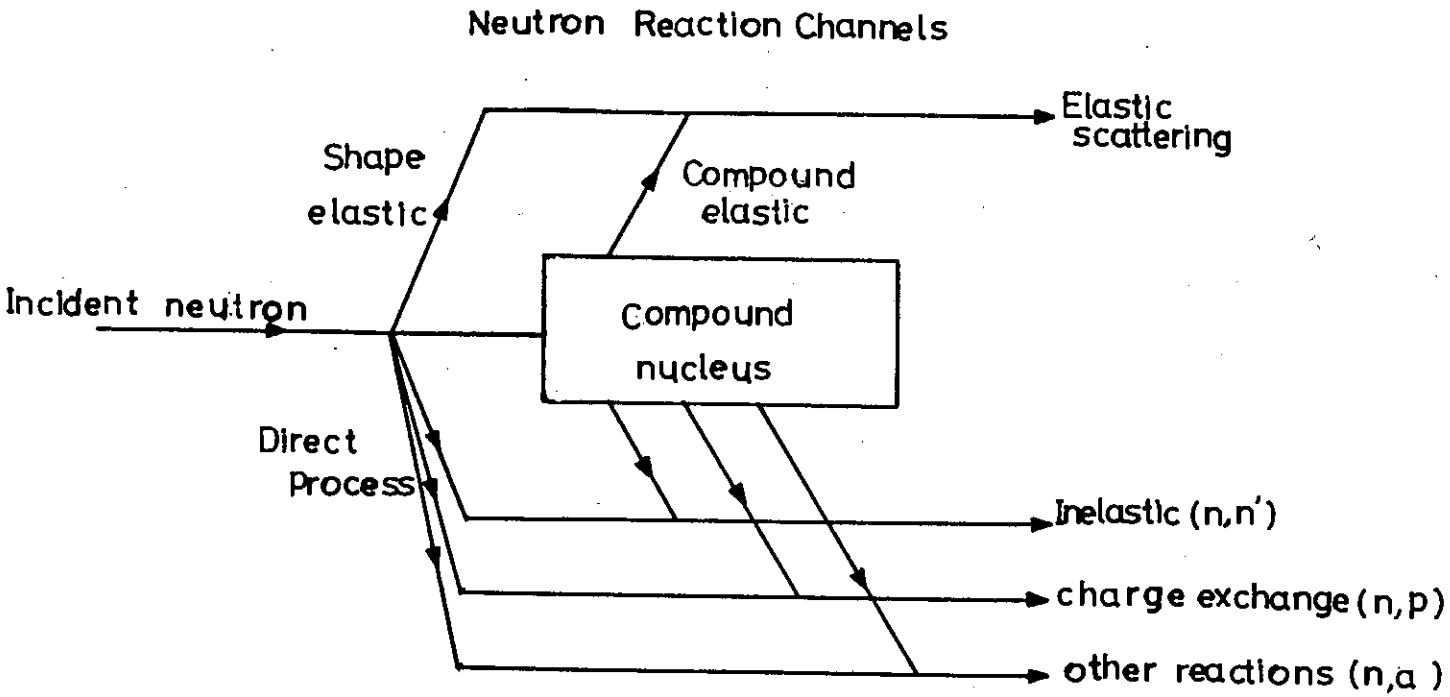

Figure (1.1): Direct and Compound Nucleus Processes in Nuclear Reactions.

traverse the nuclear diameter, usually about 10^{-22} second. The decay of the compound nucleus takes much longer time, of the order of 10^{-13} to 10^{-18} second. At present even with the most refined electronics the time delay between the two processes can not be resolved experimentally. However where competing direct and compound modes exist in the same reaction channel, if one feature is dominant, it may be deduced by inspection of the differential cross-section. Direct processes produce a highly anisotropic distribution, often like a diffraction pattern with a strong forward peak and secondary maxima and minima in intensity. Compound distributions are often close to being isotropic and show symmetry about the 90° scattering angle in centre-of-mass coordinates.

The compound and direct reactions have different kinematic characteristics. A direct, one step reaction favours the transfer of only a relatively small amount of energy and readily feeds the ground and low excited states of the residual nucleus. On the other hand, a compound nucleus prefers to evaporate particles with low energies and preferentially feeds the higher excited states in the residual nucleus.

This tendency for the low-lying states of nuclei to be populated by direct reactions is one of the main reasons for the importance of these reactions. The nucleus represents a complicated many-body problem and, in general, we can only expect the existing theories of nuclear structure to give accurate and detailed explanations of the structure of these isolated low energy quantum states. The direct reactions have a relatively simple nature, with no complication from an intermediate compound system and are well suited to giving information about the relationship between the ground state

of the target nucleus and the ground or a particular excited state of the residual nucleus. The same is not true for the compound nucleus. The dense, highly excited states of nuclei generally have complicated structure and we can only expect to understand their properties in an average or statistical way[1].

1.2 Neutron Scattering

The type of reaction of interest in the present study is fast neutron (14.1 MeV) scattering. Due to the absence of the long range Coulomb force, neutrons do not suffer any Coulomb interaction and hence are not repelled by the target nucleus. This allows them to be used as probes with considerably lower energies than that of protons and can also simplify the calculations as the relatively slowly decaying Coulomb interaction requires many partial waves in the analysis. Neutrons, on the other hand, experience only short range strong interaction neutron scattering. Neutron scattering can therefore give direct information about the strong interaction and neutron-scattering data should yield more detailed information about the nuclear potential than can be obtained for example with protons as a probe.

For neutron-nucleus scattering the energy region between 8 and 14 MeV is of special applied and theoretical interest. From the applied point of view, the differential cross-sections for elastic and inelastic scattering from a lengthy list of nuclei are important for design considerations for fusion reactors.

It is necessary to measure these cross-sections for a large

number of nuclei and at a sufficient number of energies, so that the required data can either be obtained directly or else be determined from some suitable parameterization.

From the theoretical point of view, the region above approximately 10 MeV is a fertile testing ground for nucleon-nucleus direct reaction model calculations, as the compound nucleus contributions are generally negligible in this energy region[2,3].

A final interest in having cross-section data at energies around 10-14 MeV relates to the success of proton inelastic scattering cross-section data in the 10-20 MeV region in yielding a large quantity of nuclear structure information such as nuclear deformations. Neutron data in the same energy range have been useful in a similar way, but the quantity of these data is rather poor, and additional inelastic data would be valuable for comparing the success of calculations for charged particle probes and for neutrons inelastically scattered from similar nuclei. The central objective of this work, as will be discussed later, was to design and build a neutron scattering system which is capable of measuring inelastic scattering cross-sections to the low lying and higher excited states of nuclei with sufficient energy resolution and accuracy.

1.3 The Neutron Optical Model

The shape of the observed neutron total cross-sections as a function of energy and mass number A changes significantly over the range of A. This change is, however, not random but gradual. Nuclei with small differences in A show almost the same behaviour[4,5].

This generally smooth variation of total X-section with target nucleus and neutron energy suggested to Feshbach, Porter and Weisskopf[6] that the interaction of a neutron with a nucleus resulting in these characteristic shapes, does not depend on detailed features of nuclear structure but on some general properties which vary slowly with A, say, nuclear radius. Feshbach, Porter and Weisskopf therefore proposed a nuclear model which predicted the total and reaction cross-sections together with the differential elastic cross-section. In this model the nucleus was replaced by a complex one body potential that did not depend on the details of nuclear structure, an idea that had already been applied with success to scattering of 18 MeV protons from Aℓ by Le Levier and Saxon[7]. The model proposed by Feshbach and his colleagues defines the elastic cross-section as the cross-section for scattering without change of the quantum state of the nucleus. The reaction cross-section includes all processes in which the residual nucleus is different from or in a state different from that of the target nucleus and it is considered to occur after compound nucleus formation. Hence the compound nucleus formation is considered as an absorption of the incident beam and is described by the imaginary part of a complex potential:

$$V(r) = V_o(r) + iV_1(r) \qquad (1.1)$$

acting upon the incoming neutron. The elastic scattering is, however, caused by the real part of the potential which describes the average potential energy of the neutron within the nucleus.

The potential in (1.1) depends in a simple way upon the mass number A through the radius of the nucleus r.

In the early work of the optical model Feshbach et al.[6]

assumed the potential (1.1) to be a complex square well of the form:

$$V(r) = -V_o(1 + i\xi) \quad \text{for} \quad r < R$$
$$V(r) = 0 \quad \text{for} \quad r > R \qquad (1.2)$$

in which R is the nuclear radius.

This potential reproduced the total cross-section for neutrons, the angular dependence of the elastic scattering and the cross-section for the formation of the compound nucleus.

Elastic scattering and reaction cross-sections performed with high energy resolution exhibit strong fluctuations with energy, which are referred to as resonances. It is known that the energy level structure of the compound nucleus is responsible for these fluctuations, but provided that experiments are performed with low-resolution, energy averaged elastic scattering cross-sections vary smoothly with energy. The one-body potential (1.2) only describes the energy averaged cross-section (gross-structure problem) and not the actual rapidly varying cross-section due to the resonances.

Further refinement to the optical potential initially taken to be square well (1.2) was introduced by Saxon and Woods[8], when the square well failed to reproduce successfully elastic scattering cross-sections for heavier nuclei and showed marked disagreement with the experimental cross-sections by predicting too large a cross-section at larger angles. They showed that this disagreement persists, even if the square well parameters are permitted to vary over an extensive range and if the nuclear charge is assumed to be distributed over the nuclear volume. The work by Saxon and Woods

suggested the potential:

$$V(r) = Vf(r) + iWg(r) \tag{1.3}$$

in which $f(r)$ and $g(r)$ are the Saxon-Woods form factors.

$$f(r) = [1 + \exp(r - R_u)/a_u]^{-1}, \quad R_u = r_u A^{1/3} \tag{1.4}$$

$g(r)$ has the volume form

$$g(r) = [1 + \exp(r - R_v)/a_v]^{-1}, \quad R_v = r_v A^{1/3} \tag{1.5}$$

where R_u, R_v are radius parameters and a_u, a_v are the surface diffuseness parameters and are related to the rate of radial fall-off of the nuclear matter distribution. Detailed calculations of the potential from the nucleon-nucleon interaction[9] confirms the overall correctness of $g(r)$ and $f(r)$, because the shape of $f(r)$ and $g(r)$ is based on the feature of all the constituent nucleon-nucleon interactions.

In 1959 Lemmer et al.[10] argued that at low energies of the order of 1 - 10 MeV, the absorption takes place mainly in the nuclear surface and the expression to represent this surface absorption is the derivative form of the Saxon-Woods form factor:

$$g_D(r) = \frac{4\exp\left[\dfrac{r - r_D A^{1/3}}{a_D}\right]}{\left[1 + \exp\left[\dfrac{r - r_D A^{1/3}}{a_D}\right]\right]^2}. \tag{1.6}$$

At high energies, of the order of 100 MeV, it is more likely that the absorption takes place throughout the nucleus and so a volume type form factor (1.5) is more appropriate[9].

In the early 1960's the optical model was extended to include neutron polarisation effects by scattering when accurate polarisation data became available. The extension resulted in the addition of a spin-orbit term to the optical model potential (1.3):

$$V_{so}(r) = V_s \left(\frac{\hbar}{m_\pi c}\right)^2 \cdot \frac{1}{r} \cdot \frac{df_s(r)}{dr} \cdot \underline{L}\cdot\underline{\sigma} \qquad (1.7)$$

where $f_s(r) = [1 + \exp(\frac{r - R_s}{a_s})]^{-1}$, $R_s = r_s A^{1/3}$.

Various analyses of differential cross-section data were performed successfully. Good fits to the experimental data can be obtained by using potential parameters $a \approx 0.6$ fm, $R \approx 1.25$ fm, $V \approx 40$ MeV, $W \approx 10$ MeV and $V_{so} \approx 8$ MeV as starting values and then adjusting them systematically to optimise the fit to selected data. The above empirical (local) optical model potential parameters have been found to have a strength which varies with bombarding energy. The energy dependence in general arises in two ways, partly because the effective interaction is non-local and partly because of an intrinsic energy dependence. In 1962 Perey and Buck[11] reanalysed the available experimental data and demonstrated that a simple non-local model was able to give a unified account of a variety of experimental data for nuclei ranging from Aℓ to Pb and energies up to 24 MeV, when allowance

for compound elastic scattering was made at lower energies.

An equivalent local potential to that of Perey and Buck was later obtained by Wilmore and Hodgson[12].

Since the early 1950's the optical model of the nucleus has been applied with remarkable success to analyse a wide body of neutron scattering data and several global parameter sets have been found that give generally excellent fits over a range of neutron energies and target nuclei. Amongst those mentioned earlier are the non-local potential of Perey and Buck[11], its local equivalent[12], and the nucleon potentials of Becchetti and Greenlees[13] for proton and neutron data of energies less than 50 MeV and nuclei $A > 40$.

In recent years calculations of varying degrees of complexity have been made in order to understand nucleon-nucleus elastic scattering from a realistic internucleon force. One approach is to obtain the optical potential essentially by considering the nuclear matter density in a finite nucleus. The work of Jeukenne et al.[14-16] and Brieva and Rook[17,18] has been particularly successful. Already the calculated potentials are able to give a good overall fit to the experimental data although not of the same quality as those obtained in phenomenological analyses. Brieva and Rook[19] studied the range of validity of their model by making a detailed comparison of theoretical results with experimental cross-section and polarisation data for proton and neutron elastic scattering from different nuclei and over a wide range of energies. They concluded that neutron scattering data above about 10 MeV incident energy is in good agreement with the calculation. Their calculation for proton scattering, however, had rather poor quality of fit, particularly in the backward angle

region.

1.3.1 The extended optical model

During the last two decades, one asked the spherical optical model approximation to reproduce qualitative and quantitative features of elastic scattering of nucleons. While it was successful, physicists went further and hoped the optical model would give a qualitative and quantitative description of elastic scattering and inelastic scattering. This required the expansion of the total wavefunction in terms of the wavefunctions in all the energetically allowed reaction channels and the solution of the corresponding many-body Schrödinger wave equation. This is an impossibly complicated task and so the spherical optical model approximation, by not considering this expansion, suffers from the disadvantage that it gives no information about the cross-section in the individual reaction channels.

The optical model can be extended to take explicit account of one or more reaction channels by expanding the total wavefunction in terms of the wavefunction in the elastic channel and in the selected reaction channels, and taking account of the remaining reaction channels by an appropriately reduced absorbing potential[20]. This extension of the optical model to inelastic scattering of particles from collective excited states led to the coupled channel optical model[21]. There is in principle no limit to the number of reaction channels that can be included in this way. In practice, however, the main limitation is computational time of solving

sets of coupled differential equations. It is useful therefore to include in such a calculation only those channels that are strongly coupled to the elastic channel, and these are usually few in number. The cross-section in weakly coupled channels can be calculated with sufficient accuracy by the distorted wave Born approximation (DWBA)[22]. In this calculation, which is based on an extension of the optical model to include the scattering from non-spherical potentials, the incoming and outgoing waves are distorted by the same potential as the corresponding elastic scattering interaction, and it is assumed that the elastic scattering is essentially unaffected by the inelastic process being considered, Buck and Hodgson[23], the non-spherical parts of the potential induce inelastic scattering to the collective states. The magnitude of the cross-section for inelastic scattering is proportional to the square of the deformation of the optical potential which can be found by comparison with experiment.

1.4 Review of Past Work

The scattering of 14 MeV neutrons is mainly governed by the direct reaction process. Being a single step process, the direct reaction, as discussed earlier in Section 1.1, favours the transfer of relatively small amounts of energy and readily feeds the ground and low excited states of the residual nucleus.

The excitation of low-lying collective nuclear states by a direct nuclear interaction has for some time been known to be an important process in the scattering of alpha particles and in proton scattering[24]. It is believed, Stelson et al.[25] that the

scattering of fast neutrons should also strongly excite these collective states. The main difficulty in measuring scattering to the low lying excited states is experimentally resolving the various scattered neutron groups. The following summarizes some of the important measurements in the energy region of 14 - 15 MeV on the excitation of low lying collective states.

Goldberg et al.[26] reported measurements for the excitation of low lying states by 14 MeV neutrons for the relatively light nuclei, ^{6}Li, ^{7}Li, ^{9}Be, ^{12}C, ^{16}O, ^{24}Mg, ^{28}Si and ^{32}S. Time of flight or the proton recoil technique in photographic emulsions were used to separate elastic and inelastic neutron groups. The observed shapes of the angular distribution for inelastic neutron scattering were fairly well reproduced by the direct interaction theory. Due to the poor energy resolution (1.3 MeV), however, their measurements were limited to light nuclei with the first excited state larger than $\gtrsim$ 2 MeV[27,28]. Clarke and Cross[29] studied elastic scattering and inelastic scattering to the first excited state for C, Mg, Si and S. Their results have been interpreted in terms of the deformed optical model and they found deformations for Mg, Si and S which agree well with the electromagnetic values. They used the time of flight technique with rather poor energy resolution (900 keV) and measured cross-sections only for the first excited state.

Stelson et al.[25] measured differential cross-sections for the inelastic scattering of 14 MeV neutrons to low lying collective states for 13 elements from Mg to Bi. Their observed shapes agreed with the prediction of the direct interaction mechanism.

Time of flight technique with 450 keV energy resolution was used in their work to separate elastic groups from inelastic groups. They studied excited states up to about 4 MeV for heavy nuclei and up to approximately 5 MeV for lighter nuclei. P. Kuijper et al.[30] investigated the elastic and inelastic scattering of 14.8 MeV neutrons by Bi, Sr and Na. They also used the time of flight technique. Their energy resolution was however poor (900 keV for 14 MeV incident neutron energy). Neutron groups due to the excitation of states at 2.6 MeV, 4.2 MeV and 5.5 MeV in Bi and at 1.84 and 2.74 MeV in Sr were observed. They showed the angular distributions of inelastic scattering were consistent with the DWBA prediction. The magnitude of their cross-section for Bi was however substantially higher than that of Stelson et al.[25]. As a result of the larger cross-section measured, their calculated deformation parameter for the excited states of Bi was 1.8 times larger than that reported by Stelson et al.

Excitation of the states of Bismuth at 2.66, 4.36 and 5.80 MeV by 14 MeV neutrons was studied by Matoba et al.[31] and they interpreted their data by DWBA calculation. The time of flight system they used for separating neutron groups also suffered from poor energy resolution (650 keV for 14 MeV neutrons).

1.5 Experimental Method

The major experimental difficulty for the measurement of neutron scattering from the excited states is the limited ability of neutron scattering systems to separate various neutron groups.

The review of past work shows that the energy resolution achieved in each case was the decisive and also the limiting factor in their final success in order to do useful inelastic scattering measurements, particularly when medium and heavy nuclei with low excited states were involved.

Due to the neutral nature of the neutron the time of flight (T.O.F.) technique is at present the most powerful and widely used technique for neutron spectroscopy. It is in principle the measurement of neutron energy by measuring the time taken for it to cover a certain distance. This technique has been used by many experimenters elsewhere. Watson et al.[32] used a time of flight system for high neutron energy study (50 MeV) and Rapaport et al.[33] measured inelastic cross-sections of 7 - 26 MeV neutrons by the time of flight technique.

Another less successful technique being adopted in recent years, mainly for low neutron energy experiments, is proton recoil spectrum unfolding[34]. This technique is based on the unfolding of proton recoil pulse height data measured with organic scintillators, and involves processing of the proton recoil spectrum by rather complicated computer programs which introduce some uncertainty in spectrum unfolding results. The performance of this technique is ultimately dependent upon the pulse height resolution of the detector.

On the other hand, however, the interpretation of the time of flight spectrum is usually a much more straightforward task and does not require much effort provided the various energy groups are reasonably separated.

Two methods of time of flight spectroscopy are known, depending on whether pulsed beam accelerators or d.c. beam accelerators are employed in the T.O.F. system. In the pulsed beam time of flight method a sub nano second pulsed beam from an accelerator bombards the neutron producing target. The neutron time of flight from the target to the scattering sample and then to the neutron detector is measured and with a sufficiently long flight path elastic and different inelastic neutrons can be identified. The beam pickoff and the neutron detector record zero time "START" and "STOP" of the flight time respectively.

In an alternative method with a continuous d.c. beam accelerator, the associated particle technique may be utilised for time of flight spectroscopy, The associated particle, emitted in coincidence with the neutron, provides the "START" pulse and the neutron detector provides the "STOP" pulse.

Due to the numerous attractive features of the time of flight technique in general and the associated particle technique in particular, it was decided that the latter method should be employed in our laboratory, in which a d.c. beam of deuteron of about 250 keV energy bombards a tritium target to undergo the $^{3}_{1}H(d,n)^{4}_{2}He$ reaction. Neutrons are then scattered by a scattering sample before being detected by a neutron detector at about 12.6 m distance from the target. In this arrangement the neutron and its

associated alpha particle are detected in coincidence and the finite beam pulsed time duration in the pulsed beam time of flight technique does not contribute to the overall time spread of the associated particle T.O.F. spectrum. In addition the coincidence detection method provides "electronic collimation" of the neutron beam with the effect of considerable reduction in background.

The choice of flight path depends upon the overall time resolution of the detectors and electronics, the energy resolution that one would aim for, and the affordable detector size for maintaining useful counting efficiency without deteriorating the time resolution of the detector.

The central interest of this project is to develop and construct a complete time of flight system which includes the beam transport system, target and associated particle detector assembly, high intrinsic efficiency neutron detector and its associated electronics with good time resolution, neutron collimator and shielding and finally the design of the necessary electronics for data collection and transfer.

It was decided to measure neutron scattering from Bismuth-209 for the following reasons:

Inelastic scattering to bismuth is useful in identifying collective states in which the lead 208 core is excited.

The previous measurements on the differential inelastic cross-section of bismuth at 14 MeV suffer from being limited to only a few excited states and also from a large disagreement existing among these data. It seemed therefore probable that with better energy resolution, differential inelastic scattering

to higher and more states could be investigated. Being a single isotope (100% abundancy) Bismuth 209 has the advantage of resulting in less complicated scattering spectra for analysis.

This report presents in the following chapters a detailed description of the design, building and testing procedure of various parts of the time of flight scattering system, with its associated instrumentation. The system has been designed so that it is possible to achieve an energy resolution of better than 300 keV for 14 MeV neutrons. This energy resolution is sufficient for most nuclei in particular for medium and light nuclei.

A computer program necessary for the analysis of time of flight spectra with overlapping peaks was developed specially for this project. Differential elastic and inelastic scattering of Bismuth is presented.

For analysis of the differential cross-section data the Distorted Wave Born Approximation (DWBA) optical model program (DWUCK-4)[35] was modified for the EMAS (Edinburgh Multi Access System) FORTRAN compiler.

CHAPTER 2

DESIGN AND CONSTRUCTION OF ASSOCIATED PARTICLE TIME OF FLIGHT (T.O.F) SYSTEM

2.1 Introduction to Neutron T.O.F. Method

There are a number of reasons why it is difficult to measure neutron energies with high resolution and reasonable efficiency. Among them are the lack of net electric charge on the neutron, which rules out the use of all forms of electro-magnetic and direct ionisation spectrometers, the difficulties of producing well-collimated, intense fluxes of neutrons within narrow ranges of energy, the high level of background radiation that frequently accompanies the neutron group of interest due to competing reactions in the neutron producing target, and the need to use indirect methods for detecting neutrons. In spite of these difficulties, several methods of neutron spectroscopy have been developed, most important of them is the measurement of proton recoil energy and time of flight measurements. The latter has emerged as the leading method up date; it is widely used throughout nuclear and particle physics and is the best technique known for energy determination of neutrons emerging from reactions such as (n,n'), (^{3}He,n), (P,n) and (^{4}He,n).

Three years after Chadwick's discovery of the neutron in 1932, Dunning et al.[36] developed a neutron velocity selector. A two shutter system of rotating metal discs, each with sectors of cadmium, was used to generate pulses of neutrons from the continuous flux from

a radon-beryllium source surrounded by paraffin wax as moderating material, and to select the neutron groups of definite speed. The energy of the neutrons selected depended on the distance between the discs, on their speed of rotation, and on their relative phase. This work formed the basis for the general development of neutron velocity selectors, or time of flight spectrometers.

In 1938, Alvarez[37] used the time of flight technique to discriminate fast (MeV) neutrons and low energy (eV) neutrons. According to Alvarez the possibility of using neutron T.O.F. spectroscopy as a general method had been discussed at Berkeley as early as 1936. During two decades following the work of Alvarez, pulsed neutron sources became available using reactions induced by protons, deuterons and alpha particles from Cockcroft-Walton generators, Cyclotrons and Van de Graaff accelerators.

The principle of the T.O.F. method is as follows. The speed of a neutron can be determined by measuring the time t_n that it takes to travel a measured distance ℓ in free space. For non-relativistic neutrons equation (2.1) applies to t_n, ℓ, and E_n:

$$\left(\frac{t_n}{\ell}\right)_{N.R} = \left[\frac{E_o}{2E_nC^2}\right]^{\frac{1}{2}} = \frac{72.298}{\sqrt{E_n}} \ n_s/m \qquad (2.1)$$

In order to determine t_n one needs to know the start and stop time of the neutron under investigation.

An essential part of the problem of neutron T.O.F. measurement is therefore the precise determination of the starting time or "zero time" of the neutron. Three basic methods have been commonly used for obtaining this zero time. These methods are, namely, oscillator

pickoff, target pick-off and the associated particle method. The first two methods require pulsed beams, while the third, the associated particle method, makes possible time of flight measurements with d.c. beams.

In addition, the associated particle technique has other advantages, such as:

(1) When only two particles are produced in the reaction, as in $^{2}H(d,n)^{3}_{2}He$ and $^{3}H(d,n)^{4}_{2}He$, the two detector angles, neutron and the associated particle detectors, are no longer independent, with the result that a beam of neutrons having a known and well defined direction and flux is obtained without the use of a collimator. Thus the neutron beam is still monoenergetic after its direction is defined and degradation of the neutron energy by scattering in a collimator is avoided.

(2) The time zero is obtained without the use of a pulsed neutron source, and with an uncertainty dependent only on electronics and on the alpha path geometry. In the case of the pulsed beam, however, another source of uncertainty is involved in addition to the electronics uncertainty, that is the pulse burst duration which is in fact the limiting factor in the time resolution achievable in a pulsed beam T.O.F. system.

If the neutron flight time uncertainty from all sources is Δt_n and the distance uncertainty due to the finite thickness of the neutron producing target, and the finite thickness of the neutron detector, is $\Delta \ell$ then for a non-relativistic neutron the uncertainty ΔE_n in measuring the kinetic energy E_n is:

$$\Delta E_n = 2E_n \left[\left(\frac{\Delta \ell}{\ell}\right)^2 + \left(\frac{\Delta t_n}{t_n}\right)^2 \right]^{\frac{1}{2}} . \qquad (2.2)$$

If, as is often the case $\frac{\Delta \ell}{\ell} << \frac{\Delta t_n}{t_n}$ then:

$$\frac{\Delta E_n}{E_n} \simeq 2 \frac{\Delta t_n}{t_n} = 2 V_n \frac{\Delta t_n}{\ell} . \qquad (2.3)$$

The equation (2.3) shows that in order to improve the energy resolution ΔE_n at a certain neutron energy E_n and with the achievable time resolution Δt_n, the flight path ℓ should be increased. For instance, for 14 MeV neutron energy, a desired energy resolution of better than 200 keV and with a time resolution of around 1.5ns (1.5×10^{-9} second) equation (2.2) results in the requirement of a neutron flight path of over 11 metres.

The increase of the neutron flight path is, however, limited by the resolving time of the time of flight system since the solid angle varies as the square of the neutron flight path and the random coincidence rate:

$$\text{Random rate} = 2\tau N^2 \Omega_A \Omega_n \varepsilon_A \varepsilon_n \qquad (2.4)$$

would soon dominate the real coincidence rate

$$\text{Real rate} = N \Omega_A \Omega_n \varepsilon_A \varepsilon_n \qquad (2.5)$$

and would become the limiting feature as flight path was increased to provide neutron energy resolution. In (2.4) and (2.5) N is the neutron source disintegration rate and τ is the resolving time

of the system, $\Omega_A \varepsilon_A$ and $\Omega_n \varepsilon_n$ are the product of the solid angle and efficiency respectively of the neutron and the associated particle detector.

To use such a long flight path successfully, the real coincidence rate should be increased by the choice of a reasonably large scattering sample, large neutron detector with higher efficiency, while suppressing random coincidence rate by designing an efficient collimator and shielding both for neutron producing target and for the neutron detector.

2.2 Basic Design Consideration for Associated Particle T.O.F. System

2.2.1 Design and construction of the beam transport and vacuum system

Having determined the necessary neutron flight path for achieving sufficient energy resolution, the next step was to decide how the required long flight path could be fitted into the laboratory. The insufficient length of the laboratory was the major limitation for accommodating the necessary flight path. In addition two other experiments were running when this work started. They occupied, with their equipment and shieldings, most of the laboratory floor. The work therefore had to be preceded by arranging a 3 metre extension of the beam line from the analysing magnet towards the laboratory end wall, attaching a magnet chamber to the beam line with the aim of bending the beam upwards and by taking the beam to a suitable height from the floor to the space above the accelerator and other beam lines to accommodate the required flight path (Fig. 2.1).

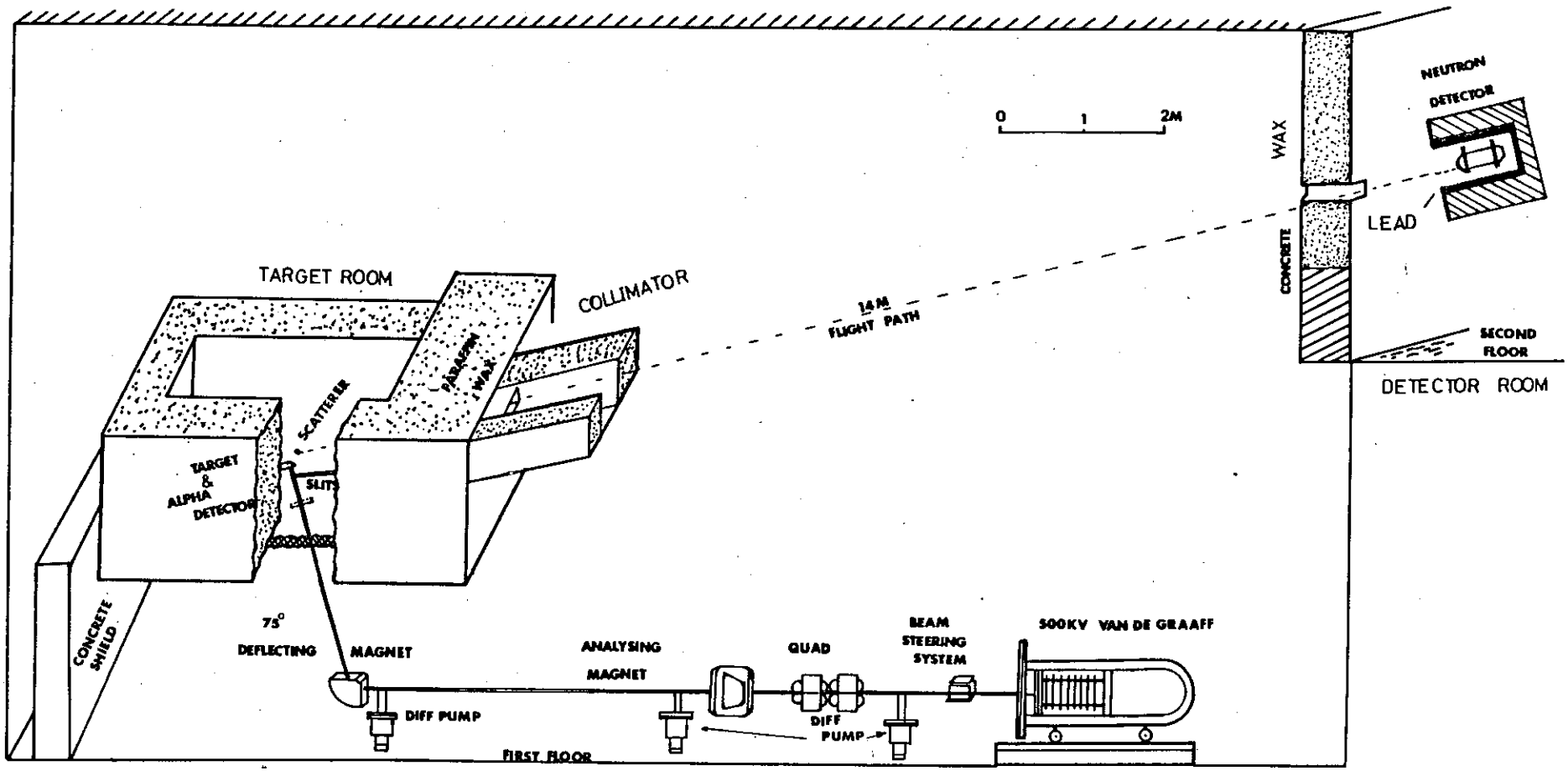

Figure 2.1: Experimental layout of high resolution neutron time-of-flight (T.O.F.) system.

First a multi port magnet chamber was coupled to the beam line and the deflecting magnet carefully positioned to provide a facility to experiment and to examine the deflected beam at several angles to check the capability of the magnet to maintain the focus and stability of the beam.

To establish the optimum condition of the deflecting system for achieving a well focused and stable beam, some tests were carried out which involved running the accelerator at various deuteron energies and also deflecting the beam through various angles while checking the beam stability and focus on a quartz blank at the end of each magnet chamber outlet.

In order to decide the deuteron energy to be used for neutron production a compromise had to be made between the better focusing condition of the accelerator beam at energies above $\sim$ 250 keV and the necessity for reducing the heat produced in the deflecting magnet coils, which was more of a problem as deuteron energy was increased. Since the neutron producing reaction would give maximum yield at lower deuteron energy (around 100 keV) and also because of the desire to reduce the power consumed in the magnet by feeding less current through it, it was decided to use deuterons of a minimum energy of 250 keV. At this energy the tests indicated that deflecting the beam through 90° was not possible without overloading the magnet supply and overheating the magnet coil itself. The system was then set up for a deflecting angle of 75° and the multi angle magnet chamber was replaced with a newly designed and specially built magnet chamber having a beam outlet only at 75°. The purpose of this replacement was to reduce

the chance of vacuum leaks by using a chamber with a reduced number of brazed joints. The chamber was made from 38 mm × 18 mm rectangular section waveguide.

To transport the beam to a suitable height after deflection a further upward extension of the beam line was necessary. This extension amounted to about 2 metres from the magnet chamber to the $^{3}_{1}H(d,n)^{4}_{2}He$ reaction chamber.

At a distance of 65 cm from the neutron producing target and along the upward extension of the beam line a stabilizing slit system was installed to deal by feedback, with any instability of the beam due to the energy fluctuation of the accelerator in the course of experiment.

Since the existing vacuum pumping system could not cope with the new beam line system after extension, two more pumping systems had to be added, one in the vicinity of the deflecting magnet supported on the laboratory floor and the second pump close to the target chamber which was supported by a rigid framework at the height of $\sim$ 2 metres from the laboratory floor.

Further beam stability and steering tests were carried out with the addition of a small magnet for fine adjustment of the deuteron beam vertically before entering the deflecting magnet chamber.

A substantial amount of framework had to be designed and constructed prior to setting up the vacuum beam line in order to support firmly and reliably the beam line, its vacuum pumping system, target chamber and the necessary equipment in the target area. This framework supported satisfactorily massive paraffin wax shielding used around the target area, making a "target room".

with paraffin wax walls. This heavy shielding was required both as biological shielding around the tritium target and for the background suppression. Attached to the "target room" is a 3 metres long collimator which was also supported by the framework. The framework is designed so that access to target for changing and to vacuum pump system for servicing is relatively easy.

2.2.2 Design of the T.O.F. system

Setting up of the beam transport vacuum system was the first step towards the design and construction of a high resolution neutron time of flight system to be employed for accurate measurement of differential elastic and inelastic scattering cross-sections at 14.1 MeV neutron energy over the angular range of 20 to 160 degrees.

The system was designed so that the space above the beam lines and the accelerator could be utilized for the long flight path of the neutrons, Figs. 2.1 and 2.2.

Deuterons with 250 keV energy undergo the $^{3}H(d,n)^{4}_{2}He$ reaction on a thin tritium target, producing 14.1 MeV neutrons.

Neutrons from the target are scattered by a cylindrical (50 mm dia. × 50 mm high) scattering sample which was positioned at an approximate distance of 20 cm from the centre of target and at the centre of the neutron beam defined by detection of the associated $^{4}_{2}He$ nuclei in a plastic scintillation counter. The distance between target and scattering sample had to be increased to about 28 cm for 20° angle of scattering to avoid the target

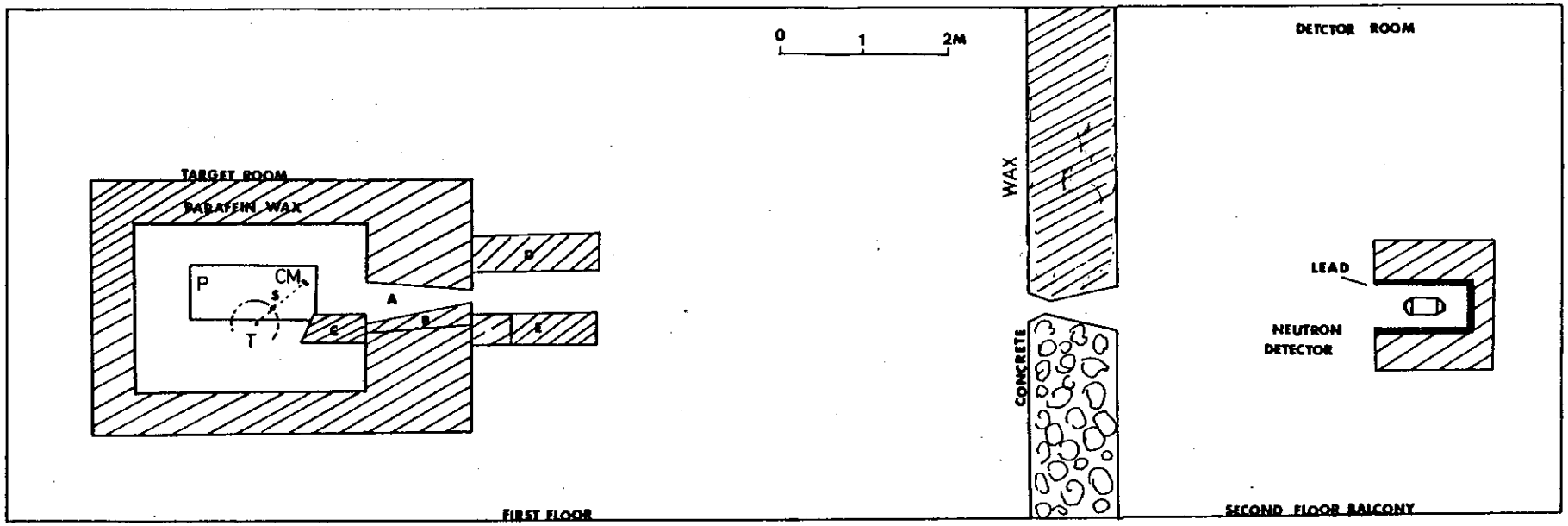

Figure 2.2: Part of the floor plan of the T.O.F. Experimental layout.

A	Main collimator	CM	Neutron beam monitor
B	Tapered collimator insert	P	Platform parallel to the scattering plane.
C	Shadow shield	S	Scattering sample
D & E	Moveable collimator	T	Neutron producing target

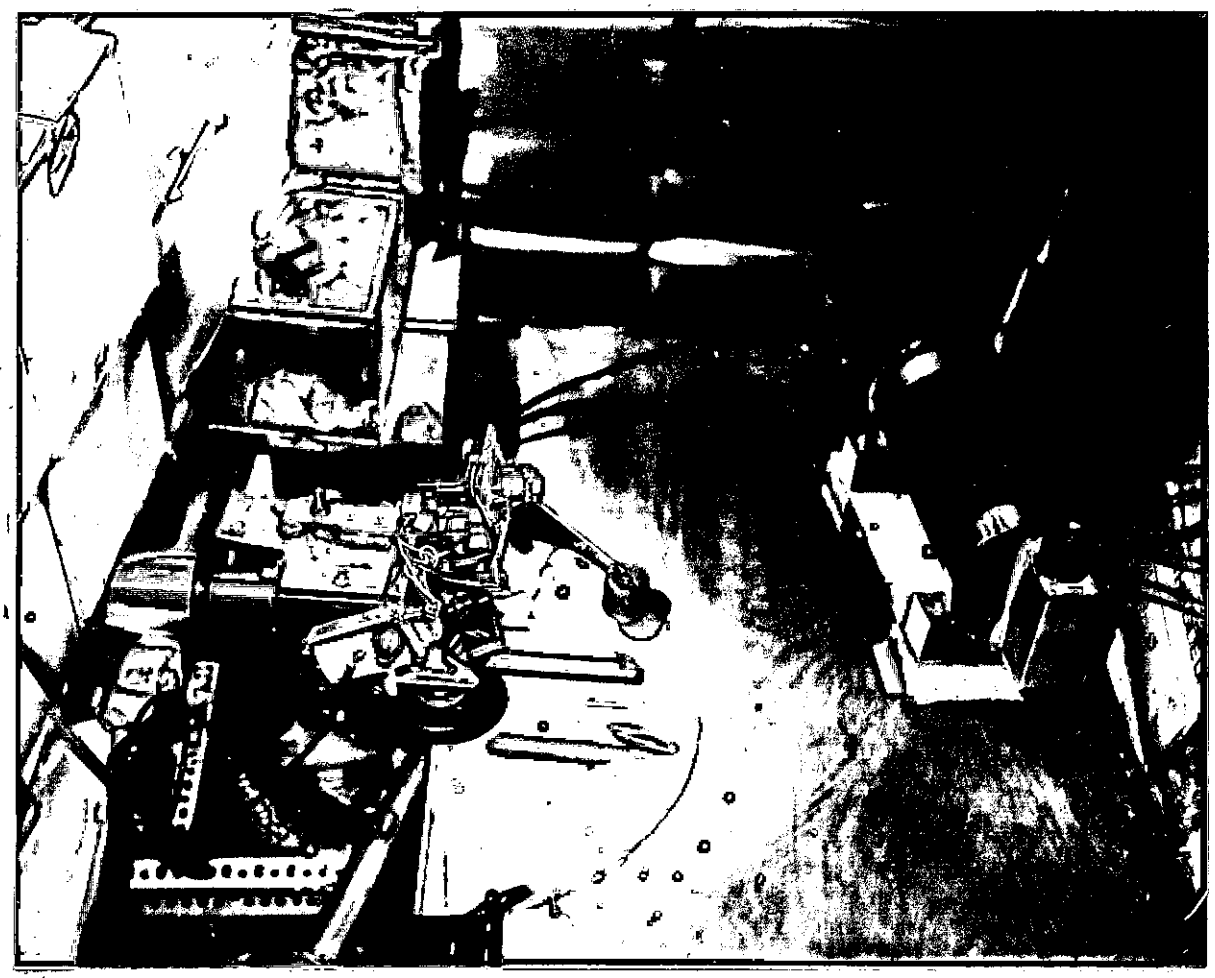

Part of the target room. Position of the scattering sample and beam monitor detector in relation to the beam line, and target chamber is shown at 90^{o} scattering angle.

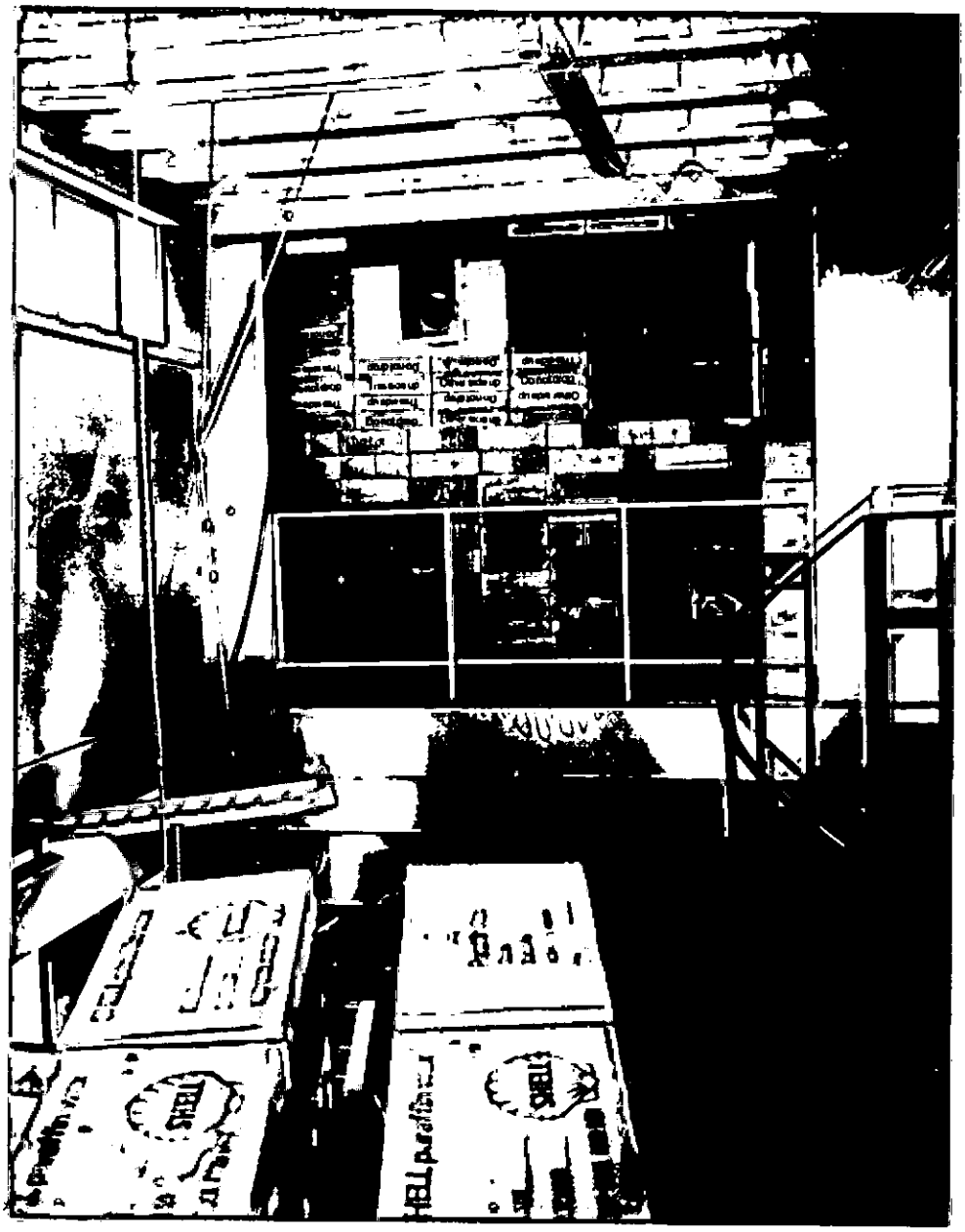

View of the neutron detector room from the collimator position. Part of the extension of the main collimator can be seen at the bottom of the picture.

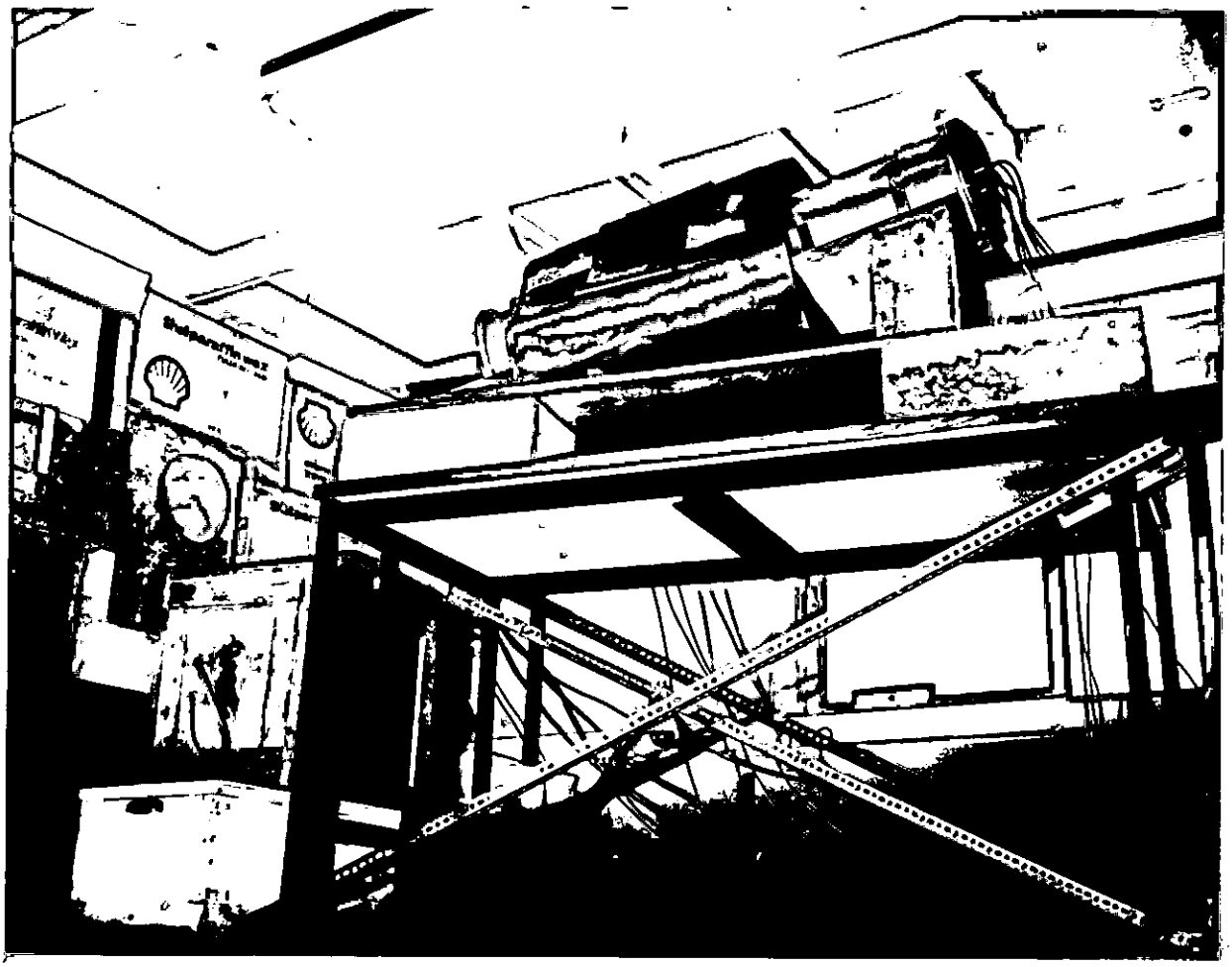

The large neutron detector position at 2.5 metres above the "detector room" floor. The detector collimator made into the paraffin wax wall is also shown.

being seen by the detector.

The choice of scattering sample size was a compromise between achieving high scattered flux and minimising finite sample size effects such as neutron flux attenuation and multiple scattering, whereas target to sample distance was governed by the size of the neutron cone at the scattering sample position and the angular range over which measurement is to be performed. Sample to neutron detector distance was chosen on the basis of the distance required to achieve the desired energy resolution and space available in the laboratory.

To change the scattering angle the scattering sample was rotated around the neutron producing target, by rotating the target chamber and the scattering sample fixed to it, around the beam line axis in the scattering plane, while the neutron detector and its associated shielding stays stationary at a fixed position.

Having determined the dimensions of target-scattering sample, neutron detector geometry, a full size layout of the target-scatterer region was drawn to establish the dimensions of the neutron collimator aperture to cover the whole angular range of interest and to ensure that the neutron cone monitor, which is moved around the target assembly in the same manner as the scattering sample, can not be "seen" by the neutron detector at any particular scattering angle between 20° - 160°.

On the question of the design of the neutron detector a compromise was made between detection efficiency and time resolution of the detector. On the basis of this compromise a very large neutron detector, consisting of 8 litres liquid scintillator, was

designed and made for the present work, which meets both requirements of high efficiency and good timing properties.

More than 6 tonnes of paraffin wax and a ton of concrete was used for containing unwanted neutron background at the target area, neutron collimation, and shielding the neutron detector.

Two other neutron detectors, designed for handling high counting rates, were made. These detectors were used for neutron monitoring, normalization and test purposes.

A table shape platform 75 cm × 150 cm, positioned near the target chamber parallel to the reaction plane, supports the neutron cone monitor detector in the reaction plane, Fig. (2.2).

2.3 $^{3}H(d,n)^{4}_{2}He$ As Neutron Producing Reaction

The 14.1 MeV neutron beam used for this study was supplied through the $^{3}H(d,n)^{4}He$ reaction. Neutrons of energies up to 30 MeV have been produced by this reaction[38] which is attractive in many ways. The very high Q value of the reaction, 17.586 MeV, makes possible the production of high energy neutrons with relatively low input energy. Because of this high Q value, the neutron energy is relatively insensitive to the angle of emission for the region of low deuteron bombarding energy, and high reaction cross-section. At a deuteron energy of 250 keV the neutron energy varies around 14.1 MeV at 90° by only about 7%. The alpha particle produced in the reaction associated with 14.1 MeV neutrons has an energy of 3.7 MeV and makes this reaction particularly attractive for high energy neutron time of flight experiments with low energy accelerators.

Figs. 2.3 - 2.5 show the kinematics of the D-T reaction calculated from the formulation given by Marion and Young[39].

2.4 $^{3}H(d,n)^{4}_{2}He$ Reaction Chamber Assembly

Fig. (2.6) shows a sectional view of the $^{3}H(d,n)^{4}_{2}He$ reaction chamber for the production of 14.1 MeV neutrons. The chamber was rectangular of 198 mm length and 100 mm width, made of stainless steel, which has a much smaller fast neutron cross-section per unit of strength than other materials such as aluminium alloy or brass. A cylindrical steel tube of 60 mm external diameter, fixed to one side of the chamber, coupled it to the deuteron beam line and a nearby cold trapped vacuum pump.

The target, supplied by Amersham International, consisted of a tritium impregnated titanium layer on a copper backing. The target was soft soldered onto the centre of a thin copper target holder of 70 mm diameter, which is in turn fixed to a circular stainless steel base. A pair of tubes attached to this base provides sufficient water cooling to avoid thermal outgasing of tritium from the titanium. The target holder was attached to the chamber by means of four hand tightened screws allowing easy access to the target. The angle between the target holder disc and the incident deuteron beam is 35°. This disc is electrically isolated from the chamber by a rubber O ring and insulating inserts around the screws to make an approximate measurement of beam current possible. The focused deuteron beam of 250 keV

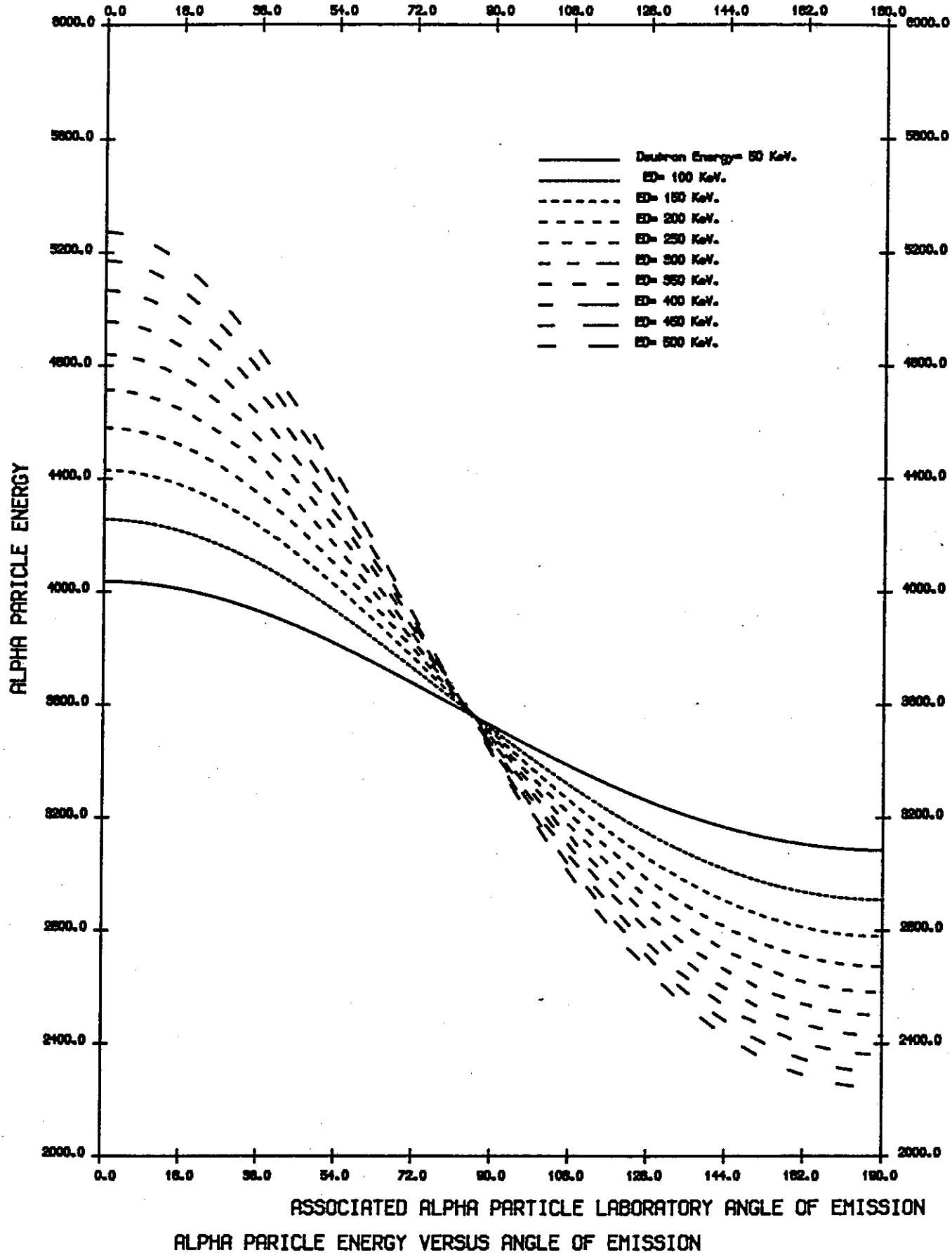
Deuteron Energy= 50 KeV.
ED= 100 KeV.
ED= 150 KeV.
ED= 200 KeV.
ED= 250 KeV.
ED= 300 KeV.
ED= 350 KeV.
ED= 400 KeV.
ED= 450 KeV.
ED= 500 KeV.
ALPHA PARICLE ENERGY
ASSOCIATED ALPHA PARTICLE LABORATORY ANGLE OF EMISSION
ALPHA PARICLE ENERGY VERSUS ANGLE OF EMISSION

Figure 2.3.

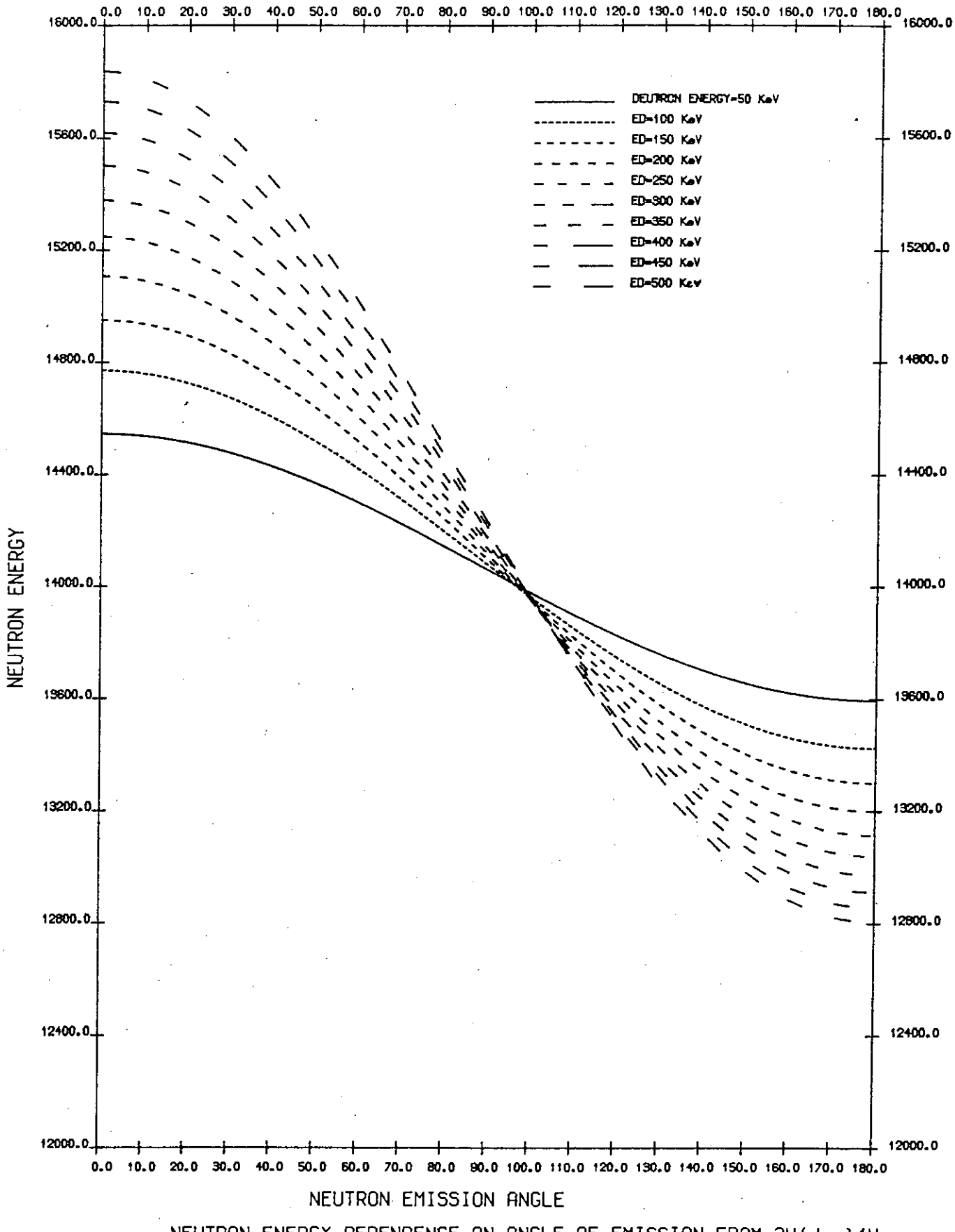
DEUTRON ENERGY=50 KeV
ED=100 KeV
ED=150 KeV
ED=200 KeV
ED=250 KeV
ED=300 KeV
ED=350 KeV
ED=400 KeV
ED=450 KeV
ED=500 KeV
NEUTRON ENERGY
NEUTRON EMISSION ANGLE
NEUTRON ENERGY DEPENDENCE ON ANGLE OF EMISSION FROM 3H(d,n)4He

Figure 2.4.

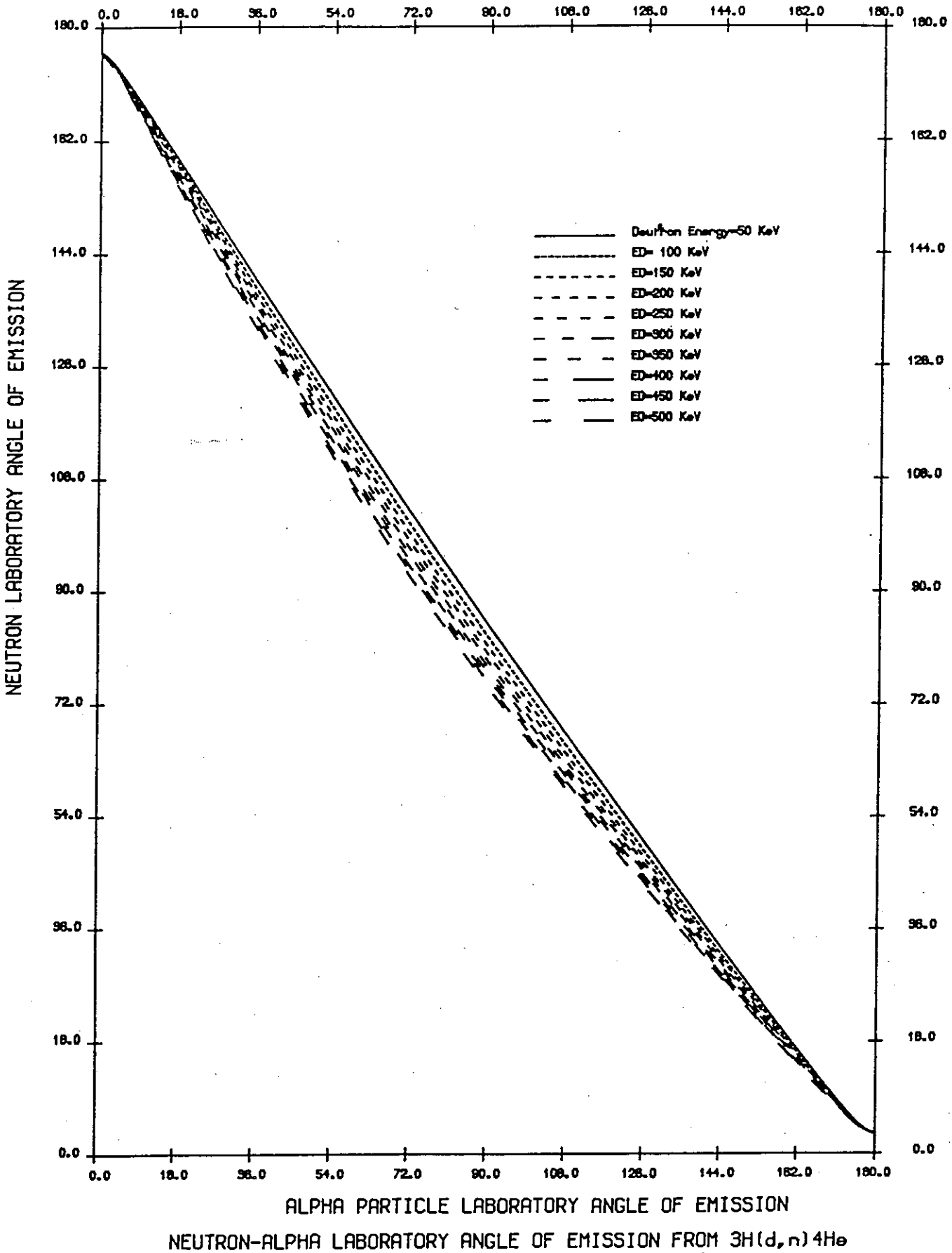
0.0
18.0
36.0
54.0
72.0
90.0
108.0
126.0
144.0
162.0
180.0
Deuteron Energy=50 KeV
ED= 100 KeV
ED=150 KeV
ED=200 KeV
ED=250 KeV
ED=300 KeV
ED=350 KeV
ED=400 KeV
ED=450 KeV
ED=500 KeV
NEUTRON LABORATORY ANGLE OF EMISSION
ALPHA PARTICLE LABORATORY ANGLE OF EMISSION
NEUTRON-ALPHA LABORATORY ANGLE OF EMISSION FROM 3H(d,n)4He

Figure 2.5.

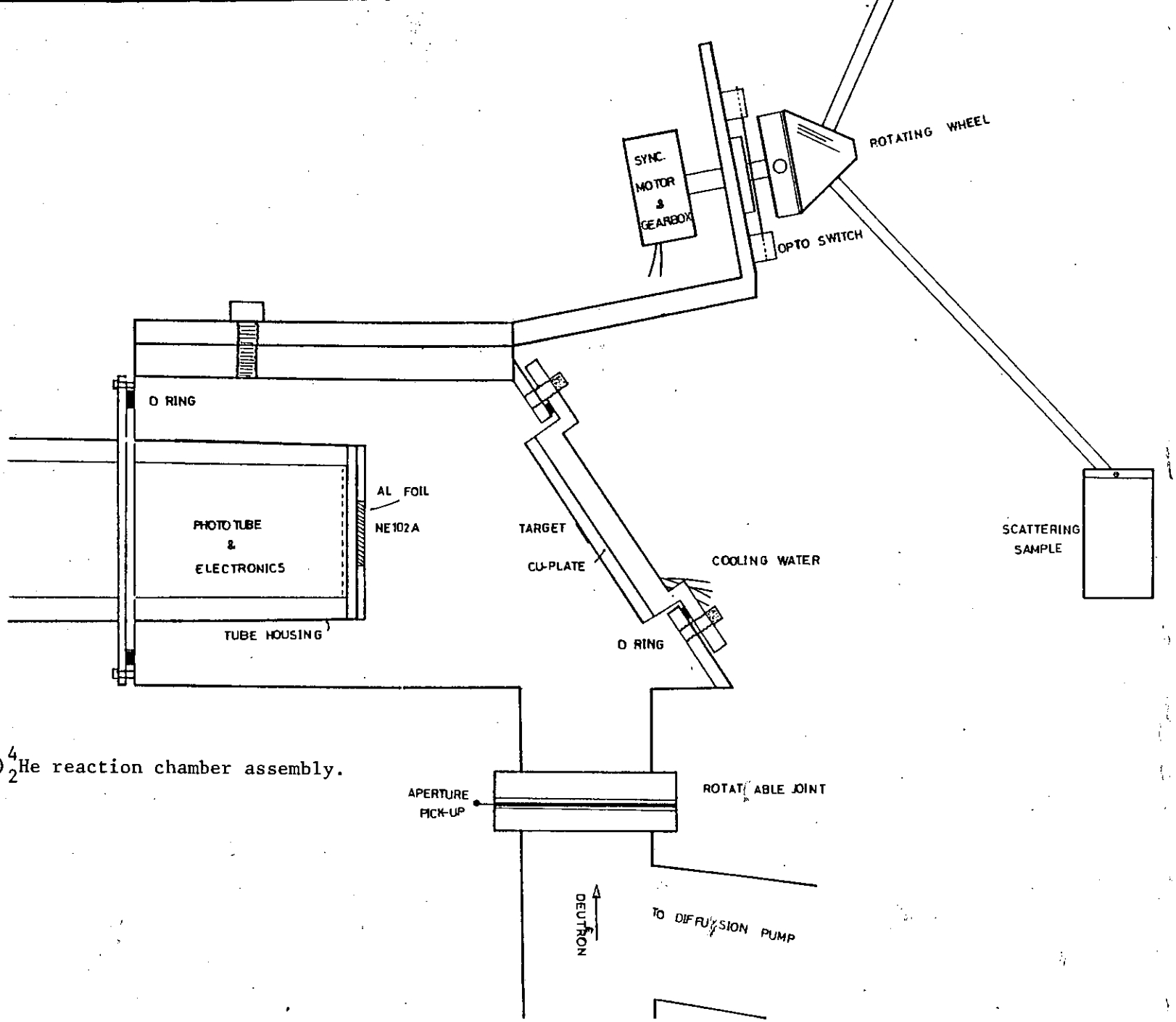

Figure 2.6: $^{3}_{1}H(d,n)^{4}_{2}He$ reaction chamber assembly.

energy bombards the target through a 2 mm diameter aperture in a circular aluminium disc fitted in the beam line at a distance of approximately 20 cm from the target centre. This aperture is also electrically isolated from the rest of the beam line and deuteron current on it was used to optimise the accelerator condition and the deflection angle.

Although the $^{3}H(d,n)^{4}_{2}He$ reaction has a maximum yield at 100 keV deuteron energy, the 250 keV deuteron energy chosen, was a compromise between the quality of accelerator focus and obtainable yield. Below this energy the beam focus deteriorates. In addition the use of a low energy deuteron beam was beneficial in order to reduce heat produced in the deflecting magnet. The energy loss of 250 keV in Titanium is 88 keV[40]. The average deuteron energy is therefore estimated to be 200 ± 50 keV and the yield obtained at this energy was found to be adequate.

An aluminium plate with a rectangular aperture of 25 mm height and 12.5 mm width and at a distance of 84 mm from the centre of the target defines the associated alpha particle cone. The cone is centred on an angle of (80° ± 0.5°) to the incident deuteron beam. The $^{4}_{2}He$ particle detector is discussed in detail in Section 2.5. A thin scintillator was used with the scintillator on the inside of a window in the vacuum chamber. The photomultiplier was fitted into a light tight aluminium tube and bolted to the reaction chamber in contact with the window. The light tight tube conveniently houses a 2" photomultiplier (56 AVP) and the photomultiplier base. This arrangement makes access to the alpha detector photomultiplier

assembly possible without disturbing the vacuum system.

The neutron beam associated with the detected $^{4}_{2}He$ particles is emitted at an angle of 88°degrees relative to the incident deuteron beam. The energy of alpha particles and that of neutrons at these angles is 3.7 MeV and 14.1 MeV respectively, Figs. (2.3) - (2.5).

2.5 The Associated Alpha Particle Detector

There are few reactions other than $^{3}H(d,n)^{4}_{2}He$ that might take place in the tritium target[41,42] and result in other particles in addition to $^{4}_{2}He$ particles. These particles are, namely:

(i) Primary or scattered neutrons

(ii) Coulomb scattered deuterons

(iii) ^{3}He particles from the $^{2}H(d,n)^{3}He$ reaction and tritons from the $^{2}H(d,p)T$ reaction, both of which are due to the drive in deuterons.

(iv) $^{4}_{2}He$ from the $^{3}He(d,p)^{4}_{2}He$ reaction

(v) Protons from $^{12}C(d,p)^{13}C$ reaction originating from carbon deposited on the target.

The alpha detector has, however, negligible efficiency for either scattered or primary neutrons due to the detector thickness.

To reduce the large number of elastically scattered deuteron and to exclude light from the target, a piece of aluminium foil of 0.0025 mm thickness was introduced in front of the NE102A plastic scintillator.

The reactions pointed out above ((ii) to (v)) have comparatively low cross section[43]. In fact, since the target life time was very short due to the oil contamination, possibly from vacuum pumps, there was hardly enough time for significant deuteron drive in process to occur and therefore the contribution of $^{2}H(d,n)^{3}He$ and $^{2}H(d,p)T$ reactions is negligible. All particles, including $^{4}_{2}He$ particles coming through the aluminium foil deposit some energy and the detector's thickness is chosen so that particle discrimination can be made.

The range of deuterons of 250 keV energy in aluminium foil is estimated to be 0.0023 mm[40], and thus they are stopped within the foil. Alpha particles from the D-T reaction, however, reach the scintillator with 3.3 MeV energy after losing 0.43 MeV in the foil[44] and therefore have a range of 0.01 mm in the plastic scintillator[45] in which they are detected with 100% efficiency.

The scintillator NE102A, of 0.8 mm thickness, was the thinnest available (supplied by Nuclear Enterprises, Edinburgh), chosen in order to reduce the detection of primary neutrons and protons to a minimum.

The neutron detection efficiency of the alpha detector was calculated to be only 0.3% for 14 MeV neutrons, using either the Drosg formula[46] or that of Fowler et al.[47].

For use as alpha detector initially a disc of NE102A plastic scintillator (Ø25mm × 2 mm) was machined from a large piece of scintillator and polished with perspex polish No. 3, manufactured by I.C.I. Due to its excessive thickness, however, this detector was found to be more sensitive to primary neutrons with the detection

efficiency of 0.7%. The detector was particularly sensitive to the product of the $^{12}_{6}C(d,n)^{13}_{7}N$ reaction which leads to the emission of a positron from $^{13}_{7}N$. From the increase in yield of positrons or possibly annihilation photons as the running progressed and from the half life of $^{13}_{7}N$ ($\sim$ 10 minutes), it was concluded that the $^{12}_{6}C(d,n)^{13}_{7}N$ reaction was involved. As the solution to this problem which could increase random background, thin NE102A plastic scintillator commercially available from Nuclear Enterprises Ltd. was used.

To cope with the high alpha counting rate, which can easily cause saturation in the photomultiplier and therefore result in pulse height instability, a special dynode chain had to be designed for the associated alpha particle detector. High power Zener diodes were employed between photocathode and first dynode where focusing of the photoelectrons is of great importance and also over the last five stages of the tube where space charge saturation is more likely to occur. The tapered voltage distribution at the end of the tube ensured unsaturated fast signals suitable for timing application. To achieve a high degree of stability the chain design provides a current of 100 times that of average current at the anode. Fig. (2.7) shows the dynode chain designed to handle counting rates of more than 3×10^5 c/sec.

The alpha detector with thinner scintillator and the newly designed dynode chain were carefully tested to examine the performance of the detector at high counting rates. The behaviour of the detector proved to be satisfactory and no serious saturation of the photomultiplier tube due to the high counting rate was observed. Fig. (2.8) demonstrates the alpha spectrum from

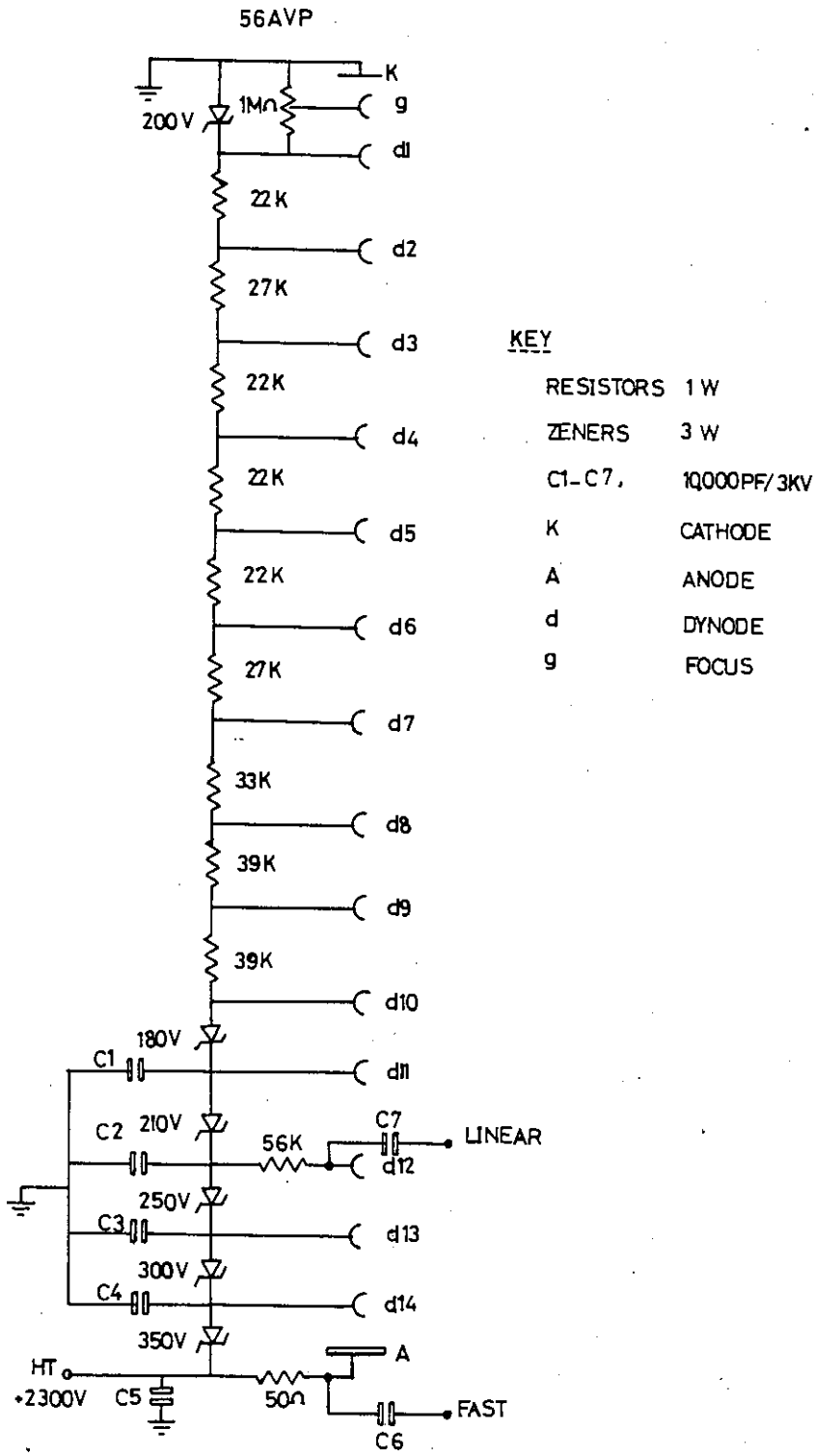

Figure 2.7: Associated particle detector dynode chain.

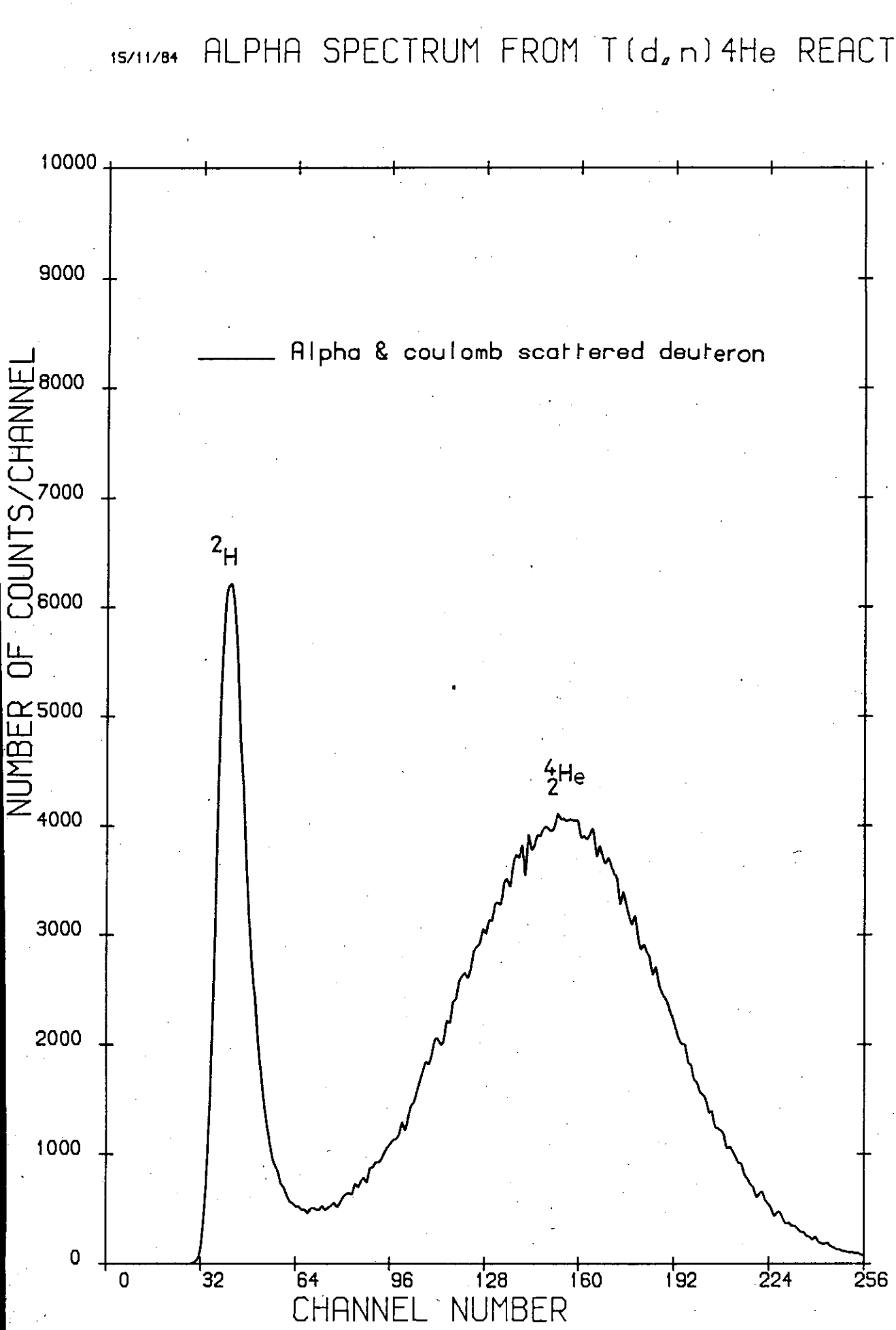
15/11/84 ALPHA SPECTRUM FROM T(d,n)4He REACTION
Alpha & coulomb scattered deuteron
$^{2}_{1}H$
$^{4}_{2}He$
NUMBER OF COUNTS/CHANNEL
CHANNEL NUMBER
10000
9000
8000
7000
6000
5000
4000
3000
2000
1000
0
0
32
64
96
128
160
192
224
256

Figure 2.8.

$^{3}H(d,n)^{4}_{2}He$ reaction.

The timing performance of the associated alpha particle detector was also tested, together with one of our large neutron detectors (Chapter 3) (Ø20 cm × 5 cm), NE224 liquid scintillator. The test was carried out by detecting direct 14.1 neutrons from the $^{3}H(d,n)^{4}_{2}He$ reaction at about 13 metres flight path. A time resolution of almost 1 nano second (10^{-9} second) (FWHM) was achieved with approximately 2 MeV proton energy threshold. This time spread includes all sources of time spread such as neutron flight path spread, due to the finite size of the neutron detector, alpha particle flight path spread, and time spread as a result of the electronics triggering.

The block diagram for the time resolution test is shown in Fig. (2.9).

2.6 The Three Position Sample Changer Hardware and Electronics

A. Hardware

Change of scattering sample to reference sample and removing the sample from the neutron beam for background determination could be achieved automatically by means of the sample changer and its associated electronics. This automation was essential to avoid the hazardous procedure of changing the scattering sample manually in the presence of the high neutron flux from the tritium target.

Fig. (2.10) shows the sample changer hardware. It consists of three identical Ø25 mm ID and 5 mm depth cup holders. Each cup is vacuum brazed to a stainless steel tube arm. The three

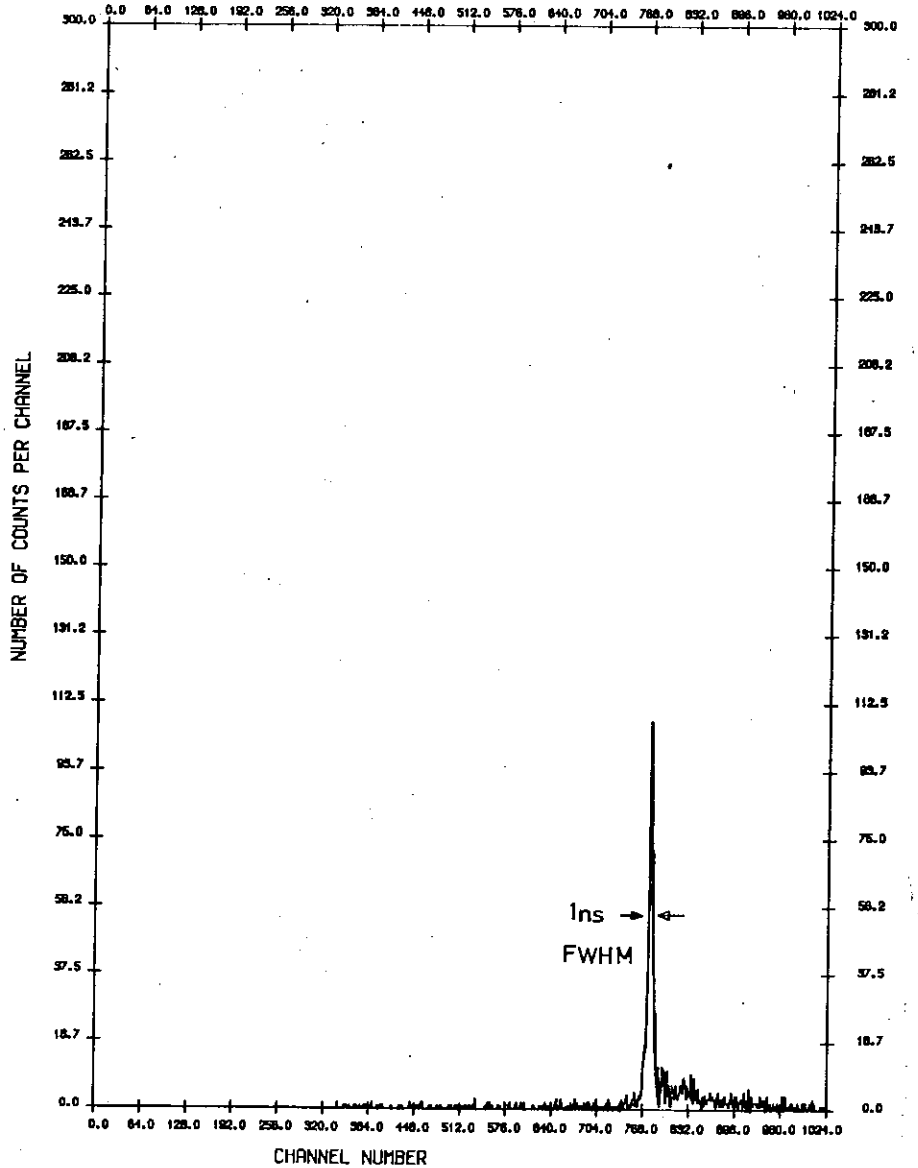

(a)

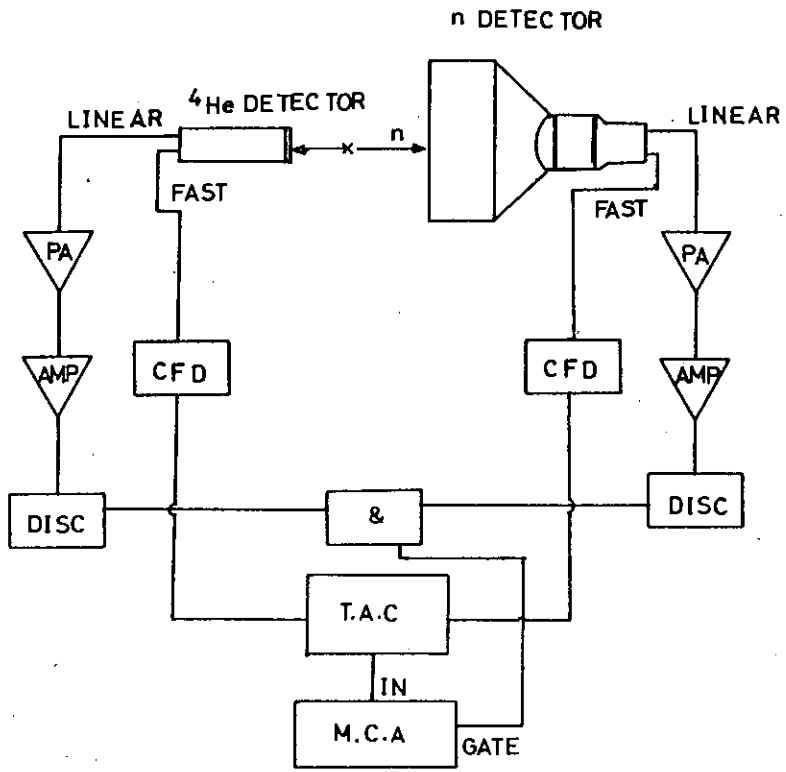

Figure 2.9a, b: Electronics block diagram for the time resolution test and the coincidence timing spectrum.

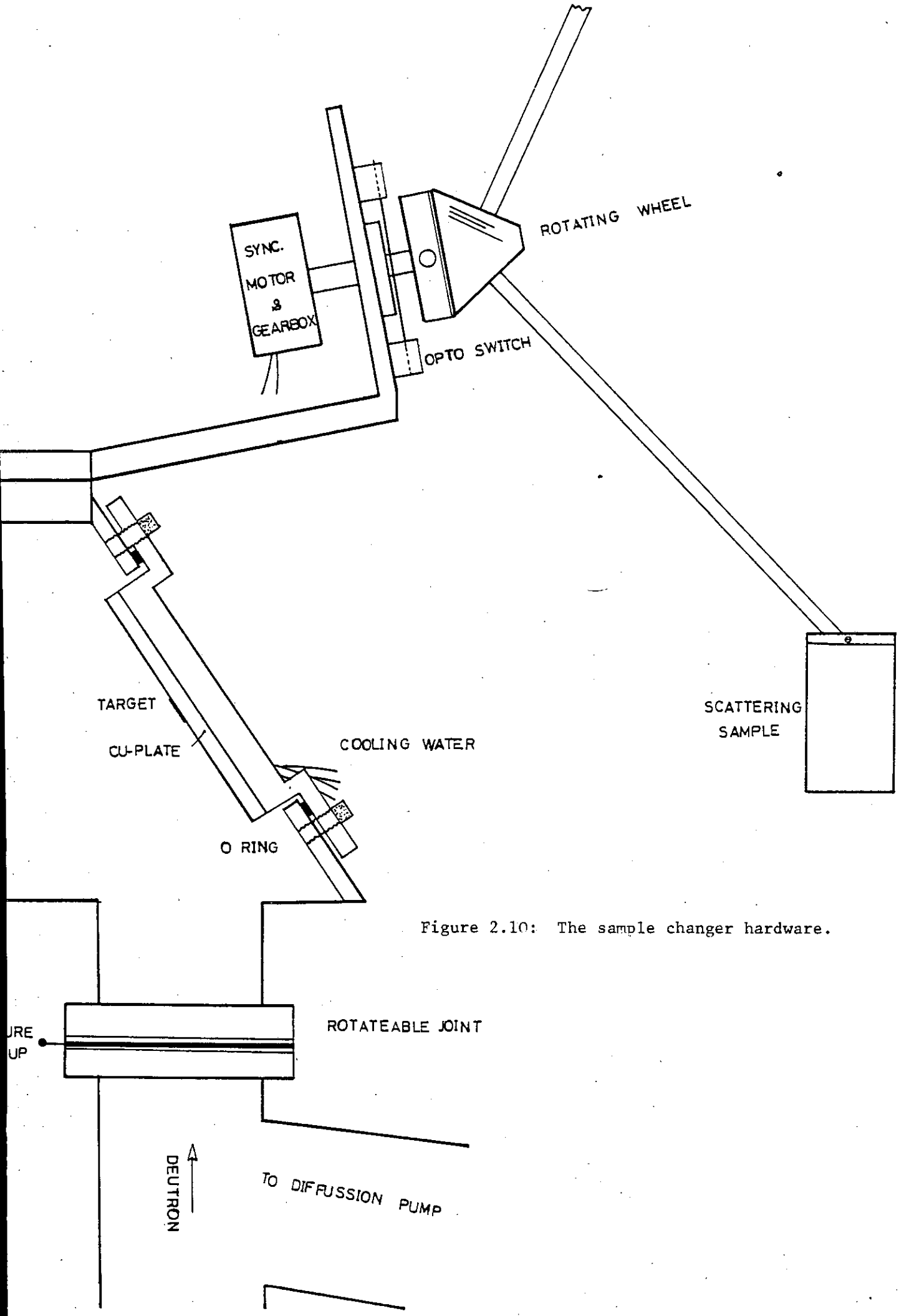

Figure 2.10: The sample changer hardware.

stainless steel tubes are inserted into three holes made round a conical shaped wheel at 120° intervals. Sample arms are held firmly inside these holes by means of a compressed O ring mechanism.

An electric synchronous a.c. motor and gearbox drive system, rotates the wheel with a speed of 1 revolution per minute when it receives a signal from the pulse height analyser (NE4694) through the control electronics unit which is especially designed and built for this experiment.

The accurate positioning of scattering samples is achieved by using three opto slots. A perspex disc rotating on the same axis as the sample changer is continuously passing through the opto slots and with a light barrier black tape on the edge of it, can intercept the infra-red light and trigger the slotted opto switch. The position of the opto switches on the fixed body of the sample changer can be accurately adjusted to result in precise positioning of the scattering sample inside the neutron cone.

A small bearing supports the wheel's shaft inside the main body of the sample changer. The whole mechanism, made of aluminium, is fitted on top of the reaction chamber making an angle of about 10° with the top surface of the chamber. The design allows easy alteration of target to sample distance and movement of the sample in three dimensions.

B. Solid State Control Electronics

Fig. (2.11) shows the solid state control electronics of the sample changer. The operating sequences are the following:

The electric a.c. motor stays on until one of the three positions sensed by the three slotted opto switches is reached, one of these switches is then activated which transmits a logic signal through a pulse driving circuit (2N1711), a Schmitt trigger (7414) and a precision timer (RS2240) to a triac (RS308-196) which controls the power to the motor. The motor is then switched off and both (400 Laben and NE1024) analysers and the scalers are switched to "COUNT" mode by the timer signal. The information provided by the status of the three opto switches (3 bit word) is simultaneously used by a 74139 (2-to-4 decoder/Multiplexer) for routing the data to the appropriate subgroup and appropriate scaler.

After the preset time governed by the RS2240 programable timer elapses analysers and scalers are switched to "STOP" mode and the motor is switched "ON" through the triac.

The status of the sample changer and the motor is displayed by three light emitting diodes (LED) on the front panel of the sample changer control unit in the control room of the accelerator.

The conventional 74 series TTL logic was used for the control circuitry. It was however necessary to design a special driving unit for automatic operation of the Laben 400 channel analyser which is based on RTL logic circuitry.

Fig. 2.12 shows the interconnection between various parts of the data storage units.

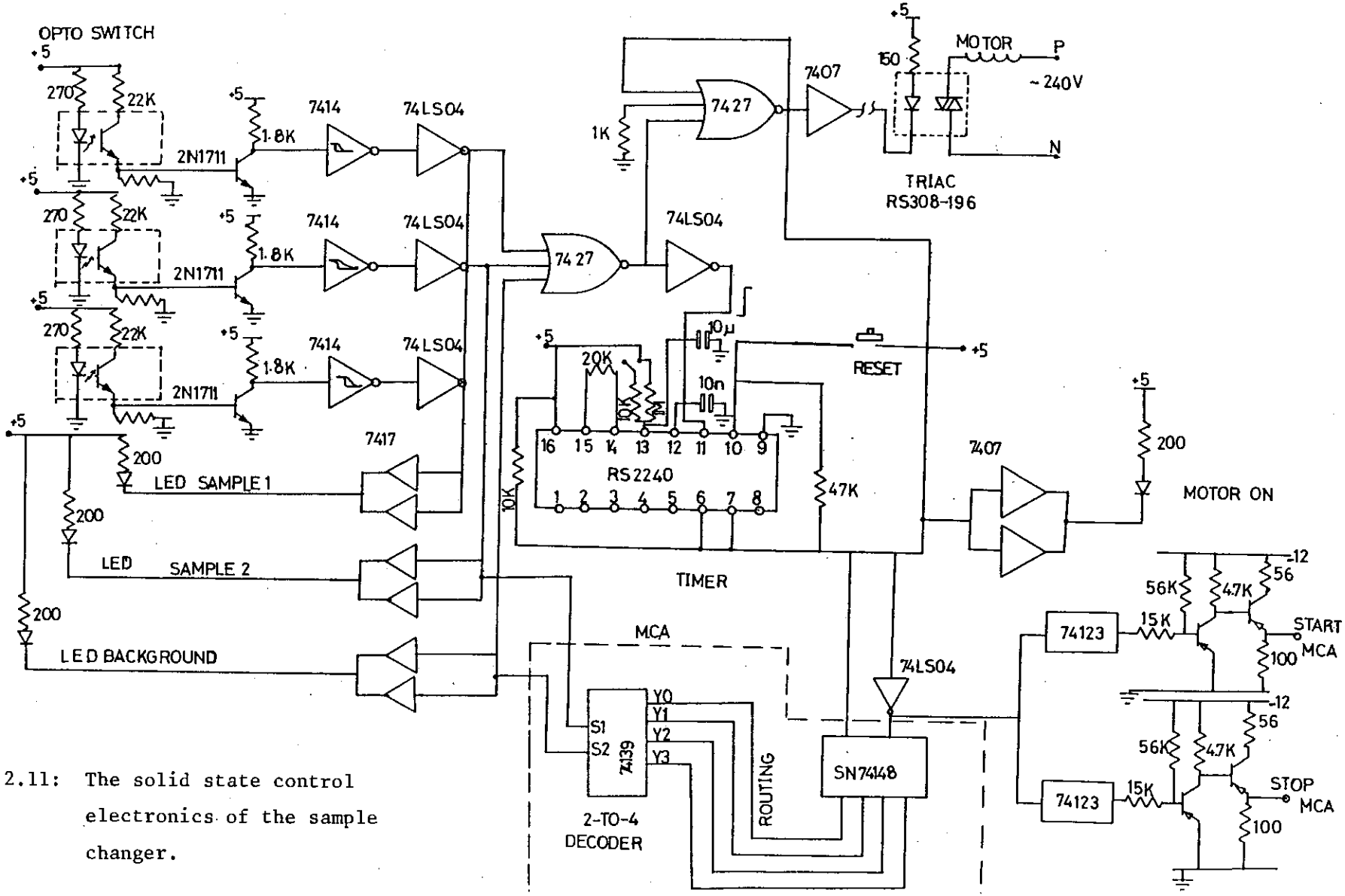

Figure 2.11: The solid state control electronics of the sample changer.

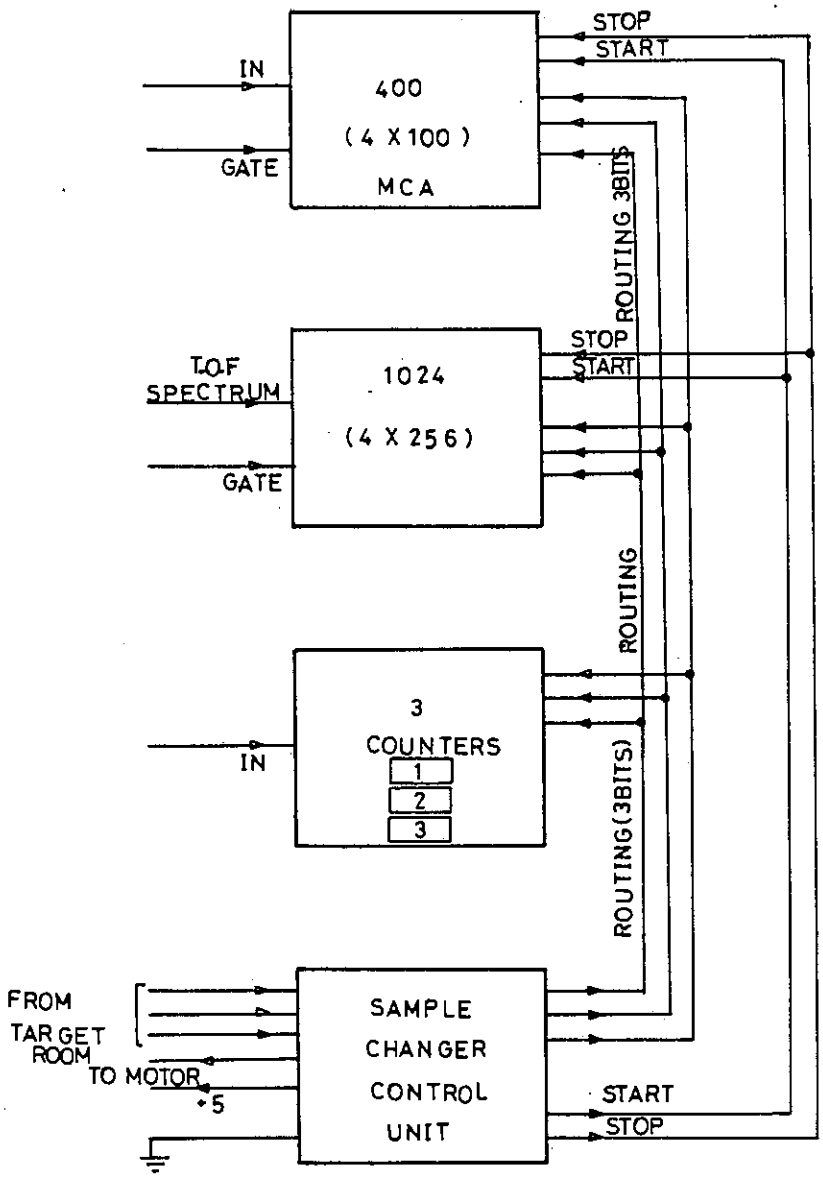

Figure 2.12: The interconnection between various parts of the data storage units.

2.7 Shielding and Collimation for Fast Neutrons

Measurement of elastic and inelastic differential cross-section for fast neutrons involves severe shielding problems.

To demonstrate the severity of the problem of reducing unwanted neutron flux at the detector position a comparison can be made between the number of sample neutrons and source neutrons at the neutron detector position. An estimate[48,49] of the number of scattered neutrons may be obtained from the equation:

$$s\varepsilon = I\Omega_1[1 - \exp(-N\sigma_T)][\sigma_s(\theta)/\sigma_T]\Omega_2\varepsilon \qquad (2.5)$$

where I is the number of neutrons emitted per second per steradian in the direction of the scattering sample, and Ω_1 is the solid angle subtended by the scattering sample at the primary neutron source. The scatterer interacts with the fraction $[1 - \exp(-N\sigma_T)]$ of the incident neutron flux, where N is the number of scattering nuclei/cm^2 and σ_T is the neutron total cross-section. The portion of the neutron flux which interacts with the scattering nuclei and scatters through the angle θ into the unit solid angle in the direction of the neutron detector is just $\sigma_s(\theta)/\sigma_T$. The detector which subtends the solid angle Ω_2 from the scattering sample has an efficiency ε.

To assess the shielding efficiency required for low cross-section measurement experiments, the numerical value of the signal to background ratio was estimated as follows:

Primary neutron source	$^{3}H(d,n)^{4}_{2}He$ reaction
Typical yield	$\approx 10^{7}$ neutron/sec.μA.
Detector diameter	20 cm
Detector efficiency	10%
Sample size	5 cm × 5 cm diameter
Magnitude of the cross-section under investigation	10 mb/sr
Source to scatterer distance	$\approx$ 20 cm
Scatterer to detector distance	1300 cm.

If air scattering attenuation was assumed to be negligible, scattered neutrons from the scattering sample using equation (2.5) would amount to:

'Sample' neutrons = 10.8 Counts/hour.μA.

Direct neutron flux from the source to detector in the absence of any shielding would be

'Direct flux' $\approx$ 2×10^{5} Counts/hour.μA

and hence

Sample scattered flux/ Direct flux = 50×10^{-6}.

To achieve a ratio of scattered neutron yield to background of at least 100:1, it can easily be seen that an attenuation of the order of 10^{6} of direct neutron is essential for high sensitivity cross-section measurements of about 10 mb/sr. To attenuate the direct neutron flux by a factor of 10^{6} before it reaches the detector, a minimum thickness of 250 cm of paraffin wax is required[49].

Fortunately the geometry of the experiment allows the use of such a massive bulk of paraffin wax between target and the neutron detector. In addition, since previous considerations[50] have shown that it would be advantageous to keep the neutron detector in a fixed position and change the direction of the incident neutrons by turning the target and scattering sample around an axis (Fig. (2.10)), this arrangement allows sufficient build up of shielding at the vicinity of the fixed neutron detector.

In the present work attention was focused on two major points:

(a) Suppressing the background due to the source neutrons in the target area in order to reduce the release of neutrons towards the neutron detector direction.

(b) Reducing neutron and gamma background at the detector area.

Fig. (2.1) and Fig. (2.2) illustrate the shielding and neutron collimation arrangement in detail.

2.7.1 Shielding material

Two essential criteria must be met by an appropriate type of shielding:

The attenuation for fast neutrons should be large and the number of neutrons scattered into the collimator channel by the material of the collimator itself should be small. Materials with a differential scattering cross-section highly peaked in the forward direction scatter the incident neutrons deep into the collimator

channel with negligible energy loss. Heavy materials like Iron, Copper, Tungsten and Lead behave in such a way[50]. On the other hand, for neutron energies above 3 MeV, these materials attenuate the neutron flux density more than lighter materials, and therefore, their use is certainly advantageous in close geometry experiments.

As shown in Fig. (2.1) most of the shielding material used in this work is high melting point paraffin wax. This is due to the relatively low expense of paraffin wax and the simplicity of shaping and casting it into any desired shape of collimator. Paraffin wax does not, however, attenuate fast neutrons as much as heavy materials of the same thickness, as outlined above.

Using the macroscopic non-elastic absorption coefficient given in (49), an estimated 250 cm length of paraffin wax was needed to achieve attenuation of direct neutron by 10^6.

2.7.2 Collimator and Shielding at the target area

Fig. (2.1) shows collimator and shielding at the target area. A small room (approximately 1.5 m × 2.0 m) built around the target and the scattering sample, confined most of the unwanted neutrons inside the target room. This room consisted of walls made of paraffin wax of at least 50 cm thickness. The thickness of the room in the direction of the neutron detector, however, exceeds 130 cm to provide part of the direct neutron attenuation required.

A very carefully designed and shaped aperture of 14 cm × 40 cm cross-section and 130 cm long plays the role of the preshield neutron

collimator. This collimator was made by casting melted paraffin wax into prefabricated wooden boxes positioned carefully at the desired distance and height from the neutron producing target. The accurate positioning of these boxes was performed prior to filling, using a telescope at the neutron detector position. A first approach to a suitable design of this channel shaped collimator was achieved by simple consideration and calculation based on geometrical optics. A simple ray tracing between the origin of the neutrons (i.e. target) and the scatterer and from the scatterer to where they are detected (i.e. neutron detector) defined the shape of the tapered neutron collimator.

To reduce the scattered background from the entrance part of the preshield neutron collimator, those walls irradiated by primary neutrons were tapered. The taper was made large enough to prevent these walls coming into the detector's view. This is very crucial because otherwise scattered neutrons from the sample may hit the walls of the collimator channel and reach the detector by small angle scattering. This effect would result in additional neutrons reaching the detector due to the collimator itself and it can not be estimated by "sample in - sample out" measurements.

A telescope positioned at the detector end was used to check if the collimator was sufficiently tapered and to ensure that the whole of the detector can view the sample without being obscured by the collimator walls.

In order to reduce the size of the collimator aperture to a minimum, several tapered paraffin wax slab inserts of various

thicknesses were carefully designed and made by casting paraffin wax into especially prepared cardboard boxes with the desired dimensions. Bubbles in the cast were avoided by gradual filling of the boxes. These paraffin slab inserts can be suitably inserted into the channel collimator to adjust the aperture size to be optimum for different scattering angles. The tapered shape of the collimator is preserved even after adding any of these inserts into the collimator.

The collimator channel was extended by a further 150 cm by especially arranging boxes of paraffin wax to form an additional collimator and therefore provide further attenuation of the direct neutron flux. The wall at the back of the neutron producing target was extended in height to shadow the target and provide biological shielding for the rooms in the vicinity of the laboratory. The overall weight of the biological shielding and neutron collimator was in excess of 6 tonnes which was supported from the laboratory floor and above the accelerator beam line, on frameworks constructed from proprietary steel angle (Dexion).

2.7.3 Collimator and Shielding at the detector area

Neutrons originating in the target may escape from the target room and reach the detection apparatus by scattering from the laboratory walls, air or any shield or apparatus near the detector. Although this type of background is much reduced by limiting the solid angle subtended by target collimator (preshield), it can be

further reduced by a second collimator nearer the detector. This procedure ensured that the target and detector are reciprocally entirely in view and both were well inside the cone defined by the two collimators.

In this work the neutron detector was located in a room at a distance of 13 metres from the target. The detector room is completely separated from the accelerator and target room by a thick (> 50 cm) wall, made in part of concrete and in part of paraffin wax. The detector was positioned at about 2.5 metres above the room floor and a cylindrical channel made into the wall of paraffin wax plays the role of the detector collimator. The cylindrical channel had to be made inside a large (60 cm × 60 cm × 60 cm) wooden box using a cylindrical tube with its axis positioned carefully in correct direction. The box was then filled with melted paraffin wax after it was located in the right position determined by a laser beam set along the detector axis to illuminate the centre of the scattering sample. In the process of filling the channel box the laser beam provided a continuous check on the accurate positioning of the box.

The use of a laser beam for alignment of detector, scattering sample and collimators was found to be advantageous over the use of a telescope, both because of the simplicity of use and its accuracy.

Lead sheet was wrapped round the large neutron detector to a thickness of 5 cm to reduce the gamma ray counting rate due to gamma rays produced by neutron capture in the shielding and other materials near the detector. This reduced the gamma ray counting rate to be dealt with the pulse shape discrimination circuitry discussed in the next chapter.

CHAPTER 3

NEUTRON DETECTORS

3.1 Introduction

The success of the time of flight technique largely depends on the availability of neutron detectors with good timing property. This is because, as was shown in equation (2.2), the energy resolution in the time of flight method is directly proportional to the time resolution of the system. The demand for good energy resolution has thus prompted the development of good time resolution ($\simeq$ 1ns = 10^{-9}s) neutron detectors capable of maintaining reasonable count rates in long flight path ($\gtrsim$ 10m) measurements.

The standard approach to the problem of maintaining sufficient counting rate is to increase the solid angle subtended by the detector through increasing the sensitive volume of the neutron detector. There is, however, a limit to which one can increase the size of the neutron detector, since the uncertainty in neutron detection time and flight path becomes more considerable as detector dimensions increase.

Methods successfully attempted include assembling an array of relatively small good time resolution detectors[51-54]. There are, however, drawbacks concerning an array of several detectors such as complexity in associated electronics and problems in providing good shielding for them against neutron and gamma background.

As a better alternative long plastic scintillator slabs or cylinders containing liquid scintillator viewed from both ends and

compensated for variations in light propagation time and neutron flight path have been reported[55-65]. Goodman et al.[63,66] have demonstrated that it is possible to use only one photomultiplier to view a long scintillator. To compensate for variation in light propagation time and neutron flight path, the detector has to be tilted in relation to the direction of incident neutrons. The tilting angle would depend upon neutron energy.

Since the objective of this work was to design and construct a neutron time-of-flight system with good energy resolution, the design and development of the neutron detector was given special importance. The study initiated by investigating the timing limitation of the components used in a neutron detector, namely photomultiplier and scintillator. The various methods by which the timing signal is derived from the photomultiplier by electronic processing of the scintillation pulse was also studied.

The following describes various tests carried out on a few different scintillator types and sizes and also tests on various types of photomultipliers. The scintillators were all made for this study in our laboratory.

In order to study the relation between scintillator size and the achievable time resolution tests were carried out by observing the coincident gamma rays from a ^{60}Co source with the detector under investigation and a small 2.5 × 2.5 cm diam. NE102A Plastic Scintillator. Fig. (3.1) shows a typical fast coincidence electronics block diagram.

The first test consisted of coupling various sizes of scintillator to the same photomultiplier and therefore studying

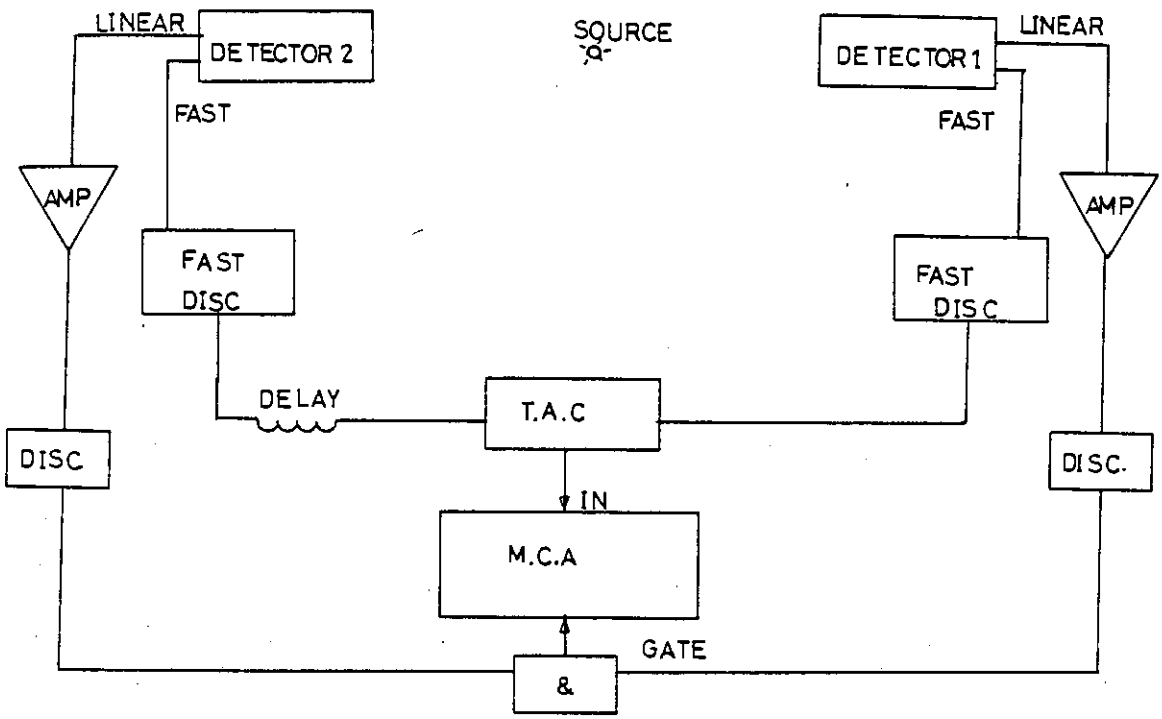

Figure 3.1: A typical fast coincidence system electronics block diagram.

the effect of the scintillator size. Table 3.1 shows how the time spread can increase in a scintillator detector as a function of mere scintillator size.

The addition of a light guide to a scintillation detector system can substantially deteriorate the timing properties of the detector. Table (3.2) demonstrates this effect.

Time spread contribution of the photomultiplier due to the inherent timing properties of the phototube was estimated by using two timing systems with scintillators identical both in type and size. The results are shown in Table (3.3).

To reach the final conclusion about timing limitation of the XP1040 phototube, a test was carried out in which a small Ø2.5× 2.5 cm NE224 scintillator was used. The scintillator was coupled to the centre of the 5" diameter photocathode in order to minimize the time variation due to the transit time spread of electrons between photocathode and first dynode. The best time resolution achieved with this arrangement was 1.4 ns. This test, along with that of Table (3.3), suggested that the XP1040 photomultiplier is not particularly suitable for high time resolution work, especially when a large volume of scintillator is involved.

Comparisons were made between the results obtained with the same size container filled with different scintillators, which suggested that the time resolution obtainable with NE224 is normally up to 35% superior to that of NE213, Table (3.4).

TABLE 3.1

Scintillator type	Size (Cm)	Photomultiplier	Time resolution (ns) FWHM	Comment
NE213	Ø3.5 × 3	EMI9814B	1.10	
NE213	Ø4 × 4	EMI9814B	1.10	
NE213	Ø7 × 152	EMI9814B	1.70	Radiation was limited to end of the scintillator tube near photomultiplier
NE213	Ø7 × 152	EMI9814B	2.8	Radiation was limited to the middle of the scintillator tube.
NE213	Ø7 × 152	EMI9814B	4.0	Radiation was limited to the far end of the scintillator tube.

TABLE 3.2

Scintillator type	Size (cm)	Photomultiplier	Time Resolution (ns) FWHM	Comment
Plastic NE102A	Ø12.5 × 5	XP1040	2.0	NO light guide
Plastic NE102A	Ø12.5 × 5	XP1040	2.7	WITH light guide
NE213	Ø12.5 × 5	XP1040	2.4	NO light guide
NE213	Ø12.5 × 5	XP1040	3.8	WITH light guide

TABLE 3.3

Scintillator type	Size (cm)	Time Resolution (ns) FWHM EMI9814B/XP1040		Position of Radiation
NE213	Ø7 × 152	1.7	2.8	near end
NE213	Ø7 × 152	2.8	5.5	middle
NE213	Ø7 × 152	4.0	10.0	far end

TABLE 3.4

Scintillator Type	Size (cm)	Type of Photo-multiplier	Time Resolution (ns) FWHM
NE213	Ø12.5 × 5	XP1040	2.4
NE224	Ø12.5 × 5	XP1040	1.5

The use of NE102A Plastic Scintillator was not considered since the pulse shape discrimination technique cannot be applied to this scintillator although it is faster than both NE213 and NE224[67].

3.2 The Choice of High Intrinsic Efficiency Detector

Preliminary estimation of the counting rate suggested that the choice of a thick, large volume scintillator to achieve the necessary detection efficiency appeared to be inevitable for the flight path concerned.

Tests described in the previous section provided us with basic information for the design of the neutron detector. On the basis of these results, in an attempt to minimise the contributions of the phototube and the scintillator to time spread, faster phototubes and scintillators were employed.

The initial analytical efficiency calculation (Chapter 4) also predicted detection efficiency proportional to the thickness of the scintillator material for detectors with the same diameter. A thick detector with electronic time compensation in which the time spread

due to the scintillator size is dealt with by time compensation then seemed to be an attractive solution to the problem.

Among the large photomultipliers (≃ 12 cm diameter) available the RCA4522 was selected because it was likely to result in better time resolution due to its rather good timing characteristics. The convex surface of the photocathode of RCA4522 is believed to be useful in reducing electrons' transit time spread between photocathode and the first dynode.

Prior to construction of a thick large volume (Ø20 × 25 cm) detector a thinner version (Ø20 × 5cm) of the detector which does not require any time compensation, was made using the same photomultiplier and scintillator material. Since after the various tests were made, the design proved to be successful, it was then decided to proceed with the construction of a detector 5 times thicker.

The remainder of this chapter is mainly devoted to the detailed description and performance comparison of neutron detectors.

3.3 The Large Single Photomultiplier Detector and Its Performance

3.3.1 Detector description

The single tube large detector light guide configuration consisted of a 20 cm diameter by 5 cm thickness cylindrical cell and a conical shaped light guide, both machined from a single piece of perspex in order to provide a more efficient light collection arrangement. The front flat face of the cell is machined separately and glued to the main body using Ico Cyano Acrylic adhesive

Figure 3.2a: Thin neutron detector.

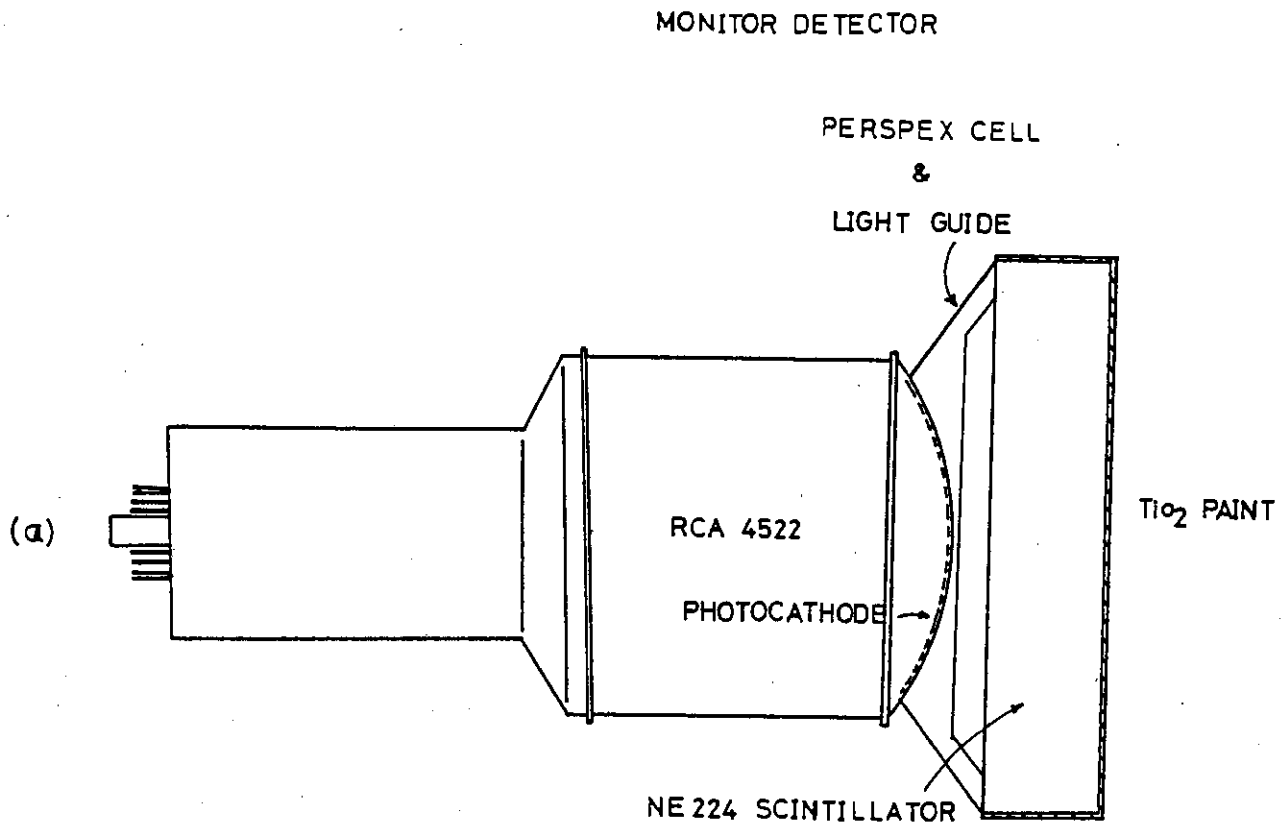

Figure 3.2b: Light tight package.

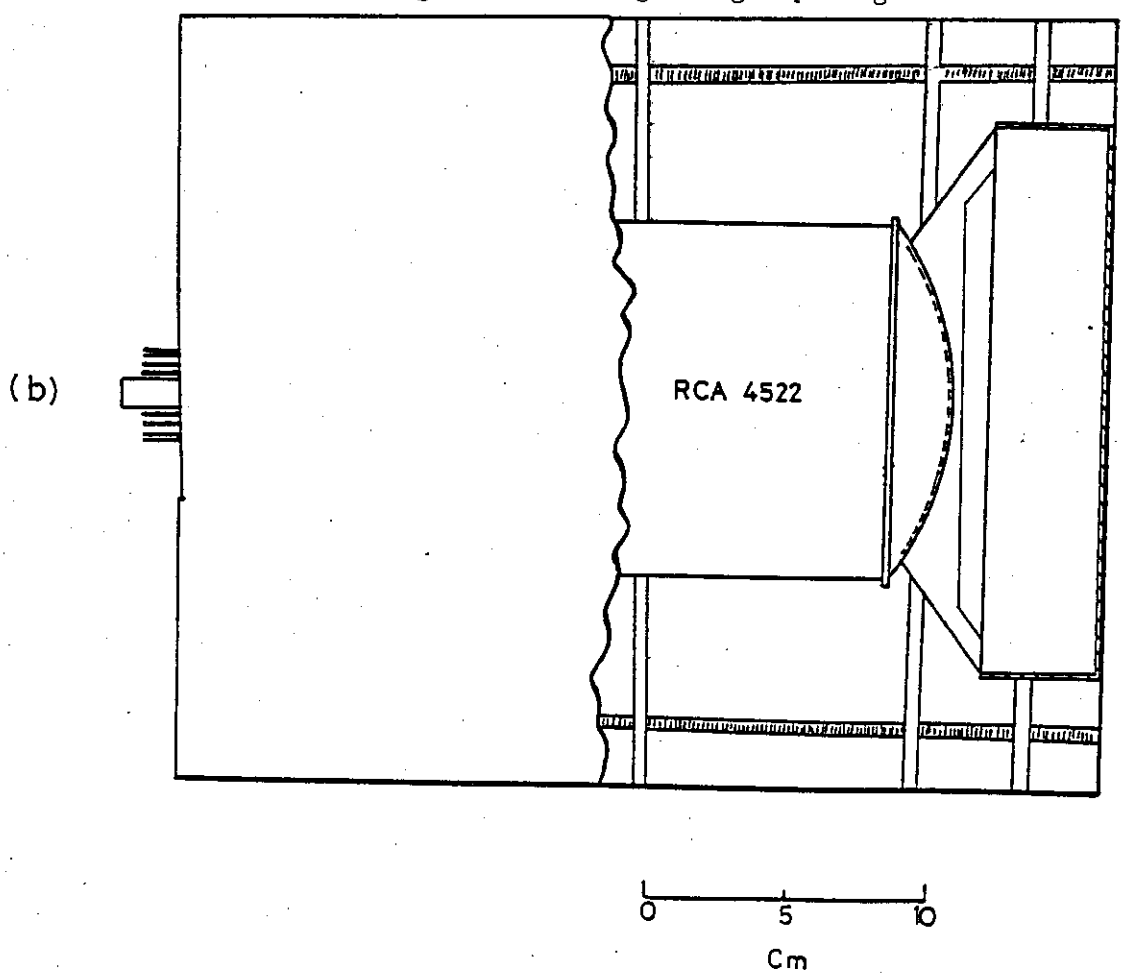

(Superglue). In order to make a perfect optical matching between photomultiplier and the light guide, the 11.4 cm. diameter convex surface of the photocathode envelope the RCA4522 photomultiplier was coupled to the tapered concave end of the light guide using a thin layer of silicon grease. The outer surface of the perspex cell and light guide was painted with TiO_2 reflective paint (NE562) using several thin coatings. The cell was then filled with NE-224 liquid scintillator through a small filling hole in the side of the light guide and then sealed with a stainless steel screw and PTFE washer. No expansion chamber was provided with this detector. A large nitrogen bubble, however, allows for the expansion of the liquid. The existence of the bubble could only be noticed when the detector was used near to vertically rather than horizontally.

The 5 cm thickness of the scintillator cell was chosen to give an acceptable time spread due to flight time of neutrons in the scintillator (0.96×10^{-9} second for 14 MeV neutrons).

Magnetic shielding was also provided for the photomultiplier. The photomultiplier and the scintillator were held firmly together with the special arrangement shown in Fig. (3.2a) and then accommodated in an aluminium light tight box (Fig. (3.2b)).

3.3.2 Dynode chain design

A voltage divider circuit had to be designed specifically for fast pulse application. In fast pulse application the wiring of the dynode chain and, in particular, the wiring of the anode is very critical if linearity and pulse shape are to be preserved.

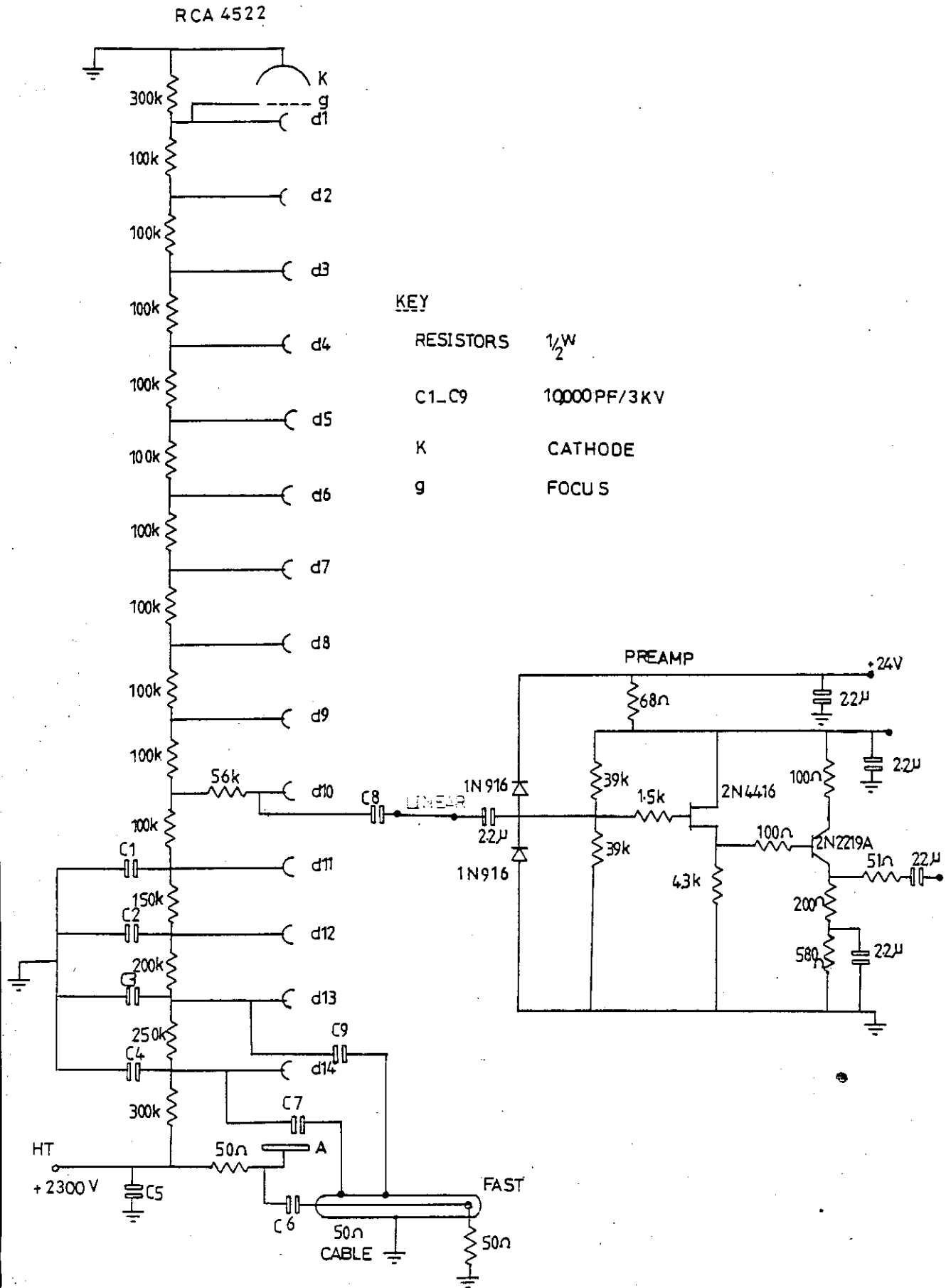

Figure 3.3: The dynode chain and the fast preamplifier for the thin neutron detector.

To ensure the linearity of the tube, when the tube is running at higher voltage for faster anode signal and better transit time spread, or when a large amount of energy is deposited in the scintillator, a tapered voltage divider was designed to overcome the limitation on current output (into a 50Ω system) due to occurrence of space charge at the last few stages. This tapered divider places 3 to 4 times the normal interstage potential difference across the last stage. The progression is gradual in order to maintain proper electrostatic focus between the last few stages. The linearity of anode current had to be ensured as the constant fraction timing was applied. This linearity is equally essential for linear signal for good pulse shape discrimination (P.S.D.) response.

Dynode chain components were mounted on the tube base with no extra lead, that is because stray capacitance resulting from the length of the wire connecting the dynode chain to the tube greatly contributes to the increase in the decay time and to the noise of the tube signal. The dynode chain and the fast preamplifier for the thin neutron detector are shown in Fig. (3.3). This design is a modified version of that suggested by the manufacturer (RCA).

3.3.3 Detector performance

A) Energy calibration and gamma ray response linearity test

Accurate knowledge of the energy calibration of a neutron detector is essential in order to estimate the counting efficiency of the neutron detector for different neutron energies.

Energy calibration was performed by using standard gamma ray sources and calibrating each spectrum in terms of electron energy. For photon energies up to 3 MeV Compton scattering dominates in the NE224 scintillator and mono energetic gamma radiation produces recoil electrons having energies up to a maximum of:

$$E_c = \frac{2E_\gamma^2}{(0.511 + 2E_\gamma)} .$$

This yields the well known Compton distribution with a sharp edge (Compton peak). Prescott and Rupall[68] and Beghian and Wilensky[69] have concluded that the $^2/_3$ point of the sharp edge of the Compton distribution is the best estimate of the maximum electron recoil energy.

The $^2/_3$ point of ^{22}Na, ^{137}Cs and ^{60}Co gamma spectra Compton edges were therefore used to determine the energy calibration and the linearity of response of the large scintillator, photomultiplier dynode chain and its associated electronics.

As Fig. (3.4) suggests energy resolution of the detector is remarkably good for such a large scintillator. Fig. (3.5) shows a typical linear relation in detector response to the gamma radiation with different energies.

B) Time resolution performance test

A test of the timing properties of the detector was made with a ^{60}Co gamma source using a small 2.5 × 2.5 cm NE224 scintillator mounted on a RCA8575 photomultiplier as a second detector to form a fast coincidence system. Fig. (3.6) shows the block diagram of

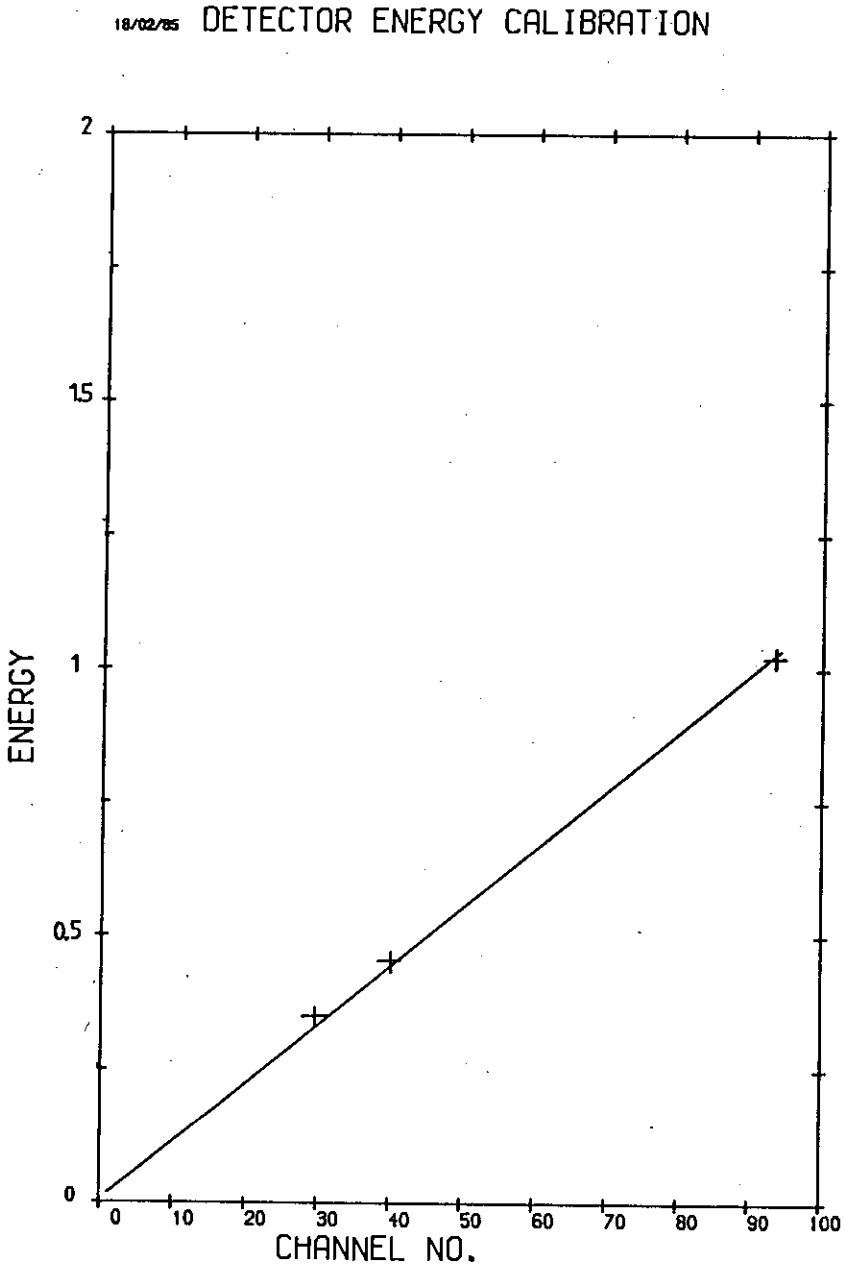

Figure 3.5

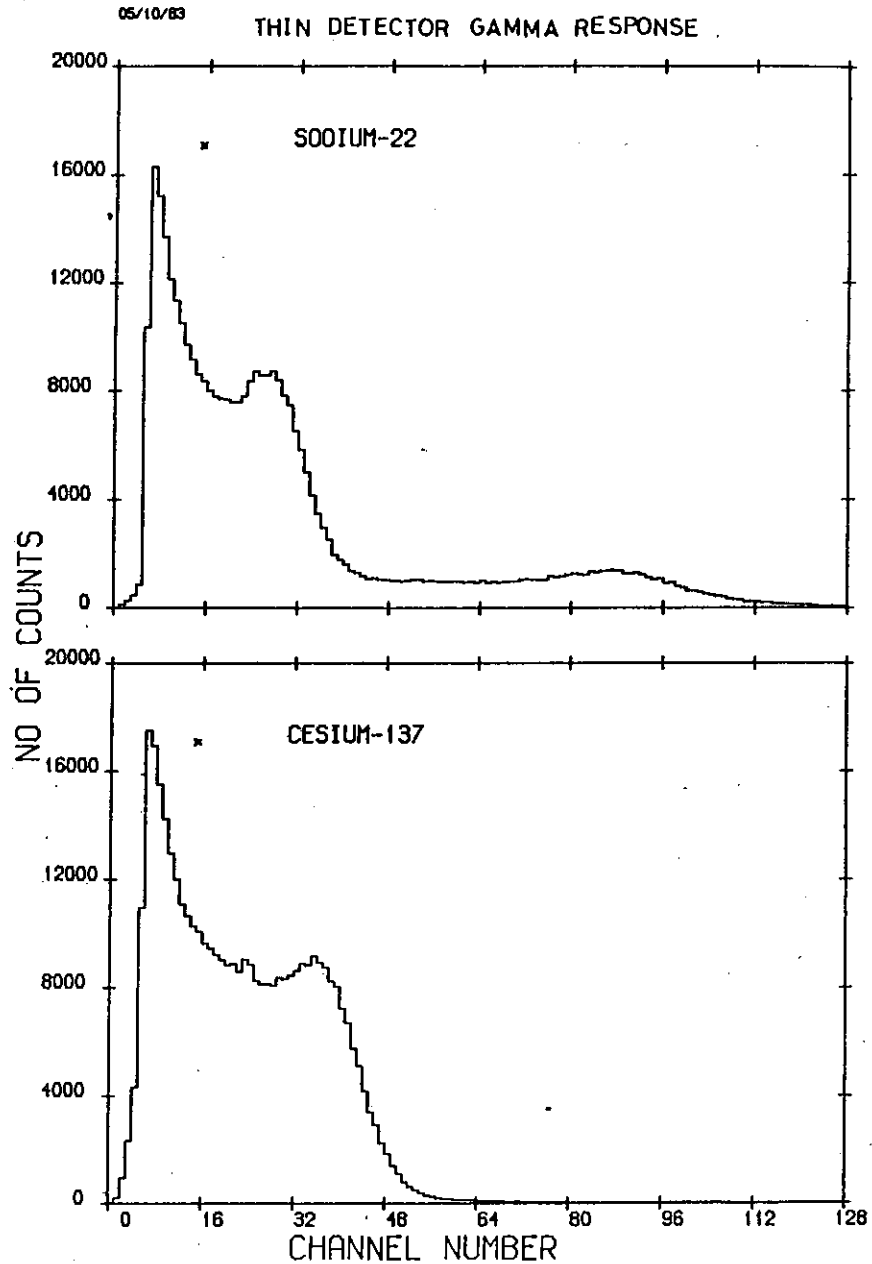

Figure 3.4.

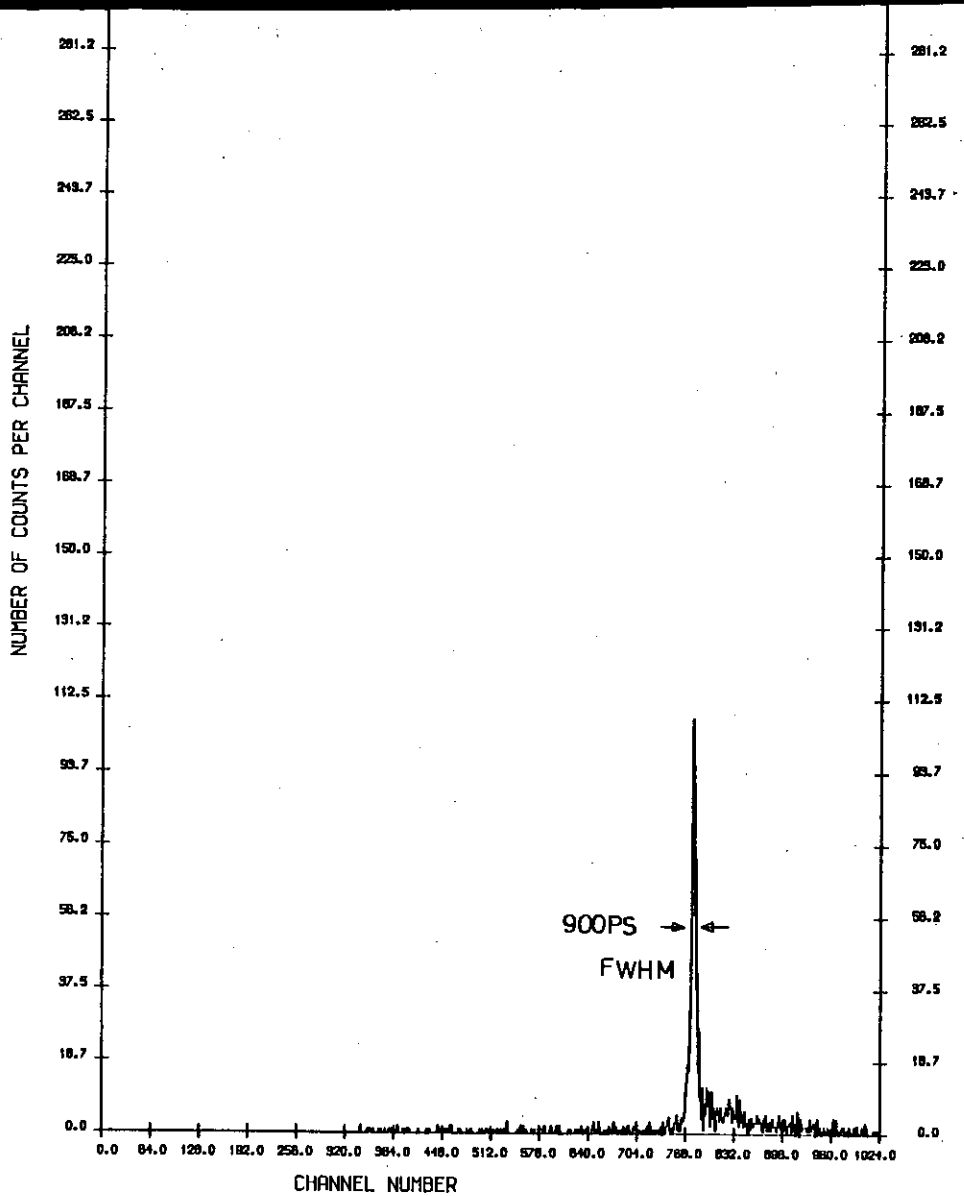

Figure 3.7

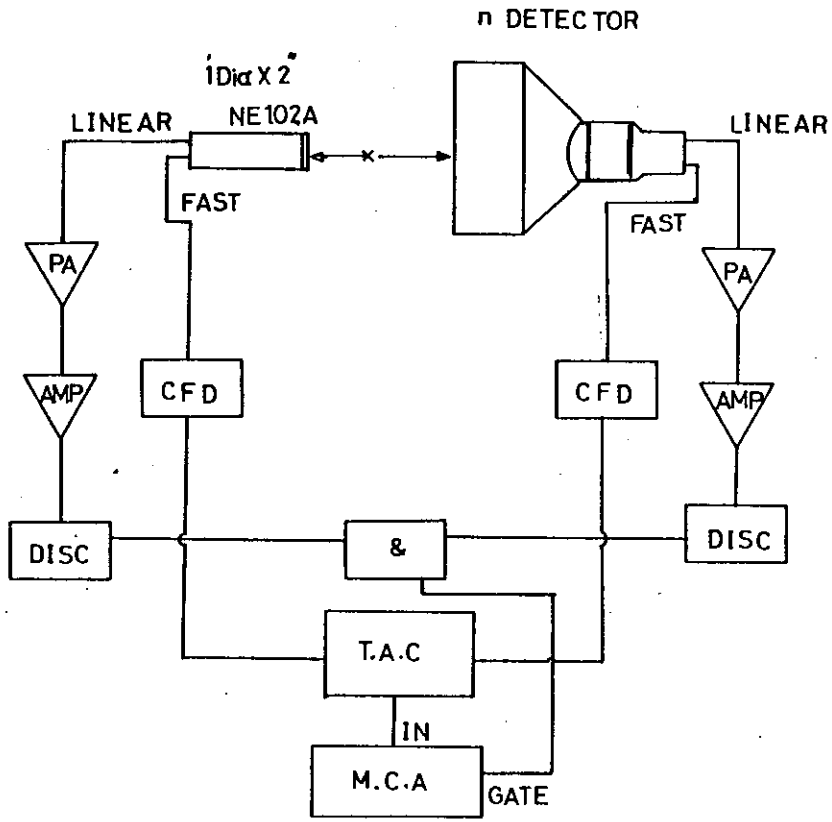

Figure 3.6.

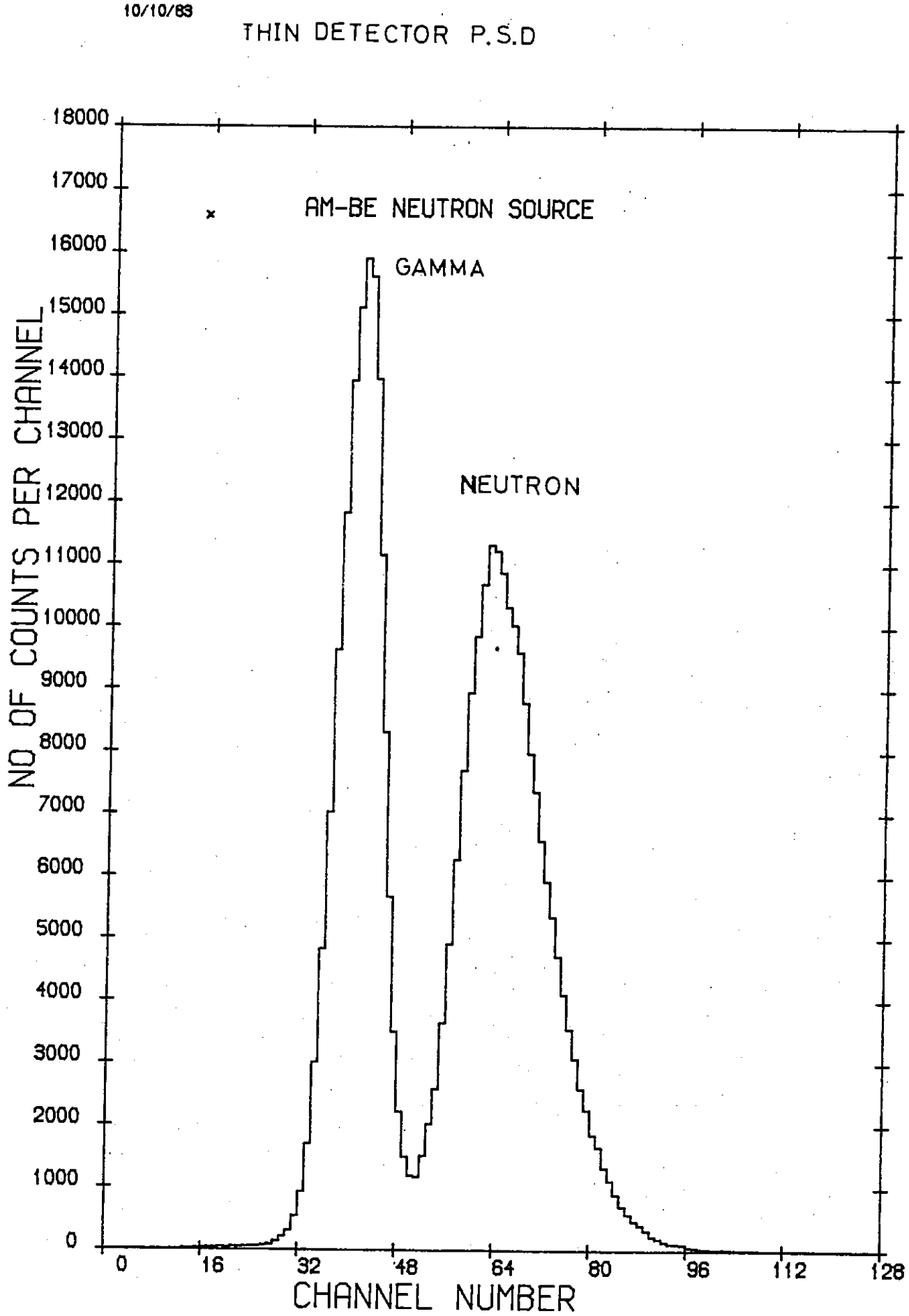
10/10/83
THIN DETECTOR P.S.D
AM-BE NEUTRON SOURCE
GAMMA
NEUTRON
NO OF COUNTS PER CHANNEL
CHANNEL NUMBER
18000
17000
16000
15000
14000
13000
12000
11000
10000
9000
8000
7000
6000
5000
4000
3000
2000
1000
0
0
16
32
48
64
80
96
112
128

Figure 3.8.

the electronics used for time resolution measurement. The timing resolution achieved was 900 PS (10^{-12} second). The spectrum Fig. (3.7) was collected with an energy threshold of 0.2 MeV electron (0.7 MeV proton energy).

C) Pulse shape discrimination test

Pulse shape discrimination of the detector was tested using a ^{241}Am-Be source. The P.S.D. unit used for this test was the circuit originally designed by Galloway and Wang[70]. Three of these units were made for this experiment. Fig. (3.8) demonstrates the pulse shape discrimination performance of the Ø20 × 5 cm neutron detector.

3.4 The Large Volume Double Photomultiplier Neutron Detector

3.4.1 Description of the detector

A detector similar to that of Carlson et al.[71] has been developed in which the intrinsic efficiency has been increased by making the scintillator relatively thick (25 cm).

The original design and the construction method had to be substantially changed. The change involved the scintillator tank which was originally reported to have been made of plexiglass tube and joined to tapered acrylic end pieces. Since Plexiglass (perspex) tube of suitable diameter (20 cm ID) was not available, an outside firm was asked to make the tube using perspex sheets of 3 mm thickness. The tube was then glued to the end perspex disc pieces and the cylinder was filled with NE224 liquid scintillator. Unfortunately on two successive occasions some cracks developed on

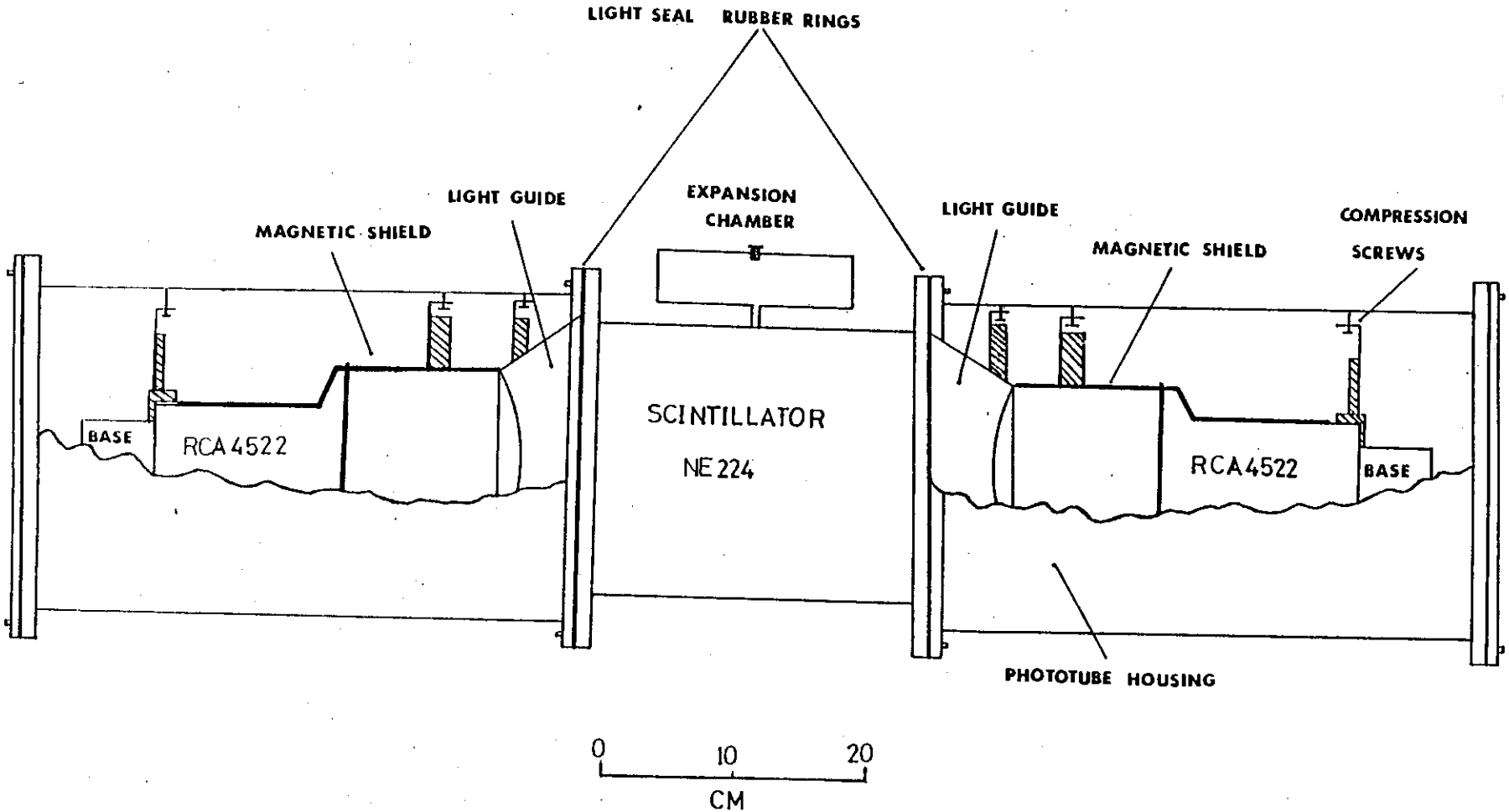

Figure 3.9: The large double photomultiplier neutron detector and its light tight package.

the surface of the perspex within about two months after filling with scintillator. As a result of these cracks the content of the scintillator was lost and therefore an alternative container design had to be considered. A similar problem has been reported by Ranjan et al.[61]. It is believed that NE224 attacks vigorously the perspex exposed to stress by mechanical strain or by solvent action from cement[72].

The basic configuration of the final neutron detector is illustrated in Fig. (3.9). The scintillator tank was fabricated from aluminium sheet of 3 mm thickness which was welded to form a tube of 20.0 cm internal diameter and 25 cm long. The welded join was checked carefully for leaks (vacuum check). The inside surface of the tube was thoroughly cleaned by sodium hydroxide (NaOH) solution for possible contamination by grease during manufacture, before being painted several times by highly reflective paint (NE562). Two glass windows, each of approximately 22 cm diameter, were glued by using Torr Seal low vapour pressure resin, to the front and rear of the tube. Torr Seal remains unattacked by NE224 and forms a hard, uncontaminating seal for the scintillator. The aluminium tank was then washed carefully with NE224 liquid scintillator and drained, to avoid any contamination prior to filling with about 8 litres of NE224 liquid scintillator. The filling was carried out through a small hole in the cylindrical tank. Since inevitably some oxygen will be absorbed by scintillator during the filling process, the scintillator was then de-oxygenated in the normal way by bubbling oxygen-free nitrogen through it, for a few hours because of the large volume of the scintillator. This length

of time for bubbling was found adequate as judged by the pulse shape discrimination test against gamma radiation, which was performed with a small sample of scintillator liquid (2.5 × 2.5 cm).

To allow for expansion of the NE224 liquid an expansion reservoir, consisting of an aluminium cylinder 5.24 cm. in diameter and about 10 cm in length, was attached to the main volume via a stainless steel neck with 3 mm canal. NE224 liquid scintillator is believed to expand about 1% for every 10 degree change of room temperature[72]. The filling hole was finally sealed with a stainless steel screw and PTFE washers.

Two short conical light guides machined from perspex, each with maximum thickness of approximately 4 cm and of 20 cm diameter (Fig. (3.10)), interface the scintillator tank to two RCA 4522 photomultipliers. To minimise any loss of light transferred from the scintillator to each photomultiplier, the surface of each light guide was carefully polished after machining using ICI Perspex Polish. The tapered end section of the light guide was machined to match the convex surface of the photocathode envelope of RCA4522 photomultipliers, whereas the other side is made flat to fit the flat surface of the glass window attached to the scintillator cylinder. Perfect optical coupling was made by adding silicon grease (refractive index $\approx$ 1.5) to the optical surfaces. To reduce bubbles on the coupling surfaces liquid paraffin was added to the silicon grease used for optical coupling. Around each photomultiplier a mu metal shield kept at earth potential was used to cancel the effect of external magnetic and electrostatic fields. The external fields may deflect electrons from their normal path between stages and cause loss of gain by

Figure 3.10. Perspex light guide used for neutron detector.

as much as 50%[73].

Two aluminium cylindrical cases, one at each end of the scintillator, house the photomultipliers with bases. The aluminium housing provides mechanical support for the photomultiplier and it also forms a light barrier. The photomultipliers are kept central inside each case by means of three rings on each side of the scintillator made of paxolin, supported by three threaded rods at 120° intervals. These rods can be adjusted so that the tube, light guide, and the scintillator are reliably kept together on the same axis. The two photomultiplier cases are bolted to the scintillator tank, one at each end. To ensure a perfect light tight arrangement each bolted joint was sealed by a rubber O ring. The overall length of the package is 120 cm.

Dynode chain base and linear dynode pulse preamplifier, the same as used with thin detector, (Fig (3.3)), were located inside the detector package. Details of the detector and its light tight package are shown in Fig. (3.9).

3.4.2 Method of derivation of timing signal

For thick, long scintillators such as the one used in this study the shape of the scintillator pulse largely depends on the position of photon production. As the released photons due to the scintillation process travel along the scintillator thickness, the light pulse undergoes increase in decay time and decrease in amplitude. Timing signals derived from such a scintillator pulse, variable in both amplitude and decay time, suffer from the introduction

of a large time walk.

Various methods of discrimination were applied to the photomultiplier anode fast signal in order to find the optimum timing method. Leading edge discrimination and Constant Fraction Discrimination (CFD) with various predetermined fractions were among those applied. Considerable improvement in timing and reduction of time walk was achieved when the CFD method with 30% fraction was used.

The constant fraction discriminator produces an output signal at a fixed time after the input pulse reaches a predetermined fraction of its amplitude. The technique is basically to convert the negative input anode signal into a zero crossing signal by mixing a portion of the input with delayed and inverted input signal (Fig. (3.11)). The zero crossing is then detected and used to trigger a pulse shaping circuit. It is well known[74-76], that this provides greatly improved time walk and time resolution characteristics over a wide range of input signal amplitudes. Model 473A ORTEC constant fraction discriminator used in this work has less than 500PS (10^{-12} second) time malk for 100:1 dynamic range.

3.4.3 Detector performance

A. Neutron detector energy calibration and response to gamma rays

The importance of the accurate knowledge of energy calibration of a neutron detector for determining counting efficiency of the detector was discussed previously (3.3.3).

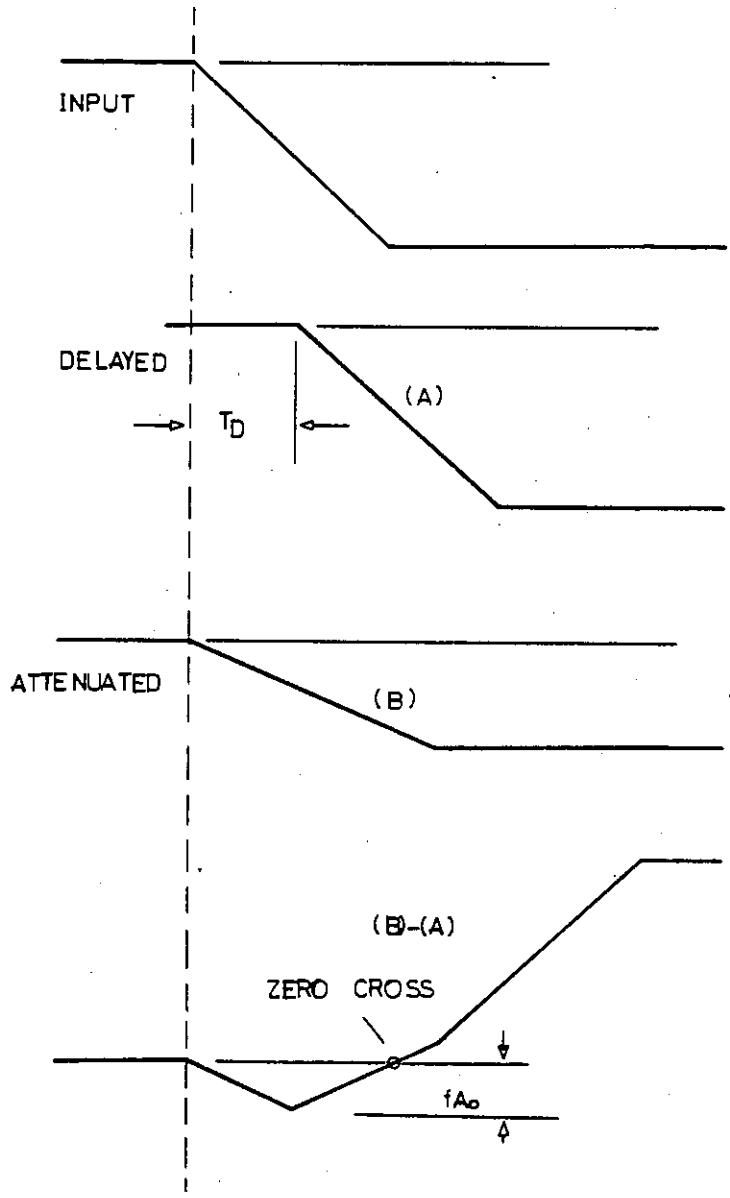

Figure 3.11: Ideal pulse shapes illustrating the Constant Fraction Discriminator (C.F.D.) operation

Three standard gamma sources, Cesium-137, Sodium-22 and Cobalt 60 were used for energy linearity test of the detector.

Linear signals from both end tubes were summed after preamplification, in a linear OR unit and the result was then amplified in a spectroscopy amplifier with suitable RC shaping. The relative timing of the two linear signals before summing was found to be critical in achieving optimum energy resolution and pulse shape discrimination performance. This timing was therefore optimised by using suitable length of 50Ω cable.

Since for photon energies up to 3 MeV Compton scattering dominates in the scintillator, the $^{2}/_{3}$ point of the sharp edge of the Compton distribution, believed to be the best estimate of the maximum electron recoil energy, Prescott and Rupaal[68] and Beghian and Wilensky[69] were used to determine the energy calibration and the response linearity of the high efficiency neutron detector, dynode chain and the associated electronics.

Figs. (3.12) and (3.13) show the response of the large detector to gamma rays and also the linearity curve. The 0.5 MeV and 1.26 MeV gamma rays from ^{22}Na source are well separated by two clearly distinguishable peaks. Taking into account the large dimensions of the detector, the energy resolution achieved is rather encouraging.

B. Neutron detector positional response uniformity

The scintillation light produced inside the scintillator undergoes attenuation before reaching the photomultiplier. The degree of this attenuation depends mainly upon the light

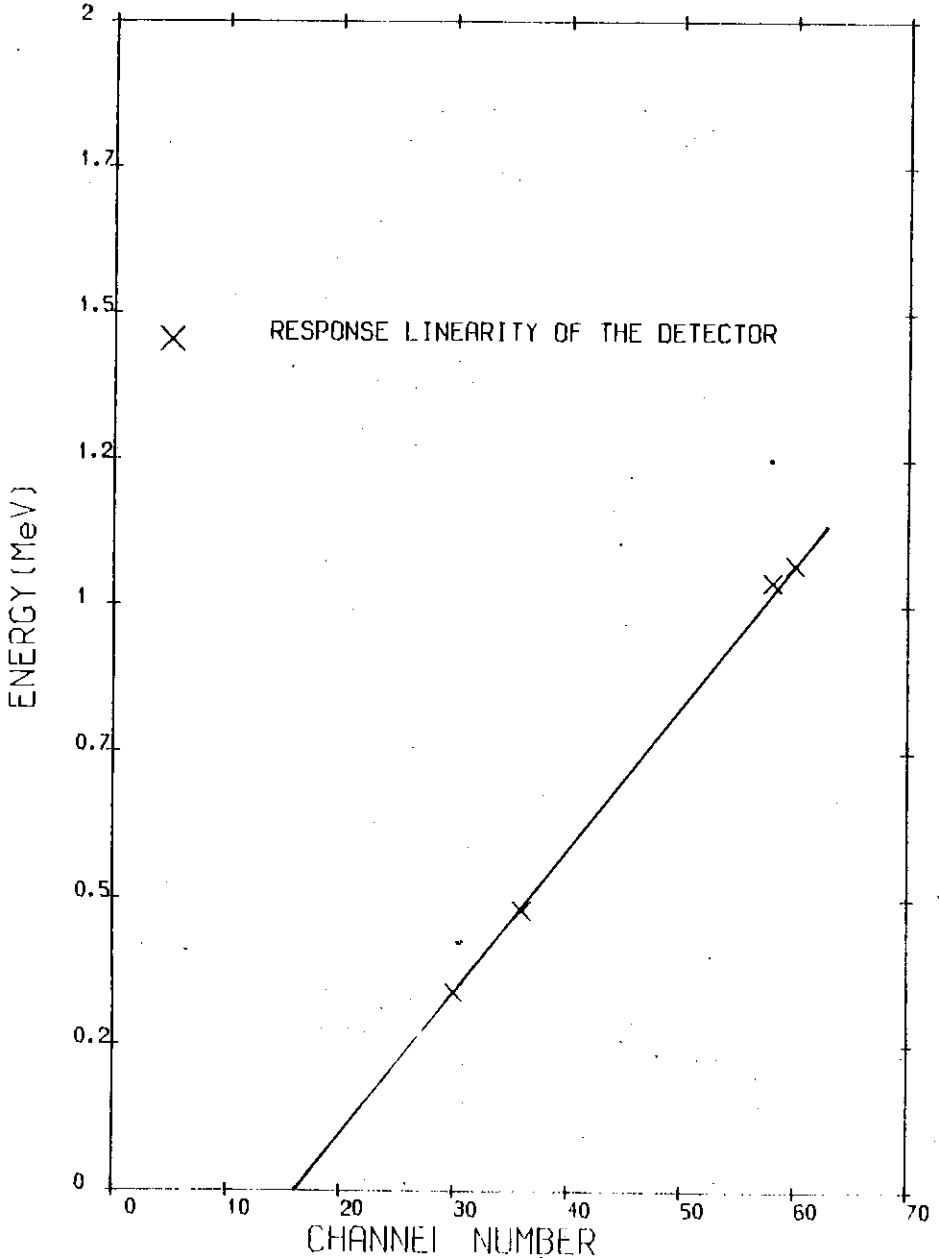

Figuee 3.13

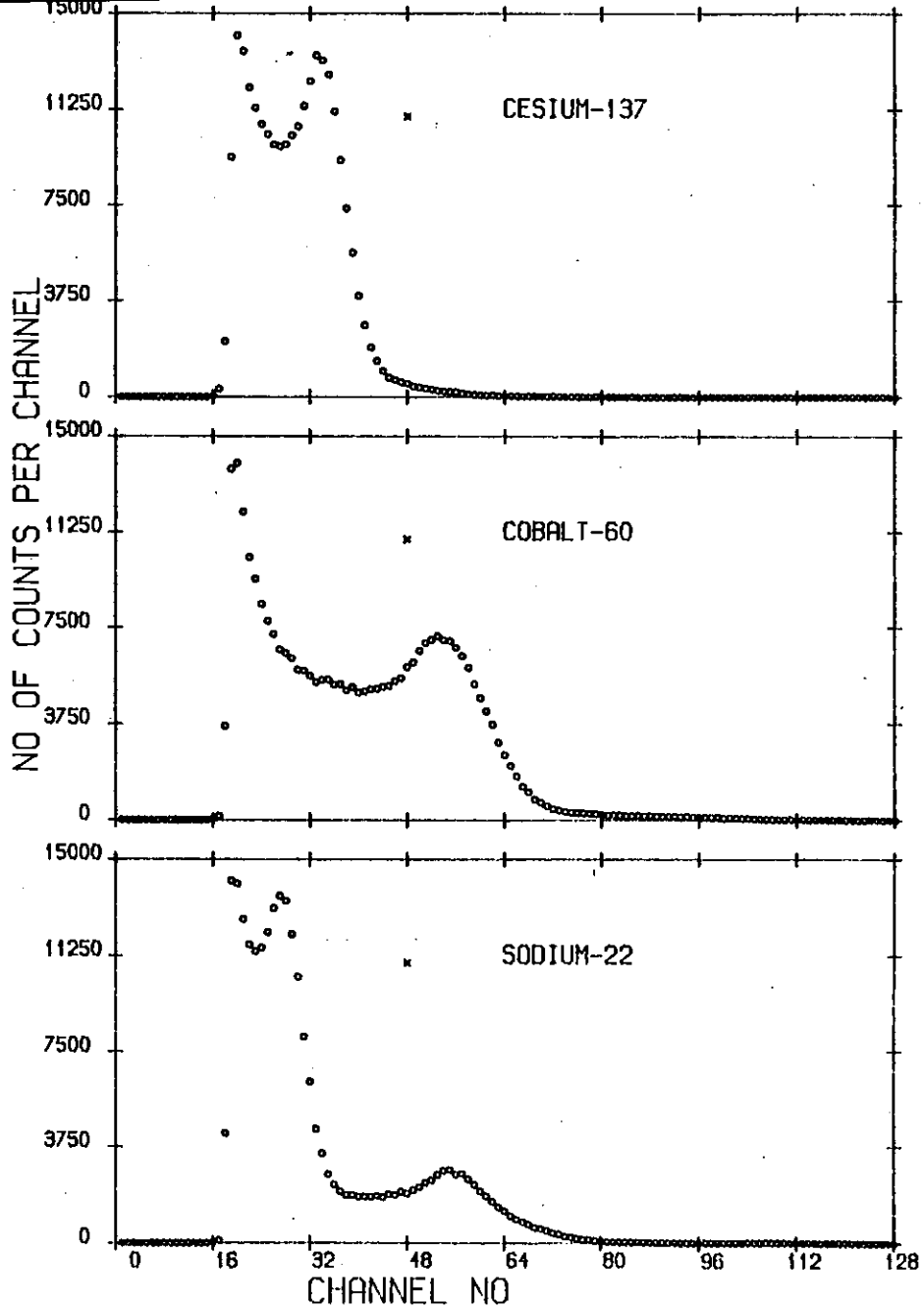

Figure 3.12.

transmission characteristics and the thickness of the scintillator material. In the double photomultiplier detector arrangement it is most likely that light, originating in the middle of the scintillator, suffers most from this effect.

The response uniformity of the detector versus location of scintillation was carefully investigated by localizing the scintillation position and recording electron recoil pulse height spectra due to gamma rays emitted by ^{137}Cs.

To localize the position of the entering radiation ^{137}Cs gamma rays were collimated through a 2 mm slit made by lead blocks of approximately 10 cm thickness. This thickness is sufficient to attenuate gamma rays emitted by Cesium by a factor of 10^5. The summed linear signal from both photomultipliers showed negligible variation in amplitude as the collimated gamma ray beam scanned the scintillator along its axis. The result of this measurement is shown in Fig. (3.14).

C. Neutron-Gamma pulse shape discrimination (P.S.D.)

Due to the size of the detector in this work, background is a rather serious problem. The origin of the background is mainly gamma and cosmic ray events. In fact the background is the limiting factor for the smallest measurable cross section. Reducing the background is therefore of vital importance.

Scintillation pulses from most liquid organic scintillators decay with fast and slow components and the relative intensity of these components is dependent upon the nature of the incident radiation.

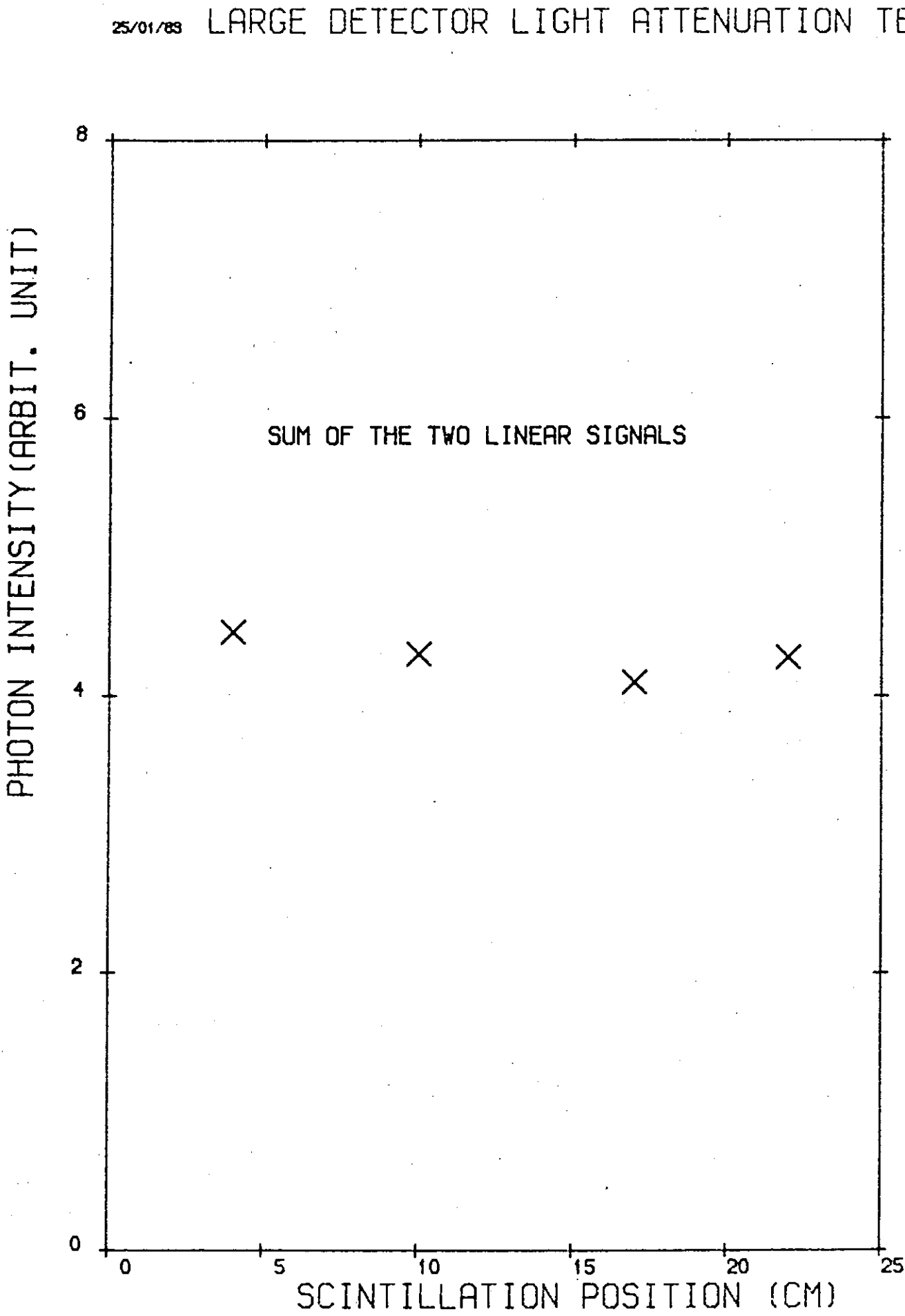
25/01/88 LARGE DETECTOR LIGHT ATTENUATION TEST
PHOTON INTENSITY(ARBIT. UNIT)
SUM OF THE TWO LINEAR SIGNALS
SCINTILLATION POSITION (CM)
0
2
4
6
8
0
5
10
15
20
25

Figure 3.14.

NE224 liquid scintillator used for neutron detection in the present work has the particular feature that the intensity ratio of the fast component to the slow component due to proton recoil from incident neutrons is less than that due to electron recoil from incident γ rays. As a result of the difference in the scintillation pulse shape it is possible to distinguish the different current pulses resulting at the photomultiplier output from the different intensity ratios. Several methods of P.S.D. have been developed[77-82], among them the zero crossing method of pulse shape discrimination used in this work, introduced by Alexander and Goulding[82] is the most commonly used technique. This technique makes use of the fact that after subsequent integration and double differentiation of the photomultiplier dynode pulse, the zero crossing time depends only upon the relative proportion of the fast and slow fluorescence components of the scintillator decay and is independent of the pulse amplitude. In Section (3.9) a neutron selector NIM module made, based on the above principle and circuit design of N.S. Wang[83], will be briefly discussed.

A two parameter data acquisition system consisting of two 256 channel Analogue to Digital Convertors (ADC) and Direct Memory Access (DMA) interface associated with the PDP 11/45 Physics Department's Computer was utilized to study the pulse shape discrimination behaviour of the neutron detector against the pulse height. The interface unit was originally designed by Watson[84] and modified by Hall[85].

Fig. (3.15) shows the block diagram of the data collection system used. The bi-dimensional display of P.S.D. versus pulse

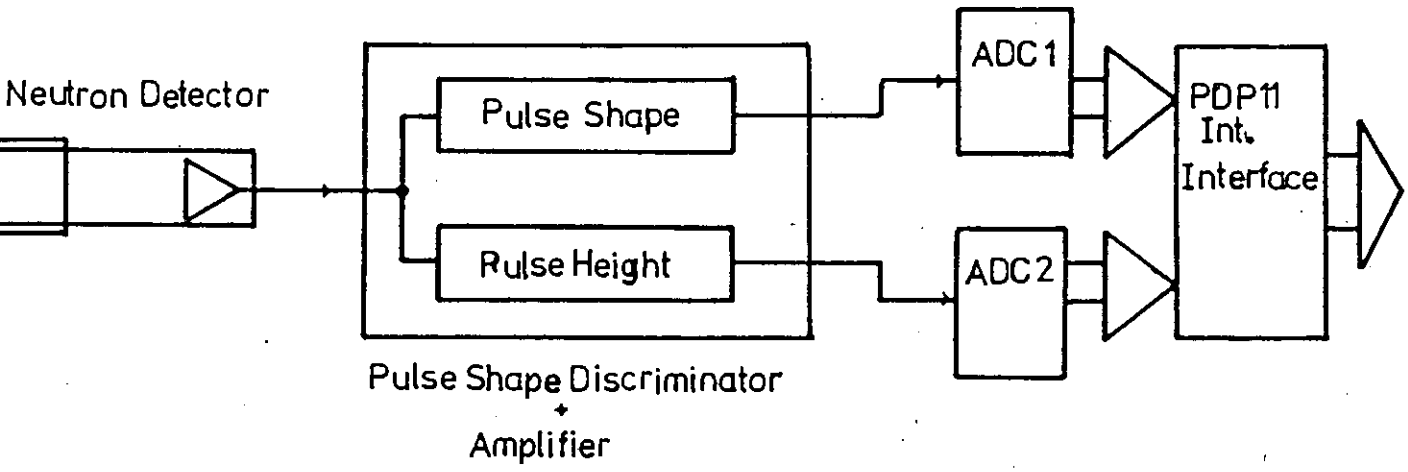

Figure 3.15.

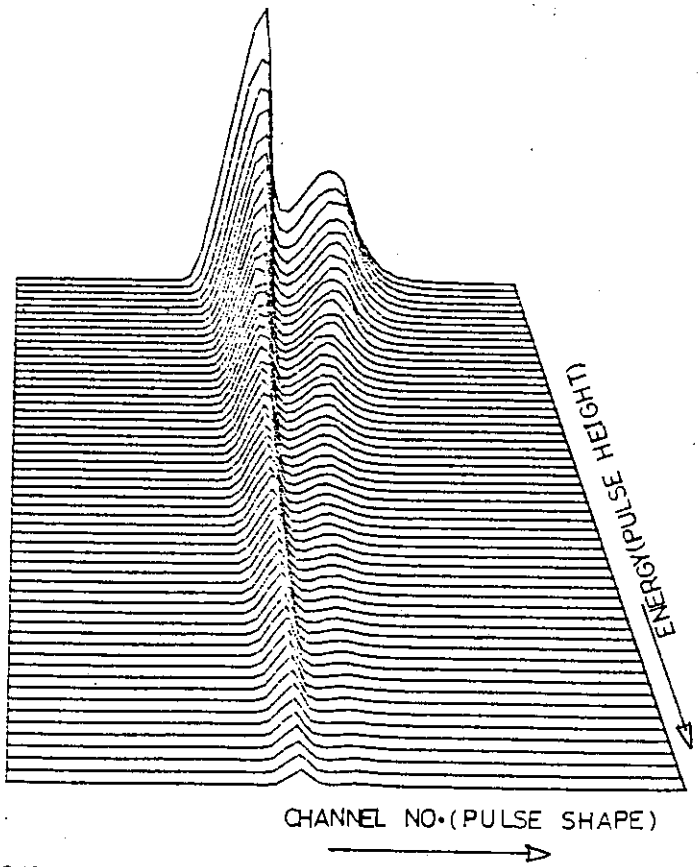

BIDIMENSIONAL VIEW OF P.S.D OF THE LARGE HIGH EFFICIENCY NEUTRON DETECTOR

Figure 3.16

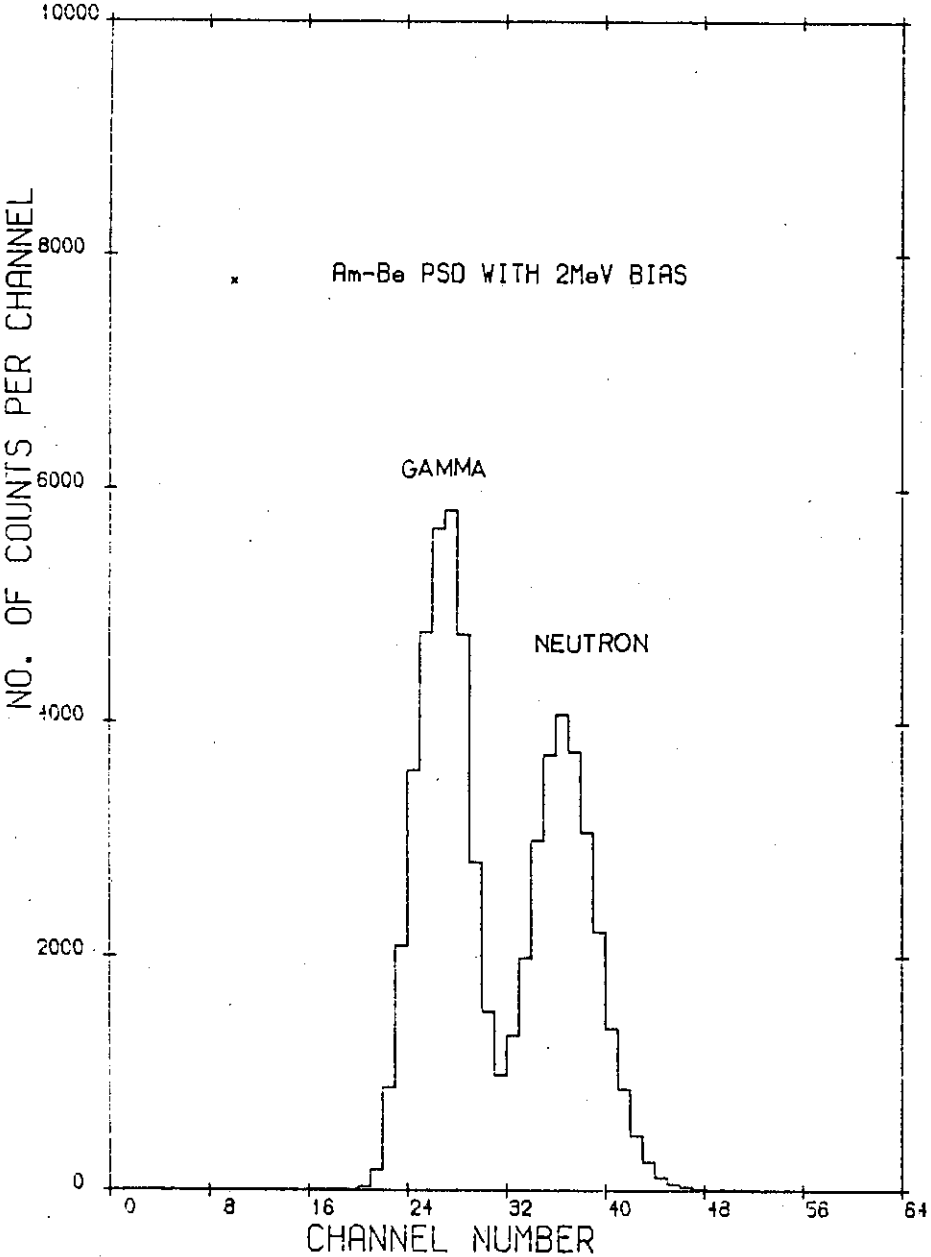

Figure 3.17

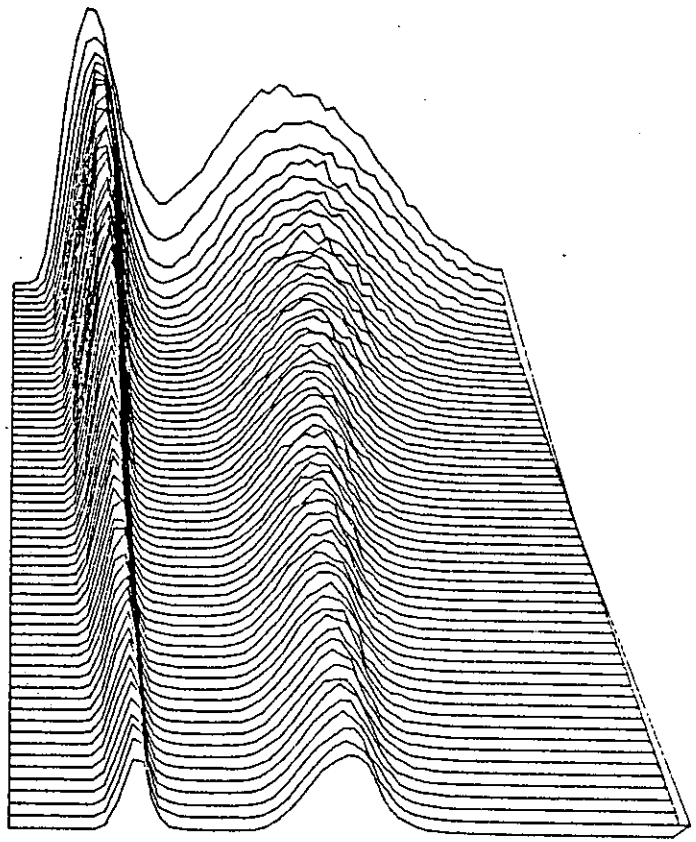

Figure 3.18.

height is also shown in Fig. (3.16) together with the P.S.D. performance at 2 MeV bias in Fig. (3.17). An ^{241}Am-Be neutron source was used for this measurement. A similar measurement using a Ø5 × 5 cm scintillator is also displayed for the purpose of comparison (Fig. (3.18)). The performance is satisfactory, although inevitably poorer than for the much smaller scintillator.

3.5 Method of Time Compensation

As the scintillator is made thicker the spread in the time of detection of mono energetic neutrons becomes significant. For 14 MeV neutrons, for example, a scintillator thickness of up to 5 cm, corresponding to time spread of 1.0 ns (10^{-9} second), can be tolerably used without having to compensate for neutron detection time and photon transit time spread. It is, however, essential, when thicker scintillator is used, to correct for these effects.

For the detector under consideration for this work, neutrons enter the scintillator in a direction parallel to the detector axis (Fig. (3.19)). Under this condition the total flight path is dependent upon the scintillation position and hence is not constant.

If the incident neutrons travel a fixed distance before interacting with the scintillator at a position x along the axis of the scintillator with the refractive index n and overall length L, then t_1 and t_2 the resulting time signals due to the detection of the scintillation photons at the rear and the front photomultipliers respectively will be:

$$t_1 = \left(\frac{L - x}{c}\right) f \cdot n \qquad (3.1a)$$

$$t_2 = \left(\frac{x}{c}\right) f \cdot n \qquad (3.1b)$$

where c is the speed of light and f is the geometrical factor expressing the fact that the average photon path is not a straight line parallel to the scintillator axis but is due to successive reflection from the scintillator wall, the path could be a zig zag shaped path.

The total neutron flight time t_n is[9,14,86-89]

$$t_n = \tfrac{1}{2}(t_1 + t_2) - \tfrac{1}{2}\, n\, Lf/c \ . \qquad (3.2)$$

By subtracting (3.1b) from (3.1a),

$$t_1 - t_2 = \left(\frac{L - x}{c}\right) f \cdot n - \frac{x}{c} f \cdot n$$

and hence

$$x = \frac{c}{2f \cdot n} (t_2 - t_1) + \tfrac{1}{2}L \ . \qquad (3.3)$$

Taking x into account, the total compensated flight time, t_D, will be

$$t_D = \left(\frac{D}{D + x}\right) t_n$$

or

$$t_D = \left(\frac{D}{D + x}\right) \left[\frac{(t_1 + t_2)}{2} - \frac{1}{2} \frac{n \cdot L \cdot f}{c}\right] \qquad (3.4)$$

t_1 and t_2, the travelling time of flight inside the scintillator before reaching to the photomultipliers are not measured directly, rather they are measured relative to an arbitrary time reference such as the one provided by the associated particle detector.

The quantity that is ultimately determined equals a constant minus the flight time.

For the double tube detector considered here:

$$T_1 = \text{const.} - t_1 \tag{3.5}$$

and $$T_2 = \text{const.} - t_2 \tag{3.6}$$

would be determined.

Substituting (3.5) and (3.6) in (3.3) shows that the expression for x remains unchanged.

$$x = \frac{c}{2f \cdot n}(T_1 - T_2) + \tfrac{1}{2}L \tag{3.7}$$

while t_D, the compensated flight time becomes:

$$t_D = \left(\frac{D}{D + x}\right)\left[\text{const.} - \tfrac{1}{2}(T_1 + T_2) - \tfrac{1}{2}\frac{n \cdot L \cdot f}{c}\right] \tag{3.8}$$

or more conveniently

$$T_D = \text{const.} - t_D = \left(\frac{D}{D + x}\right)\left(\frac{T_1 + T_2}{2}\right) + \text{const...} \tag{3.9}$$

Equation (3.9) would give the exact compensated flight time, T_D, provided f for the scintillator configuration is known. In addition, since T_D depends on x in an event by event fashion, it can only be evaluated either on-line or off-line after recording T_1 and T_2 pairs for each individual event.

Carlson et al.[71] have suggested that the energy dependent velocity of neutrons inside the scintillator can be approximated by a constant value independent of energy only in a particular energy region of interest for which the compensation is optimised. Thus inside the scintillator

$$V_n(E) \approx \beta_o c \tag{3.10}$$

where β_o is a constant and represents neutrons in the certain energy region. This approximation will be valid for some range of energies about E_o which corresponds to $\beta_o C$. As the neutron energy deviates from E_o the validity of the approximation deteriorates[71].

With the approximation in (3.10) the expression for the compensated flight, t_D, can be written as:

$$t_D \simeq t_n - \frac{x}{\beta_o c} \qquad (3.11)$$

by substituting (3.2) and (3.3) into (3.11):

$$t_D \simeq G_1(t_1 - Kt_2) + G_2$$

or, by analogy $t_D \simeq G'(T_1 - KT_2) + G_2'$

in which G_1, G_2 and G_1', G_2' are constants and also K the compensation factor is given by

$$K = \frac{1 - \beta_o\, n{\cdot}f}{1 + \beta_o\, n{\cdot}f} \qquad K < 1 \ .$$

T_1 and T_2 are given by signals from time to amplitude converters, measuring the time between detection of an associated particle and detection of the neutron by the neutron detector.

The quantity inside the brackets can be evaluated by a simple inverting and summing circuit to generate a signal proportional to $T_1 - KT_2$, the compensated flight time.

3.5.1 Time resolution test

The overall time response of the detector was investigated separately for both gamma rays and neutrons. The block diagram of the

electronics based on the time compensation method described above, is shown in Fig. (3.20).

(A) Time resolution test with gamma rays

In order to investigate the intrinsic timing properties of the detector without including beam spread contributions, the coincident gamma rays from a ^{60}Co source were observed with the large double tube detector and a small (Ø2.5 × 2.5 cm) fast scintillator detector mounted on an RCA8575 photomultiplier. Initially both front and rear detector timing properties were tested individually and the optimum setting of high voltage and the optimum method of deriving the timing signal was investigated. The timing behaviour of the compensated detector was then tested. The test results are shown in Table (3.5). Fig. (3.21) also shows the dependence of the time resolution of the detector on K.

TABLE (3.5)

Timing Performance of the double Photomultiplier Large Neutron Detector (gamma ray).

Type of detector arrangement and detectors used	Time resolution (ns) FWHM
Front detector and RCA8575 Photomultiplier with a 2.5 × 2.5 cm NE224 Scintillator	1.7
Rear detector and RCA8575 Photomultiplier with a 2.5 × 2.5cm NE224 Scintillator	∿ 1.0
Rear and front detector (compensated) RCA8575 Photomultiplier with a 2.5 × 2.5 cm NE224 Scintillator	∿ 1.0

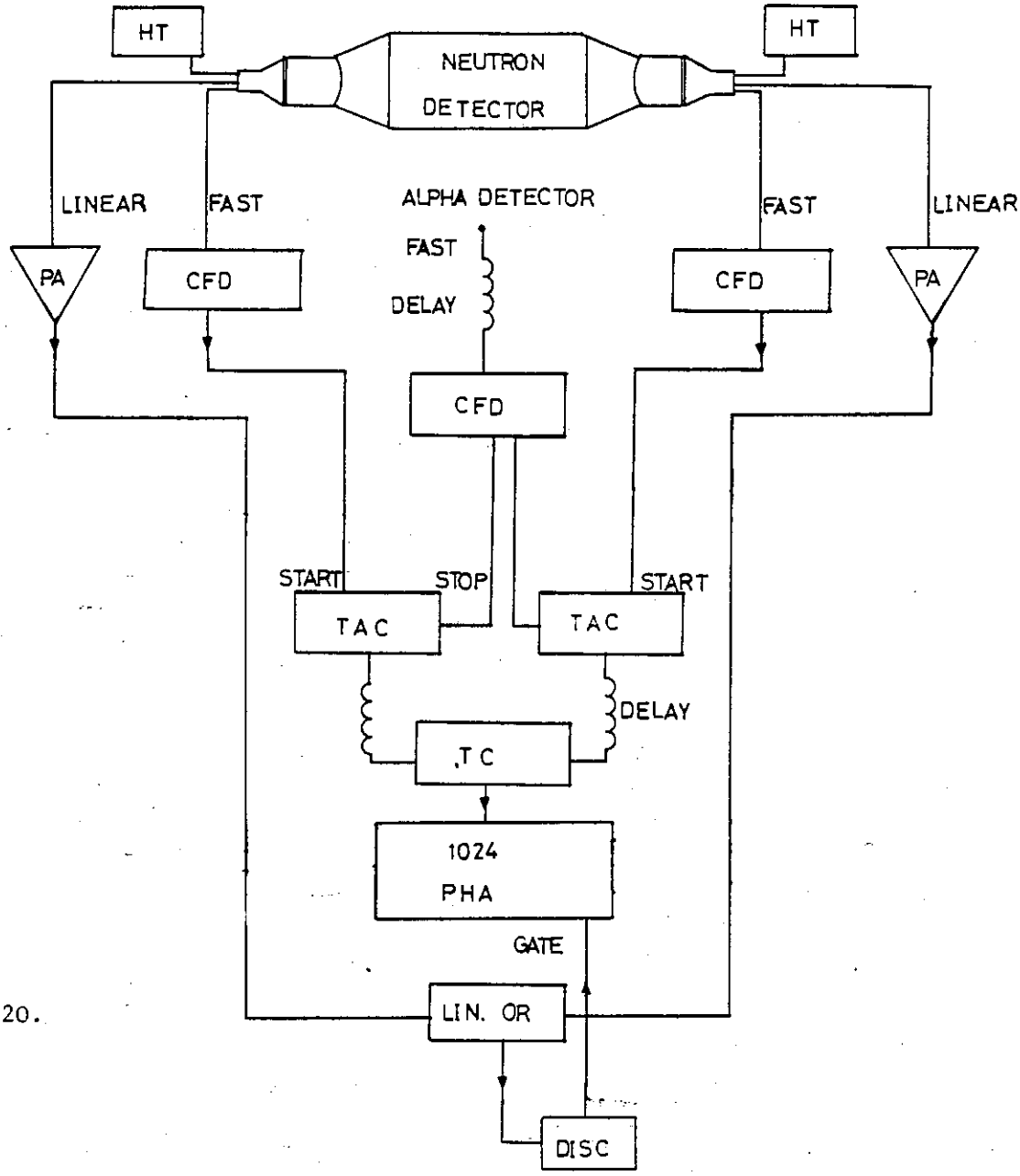

Figure 3.20.

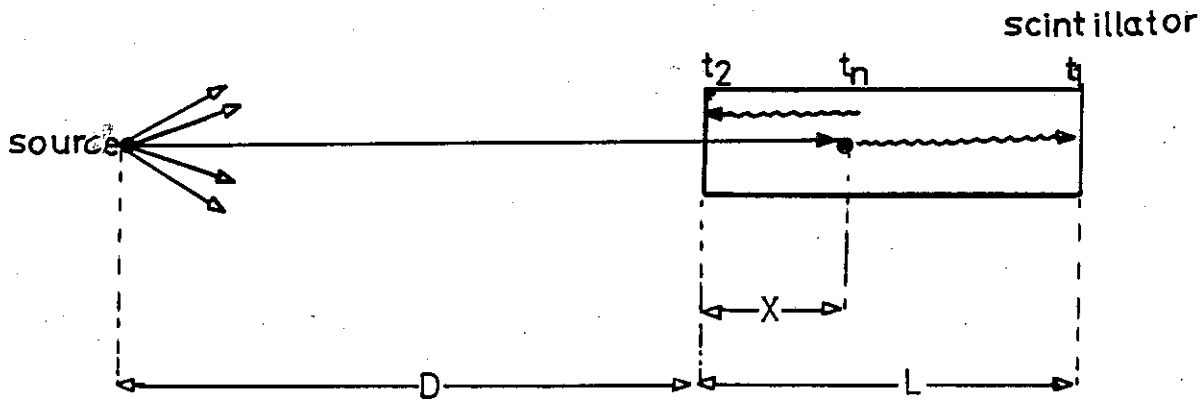

Figure 3.19.

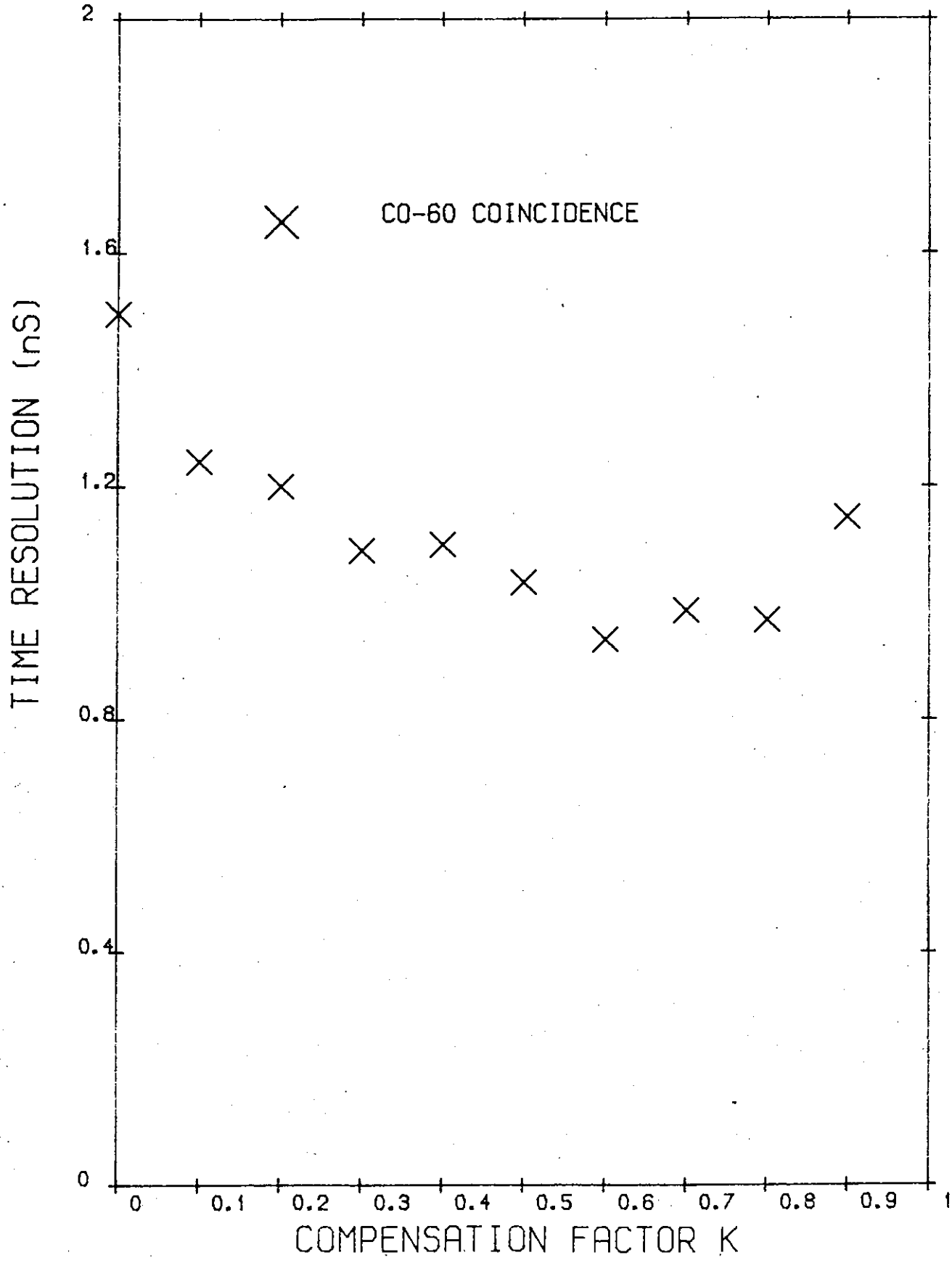
24/01/83 LARGE DETECTOR TIME RESOLUTION TEST
CO-60 COINCIDENCE
TIME RESOLUTION (nS)
2
1.6
1.2
0.8
0.4
0
0
0.1
0.2
0.3
0.4
0.5
0.6
0.7
0.8
0.9
1
COMPENSATION FACTOR K

Figure 3,21.

(B) Time resolution test with neutrons

The timing performance of the detector as a neutron counter was investigated by observing neutrons directly emitted from $^{3}H(d,n)^{4}_{2}He$ reaction at about 90° to the incident deuteron beam. The block diagram of the electronics is similar to that of Fig. (3.20).

To find the optimum time resolution achievable, the compensation factor was varied between 0 and 1.0 in steps of 0.1. The corresponding time of flight timing spectra of neutron-alpha associated particles were collected for each compensation factor. Fig. (3.22) shows the measured time resolution versus the compensation factor. The optimum time resolution achieved was better than 1.5 ns for a compensation factor of 0.3, Fig. (3.23).

3.6 The Neutron Cone Monitor Description and Construction

The neutron cone incident on the scattering sample and associated with ^{4}He particles was monitored at a distance of 60 cm from the centre of the neutron producing target, using a separate neutron detector specially designed and made for this experiment.

The cone monitor detector consisted of a thin walled (approx. 3 mm) rectangular shape Dural box with the internal dimensions of 15 cm high, 7.5 cm wide, and 5 cm deep, as shown in Fig. (3.24). The box was formed from aluminium sheets and then vacuum braised to make a perfect seal for the liquid scintillator. A 11.5 cm × 5.5 cm aperture is provided on one side of the box with a suitable recess machined to accommodate a glass window of 11 × 5 cm, through which the scintillation light can be viewed by an XP1040, 5" dia. photocathode photomultiplier. The

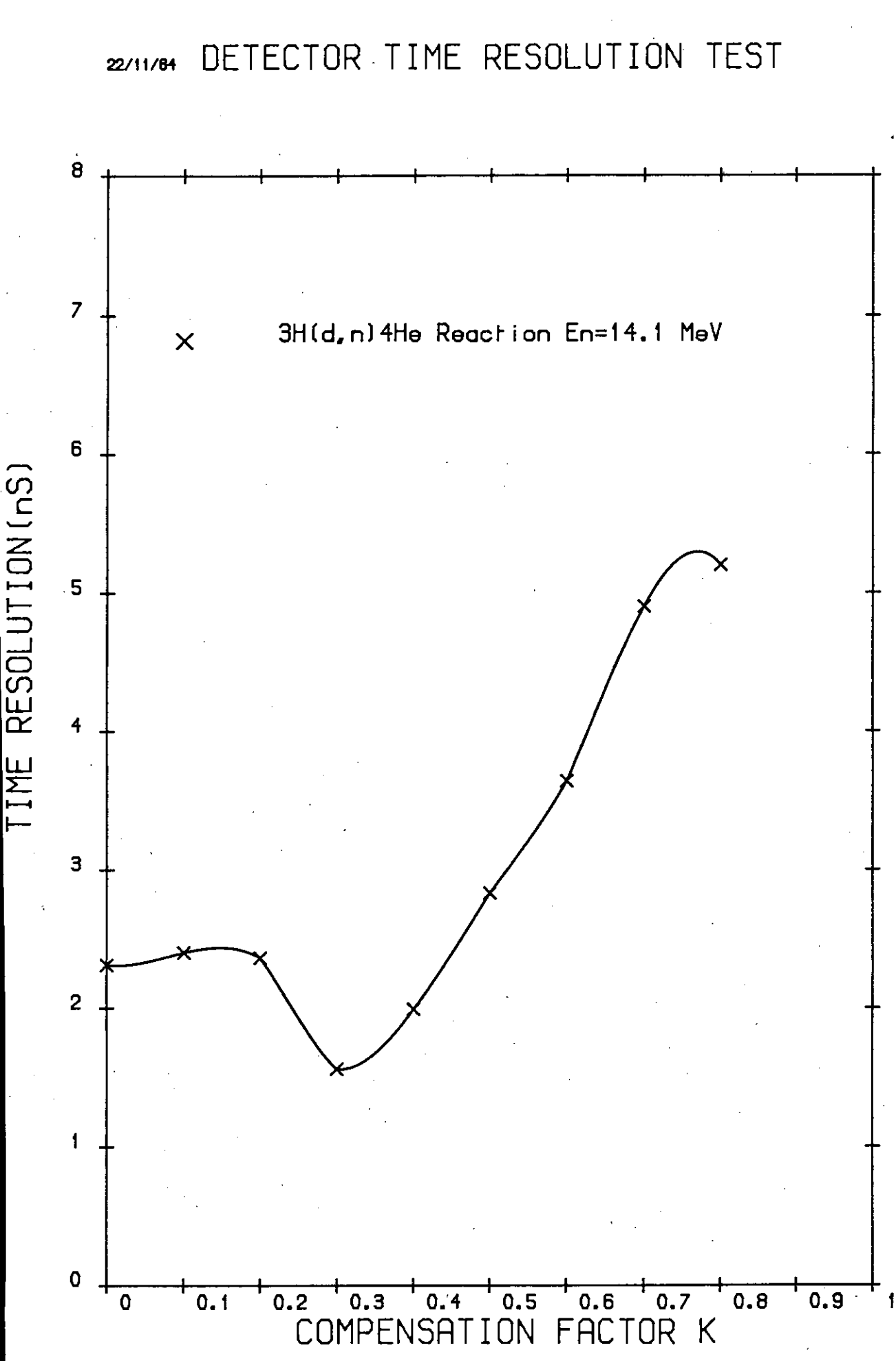
22/11/84 DETECTOR TIME RESOLUTION TEST
3H(d,n)4He Reaction En=14.1 MeV
TIME RESOLUTION(nS)
COMPENSATION FACTOR K
0
1
2
3
4
5
6
7
8
0
0.1
0.2
0.3
0.4
0.5
0.6
0.7
0.8
0.9
1

Figure 3.22.

05/06/81

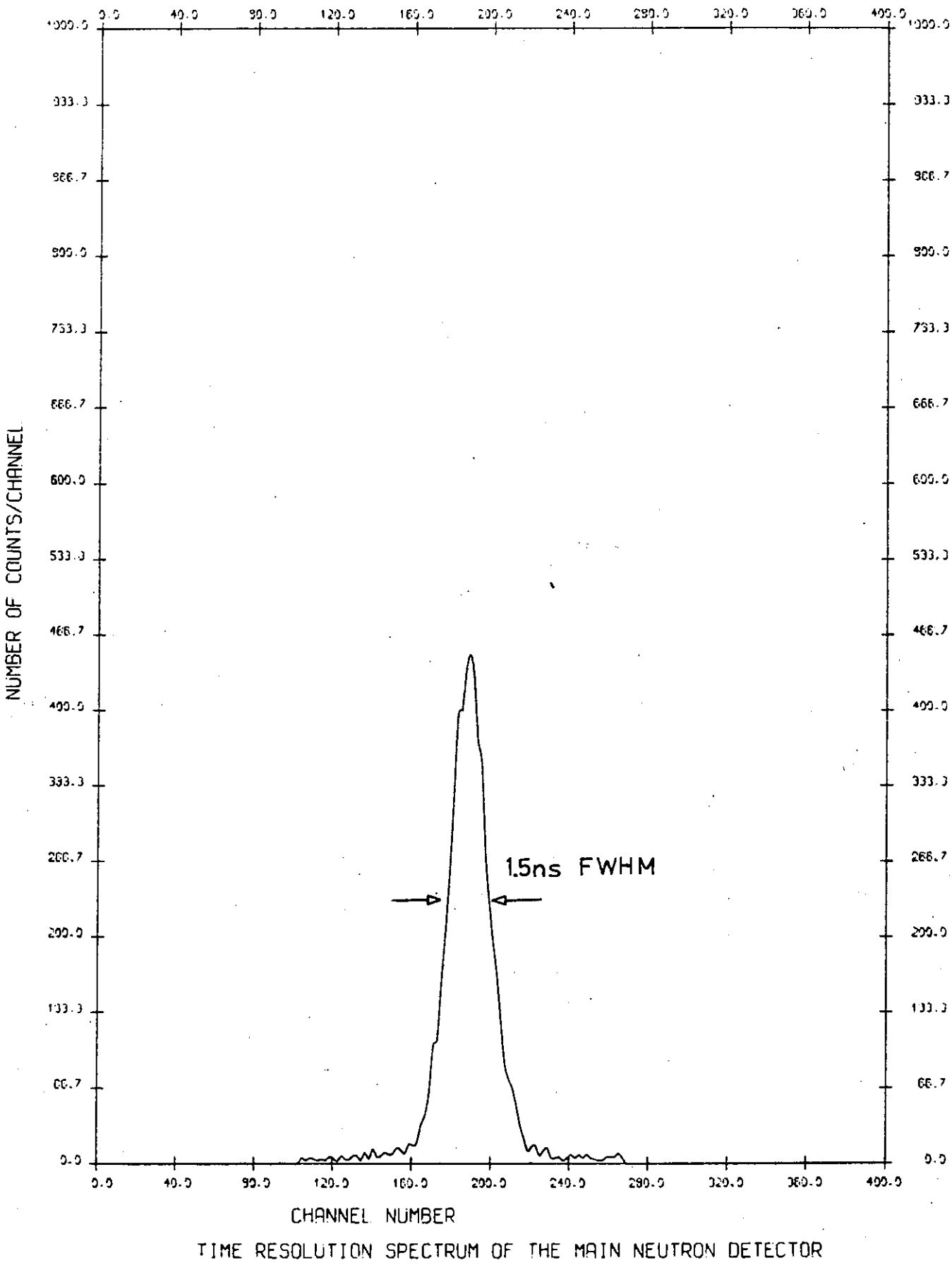

Figure 3.23.

NEUTRON MONITOR SCINTILLATOR UNIT

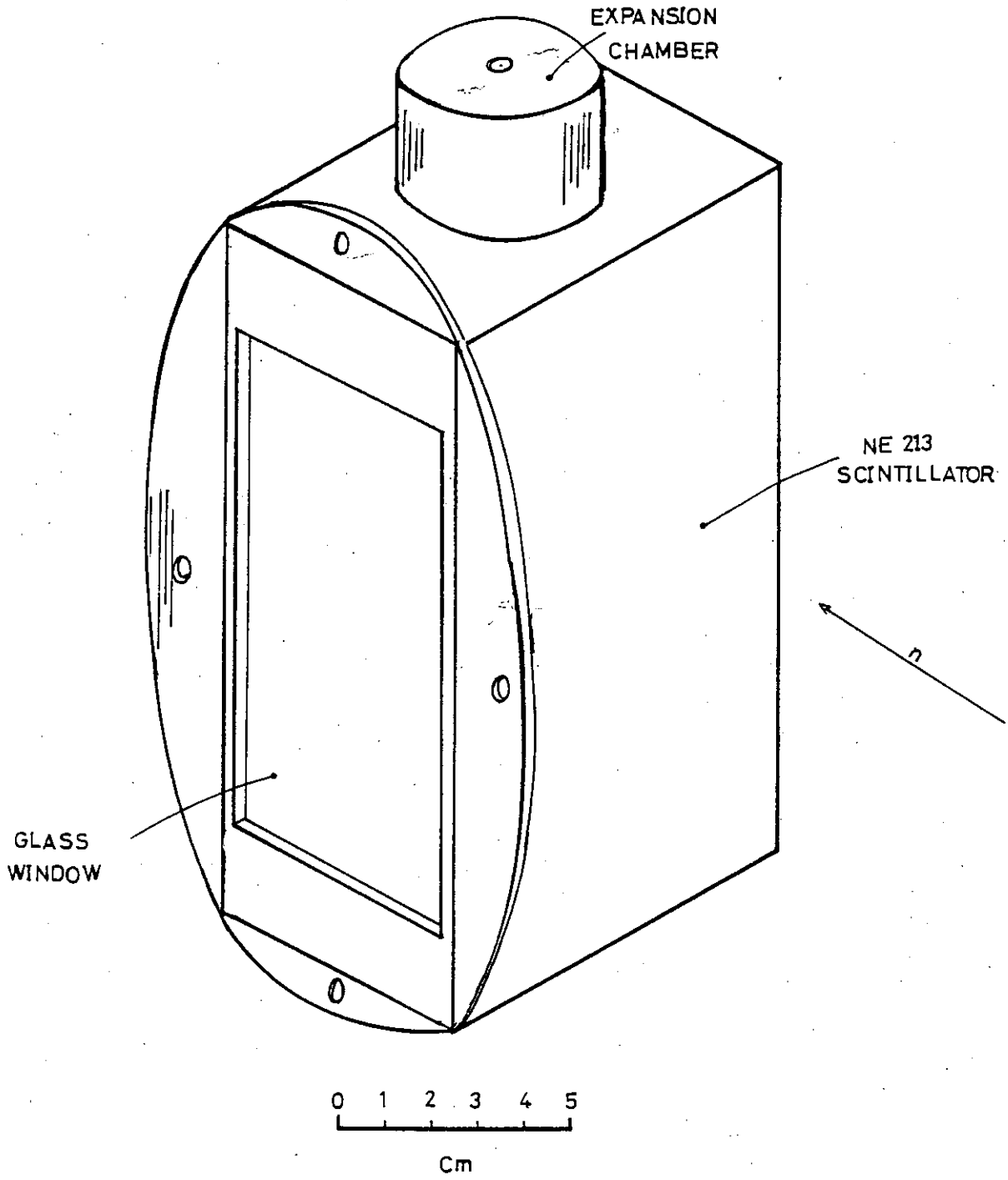

Figure 3.24

internal surface of the box was etched with sodium hydroxide (NaOH) solution before it was internally painted using highly reflective TiO_2 paint (NE562) to improve the collection of the scintillation light produced inside the scintillator.

The container was then filled with NE213 liquid scintillator. A 5 × 5 cm diameter cylindrical glass reservoir was attached to the top of the scintillator box using Torr Seal resin to provide the necessary room for the liquid expansion due to any change of temperature. The glass window of the scintillator was optically coupled to the phototube using silicon grease.

A dynode chain voltage distributor was designed specially for the XP1040 phototube to provide stable fast and unsaturated linear signals at high counting rates (Fig. (3.25)). The phototube, dynode chain and the fast preamplifier are housed in a PVC tube which provides a light shield for the photomultiplier.

The photomultiplier was kept central in the PVC tube and 4 treaded rods incorporated with springs to maintain a good optical coupling by pushing the tube against the scintillator window.

The detector and its light tight housing was then fixed onto a short wooden stand which, during the course of experiment, moved along with the scattering sample round the neutron producing target on a surface parallel to the scattering plane provided by a 75 × 150 cm wooden platform designed for this purpose, (Fig. 2.2).

3.7 Data Acquisition Electronics and Software

The block diagram of the neutron detector and the associated electronics is shown in Fig. (3.26). Fast pulses initiated at both

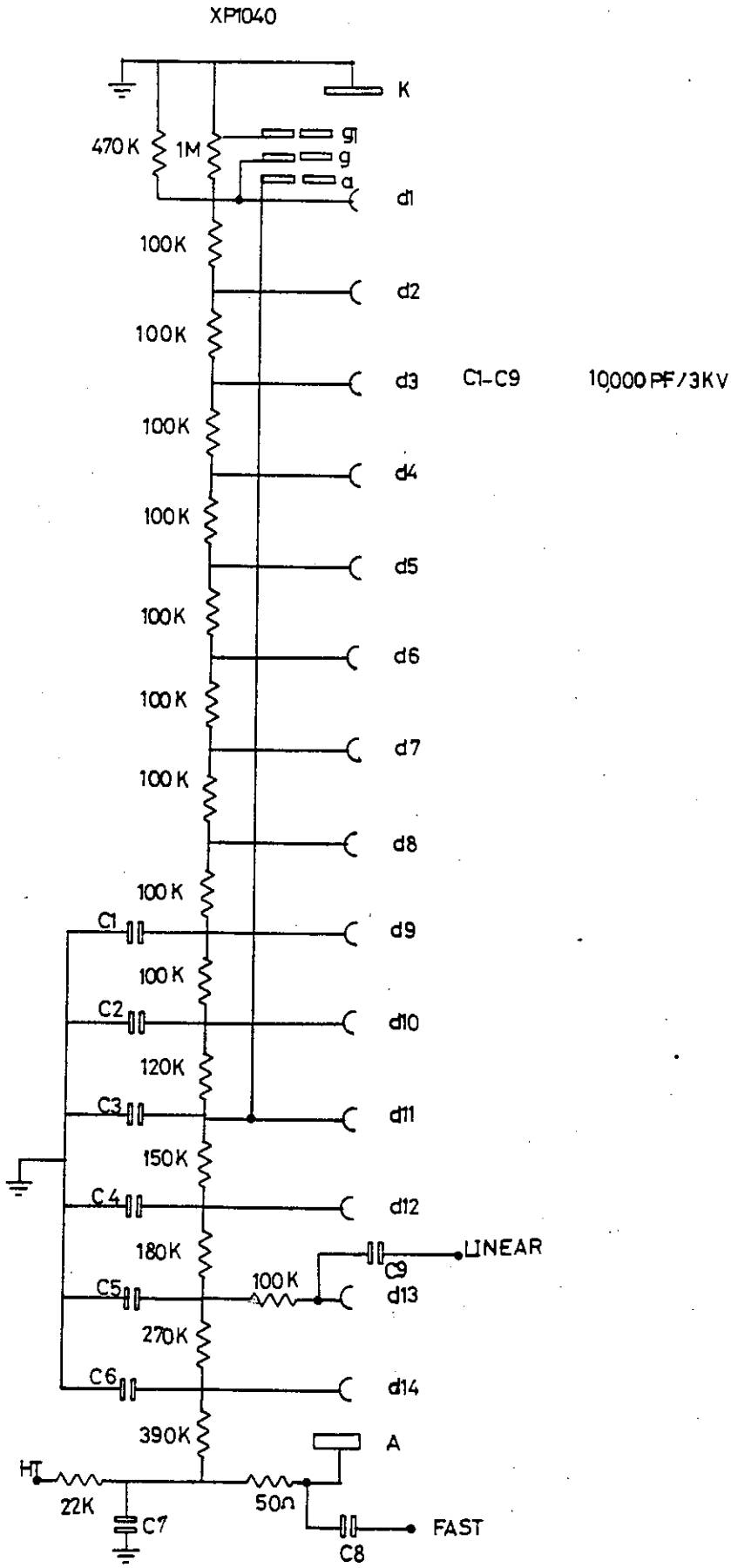
XP1040
K
470K
1M
g1
g
a
d1
100K
d2
100K
d3
C1-C9
10000 PF/3KV
100K
d4
100K
d5
100K
d6
100K
d7
100K
d8
100K
C1
d9
100K
C2
d10
120K
C3
d11
150K
C4
d12
180K
C9
LINEAR
C5
100K
d13
270K
C6
d14
390K
A
HT
22K
C7
50Ω
C8
FAST

Figure 3.25.

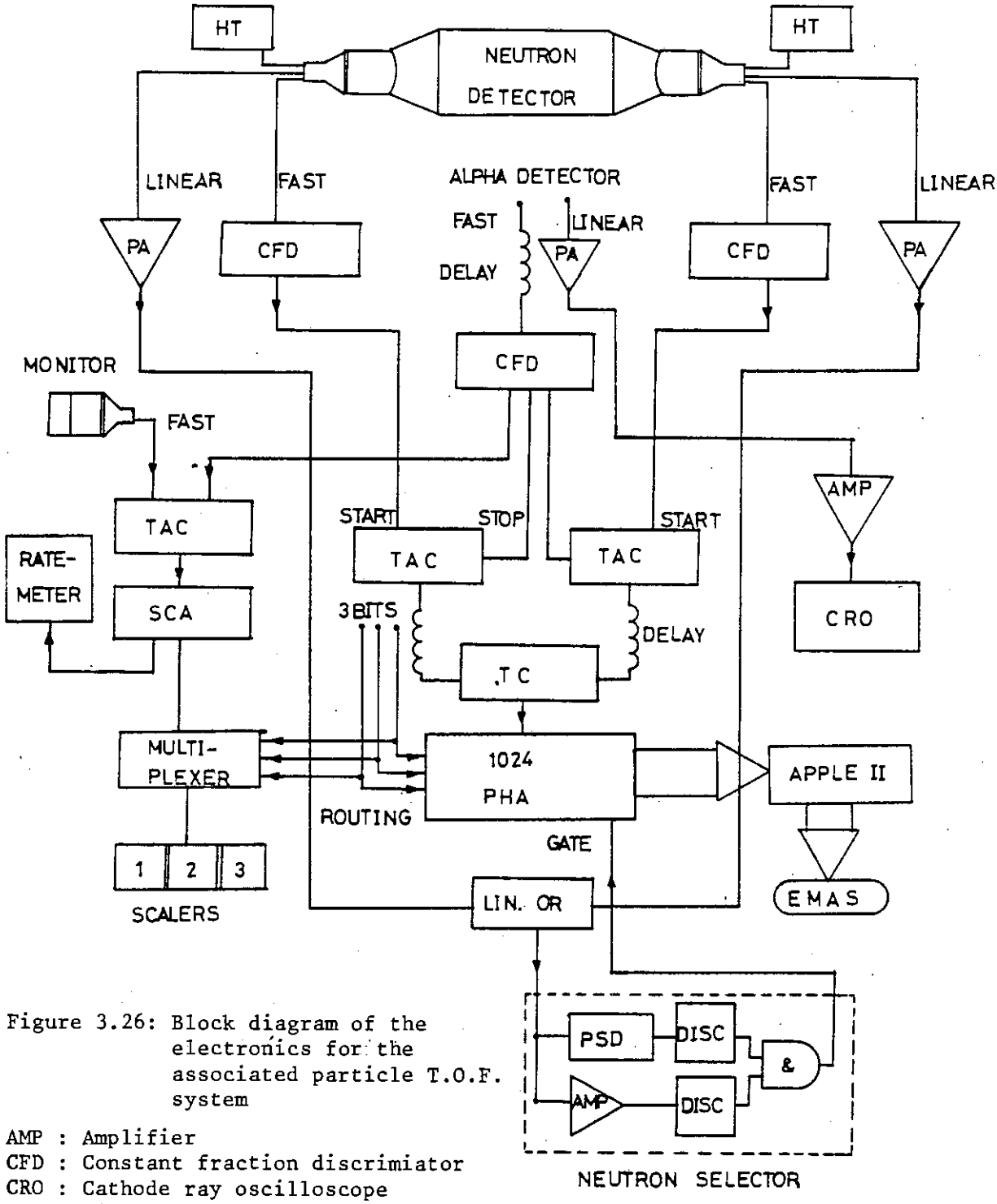

Figure 3.26: Block diagram of the electronics for the associated particle T.O.F. system

AMP : Amplifier
CFD : Constant fraction discrimiator
CRO : Cathode ray oscilloscope
DISC : Discriminator
EMAS : Edinburgh Multi Access System
H.T. : High voltage unit
PHA : Pulse height analyser
PSD : Pulse shape discriminator
SCA : Single channel analyser
TAC : Time to amplitude converter
TC : Time compensator unit

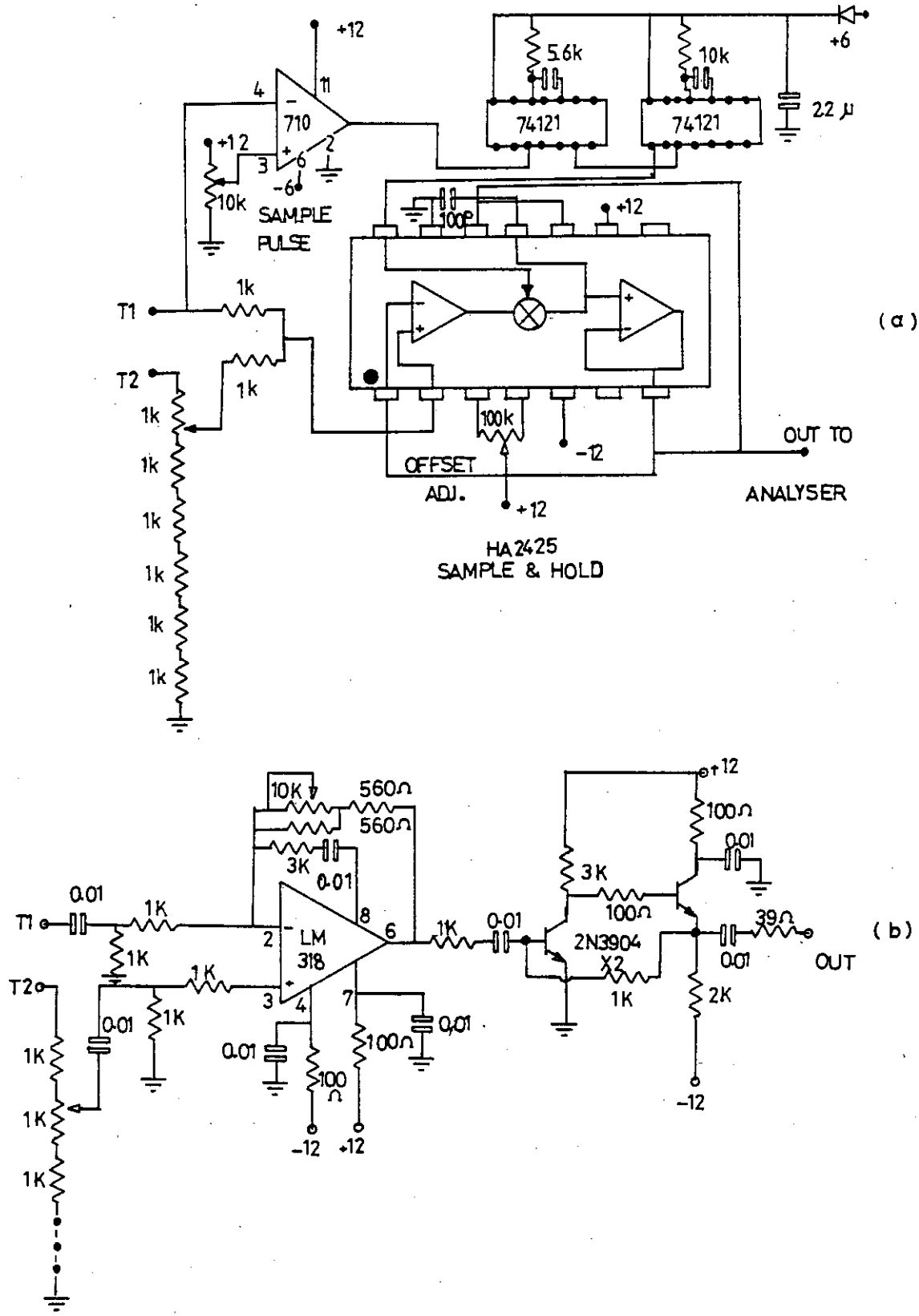

Figure 3.27a and b: Two different designs of time compensator (Sum-invert amplifier).

end detectors, in coincidence, by the detection of either gamma or neutrons in the scintillator volume, trigger two separate Constant Fraction Discriminators (CFD, ORTEC 473A), where an accurate timing signal is derived independent of the amplitude of the input signal. These pulses are then used to "START" two separate time to pulse height converters (TPHA, ORTEC 467). A fast signal derived from the associated alpha particle (thin plastic NE102A scintillator) detector in a similar manner and properly delayed provides a "STOP" pulse to the time conversion process in both time convertors.

The analogue output signals from the time convertors are fed to a custom built Sum-Invert amplifier which was designed to compensate for the transit time spread of the neutrons and photons due to the detection of a neutron or gamma ray at different positions along the length of the scintillator. Two different designs of this circuit were made and tested carefully for linearity and stability in performance. A sample and hold circuit had to be employed in the version in Fig. (3.27a), which allows sum and invert operation on time convertor pulses with different duration and rise time without causing any distortion in the resulting output signal. The performance of both designs were tested for high counting rate which arose when timing resolution of the detector was tested with a Cobalt-60 gamma source.

The compensated time convertor signals were stored in a NE4694 1024 channel pulse height analyser. The memory board of the analyser had to be modified for this experiment by adding additional circuitry (a 2-to-4 line decoder/multiplexer) to the commercial version of the analyser in order to enable us to choose any of 4×256 channel subgroups of the memory using a 3 bit word provided by the sample changer position status.

The linear outputs from the 11th dynode of each photomultiplier on the large neutron detector are preamplified and summed by a linear summing module before amplification by a conventional OP-Amp based design of circuit with RC shaping, accommodated in a single NIM module together with P.S.D. circuitry. Summing the linear signals before amplification reduces the complexity of the electronics. The time of flight spectra are gated by the neutron selector output signal which determines not only the gating energy but also the detection of a neutron by the scintillator detector.

3×256 channels T.O.F. spectra consisting of scattering sample, reference sample and background (sample out) spectra can be collected in turn for any preset time interval. Similarly an auxiliary T.O.F. data could be stored in a 3×100 channels subgroups of a Laben 400 channel pulse height analyser.

The neutron cone associated with detected alpha particles was monitored using a fast coincidence set up. A time to amplitude converter and single channel analyser (TAC and SCA, ORTEC 467) was employed to select the region of interest of the coincidence spectrum (the peak region).

Neutron cone monitor data was stored in a 8 digit triple scaler unit. Scaler overflow can only occur approximately every three hours despite high $n - \alpha$ counting rate.

An ORTEC model 441 Ratemeter displayed the alpha-neutron coincidence rate within the neutron cone and was used for optimum setting of the accelerator beam on the target.

A Cathode Ray Oscilloscope (CRO) displayed the linear alpha pulses in order to check visually the associated alpha particle detector against excessive counting rate which is likely to cause pile up or

saturate the photomultiplier during the course of the experiment. Pile up would occur more readily for the linear alpha pulses rather than for the fast signals due to the longer duration of the linear signals. Continuous visual inspection of these pulses by oscilloscope would guarantee that the fast pulses are free from distortion.

Data collected in the 1024 Channel Pulse Height Analyser (PHA) was transferred to an APPLE II microcomputer through a serial interface controlled by the program PHATRAN written in PASCAL for the present experiment.

Some of the electronic units designed and built for this work are discussed in the next sections.

3.8 Triple Scaler Unit

Normalization of the scattering cross-section data for the scattering sample, reference sample and also for the background was performed by storing the number of neutron-alpha coincidences in three separate scalers.

A triple scaler unit was therefore designed and built into a double width NIM module for use in the present experiment. Three fully integrated 8 digit RS7226A Universal Counters are employed. Each counter is accompanied by a 10MHZ external oscillator as time base for the internal circuitry of the counter.

The counter inputs accept pulses of a maximum frequency of 10MHZ in frequency and unit counter mode. Inputs can be driven from TTL logic. Only one input is provided to the triple scaler which can be multiplexed by a 2-to-4 decoder/multiplexer (74139 IC) to one of the three scalers at a time. A timer pulse from the sample

SCALER AND ROUTING CIRCUIT DIAGRAM

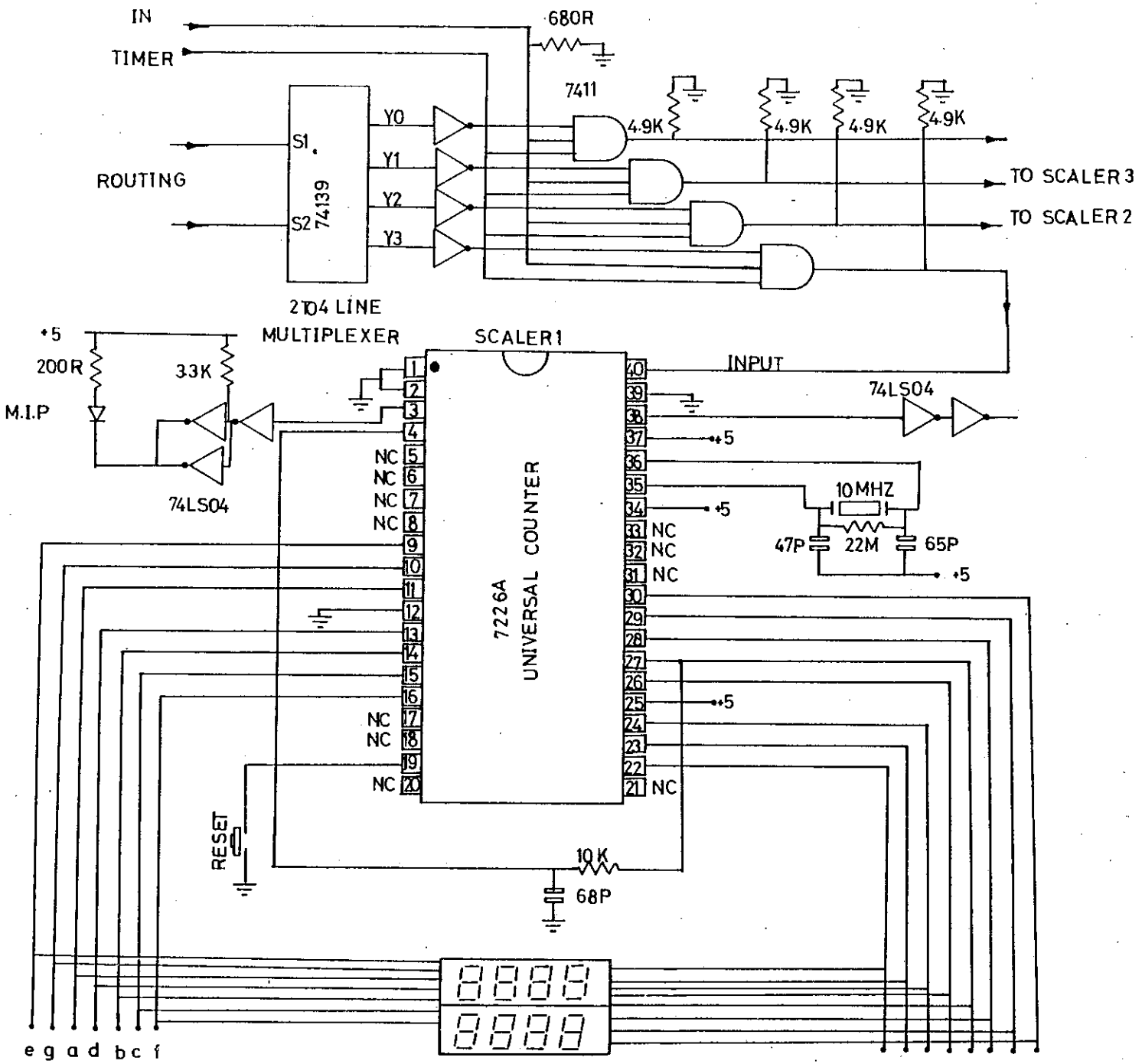

Figure 3.28.

changer control unit, opens the gate and can control the flow of information to the counter.

A 4.9KΩ pull up resistor at each input provides better noise immunity when TTL logic is used as input driver. For future development, multiplexed B.C.D. outputs and control signals are available to aid the transfer of information to other devices, such as a computer.

The on-chip display driver can drive a common anode LED display.

A detailed circuit diagram of one of the three scalers designed for this work is shown in Fig. (3.28).

3.9 Neutron Selectors

Neutron selector units were based on the principles discussed in Section 3.4.3 and were originally designed by Galloway and Wang[70]. Three of these units were made for experiment to serve as neutron selector for neutron detectors. Each unit was accommodated in a single width NIM module together with RC shaping circuitry, amplifier and energy discriminator.

The block diagram of the electronics of the neutron selector unit (P.S.D.) is shown in Fig. (3.29). Dynode pulses from the 10th dynode of the RCA4522 photomultiplier are shaped in a double differentiating - clipping amplifier after preamplification in an improved preamplifier design. The shaped pulses are then fed simultaneously into a low level and also a zero-crossing pulse height discriminator. Pulses resulting from these discriminators are then used to trigger a time to amplitude converter. The amplitude of the time converter

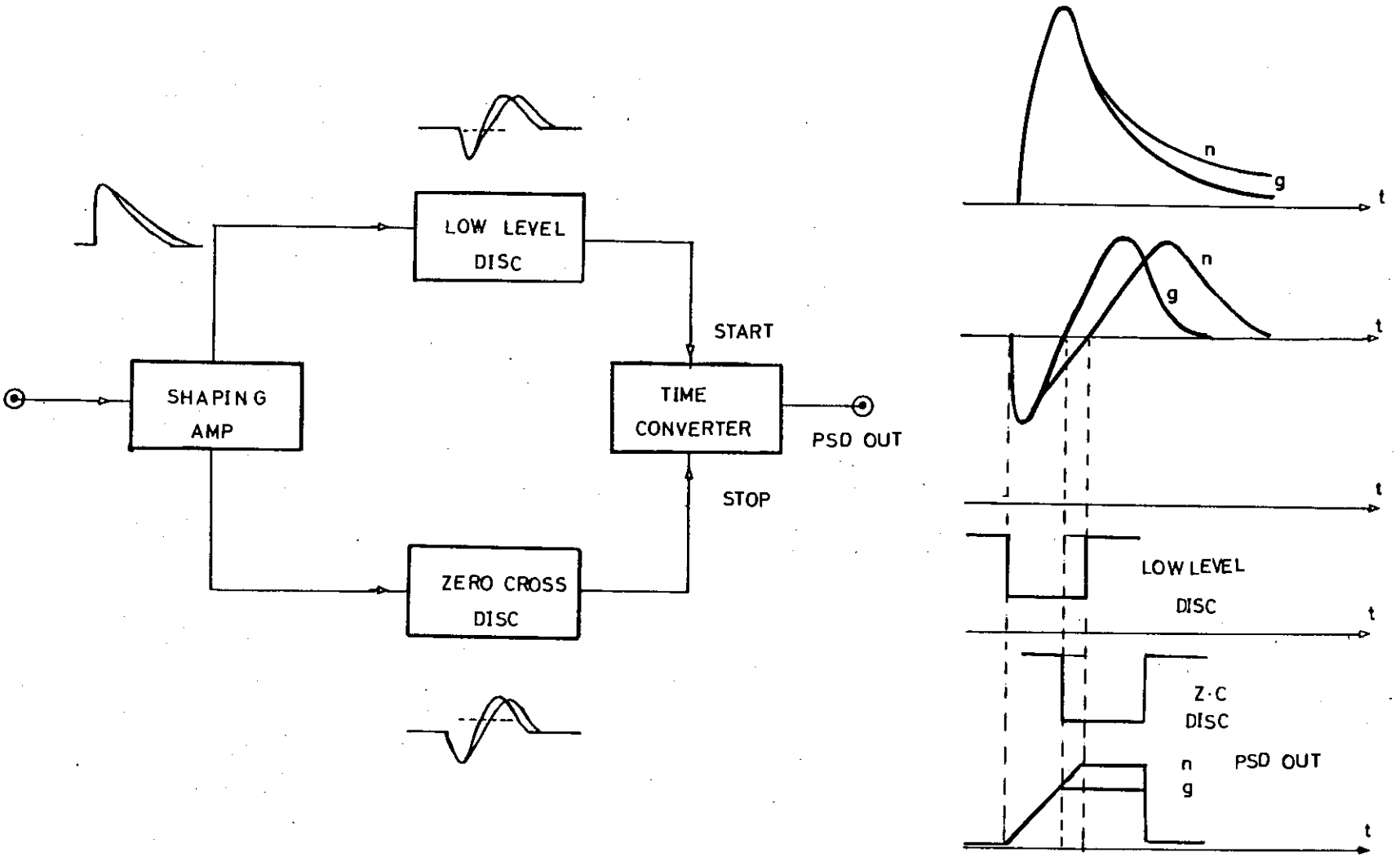

Figure 3.29: Block diagram of the pulse shape discriminator unit.

signals is proportional to the zero crossing time and is larger for neutron events than that of gamma events, a simple pulse height discriminator can therefore reject gamma events.

CHAPTER 4

GENERAL TESTING OF THE TIME OF FLIGHT SYSTEM

4.1 Neutron Beam Profile Measurement

In order to ensure that the scattering sample intercepts the neutron beam in a manner that the centre of the sample coincides with the centre of the neutron cone, the dimensions of the neutron cone and its location was established accurately. The shape of the aperture through which the associated alpha particles are detected defines the shape of the neutron cone.

The associated alpha particle detector was described in Chapter 2. Its aperture is an aluminium disc with a rectangular opening 25mm in height and 12.5mm in width machined at its centre.

Fig. (4.1) shows the electronics for the measurement of the neutron beam profile. A stilbene detector, consisting of a thin stilbene crystal 30mm × 40mm and only 3mm thick, mounted on a 56 AVP photo-multiplier was used as neutron detector. This detector was fitted on a rail system which provided smooth and accurate movement of the detector assembly with an accuracy of 0.5mm, using the ruler incorporated with the rail system. The crystal scanned the beam in such a manner that neutrons enter the crystal through its edge (3mm thickness).

Fast signals from the stilbene and alpha particle detectors were fed to two constant fraction discriminators (CFD) before being suitably delayed and then fed to a time to amplitude convertor (TAC) to form a fast coincidence system. The neutron-alpha coincidence rate selected by a single channel analyser (SCA) from the peak region of the spectrum

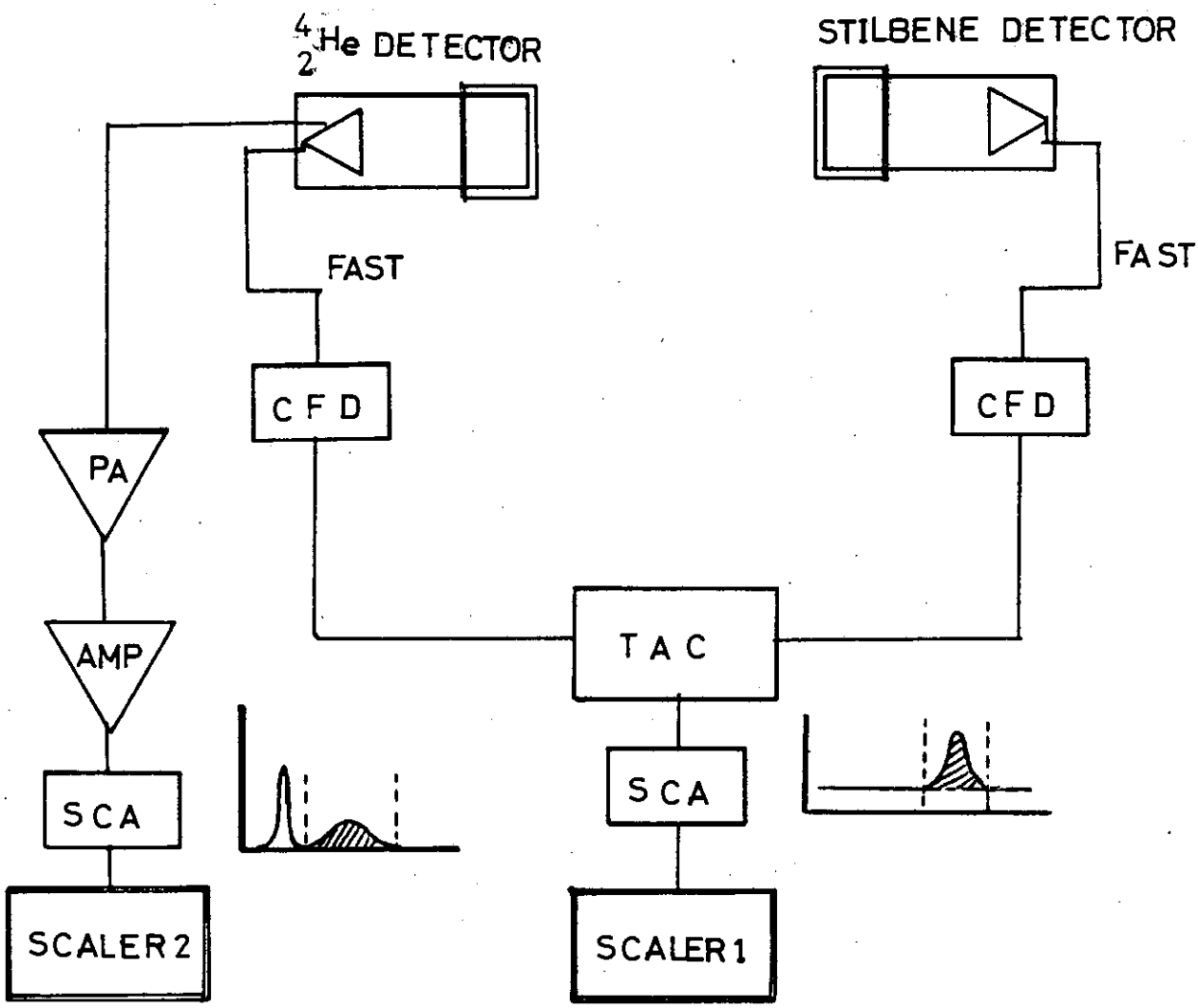

Figure 4.1: Electronics arrangement for neutron beam profile measurement.

was then recorded in the scaler 1. It was necessary to use the SCA in order to reduce the contribution of background due to random coincidences. To correct the stilbene counts for variation in neutron flux produced by the target, neutron counts were normalized by the number of alpha particles selected by a second SCA from the linear alpha spectrum and stored in scaler 2.

Similar measurements were carried out to determine the height of the neutron cone by setting up the stilbene detector rail mechanism vertically to scan the beam in 0.5 cm steps.

In Figs. (4.2) and (4.3) the neutron beam profile dimensions at 20 cm from the target are shown, the location of the scattering sample in relation to the centre of the neutron beam is also illustrated.

The coordinates of the centre of the neutron beam were identified with reference to the beam line and target chamber, using a 60 cm long arm with a pointer incorporated which was clamped round the deuteron beam line. During the course of the experiment the position of the scattering sample was checked against the position of the arm to ensure that the sample was fully illuminated by the neutron beam.

4.2 Determination of the Zero Scattering Angle

Following the positioning of the long high efficiency neutron detector at the appropriate height and angle at a distance of about 13 metres from the scattering sample, the Zero Scattering angle for the long flight path T.O.F. System had to be established. This was performed by rotating the target chamber assembly round the deuteron beam axis at 0.3 degree steps and recording the neutron-alpha coincidence rate between the alpha detector and long neutron detector,

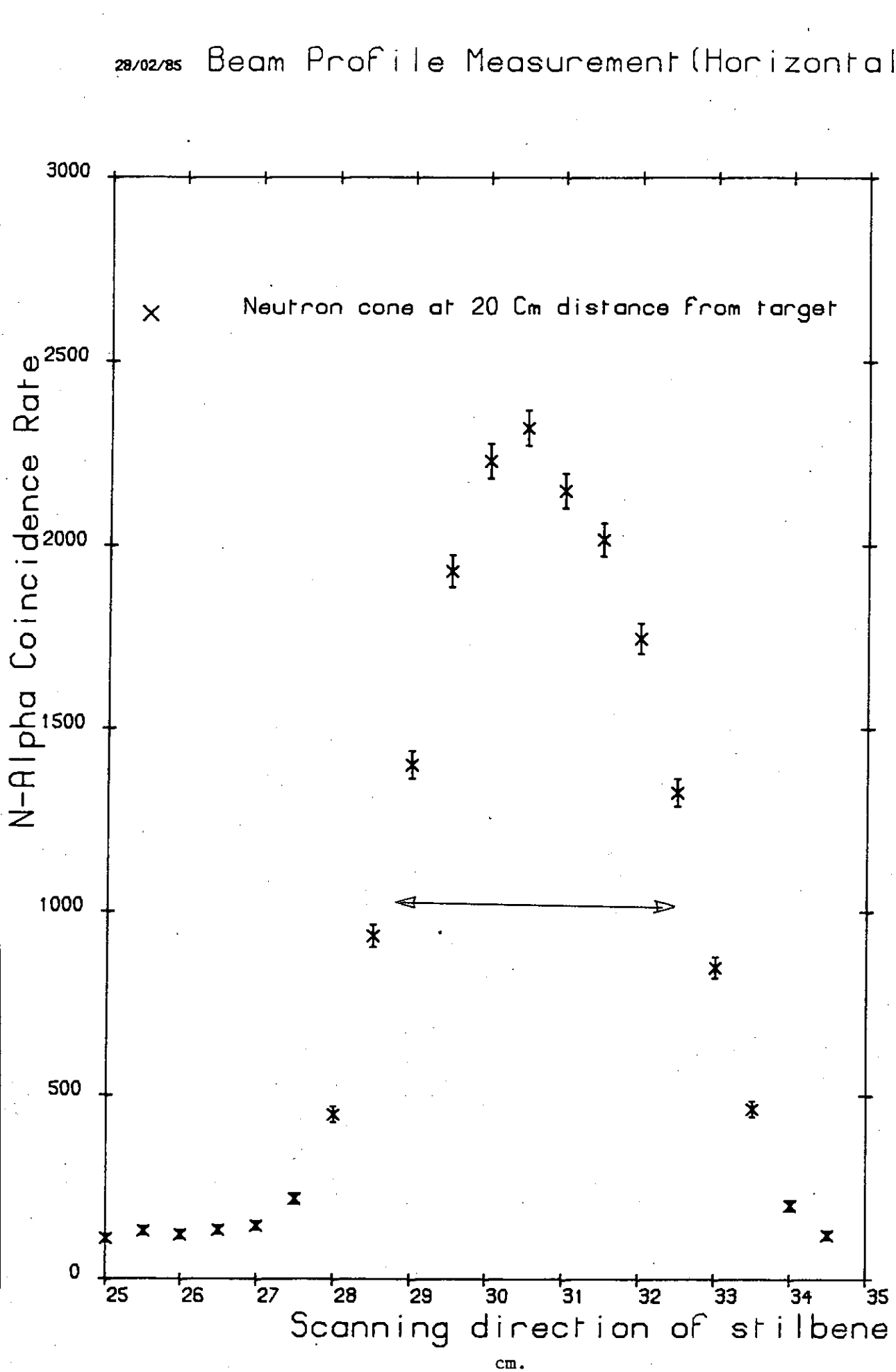
28/02/85 Beam Profile Measurement (Horizontal)
Neutron cone at 20 Cm distance from target
N-Alpha Coincidence Rate
3000
2500
2000
1500
1000
500
0
25
26
27
28
29
30
31
32
33
34
35
Scanning direction of stilbene
cm.

Figure 4.2.

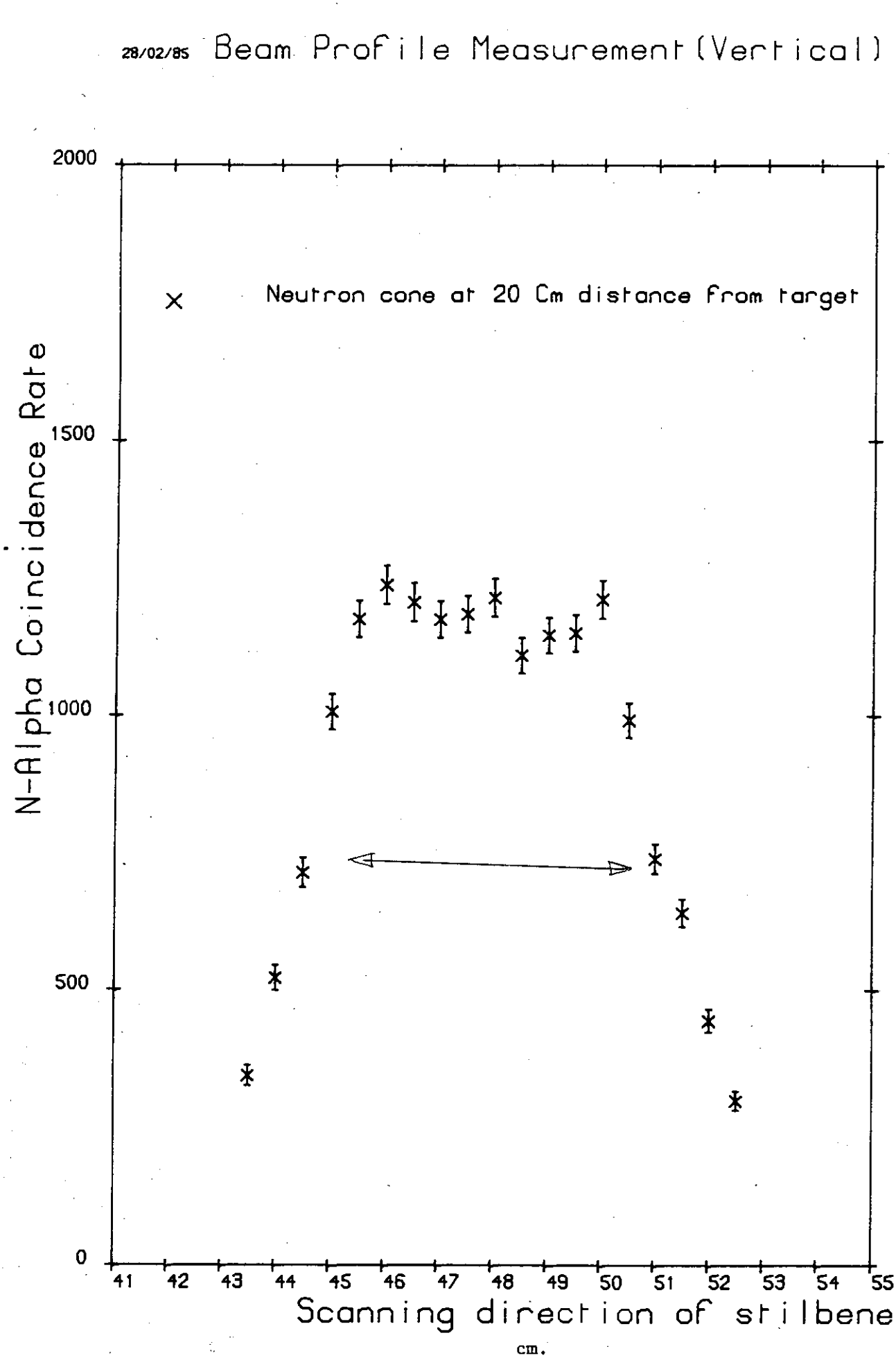
28/02/85 Beam Profile Measurement (Vertical)
Neutron cone at 20 Cm distance from target
N-Alpha Coincidence Rate
2000
1500
1000
500
0
41
42
43
44
45
46
47
48
49
50
51
52
53
54
55
Scanning direction of stilbene
cm.

Figure 4.3.

normalized with the alpha particle counting rate. The angle resulting in the maximum neutron-alpha coincidence rate was decided as being the zero scattering angle of the scattering system. The accuracy of this measurement is estimated to be 0.3 degrees. The reliability of determining the zero angle was checked by further test of the alignment of the detector axis with the collimator axis, scattering sample and the centre of the neutron-producing target using both a telescope and a laser beam.

A large protractor (60cm in diameter), machined from aluminium plate, was mounted round the deuteron beam line on a table, Fig. (2.2), parallel to the reaction plane, to provide determination of the scattering angle to an accuracy of ± 0.5 degree.

4.3 Preliminary Scattering Test with the Thin Neutron Detector

Having established the location of the neutron cone and also the zero scattering angle, a series of systematic tests were carried out for the purpose of evaluating the capability of the system in measuring differential scattering cross sections. Information such as scattered neutron counting rate, its relation with the background and the extent to which pulse shape discrimination together with the optimum energy bias can reduce the background in the time of flight spectra, was of primary interest to set up the scattering system satisfactorily.

In the first attempt to observe scattered neutron spectra the thin (Ø20 × 5cm) detector was positioned at the exit of the target collimator at a distance of about 300cm from the scattering sample. The sample was a cylinder of Iron of 2.5cm diameter and 5cm height.

Figure (4.4) shows the time of flight spectrum taken at short

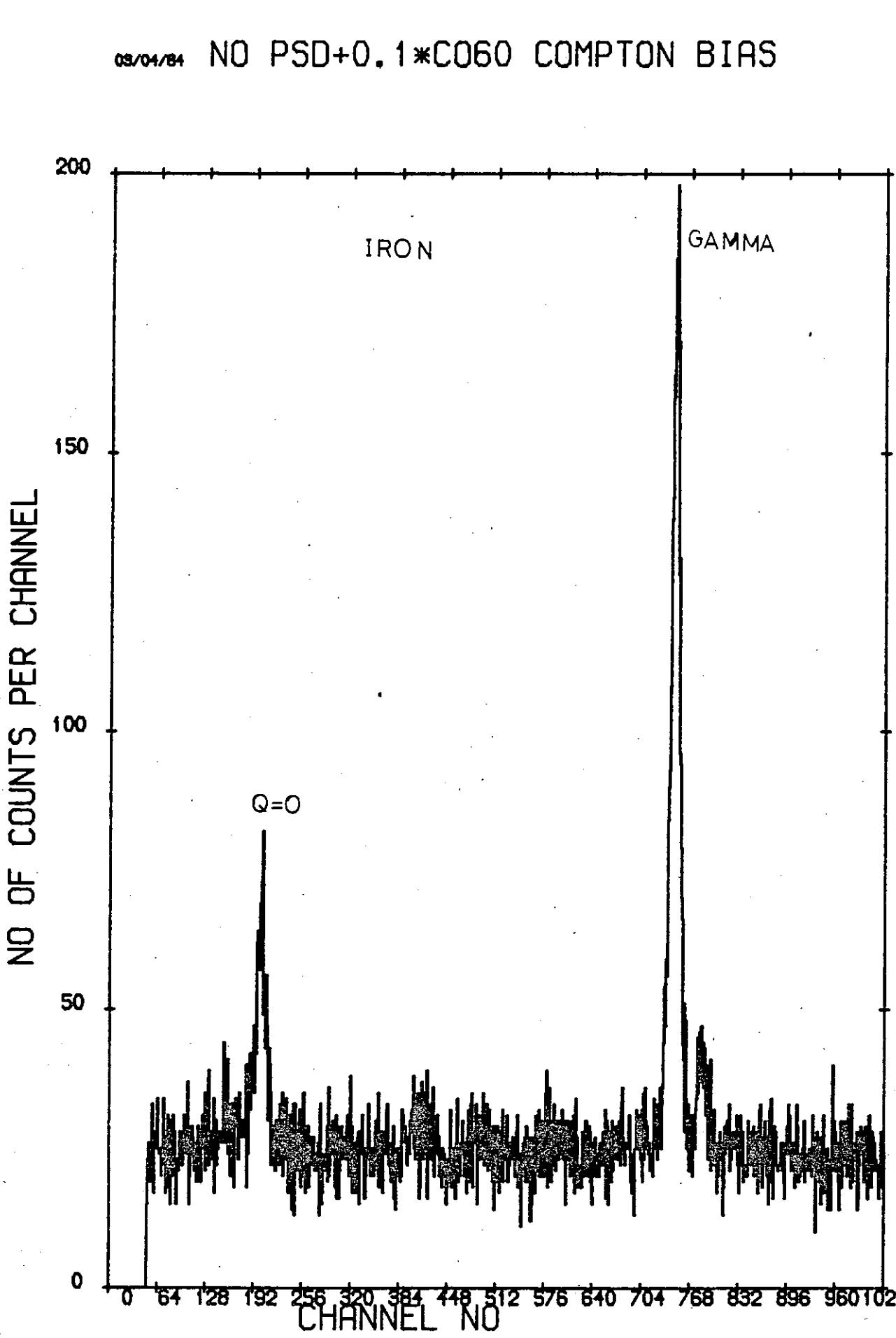
03/04/84 NO PSD+0.1*C060 COMPTON BIAS
IRON
GAMMA
Q=O
NO OF COUNTS PER CHANNEL
CHANNEL NO
0
50
100
150
200
0 64 128 192 256 320 384 448 512 576 640 704 768 832 896 960 1024

Figure 4.4.

flight path. The counting time for the collection of this spectrum was one hour. The energy bias was quite low at only 0.6 MeV proton energy and pulse shape discrimination was not applied. The prominent peak at about channel 750 is the gamma peak due to the inelastic scattering of neutrons in the scattering sample. The peak at about channel 200 is the elastic peak. As a result of the high random coincidence background and insufficient counting statistics the inelastic peak is not very clearly seen.

In the next spectrum, Fig. (4.5) collected with the same energy bias but applying neutron-gamma pulse shape discrimination, the intensity of gamma peak reduced substantially (55%) compared with that of scattered neutrons, which did not change significantly (only 15%). For even higher energy bias ($\sim$ 3.8 MeV proton energy) further reduction of the gamma peak was accompanied by the reduction of the background level and an increase of the scattered neutron to background ratio, Fig. (4.6). Table (4.1) is deduced on the basis of the three spectra shown in Figs. (4.4) to (4.6). The intensity of the gamma peak, scattered neutron peak and background was estimated simply from their height normalized with the monitor counts.

TABLE 4.1

	Neutron intensity	Gamma Intensity	Background
No P.S.D. applied, 0.6 MeV bias	54	173	27
P.S.D. applied, 0.6 MeV bias	46	79	16
P.S.D. applied, 3.8 MeV bias	43	24	5

Table 4.1 demonstrates that increasing the energy bias of the neutron detector from 0.6 to 3.8 MeV (proton energy) attenuates gamma events and

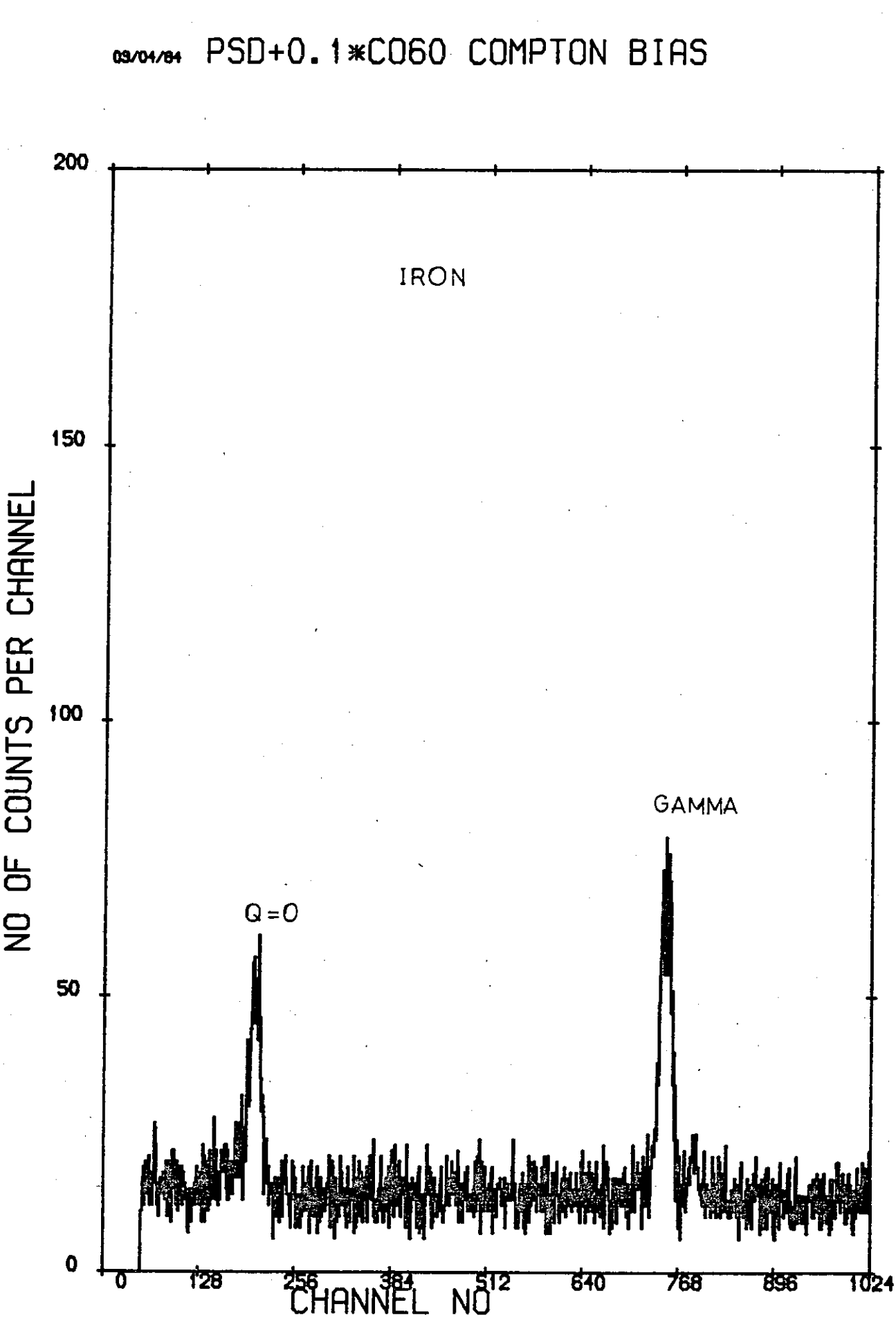
09/04/84 PSD+0.1*C060 COMPTON BIAS
IRON
GAMMA
Q=0
NO OF COUNTS PER CHANNEL
CHANNEL NO
200
150
100
50
0
0
128
256
384
512
640
768
896
1024

Figure 4.5.

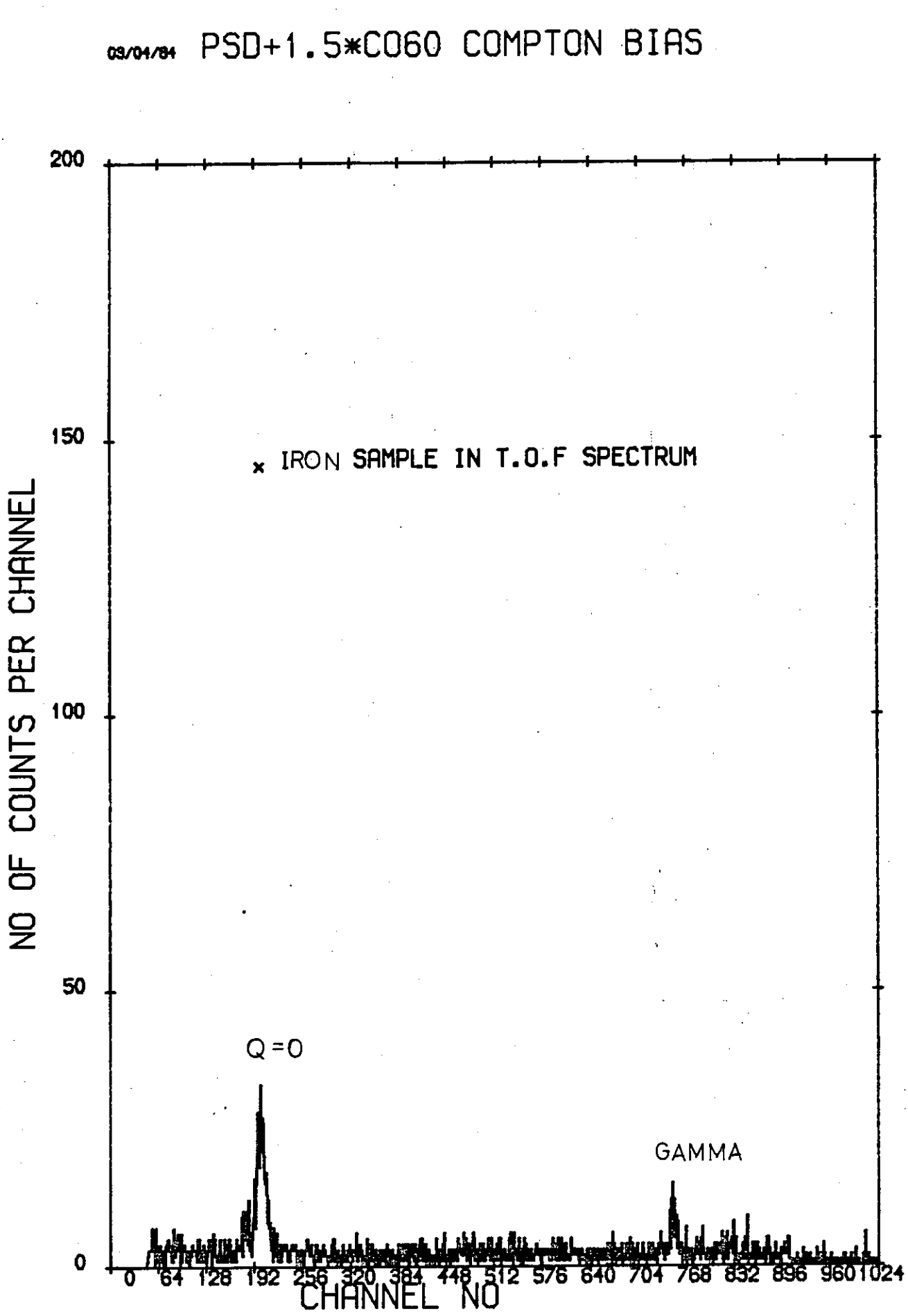
03/04/84 PSD+1.5*C060 COMPTON BIAS
200
150
100
50
0
× IRON SAMPLE IN T.O.F SPECTRUM
NO OF COUNTS PER CHANNEL
Q=0
GAMMA
0 64 128 192 256 320 384 448 512 576 640 704 768 832 896 9601024
CHANNEL NO

Figure 4.6.

random events contributing to the background, by three times, though neutron scattered events are not affected seriously. This is probably due to the improvement of neutron-gamma P.S.D. peak separation as a result of increasing the energy bias. The inelastic peak due to the scattering of neutrons from the 2^+ state of Iron at 0.846 MeV can be seen on the left side of the elastic peak, Fig. (4.6).

Tests performed with the thin detector, (Ø20cm × 5cm), at long flight path (≈ 12 metres) resulted in similar observations as with short flight path. The only difference, however, was the drop of counting rate as was expected at the rate of the inverse square of the distance.

The increase in the number of scattered neutron to background ratio suggested that the flat background observed in the T.O.F. spectra was mainly caused by accidental gamma events.

4.4 Scattering Test with the Large Volume Double Photomultiplier Neutron Detector

The performance of the high efficiency neutron detector was tested by observing the scattered neutrons at 40° scattering angle from a (Ø5cm × 5 cm) sample of Iron over a flight path of 12.6 metres. The time of flight spectra for the front and the rear photomultipliers were collected individually, before the time compensation method was applied. Fig. (4.7) shows the time of flight spectrum collected, using only the rear photomultiplier. Three observed peaks in this spectrum are due to gamma, elastic and inelastic events respectively from the high energy

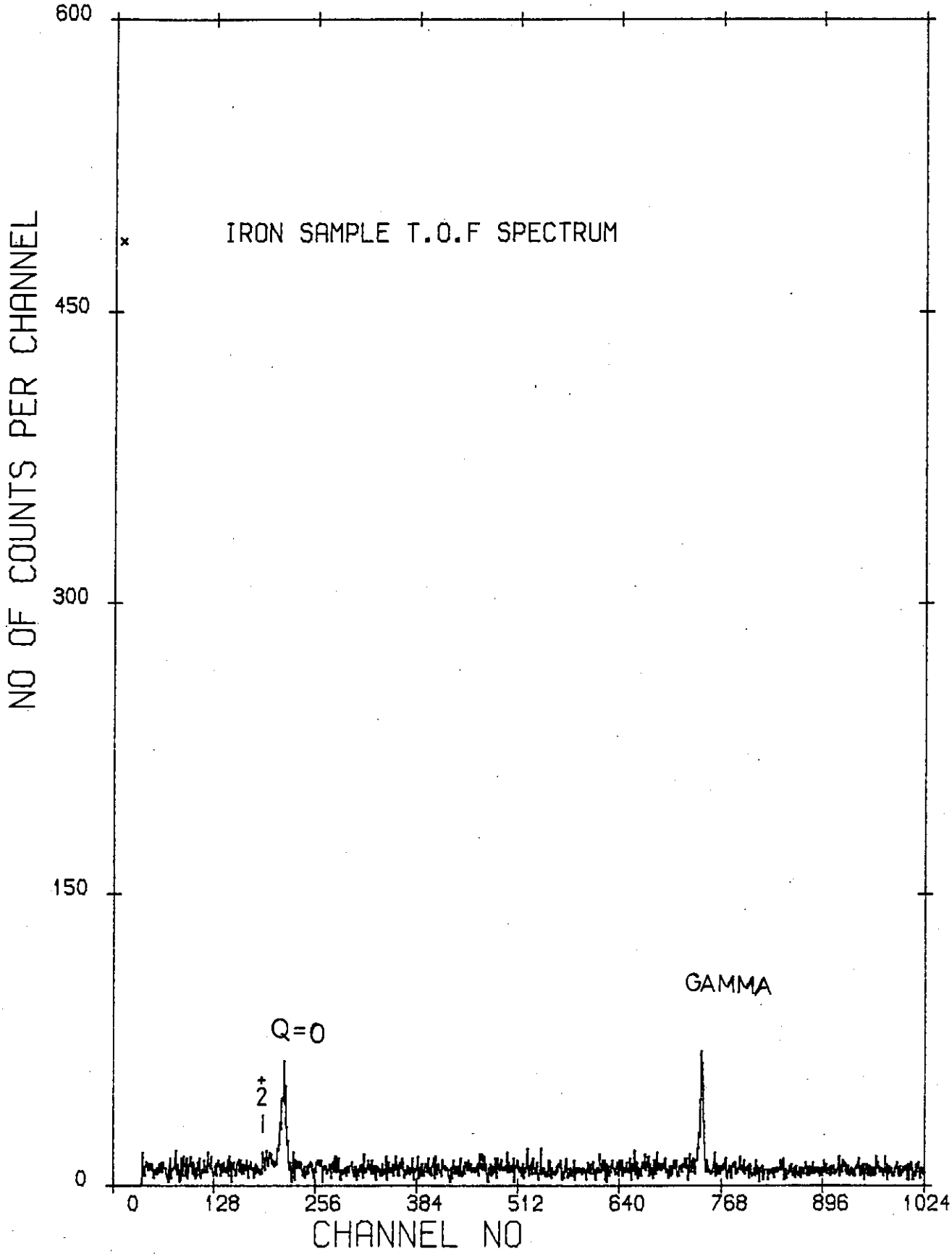
10/04/84 REAR TUBE-NO PSD, BIAS=2.4 MEV GAMMA
IRON SAMPLE T.O.F SPECTRUM
NO OF COUNTS PER CHANNEL
600
450
300
150
0
Q=0
+
2
1
GAMMA
0
128
256
384
512
640
768
896
1024
CHANNEL NO

Figure 4.7.

end of the spectrum to the low energy end.

The compensated time of flight spectra using both photomultipliers are shown in Figs. (4.8) to (4.10) for three different bias levels in order to investigate the optimum threshold energy for the neutron detector. The gamma peak is not shown because the timing spectrum has been expanded for better separation of the elastic peak and the peak due to the inelastic scattering to the 0.846 MeV state in Iron.

The time resolution achieved with the Ø5 × 5cm scattering sample was approximately 1.8ns. This time spread includes the time uncertainty caused by the finite size of the sample (5cm diameter of sample could result in a time spread of 1ns (10^{-9}s) for 14 MeV neutrons). The spectra in Figs. (4.8) to (4.10) with bias levels at 4.0 MeV, 6.0 MeV and 7.5 MeV show only slight improvement in separation between elastic and inelastic peaks as a function of energy bias. It is worth noting that these spectra are not counted for the same time, the counting time substantially increased as the bias was increased from 4.0 MeV to 6.0 MeV and then to 7.5 MeV, without significant improvement in the quality of spectra. It was then decided that an energy bias of around 4.0 MeV should be applied to the neutron detector for this measurement.

The areas under elastic and inelastic peak from Iron time of flight spectra were used to check the Iron cross section measured at 40°. The ratios:

$$\frac{\sigma_{Iron}(n,n)}{\sigma_{Iron}(n,n')} = \frac{75}{15} = 5.0$$

$$\frac{A_{elastic}}{A_{inelastic}} = \frac{574}{105} = 5.4$$

were determined, in which $\sigma_{Iron}(n,n)$, $\sigma_{Iron}(n,n')$ are Iron cross sections

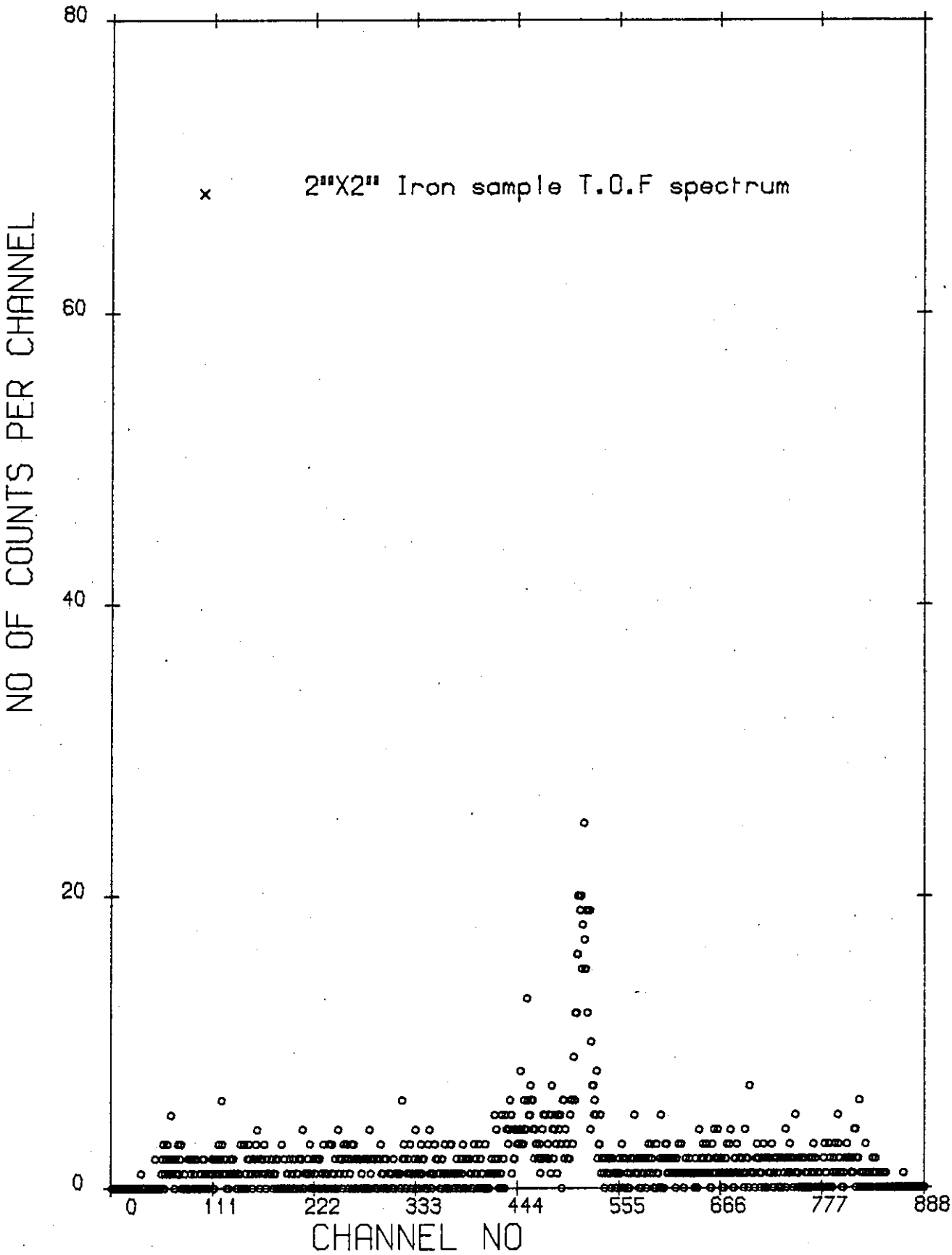
17/07/84 PSD, ENERGY BIAS=4.0 MEV PROTON
2"X2" Iron sample T.O.F spectrum
NO OF COUNTS PER CHANNEL
CHANNEL NO
0
20
40
60
80
0
111
222
333
444
555
666
777
888

Figure 4.8.

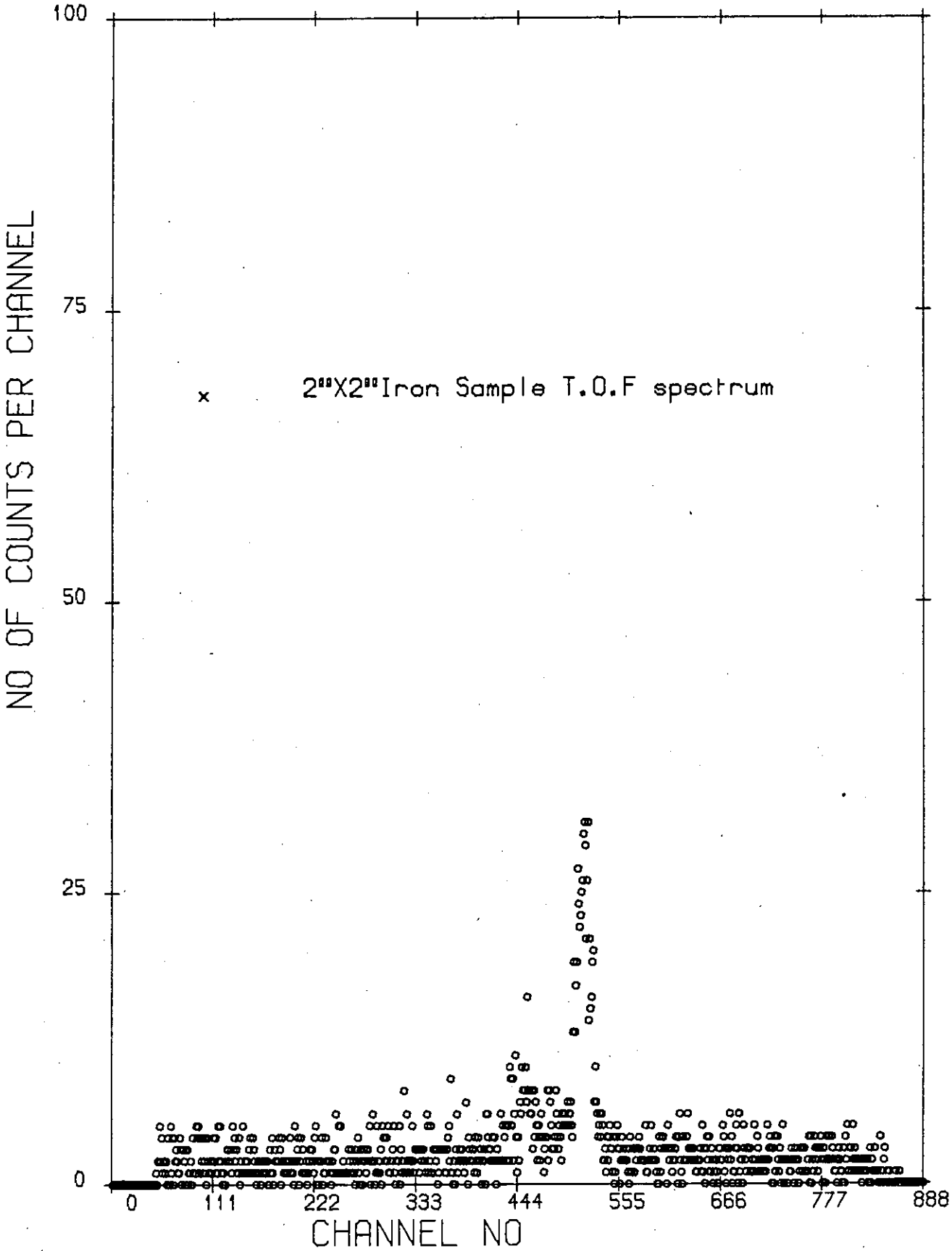
17/07/84 PSD, ENERGY BIAS=6.0 MEV PROTON
2""X2""Iron Sample T.O.F spectrum
NO OF COUNTS PER CHANNEL
CHANNEL NO
100
75
50
25
0
0
111
222
333
444
555
666
777
888

Figure 4.9.

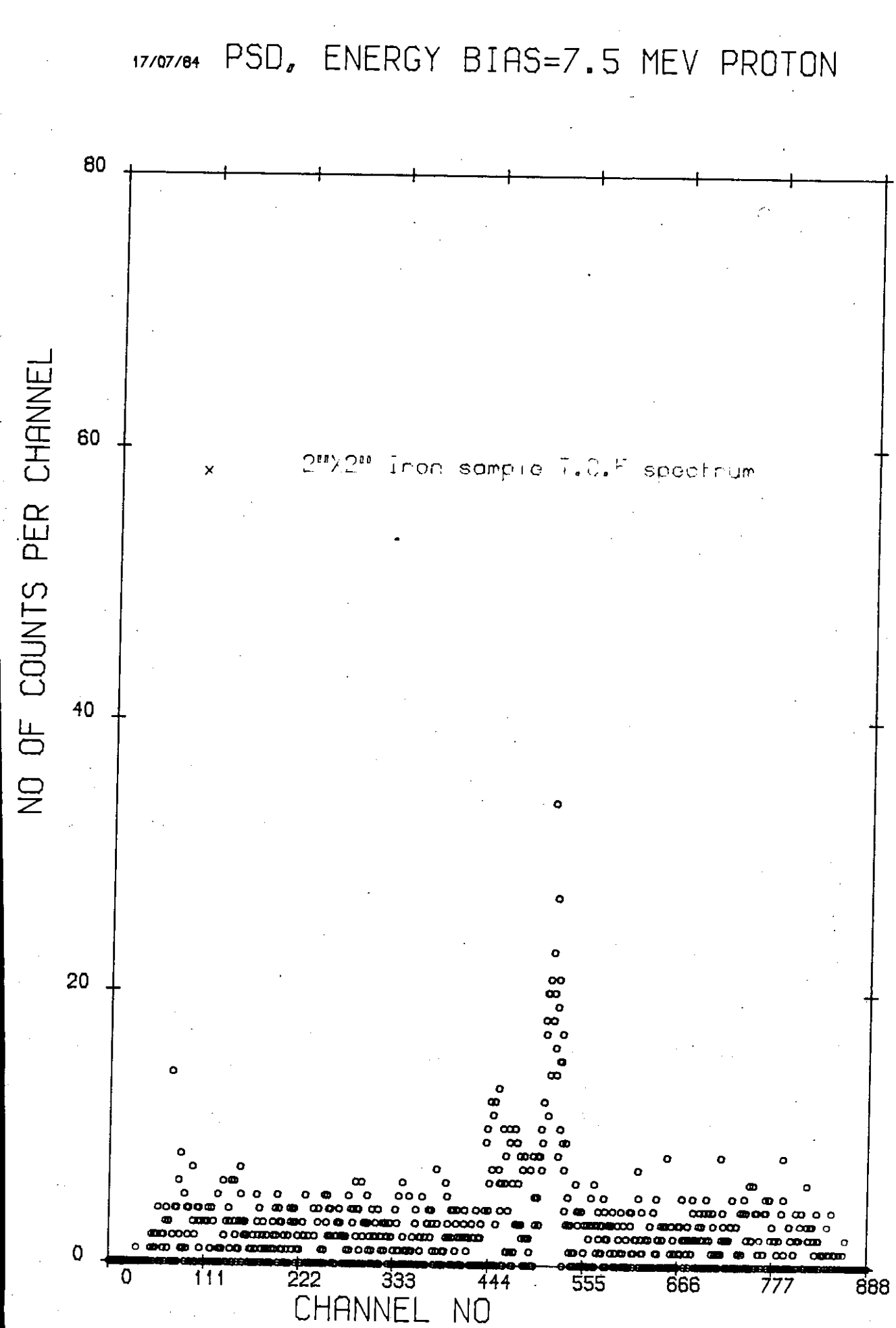
17/07/84 PSD, ENERGY BIAS=7.5 MEV PROTON
80
60
40
20
0
NO OF COUNTS PER CHANNEL
2"X2" iron sample T.C.F spectrum
0
111
222
333
444
555
666
777
888
CHANNEL NO

Figure 4.10.

for elastic and inelastic scattering respectively[90]. $A_{elastic}$ and $A_{inelastic}$ are the area under elastic and inelastic peaks respectively in the time of flight spectra, Fig. (4.9). These quantities were in good agreement within the experimental errors.

4.5 Choice of Scatterer used for the Cross Section Calibration

The scatterer for cross section calibration must be readily available in a pure form and also its cross section should be well known with reasonable accuracy. Among the elements meeting these two requirements are Hydrogen and Carbon.

Hydrogen is in gaseous state and therefore the polymer form of it with Carbon $(CH_2)_n$, under the chemical name "Polyethylene" is commonly used to avoid difficulties in dealing with a gaseous sample. The major difficulty, however, with using a polyethylene sample is the complexity of the time of flight spectrum. That is because the n - p scattering peak and the peak resulting from inelastic scattering by carbon are energetically close and, due to the kinematic broadening effect on these two peaks, it is often difficult to separate these two overlapping peaks even in the angular range of 30-35° laboratory angle for which the carbon elastic peak, carbon inelastic and n - p scattering peaks are kinematically expected to be better separated. The peak overlapping effect become more significant at energies higher than around 10 MeV with a realistically achievable energy resolution. Figs. (4.11) and (4.12) show the time of flight spectra obtained with Ø2.5 × 5cm and 5 × 5cm cylindrical polyethylene samples at 32° scattering angle. Due to the finite size of the sample and its distance from the neutron producing target (∿ 20 cm) there is a maximum angular uncertainty of

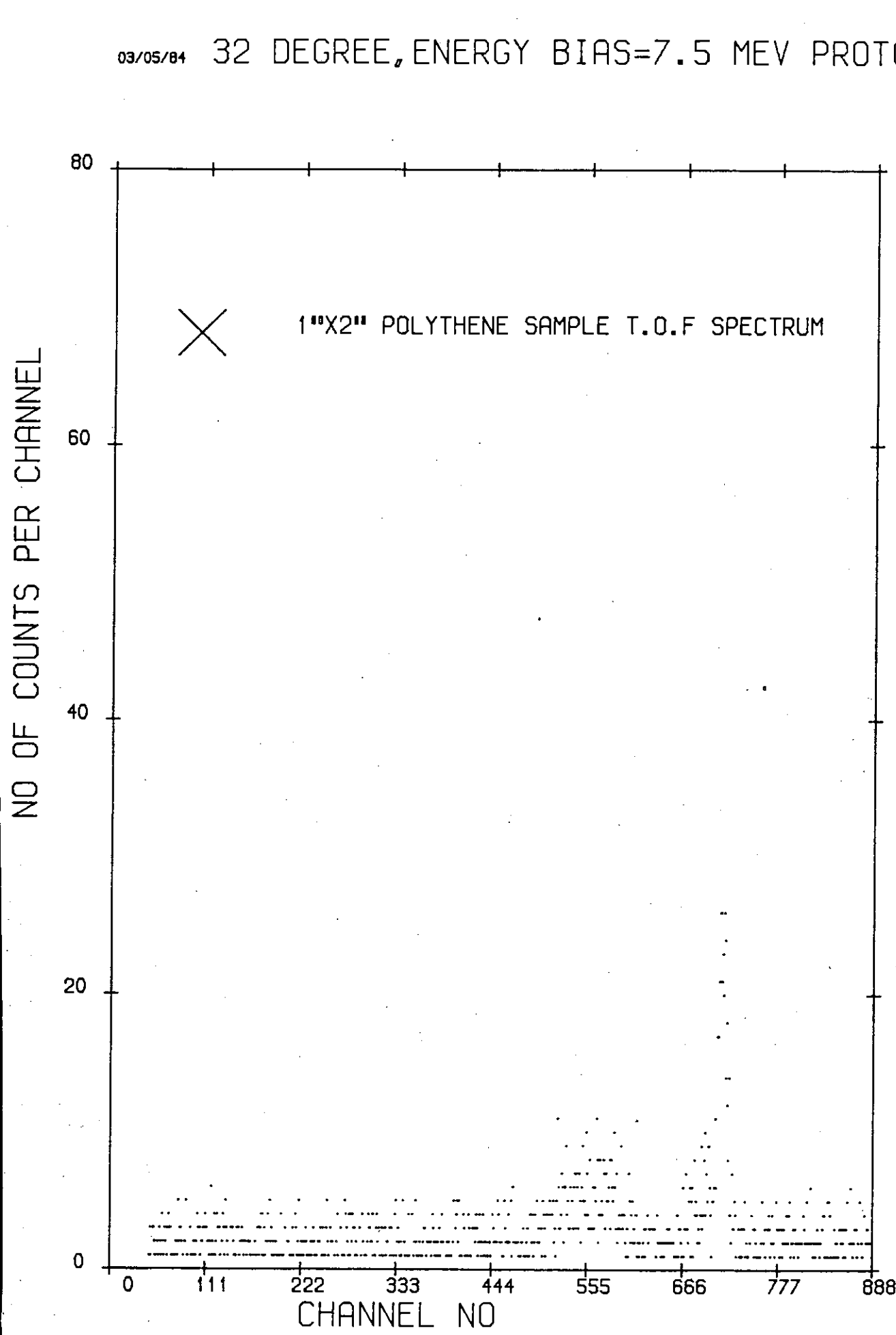
03/05/84 32 DEGREE, ENERGY BIAS=7.5 MEV PROTON
1"X2" POLYTHENE SAMPLE T.O.F SPECTRUM
NO OF COUNTS PER CHANNEL
80
60
40
20
0
0
111
222
333
444
555
666
777
888
CHANNEL NO

Figure 4.11.

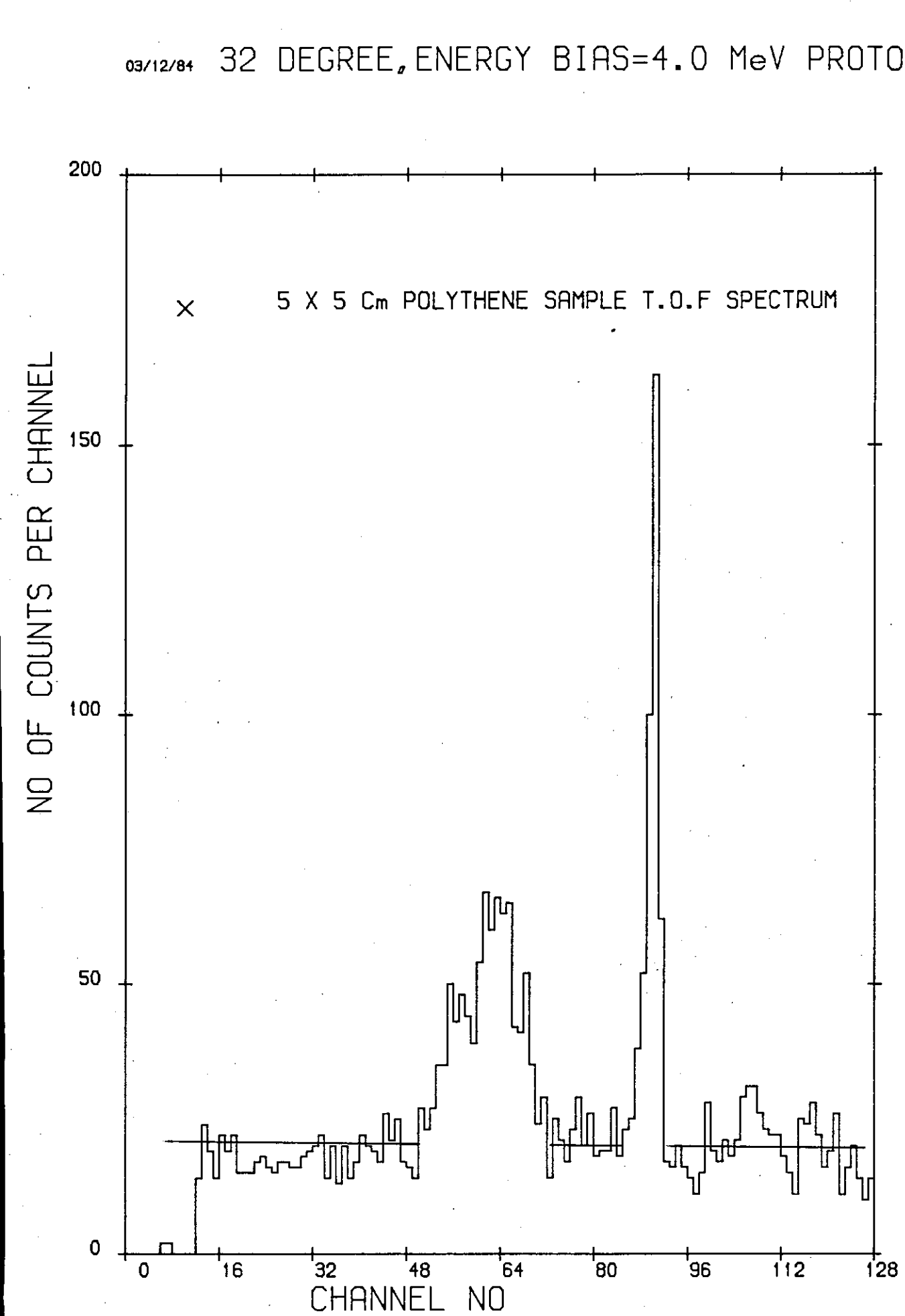
03/12/84 32 DEGREE, ENERGY BIAS=4.0 MeV PROTON
5 X 5 Cm POLYTHENE SAMPLE T.O.F SPECTRUM
NO OF COUNTS PER CHANNEL
CHANNEL NO
0
50
100
150
200
0
16
32
48
64
80
96
112
128

Figure 4.12.

($\pm 7^{o}$) in scattering angle. Since the energy of the n - p peak depends in a very sensitive way on the scattering angle, Fig. (4.13), this angular spread resulted in the broadening of the n - p peak by $\Delta E = 3.2$ MeV and the carbon inelastic peak by $\Delta E = 250$ keV, both of which are calculated on the basis of the kinematics of the n - p and n - C scattering[39]. The broadening effect caused the strong overlap of these peaks. Glasgow et al.[91] performed additional scattering measurements with a carbon sample to correct for overlap of the n - p and the inelastic n - C scattering peaks.

Another element which can be employed for cross section calibration is carbon (graphite). The carbon cross section is well known with an accuracy of 5% at 14 MeV. The elastic and inelastic carbon peaks are well separated (Q = -4.44 MeV) and so there is no possibility for the elastic peak to be contaminated with the inelastic peak. Fig. (4.14) shows the time of flight scattering spectrum of 14.1 MeV neutrons scattered from carbon at 20^{o} scattering angle.

4.6 Comparison of the Detection Efficiency of the Thin and the Thick Neutron Detector

The efficiency of the large volume double photomultiplier neutron detector was estimated by comparing its spectra to the corresponding spectra obtained with the 5cm thick detector having the same diameter. The thick compensated neutron detector was approximately 4 times more efficient for 14 MeV neutrons obtained from the $^{3}H(d,n)^{4}_{2}He$ reaction. The ratio of the volume of the time compensated detector to that of the thin detector was about 5. Probably attenuation of the incident neutrons in the detector package, base, photomultiplier and in the

Figure 4.14.

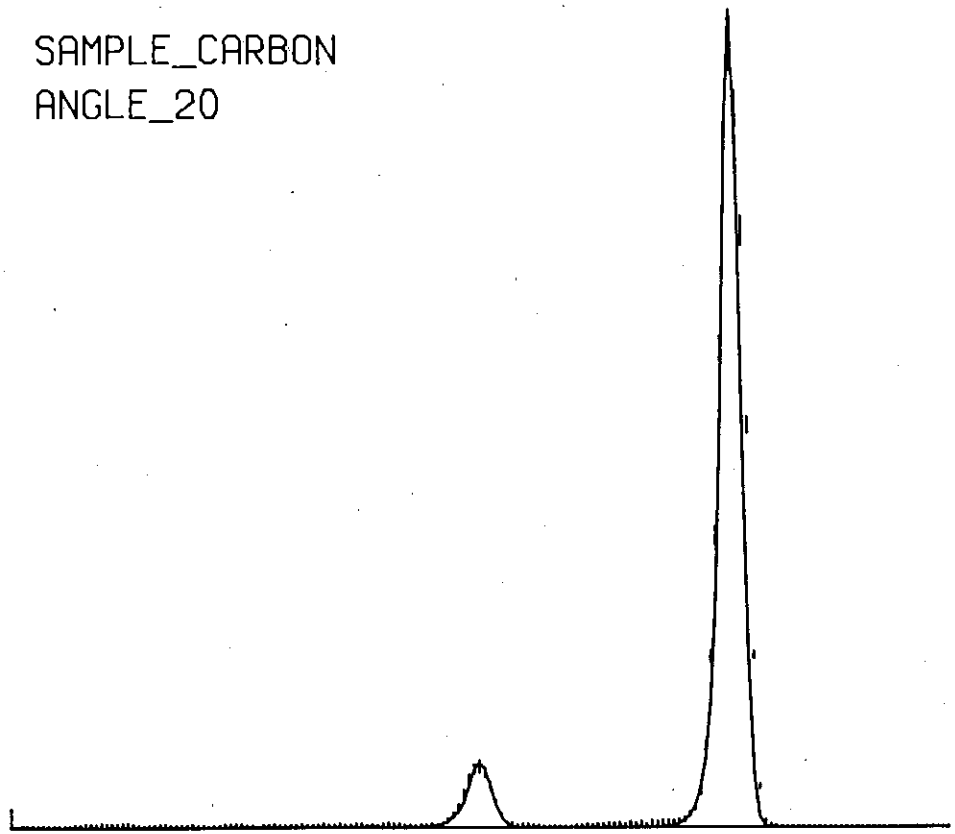

Figure 4.13.

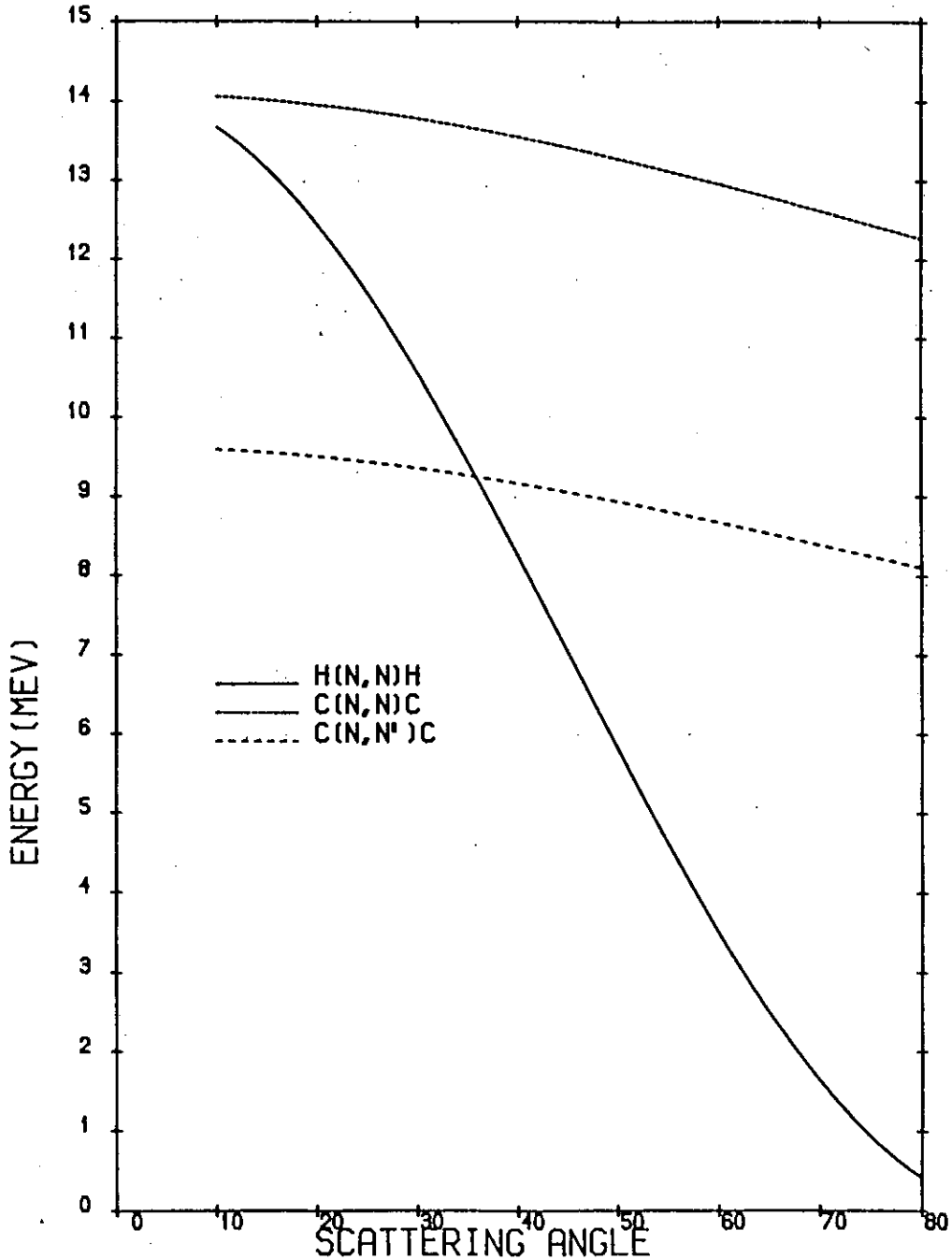

approximately 3cm thick light guide facing the incoming neutrons could account for the departure of the measured efficiency ratio from the volume ratio for these two detectors. An analytical method of neutron detection efficiency calculation is discussed in this chapter.

4.7 Analytical Calculation Method for the Calculation of the Detection Efficiency of the Neutron Detectors

The quality of angular distribution measurements on neutrons by the time of flight technique depends strongly on the precise knowledge of the energy dependence of the neutron detection efficiency, especially when light nuclei are involved.

The efficiency of a neutron detector is defined[92] as the ratio of the number of recoil protons to the number of incident neutrons or, more precisely, the efficiency ε, of a neutron detector to neutrons of a given energy is the probability of such a neutron incident on the detector within some effective area, S, producing an acceptable pulse in the attendant electronics, sufficient to enable its presence to be detected and distinguished from noise.

To apply the above definition, the mechanism of neutron detection in the scintillator has to be considered. Liquid scintillators commonly used for fast neutron detection, contain only carbon and hydrogen, the high concentration of the latter is of advantage for obtaining higher detection efficiency.

The detection efficiency determination of a neutron detector is rather difficult to perform due to the fact that different types of neutron interaction with hydrogen and carbon nuclei in the scintillator are possible and it is not a straight forward procedure to find out

which interactions result in a pulse height above the bias and which do not. The complication of efficiency calculation begins when one wishes to take into calculation the effect of neutron carbon interactions. These interactions could be classified as inelastic and elastic groups. The most important of the inelastic group is the $^{12}C(n,n')3\alpha$ reaction. Above about 12 MeV the reaction $^{12}C(n,n')3\alpha$ which has a threshold at 8.3 MeV contributes about one half of the total nonelastic cross-section[93] and therefore when neutrons with energy higher than about 12 MeV are involved it must not be neglected. However, due to the difficulties such as the lack of knowledge of the kinematics of this reaction, the distribution of the reaction energy among the reaction products, and finally because of the non-linearity of the light response curve of the scintillator, several Monte Carlo codes[94-97] for the efficiency calculation neglect the $n - 3\alpha$ process in scintillators.

In the elastic group the following interactions are likely to be undertaken by the incident neutrons in the scintillator:

(1) Double Scattering by Hydrogen.

In double scattering by hydrogen, two recoil protons are produced in such rapid succession that they are recorded as a single event with an apparent energy which would be the sum of the two proton energies if the response of the scintillator were linear.

(2) Single and multiple scattering by Carbon

The elastic interaction with carbon produces pulses well below the pulse height biases used in the present work and even multiple scattering by carbon alone still does not produce pulses above the bias. That is because of the kinematics of the neutron-carbon reaction. As is shown in Fig. (4.13) neutrons can at most transfer 28% of their

energy when they are elastically scattered from carbon.

3) Hydrogen-Carbon events increase the efficiency only if the first event produces a pulse just below the bias and the pile up of the carbon event makes it bigger than the bias. This is generally a very small contribution. In a carbon-hydrogen event the first collision degrades the neutron energy only slightly (28%) so that the situation is about the same as without a first collision except for the pile up with the small carbon pulse.

Taking into account (1-3) Drosg[46] has developed the efficiency formula:

$$\varepsilon(E,B) = \frac{E-B}{E}\left[1 - \exp(-t\Sigma_H(E)\right] \times \left[1 + \frac{B}{E-B/2}\left(1 - \exp\left(-\frac{t}{2}\cdot\Sigma_H(E-\frac{B}{2})\right)\right)\right] \tag{4.1}$$

where

$\varepsilon(E,B)$ = is the detector efficiency at neutron energy E and proton bias B.

$\Sigma_H(E)$ = The product of hydrogen number density and hydrogen cross section at energy E.

$\Sigma_C(E)$ = The product of carbon number density and carbon cross section at energy E.

t is the detector thickness.

In addition to (1-3) Fowler et al.[47] have estimated the effect of the attenuation by carbon within the scintillator volume and have derived:

$$\varepsilon(E,B) = \frac{\Sigma_H}{\Sigma}(1 - e^{-t\Sigma})\frac{E-B}{E} + \frac{B}{E}\cdot\frac{\Sigma_H}{\Sigma}(1 - e^{-t\Sigma})\cdot(1 - e^{-\frac{1}{2}t\Sigma(E-\frac{B}{2})})$$

$$\cdot \frac{\Sigma_H(E-B/2)}{\Sigma(E-B/2)} + F\frac{\Sigma_C}{\Sigma}(1 - e^{-t\Sigma})(1 - e^{-\Sigma(0.86E)\ell})$$

$$\cdot \frac{\Sigma_H(0.86E)(0.86E-B)}{\Sigma(0.86E)0.86E} \qquad (4.2)$$

where:

$$\Sigma = \Sigma_H + \Sigma_C$$

and F is the fraction of neutrons scattered by carbon which remain above the bias:

$$F = \frac{E-B}{0.28E}, \quad \text{for } E > B > 0.72E$$

$$F = 1, \quad \text{for } B \leq 0.72E$$

ℓ is equal to the mean chord length in the scintillator and is taken to equal $4V/S$, where V is the volume and S is the surface area.

Since the total carbon cross section, which has many narrow resonances, is comparable to that of hydrogen and numbers of these two nuclei in the scintillator are comparable as well, the attenuation of neutron by carbon is of real importance. Fowler et al.[47] have shown that the agreement between the measured values and the calculation is good (within a few per cent of the efficiency value) up to a neutron energy at which the carbon charged particle reactions begin to have a significant effect (18 MeV for 4 MeV bias).

In order to calculate the efficiency of our neutron detectors two FORTRAN Programs were written (EFFICINI, EFFICINII) on the basis of

equations (4.1) and (4.2). In both Programs, n - p total cross section[98] and n - c total cross sections[99] up to 20 MeV were fitted to polynomials for the purpose of interpolating the data between the experimental data points for efficiency calculation. The n - c cross section in the energy range between 0 - 20 MeV is tabulated in ref. (99, 100).

Figs. (4.15) to Fig. (4.17) show the calculated detection efficiency for two different detector sizes and various bias levels. Neglecting the multiple scattering contribution of carbon will make the calculated value lower than the actual value, whereas neglecting the flux attenuation by carbon, especially in long scintillators such as the one used here, will make the calculated value higher than the actual value.

The above method of efficiency prediction was used in the present work to determine the efficiency of both of the neutron detectors (Ø20 × 5cm and Ø20 × 25cm). The detectors were calibrated using standard gamma ray sources. The bias energy for each measurement was initially determined in terms of electron energy. The proton energy equivalent to electron energy was derived from the following expression parameterized by Madey et al.[101] for NE224 scintillator by adjustment to the experimental data:

$$T_e = T_p - 8.2(1 - \exp(-0.1T_p^{0.88})) \qquad (4.4)$$

Te and T_p are electron energy and its equivalent proton energy respectively and are expressed in MeV.

The reliability of the method described above for the detection efficiency calculations was checked, using the time of flight spectra obtained from neutrons scattered by Carbon and Polyethylene scattering samples. These spectra provided the detection efficiency check at

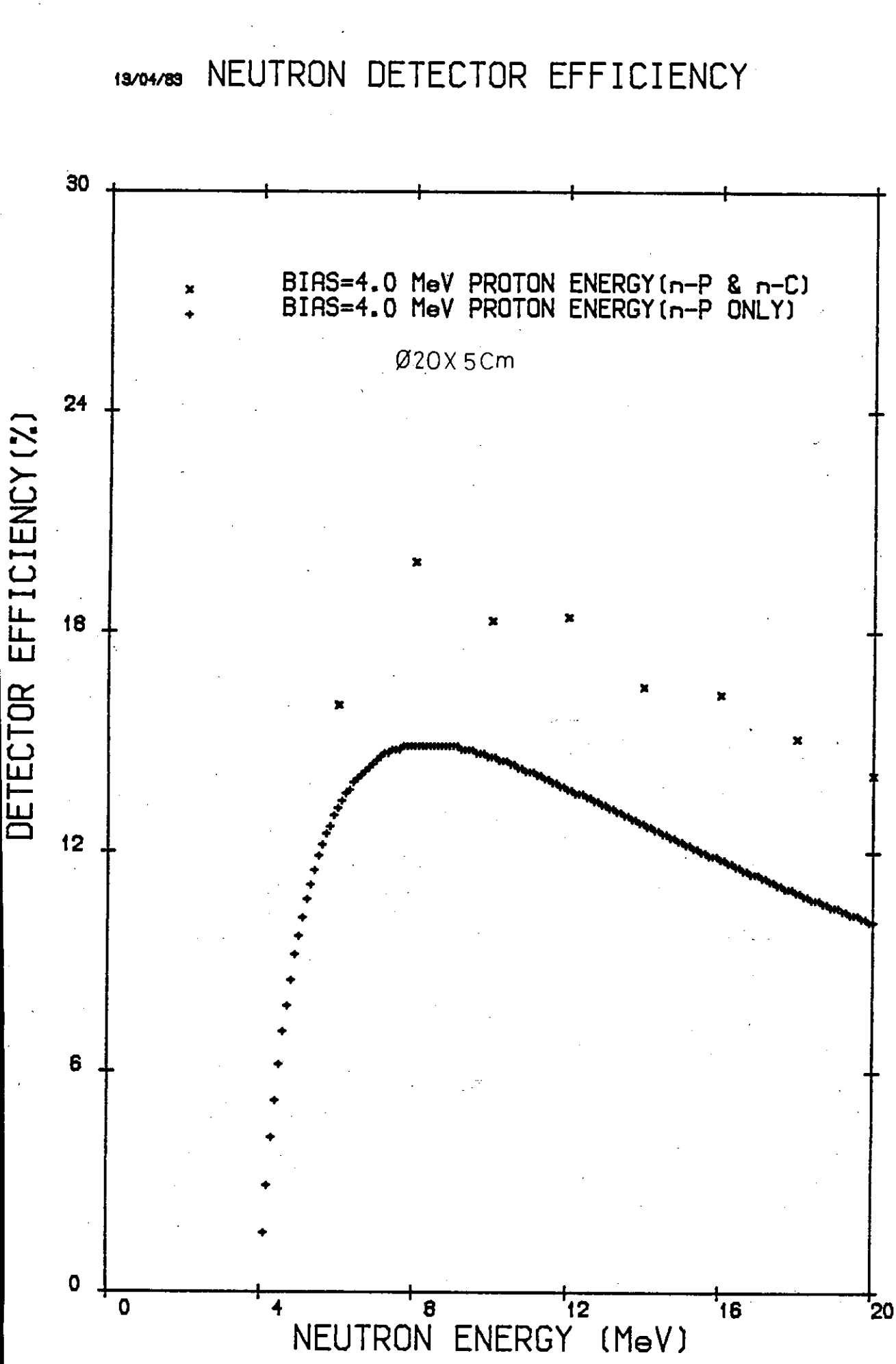
13/04/89 NEUTRON DETECTOR EFFICIENCY
BIAS=4.0 MeV PROTON ENERGY(n-P & n-C)
BIAS=4.0 MeV PROTON ENERGY(n-P ONLY)
Ø20X5Cm
DETECTOR EFFICIENCY(%)
NEUTRON ENERGY (MeV)
0
6
12
18
24
30
0
4
8
12
16
20

Figure 4.15.

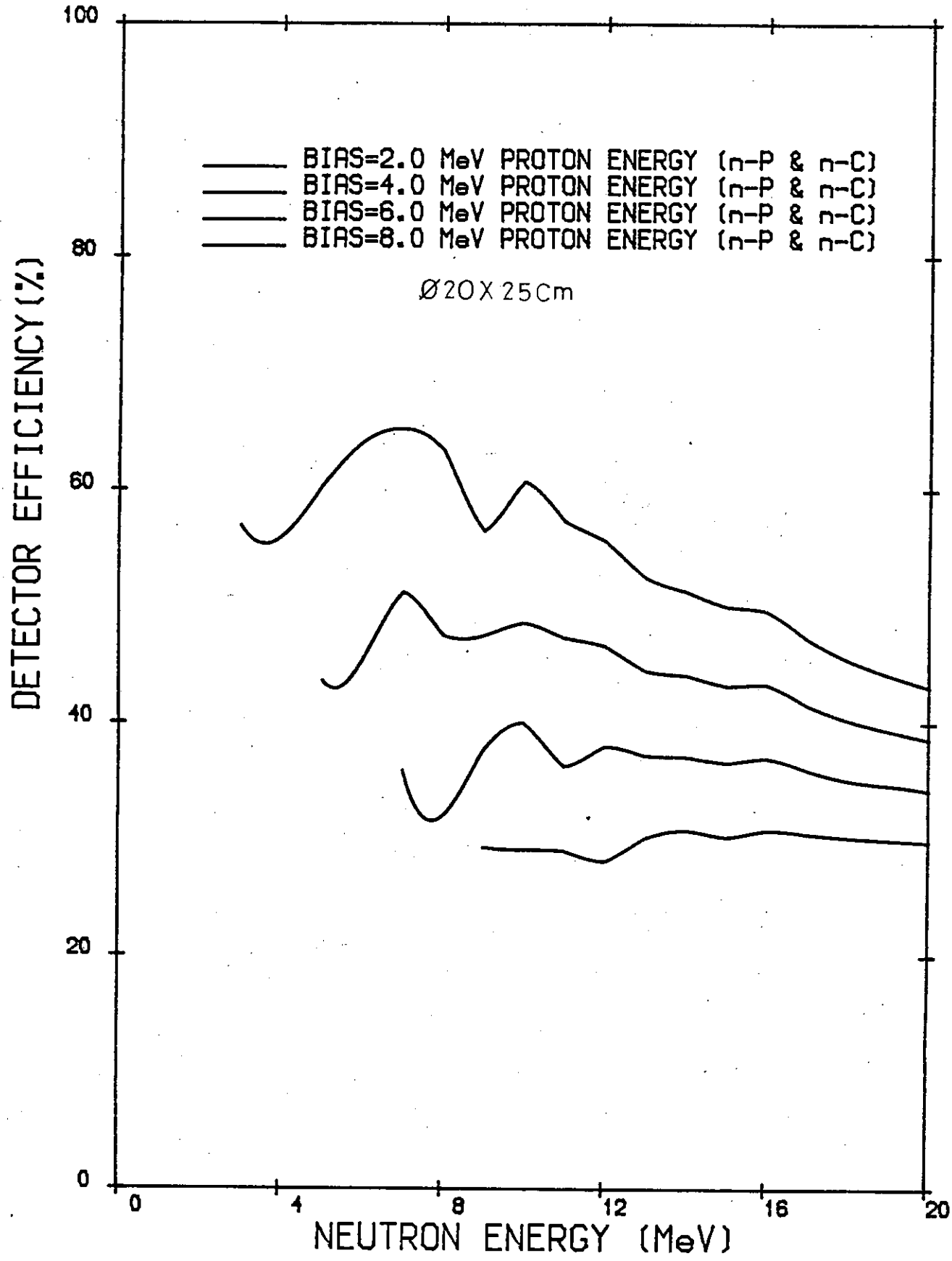
21/04/83 NEUTRON DETECTOR EFFICIENCY
BIAS=2.0 MeV PROTON ENERGY (n-P & n-C)
BIAS=4.0 MeV PROTON ENERGY (n-P & n-C)
BIAS=6.0 MeV PROTON ENERGY (n-P & n-C)
BIAS=8.0 MeV PROTON ENERGY (n-P & n-C)
Ø20X25Cm
DETECTOR EFFICIENCY(%)
NEUTRON ENERGY (MeV)
0
20
40
60
80
100
0
4
8
12
16
20

Figure 4.16.

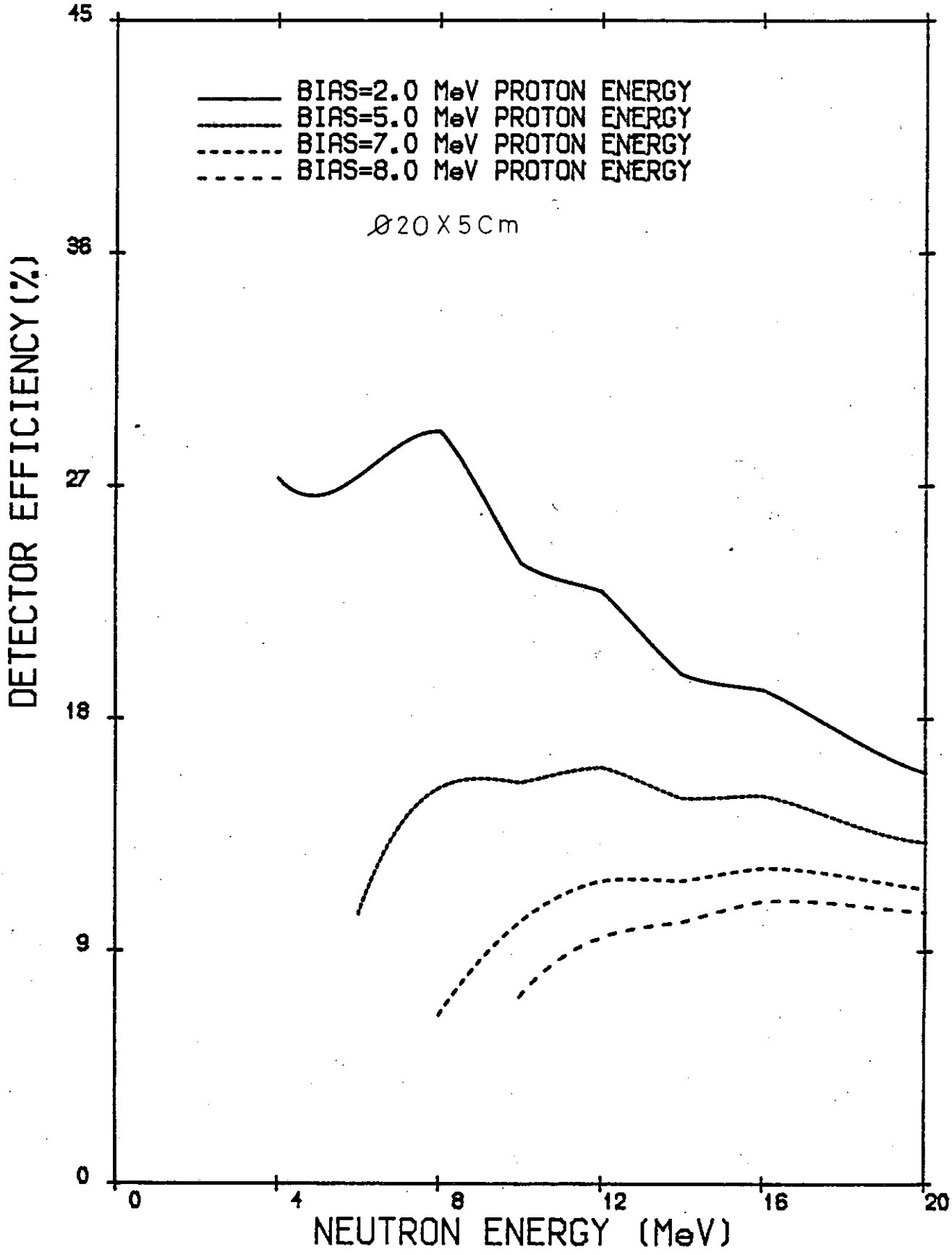
21/04/89 NEUTRON DETECTOR EFFICIENCY
BIAS=2.0 MeV PROTON ENERGY
BIAS=5.0 MeV PROTON ENERGY
BIAS=7.0 MeV PROTON ENERGY
BIAS=8.0 MeV PROTON ENERGY
Ø20X5Cm
DETECTOR EFFICIENCY(%)
NEUTRON ENERGY (MeV)
0
9
18
27
36
45
0
4
8
12
16
20

Figure 4.17.

energy regions of about 13.5 MeV, 9.2 MeV and 8.3 MeV.

Figs. (4.14) and (4.12) show the time of flight spectra of neutrons scattered from Graphite and Polyethylene. The areas under elastic and inelastic peaks extracted from these spectra were compared with the elastic and the inelastic cross sectionsof Carbon and the elastic cross section of Hydrogen.

If $\sigma_C(n,n)$ is the elastic cross section of Carbon and $\sigma_C(n,n')$ is the inelastic Carbon cross section then:

$$\begin{aligned} \sigma_C(n,n) &\propto \varepsilon(E1) \cdot A_{elastic} \\ \text{and} \quad \sigma_C(n,n') &\propto \varepsilon(E2) \cdot A_{inelastic} \end{aligned} \tag{4.5}$$

in which $\varepsilon(E1)$ and $\varepsilon(E2)$ are the detector efficiency at energy E1 and E2 respectively and $A_{elastic}$ and $A_{inelastic}$ represent the area under the elastic and the inelastic Carbon peaks.

From (4.5):

$$\frac{\sigma_C(n,n)}{\sigma_C(n,n')} = \frac{\varepsilon(E1)}{\varepsilon(E2)} \cdot \frac{A_{elastic}}{A_{inelastic}} \quad .$$

By substituting the values for $A_{elastic}$, $A_{inelastic}$, $\sigma_C(n,n)$ and $\sigma_C(n,n')$, ref. (102), the expected ratio will be:

$$\frac{143}{36.5} = \frac{\varepsilon(14\ MeV)}{\varepsilon(9.2\ MeV)} \cdot \frac{7495}{1875}$$

$$\frac{\varepsilon(14\ MeV)}{\varepsilon(9.2\ MeV)} = 98\% \quad .$$

The calculated efficiency ratio for 14 MeV and 9.2 MeV neutron is:

$$\frac{\varepsilon_{calc}(14\ MeV)}{\varepsilon_{calc}(9.2\ MeV)} = \frac{45.2}{47.3} = 95.5\%$$

Similar calculations for the Polythene spectrum and Carbon spectrum at 20^{o} scattering angle suggest the calculated and expected ratios of the detection efficiency are in agreement within 2-3%

In addition to the test described above, the analytical method of efficiency calculation was also compared with a Monte Carlo calculation reported in ref. (71) for a similar neutron detector. Fig. (4.18) shows the difference between absolute efficiencies given by these two methods at 5 MeV, 10 MeV and 15 MeV energies. The efficiencies predicted by the analytical method tend to be slightly higher than those given by the Monte Carlo calculation. Particularly at 10 MeV which appears to be the resonance region for the Carbon cross section. This discrepancy, however, is of no concern since the quantity of interest for cross section calculation is not the absolute efficiency but the relative efficiency, that is the ratio of two efficiency values. Table (4.2) shows the ratio of efficiencies at 5 MeV, 10 MeV and 15 MeV to that of 15 MeV for both analytical and Monte Carlo methods.

The larger difference between relative efficiencies given by Monte Carlo and the analytical method is at 10 MeV where resonance for Carbon cross section occurs. The resonance effects are, however, much less pronounced at the bias energy of this work, Fig. (4.19). One can then conclude that the two methods are generally in agreement within about 3%.

Table 4.2

	$\frac{\varepsilon(5)}{\varepsilon(15)}$	$\frac{\varepsilon(10)}{\varepsilon(15)}$	$\frac{\varepsilon(15)}{\varepsilon(15)}$
Monte Carlo	1.04	1.12	1
Analytical Method	1.07	1.19	1

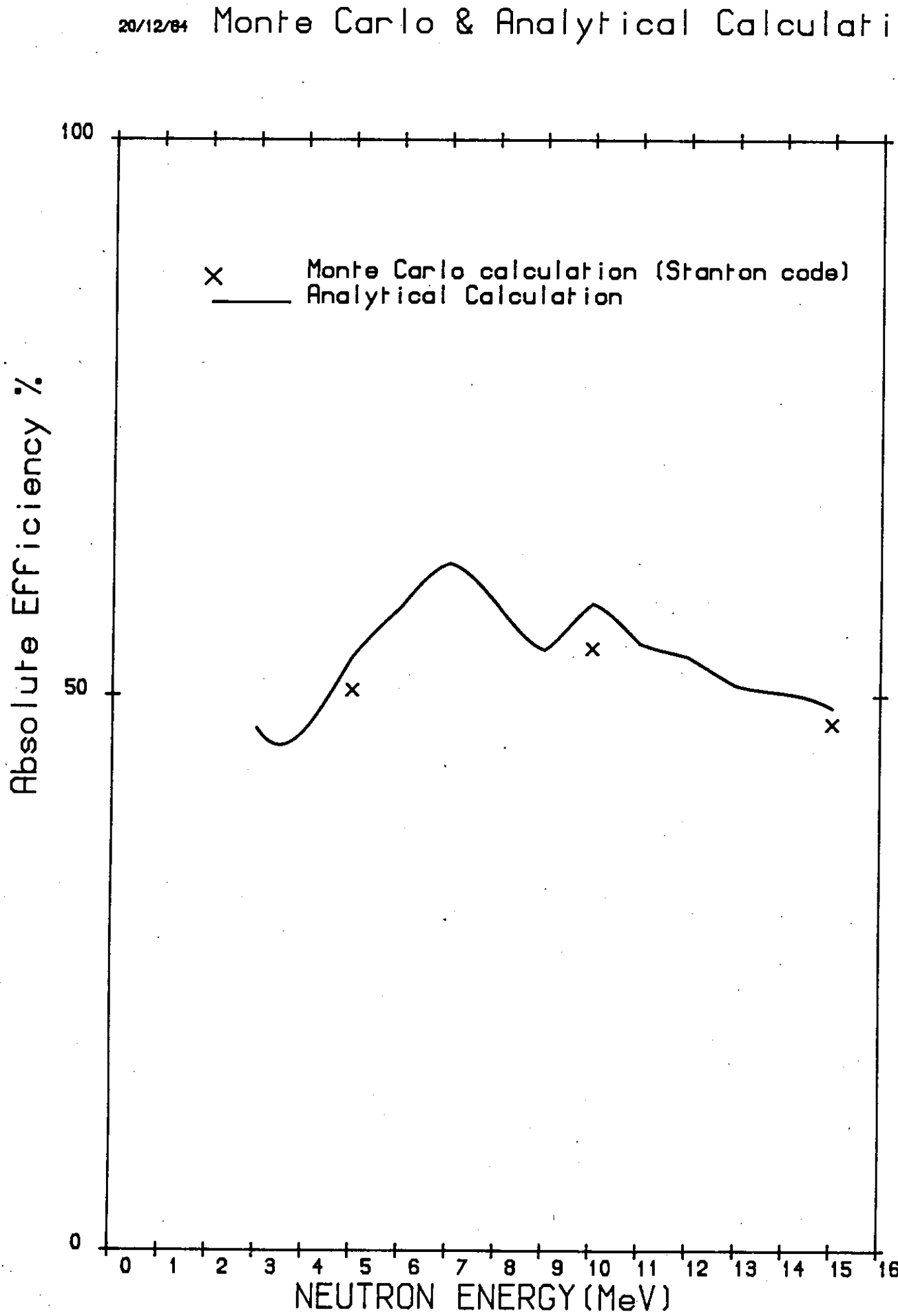
Monte Carlo & Analytical Calculations
100
50
0
Absolute Efficiency %
× Monte Carlo calculation (Stanton code)
Analytical Calculation
0 1 2 3 4 5 6 7 8 9 10 11 12 13 14 15 16
NEUTRON ENERGY (MeV)

Figure 4.18.

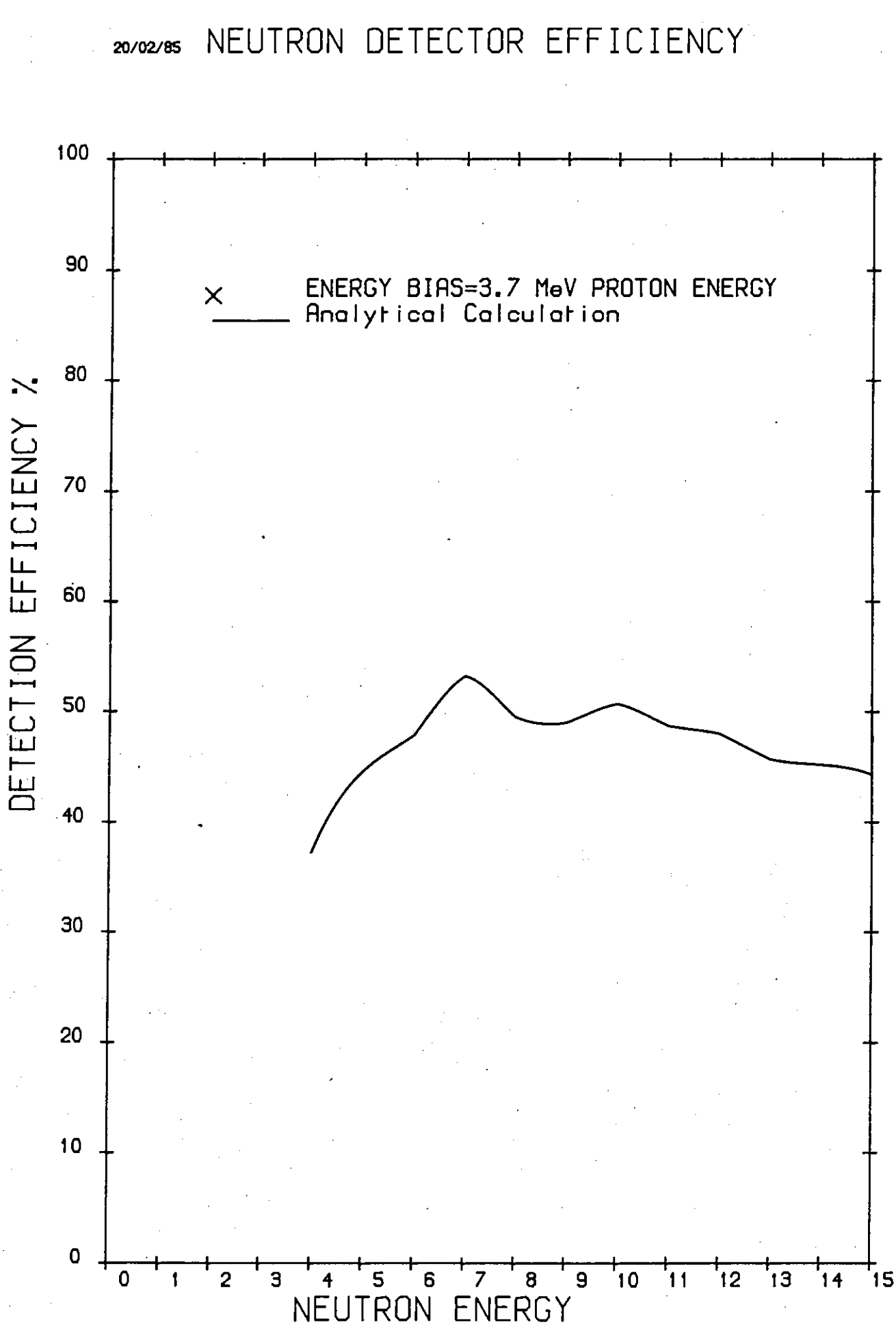
20/02/85 NEUTRON DETECTOR EFFICIENCY
ENERGY BIAS=3.7 MeV PROTON ENERGY
Analytical Calculation
DETECTION EFFICIENCY %
NEUTRON ENERGY
0
10
20
30
40
50
60
70
80
90
100
0
1
2
3
4
5
6
7
8
9
10
11
12
13
14
15

Figure 4.19.

4.8 Dependence of the Energy Resolution of the Neutron Detector on the Incident Neutron Energy

Since according to equation (3.11) the velocities of all neutrons with various energies in the scintillator was approximated by a constant value, the time compensation due to the detector size is therefore strictly correct at only one energy, E_o, which corresponds to $\beta_o C$. For some range of energies about E_o this approximation remains valid and will introduce little error into the determination of the compensated flight time, t_D. As the energy of the incident neutron deviates from E_o, however, the error introduced by the approximation will increase.

In order to show this effect on the time resolution of the neutron detector, the dependence of the time resolution achieved, at different neutron energies is shown in Fig. (4.20). The data points are obtained from the neutron time of flight spectra collected with Bismuth and Graphite samples. Energy resolution of the peaks due to scattering to the Bismuth ground state and excited states at 2.6 MeV, 4.2 MeV and 5.5 MeV are plotted along with that of ground state and 4.44 MeV excited state of Carbon. The values of time resolution include broadening effect due to the finite sample size and the contribution of the smoothing of the time of flight spectra discussed in Chapter 5. the time resolution is over 2.0ns for 14 MeV neutrons and increases to 6ns at about 7 MeV neutron energy. An energy resolution of $\approx$ 300 keV is maintained throughout the range of energies of interest, 7-14 MeV.

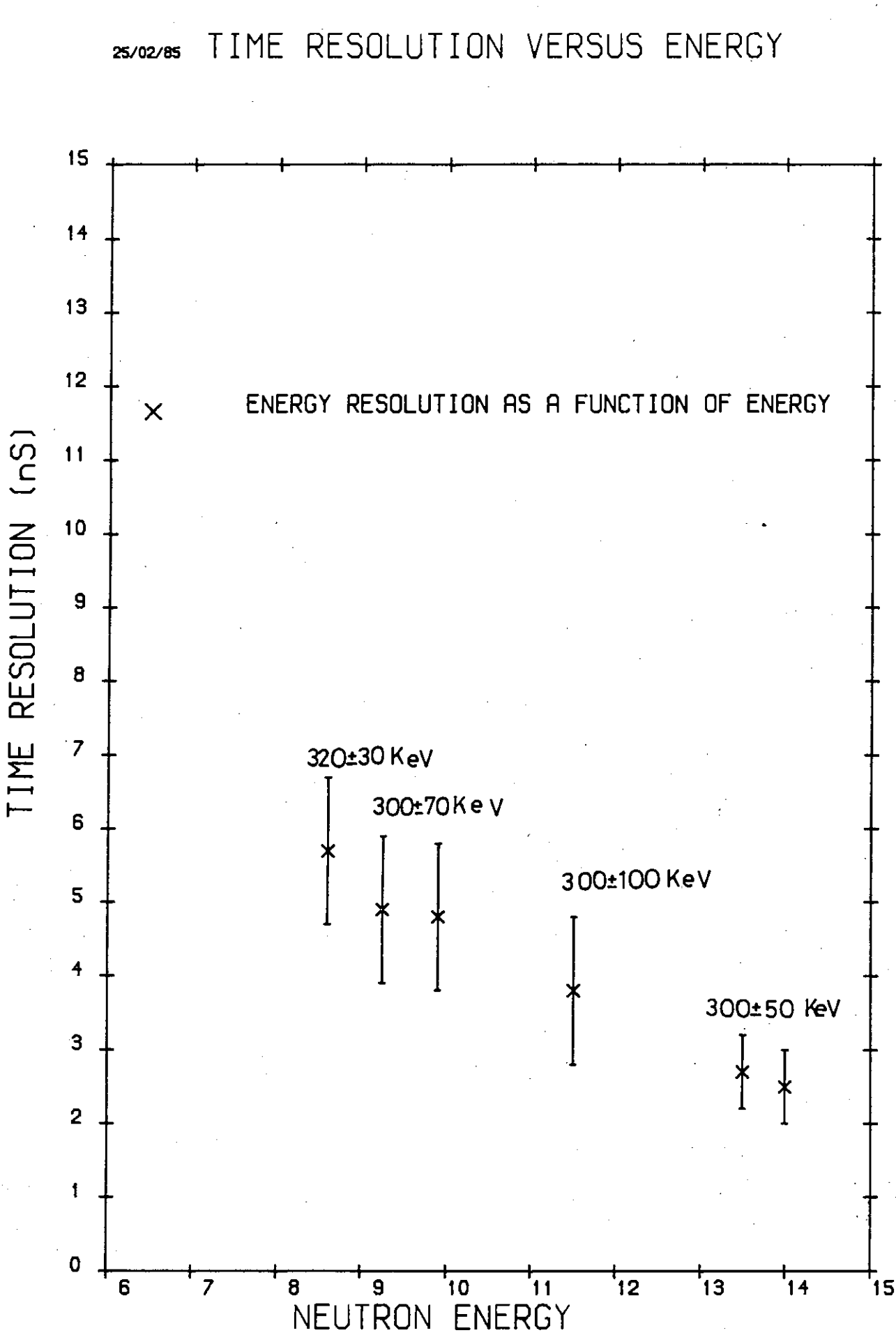
25/02/85 TIME RESOLUTION VERSUS ENERGY
ENERGY RESOLUTION AS A FUNCTION OF ENERGY
320±30 KeV
300±70 KeV
300±100 KeV
300±50 KeV
TIME RESOLUTION (nS)
NEUTRON ENERGY
0
1
2
3
4
5
6
7
8
9
10
11
12
13
14
15

Figure 4.20.

CHAPTER 5

DATA REDUCTION AND CORRECTIONS

In this chapter the method by which the differential elastic and inelastic cross sections were obtained from the experimental time of flight spectra and the correction of the data are discussed. The results are presented and compared with those from previous works.

5.1 Calculation of Cross Section from Time of Flight Spectra

5.1.1 Spectrum Smoothing

Figs. (5.1) - (5.9) show the time of flight spectra obtained from scattering of 14.1 MeV neutrons by Bismuth at angles between 20 - 90 degrees. The typical running time required to collect such a spectrum was between 60 - 70 hours. At more backward scattering angles of 80 or 90 degrees, substantially longer running time was necessary to achieve useful statistical accuracy. That is due to the small inelastic cross section of Bismuth at this energy.

In order to reduce the statistical fluctuation, the 1024 channel spectrum was smoothed initially by adding the contents of each successive 4 channels together, producing a 256 channel spectrum on which further analysis was performed. A FORTRAN program 'SMOOTH5' was written on the basis of the smoothing formula given by Hildebrand[103] This program was used for further smoothing of the spectrum.

SMOOTH5 reduces the spectrum's statistical scatter by fitting a first degree polynomial to every subgroup of 5 points by the least-squares method. The formula are of the form:

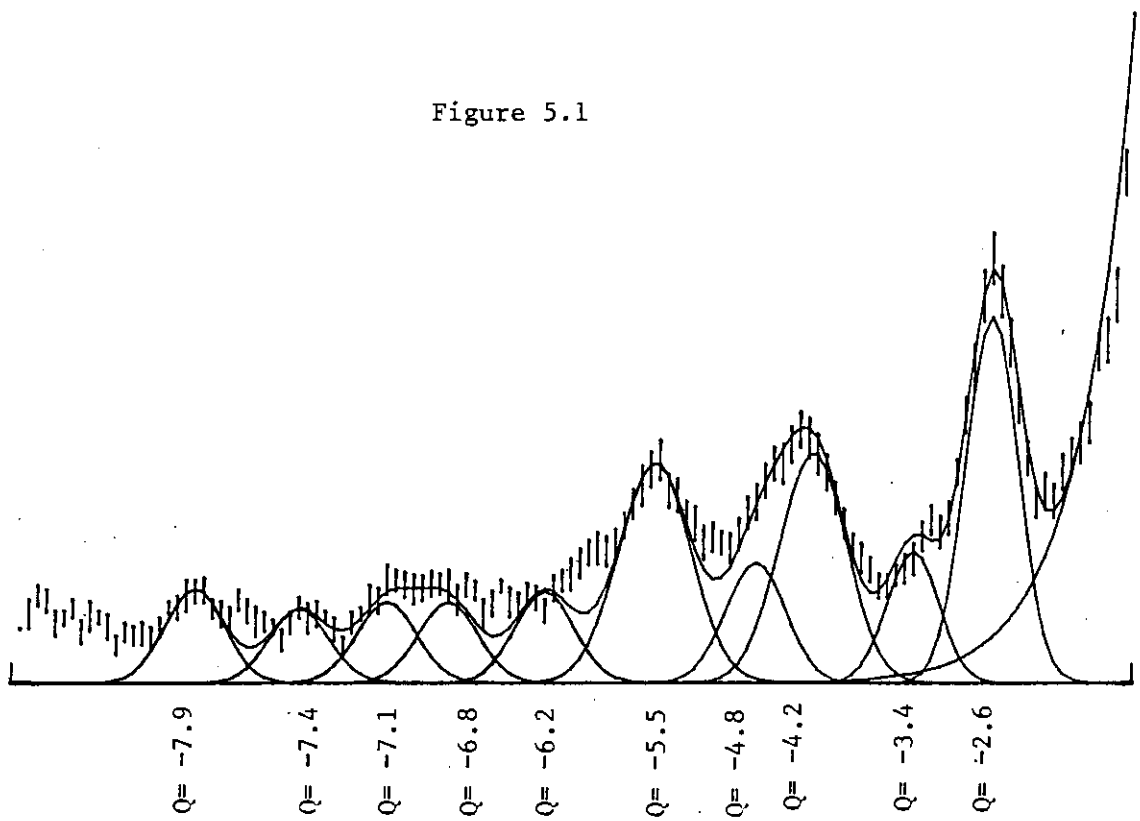

Figure 5.1

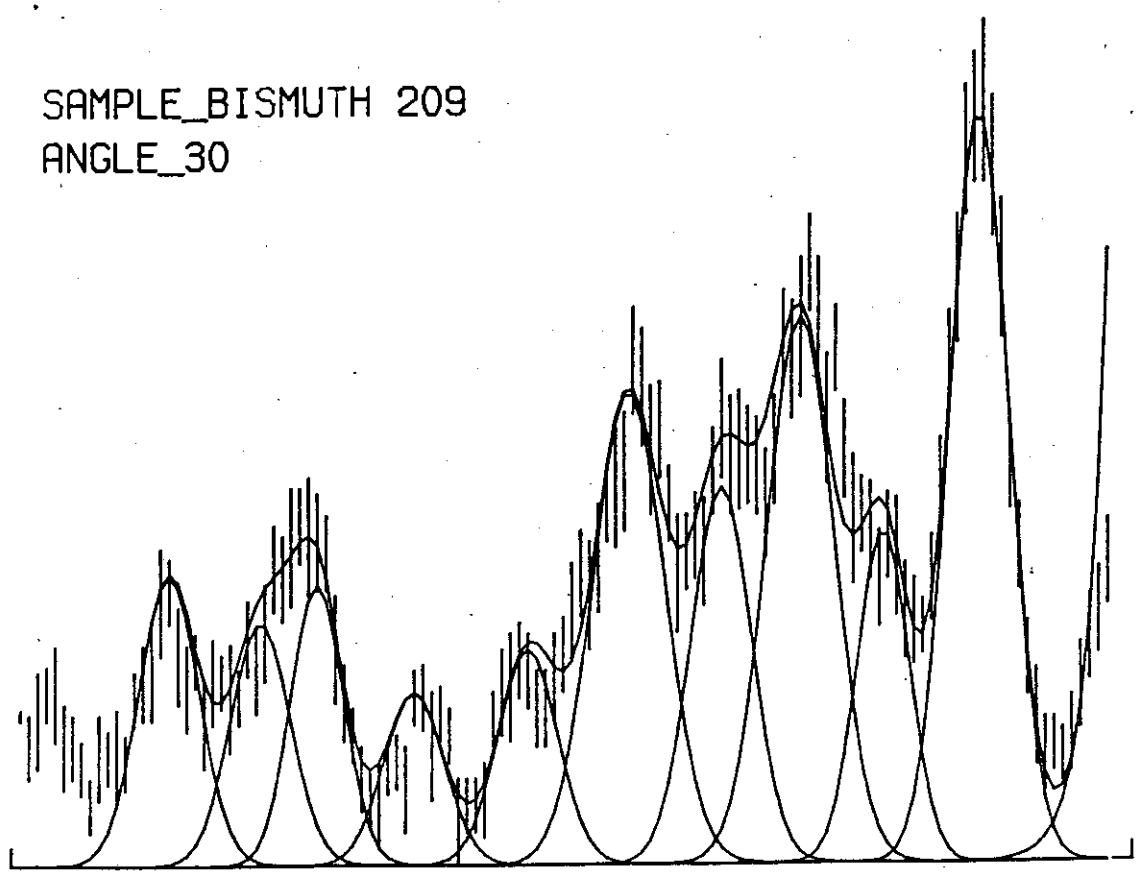

Figure 5.2

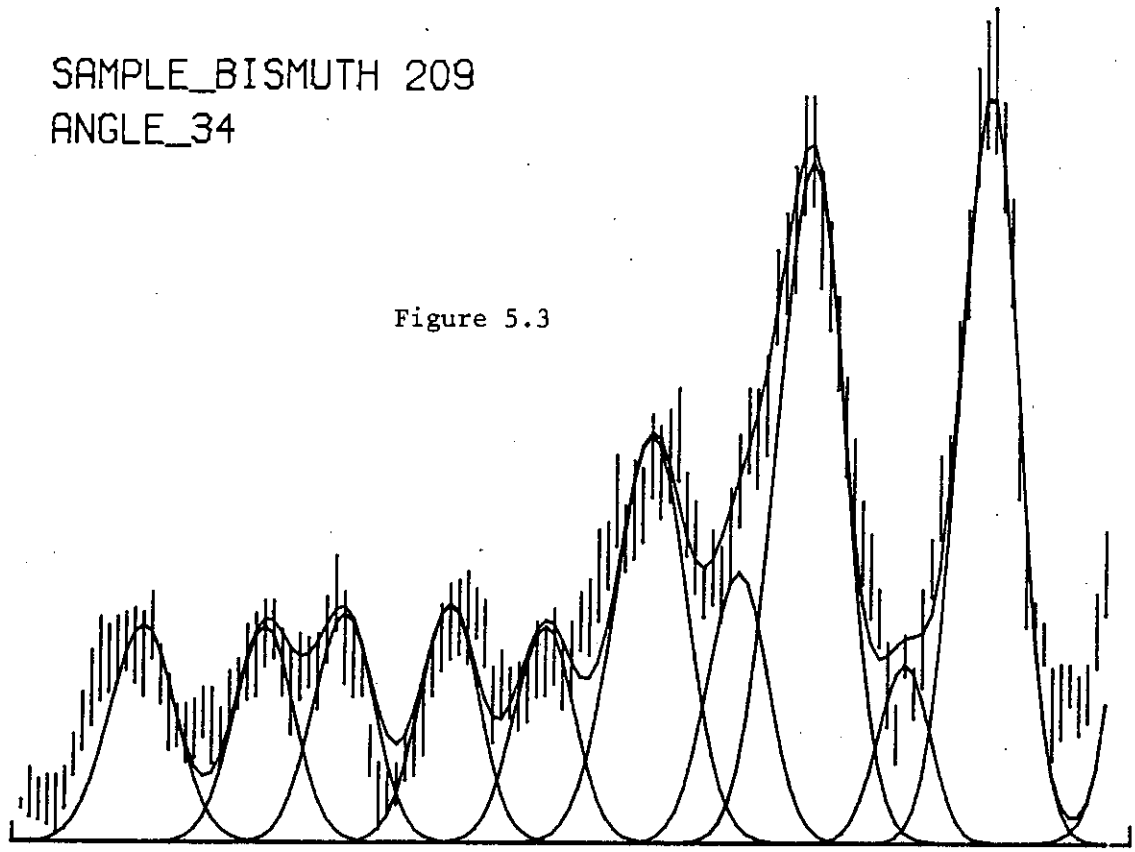

Figure 5.3

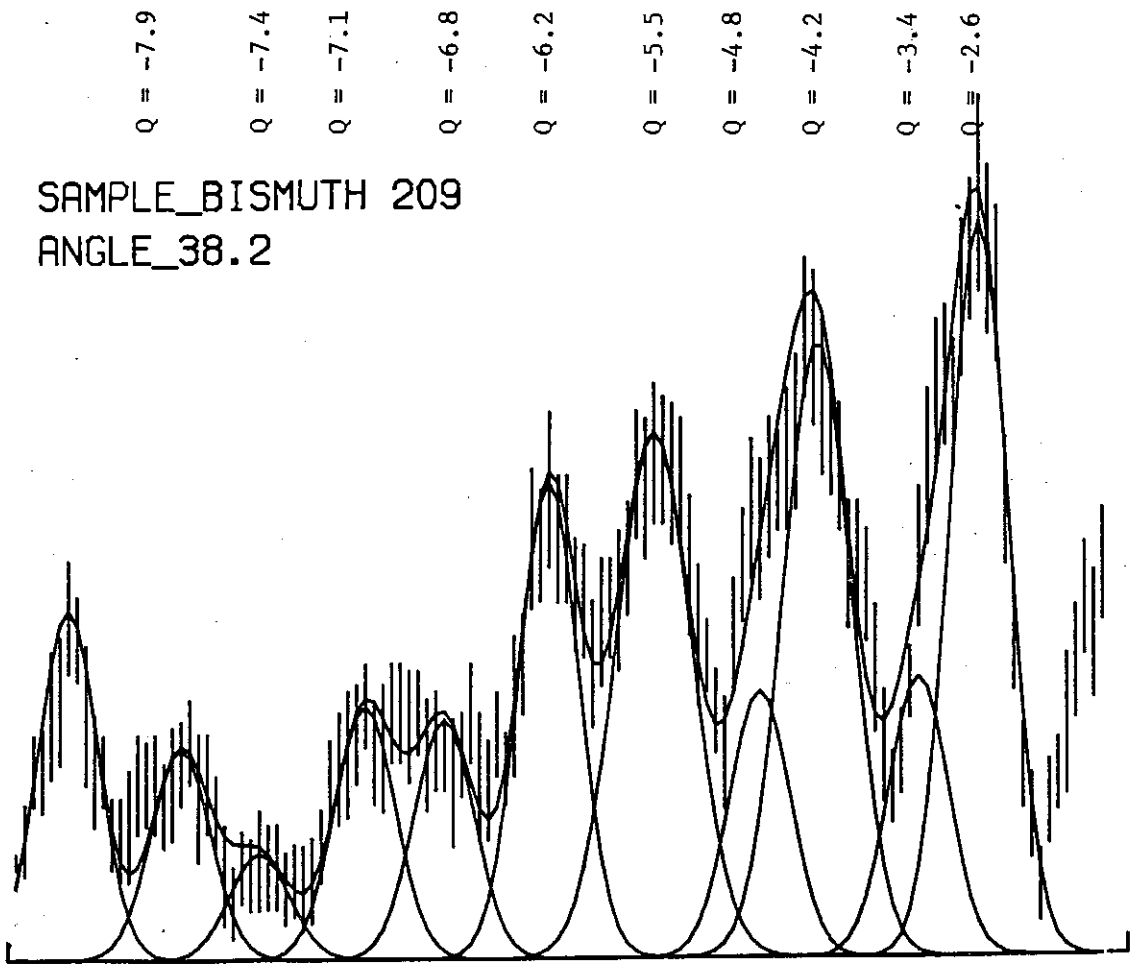

Figure 5.4.

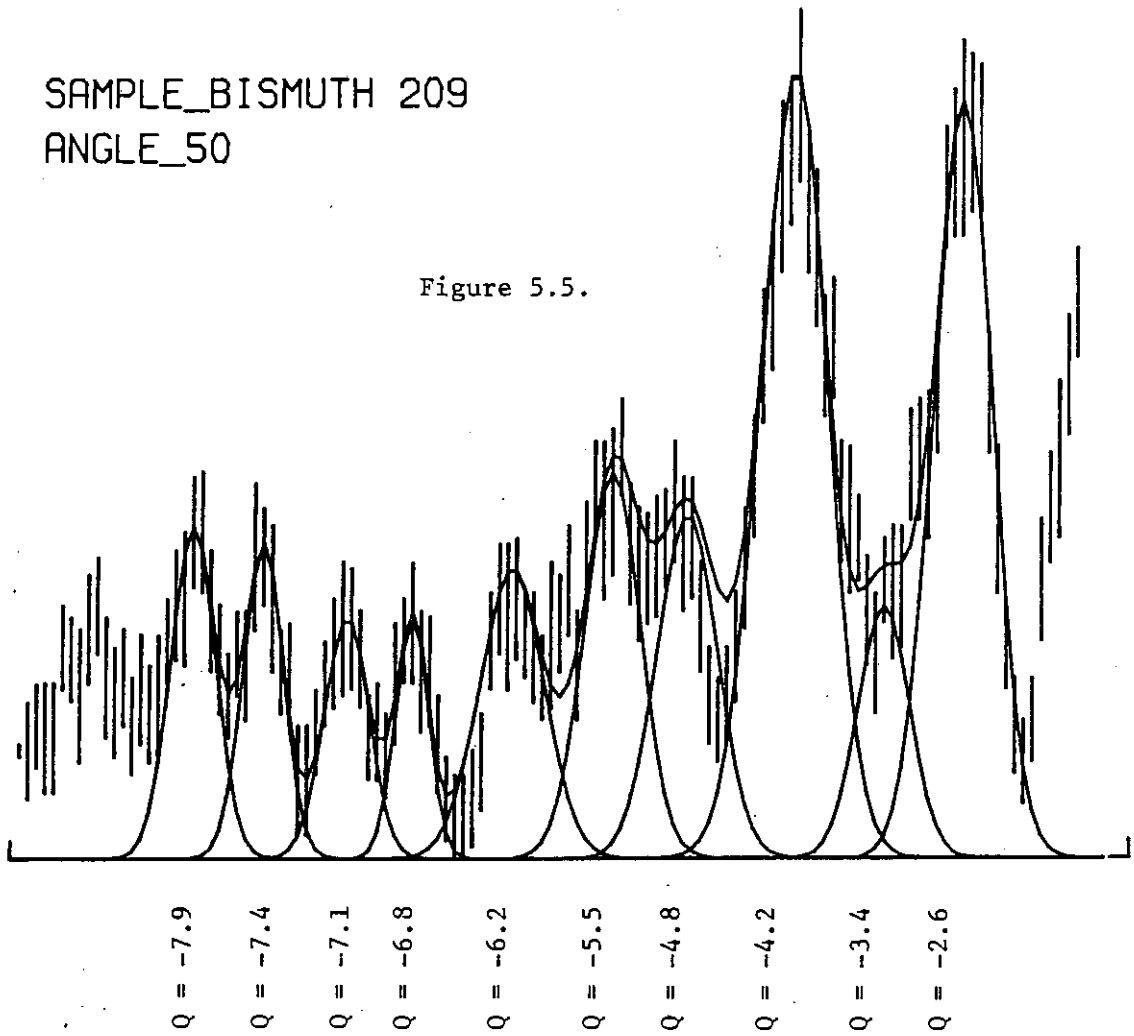

Figure 5.5.

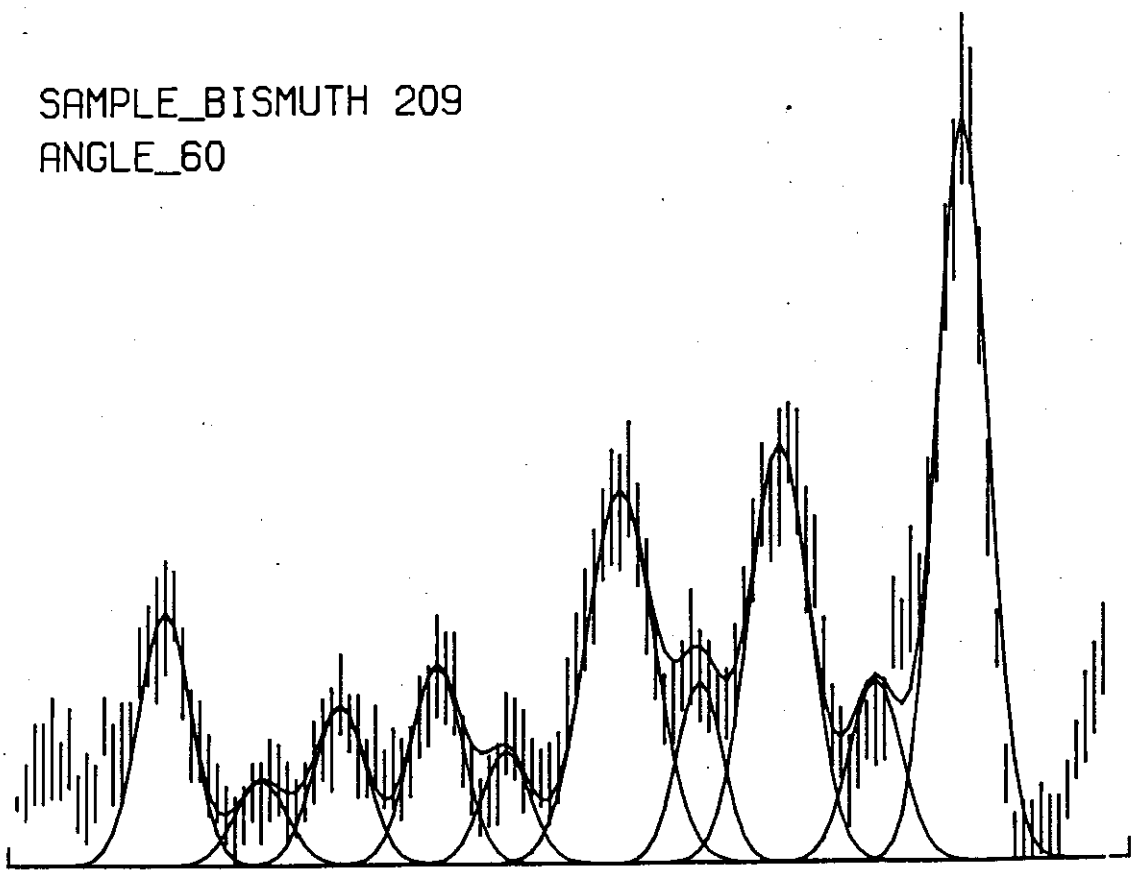

Figure 5.6.

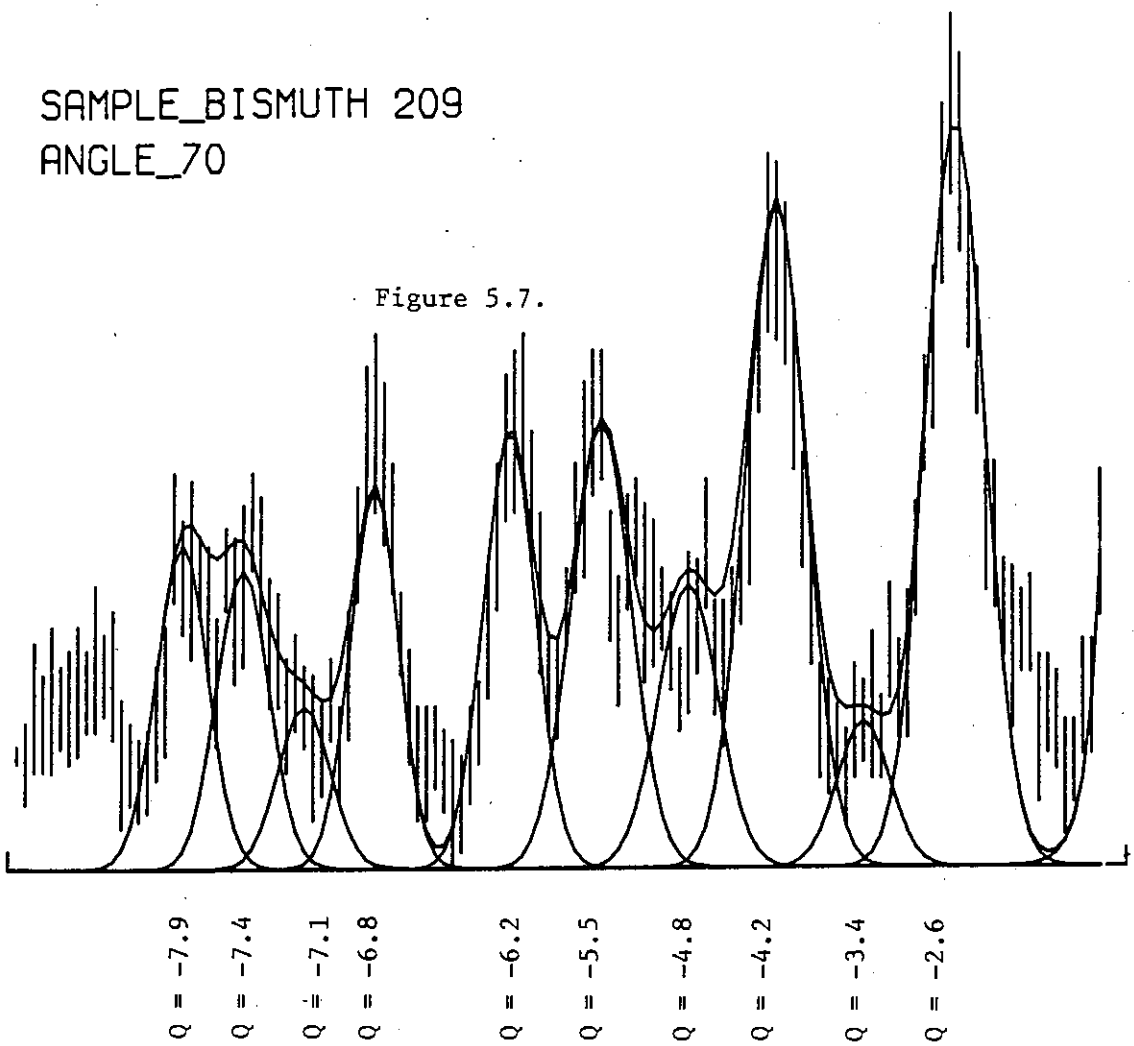

Figure 5.7.

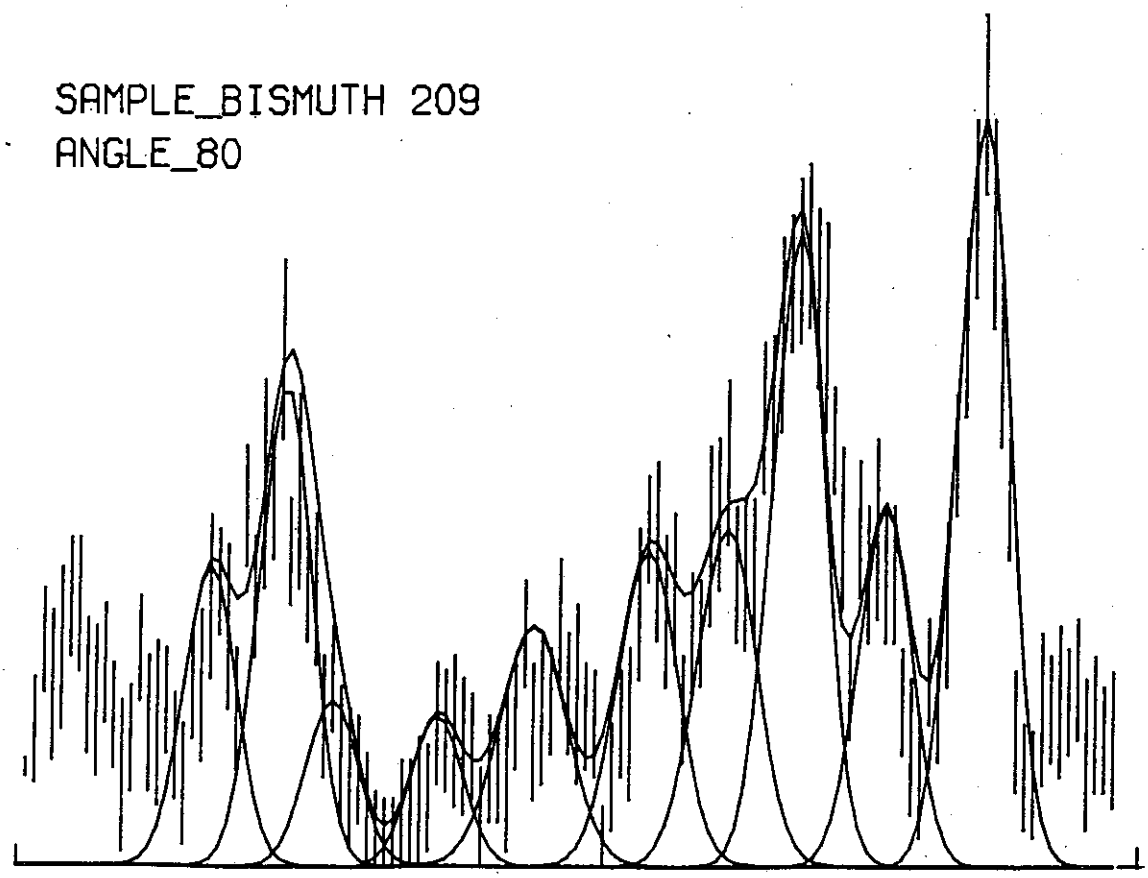

Figure 5.8.

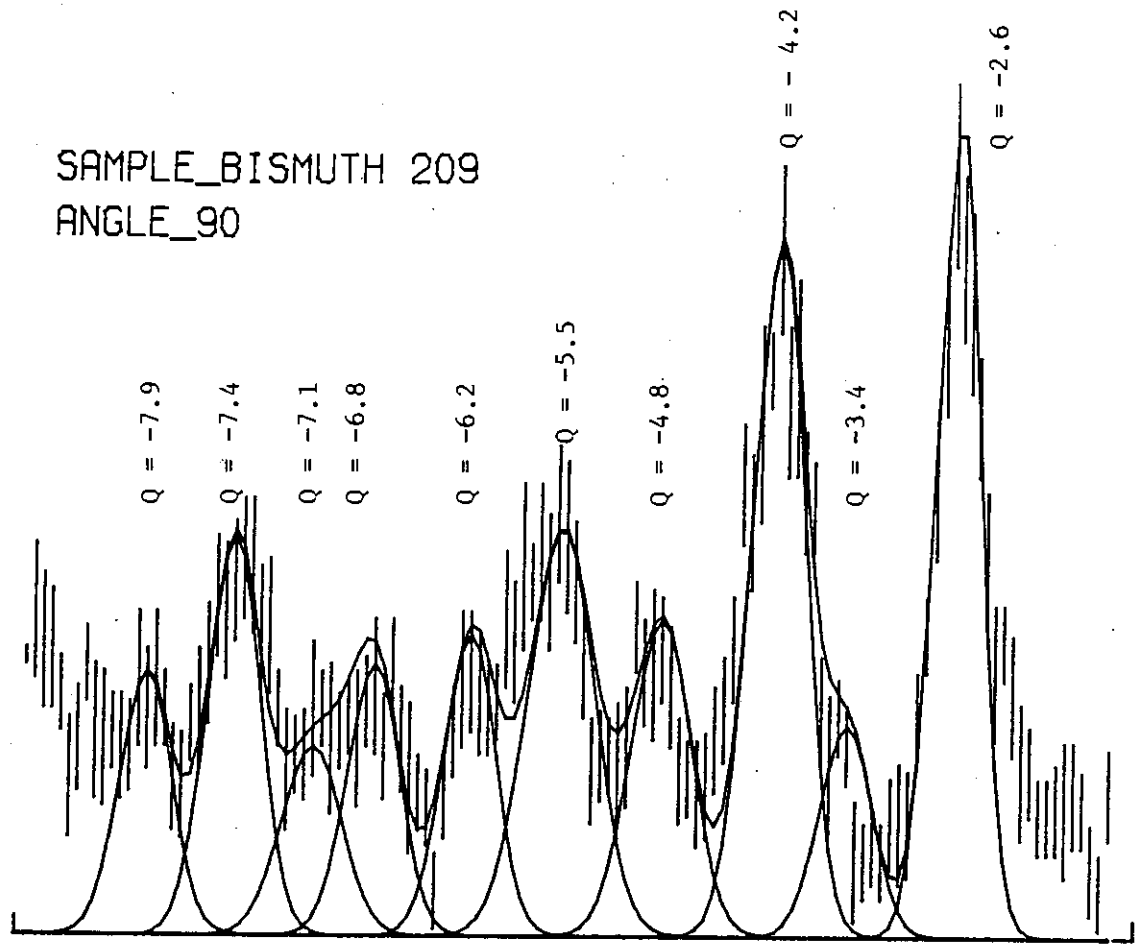

Figure 5.9

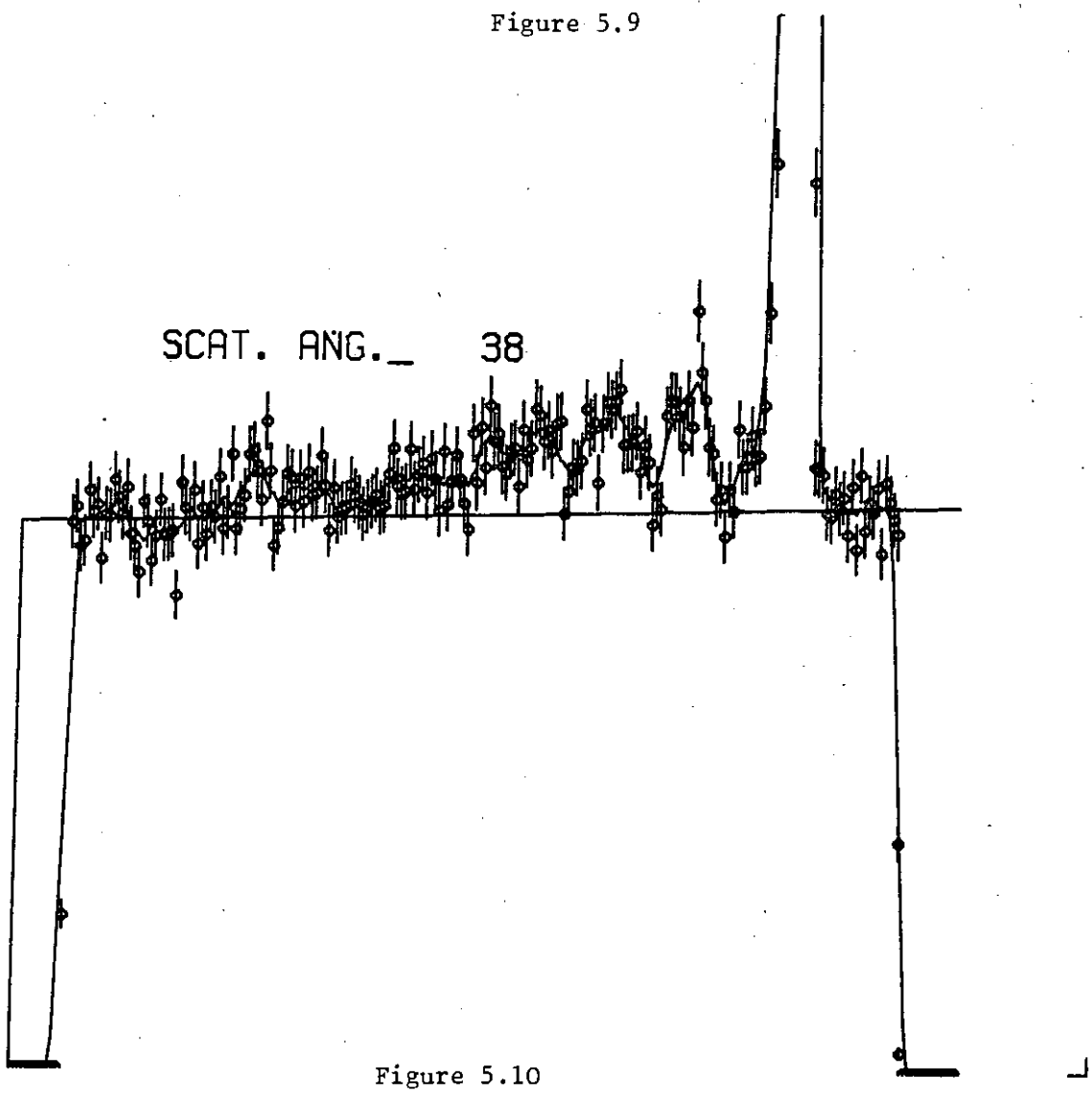

Figure 5.10

$$
\begin{aligned}
y_{-2} &= \frac{1}{5}(3f_{-2} + 2f_{-1} + f_o - f_2) \\
y_{-1} &= \frac{1}{10}(4f_{-2} + 3f_{-1} + 2f_o + f_1) \\
y_o &= \frac{1}{5}(f_{-2} + f_{-1} + f_o + f_1 + f_2) \\
&\cdot \\
&\cdot \\
&\cdot
\end{aligned}
\qquad (5.1)
$$

where the omitted formulae, for y_1 and y_2, are obtained from the formulae for y_{-1} and y_{-2} by reversing the numbering of the coordinates.

This technique of smoothing conserves the information pertaining to the desired parameters of the peaks and yields unambiguous peak structure which helped to improve the search for the peak parameters only. It could not of course improve the accuracy of the experimental data.

The parameter of interest here is the area under the peak which is conserved though the height and the width of the peak may change to allow the area conservation.

Fig. (5.10) demonstrates the effect of smoothing in the time spectrum.

5.1.2 Subtraction of the background

Flat background is one of the useful features of the associated particle method in which the background is caused by accidental coincidence and is thus structureless[104]. Fig. (5.11) shows the time of flight spectrum of neutrons scattered from a graphite sample. Apart from the regions where elastic and inelastic peaks are expected the background is flat and structureless. Similarly the spectrum obtained

by scattering from a polythene, $(CH_2)_n$, sample showed a time uncorrelated background, Fig. (5.12).

These observed time of flight spectra suggested a structureless background slightly higher at the high energy end of the spectrum, gradually reducing towards the lower energy end.

The interactive program SMOOTH5 described in the previous section (5.1.1) was capable of fitting a line with suitable height and slope, in an interactive fashion, to estimate the background level derived from the level of time of flight spectrum beyond the elastic peak and from the very low energy end of the spectrum. The reliability of visually fitting the background was checked by fitting a straight line to the background using the least-squares fitting method. This straight line normally fitted data points spread over 200 channels in the neutron energy regions where no peaks were expected, that is beyond the elastic peak and also close to the detector energy bias. The parameters of the line fitted to the background were then used for the background subtraction from the time of flight spectrum.

5.1.3 Determination of the area under the peak

Having dealt with the question of the background by choosing a method for the background subtraction, another interactive FORTRAN Program (GAUSEXP) with search routine was written for unfolding of the overlapping peaks. The peak's shapes were determined after investigating the shape of the well isolated peaks obtained from graphite and Bismuth, Figs. (5.11) and (5.10). From these spectra it was evident that the peaks could be well defined by a Gaussian distribution. However, at very forward scattering angles where the elastic

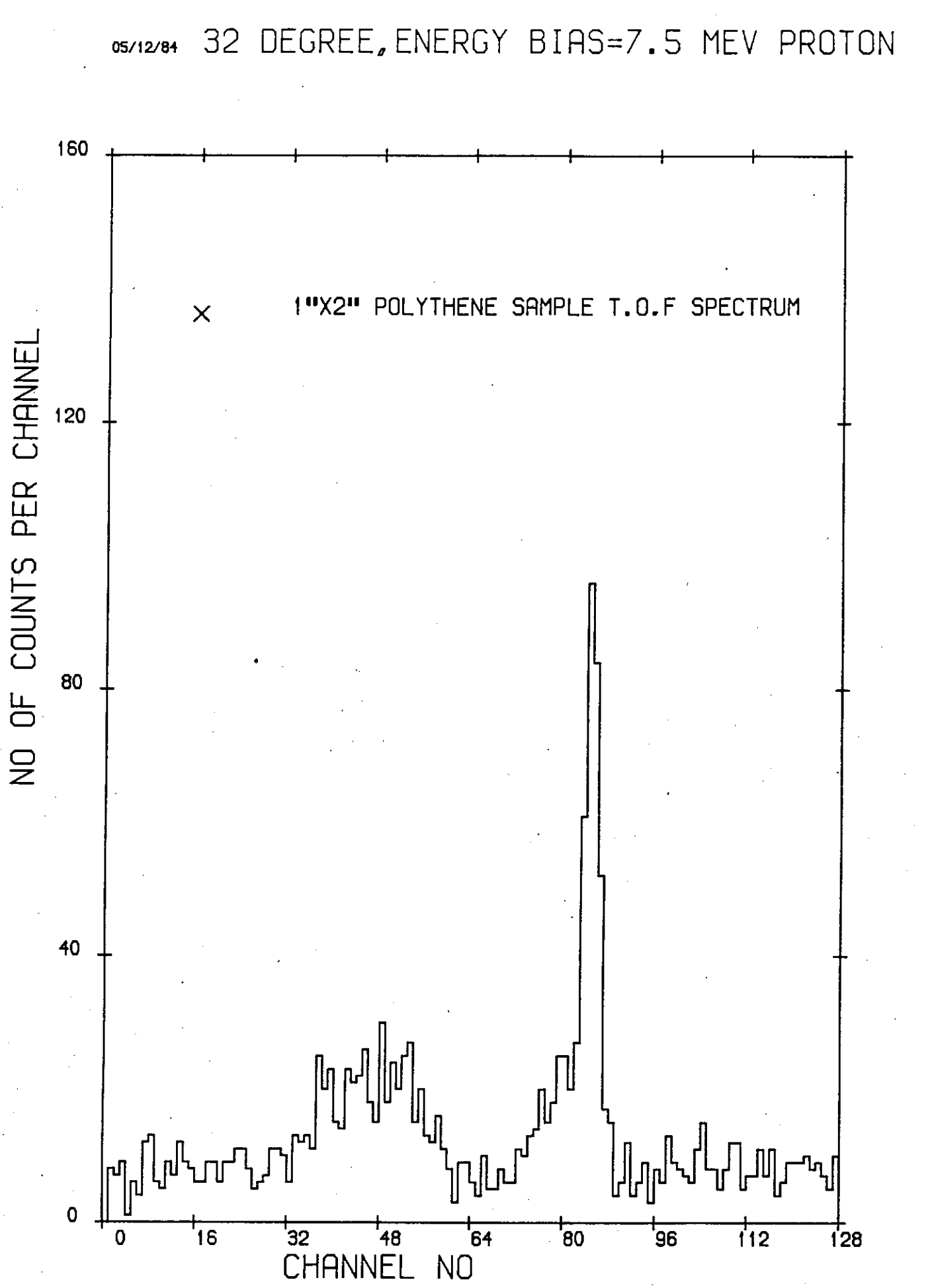
05/12/84 32 DEGREE, ENERGY BIAS=7.5 MEV PROTON
1"X2" POLYTHENE SAMPLE T.O.F SPECTRUM
NO OF COUNTS PER CHANNEL
160
120
80
40
0
0
16
32
48
64
80
96
112
128
CHANNEL NO

Figure 5.12.

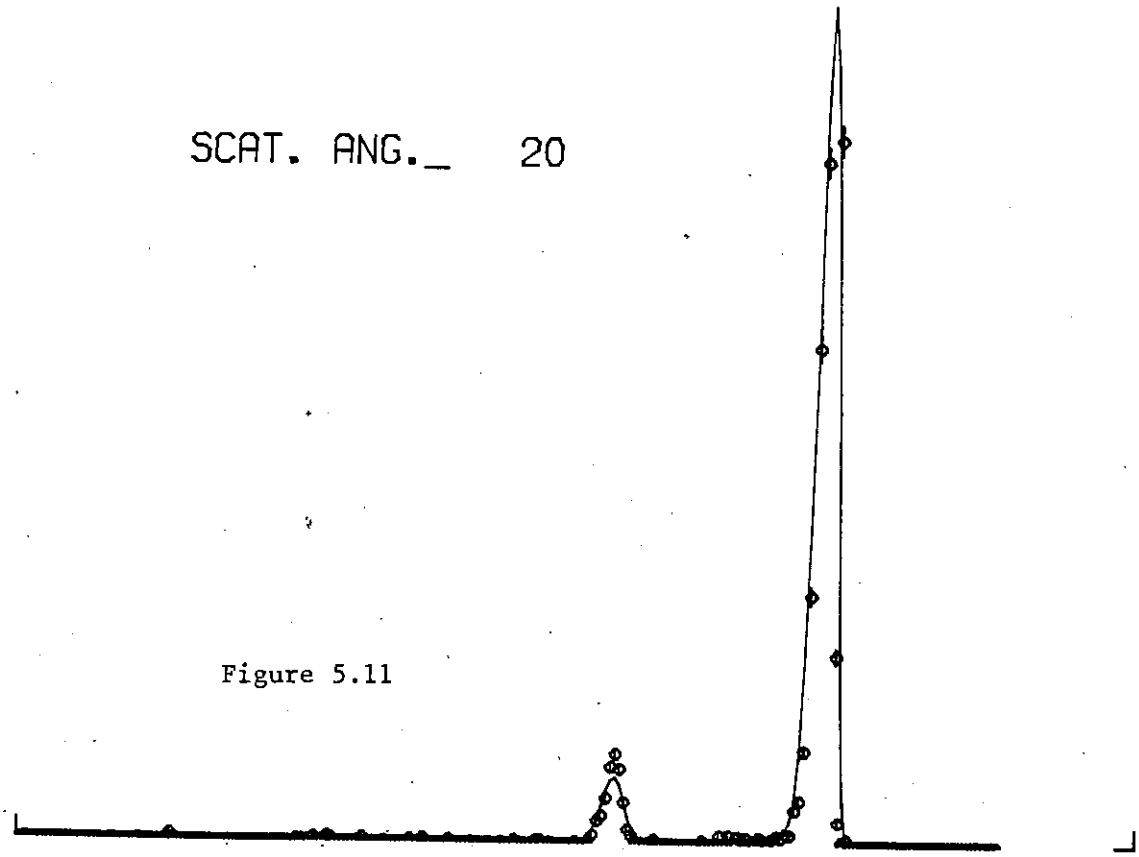

Figure 5.11

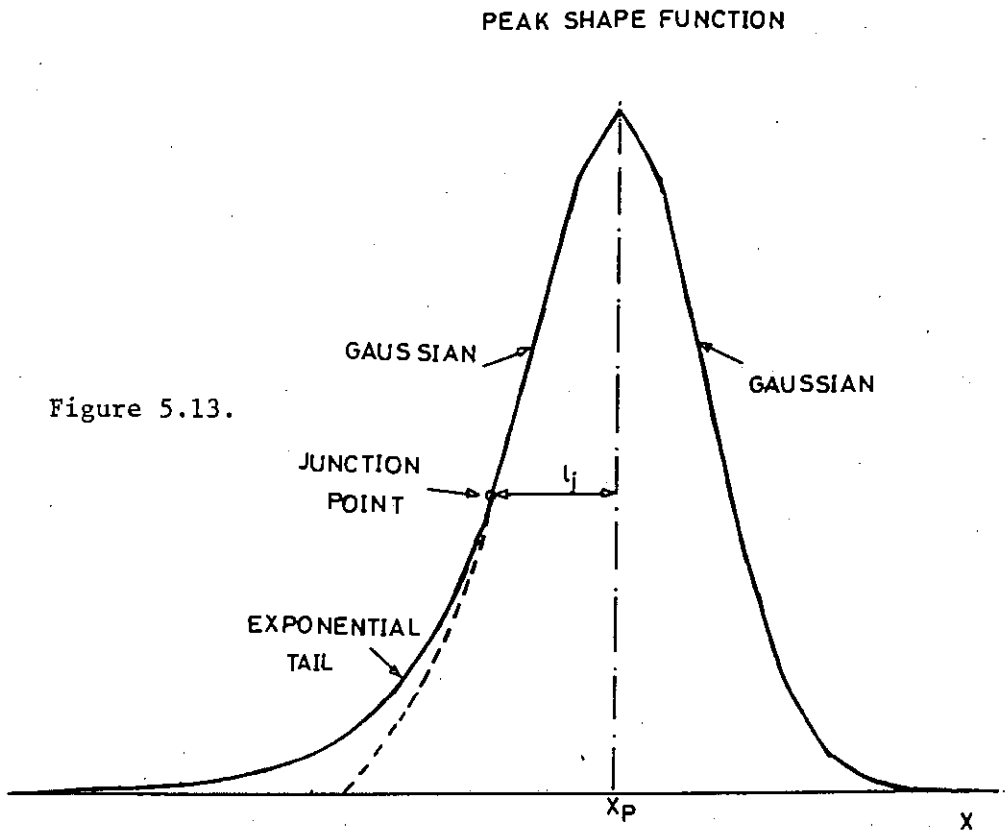

Figure 5.13.

cross section for Carbon and for Bismuth is high, some deviations of the peak shape from the Gaussian were observed on the low energy side of the peak, Fig. (5.1).

The peak profile was then empirically determined to consist of a Gaussian peak to which an exponential tail was added on the low energy side.

GAUSEXP was used to search for the best fit to the recognized peaks, taking into account the tailing.

The central part and the high energy side of the peak are described in GAUSEXP by a Gaussian and the tail by a simple exponential function. The already subtracted flat background was not represented in the peak shape.

The form of a single peak is given in Fig. (5.13). A fourth parameter ℓ_J, is introduced to the three parameter Gaussian fitting and the line shape is described as[105]

$$f_J = H_J \exp\left[\frac{\ell_J(2x - 2x_{PJ} + \ell_J)}{2\sigma_J^2}\right], \qquad (5.2)$$

$$\text{for} \quad x < x_{PJ} - \ell_J$$

and:

$$f_J = H_J \exp\left[\frac{1}{2} \cdot \frac{(x - x_{PJ})^2}{\sigma_J^2}\right] \qquad (5.3)$$

$$\text{for} \quad x \geq x_{PJ} - \ell_J$$

$$\sigma_J = (FWHM)_J/2.354$$

where:

H_J = Height of the Gaussian for the Jth peak,

σ_J = Width of the Gaussian for the Jth peak,

ℓ_J = Distance, in channel units between the peak location and the junction point of the two fitting functions.

x = Location of the peak in channel units.

x_{PJ} = Centroid of the Gaussian for the Jth peak.

$(FWHM)_J$ = Full width at half maximum of the Jth peak.

In the peak search, real peaks occurring at all scattering angles consistently were distinguished and located according to the available information on excitation energies observed in ^{208}Pb and ^{209}Bi.

Yields were obtained for isolated peaks in the spectra both by direct summation of the counts and by fitting line shapes to the peak, to check for the consistency of the yield extraction.

Due to the large number of counts under the elastic peak, particularly at more forward angles and the sharpness of the elastic peak, the magnitude of the elastic yield was quite sensitive to the quality of fitting and therefore for each case, the value of the yield given by the GAUSEXP was checked against direct summation of counts, for consistency.

In order to calculate the area under each inelastic peak, a gaussian distribution centred at the peak position was fitted to the peak. The peak's standard deviation was determined by an experimental energy-dependent resolution function and the energy spread of the group of levels related to the peak under investigation. The standard deviation for each neutron group was kept the same when fitting to the same neutron peak at all angles.

The area under the gaussian and associated exponential was

evaluated by the program after the minimum χ^2 is achieved.

A second fitting code LGFIT2, written by E. Von Meerwall[106] was modified to run on the EMAS (Edinburgh Multi Access System), ICL75 machines. Being an interactive fitting code GAUSEXP however, proved to be more efficient and was used for peak fitting throughout this work.

5.1.4 Calculation of cross sections from the experimental data

Yields, extracted by the Gaussian fitting method explained in the previous section, were used to calculate the angular distribution of cross sections. This calculation was based on the equation below[91] :

$$\frac{d\sigma}{d\Omega}(\theta,E_i) = \frac{Y_{samp}(\theta)}{Y_c(\phi)} \cdot \frac{\varepsilon_c(E_\phi)}{\varepsilon_{samp}(E_\theta)} \cdot \frac{N_c}{N_{samp}} \cdot \frac{F_c}{F_{samp}} \cdot \frac{1}{A_c} \sigma_c(\phi,E_i) \qquad (5.4)$$

where:

$\frac{d\sigma}{d\Omega}(\theta,E_i)$ = differential cross section for the scattering of neutrons of incident energy E_i through the laboratory angle θ in mb/sr.

$Y_{samp}(\theta)$, $Y_c(\phi)$ = Yield in the peak of interest in the time of flight spectrum (background subtracted), and n.c. peak in the graphite scatterer time of flight spectrum (background subtracted), respectively. Y_{samp} and Y_c are monitor normalized yields.

$\varepsilon_c(E_\phi)$, $\varepsilon_{samp}(E_\theta)$ = relative efficiency for the detection of neutrons of energy E_ϕ scattered from Carbon through ϕ.

and energy E_θ scattered from scattering sample through θ, respectively.

N_{samp}, N_c = Number of nuclei in the scattering sample and number of Carbon nuclei in Carbon sample.

$\sigma_c(\phi,E_i)$ = Carbon differential cross section for the scattering of neutrons of incident energy E_i through the laboratory angle ϕ.

A_c = the flux attenuation of the Carbon sample.

F_{samp} and F_c, the fluence attenuation factors correct for the anisotropy of the incident neutron flux from the target, and for the fact that the Carbon and the scattering samples could be of different size. In cases where the neutron producing target is isotropic as the $^3_1H(d,n)^4_2He$ reaction is and also the Carbon and the scattering sample sizes satisfy the expression:

$$H_c^2(H_c^2 + D_c^2) = H_{samp}^2(H_{samp}^2 + D_{samp}^2) \qquad (5.5)$$

where H_c, D_c and H_{samp}, D_{samp} are the height and diameter of the Carbon scatterer and those of the scattering sample, respectively, Velkley et al.[107] have shown by Monte Carlo simulation that the ratio F_c/F_{samp} can be assumed to be 1.00 ± 0.01. The criterion shown by equation (5.5) was satisfied for the Carbon and Bismuth samples used in this work.

The flux attenuation factor A_c for Carbon was calculated by using the disk approximation of Kinney[108] from equation:

$$A_c = \exp\{\tfrac{\pi}{4}[\Sigma_T(c,E_i)]R_c + \tfrac{8}{3\pi}[\Sigma_R(c,E_i)]R_c\} \qquad (5.6)$$

where:

$\Sigma_T(c,E_i)$ = the macroscopic total cross section of Carbon at the incident energy E_i

$\Sigma_R(c,E_i)$ = non-elastic macroscopic total cross section of Carbon at energy E_i

R_c = Carbon sample radius

and also by a Monte Carlo calculation[109]. Both methods of calculation were performed for the sample sizes and the geometry used in this experiment and the agreement was found to be better than 5%. Since the Monte Carlo method is expected to be the more accurate method, the flux attenuation factor obtained from MULTSCAT code was used for cross section calculation. $\sigma_c(\phi,E_1)$, carbon cross section for cross section scaling was obtained from ref. (102).

5.2 Excitation Energies Observed by 14.1 MeV Neutron Scattering

The time of flight spectra obtained from neutrons scattered by Bismuth 209 at various angles are shown in Figs. (5.1) - (5.9).

The observed inelastic neutron excitation energies were calculated from the incident energy, flight path, and flight times. The dependence of the flight path on the scattering angle due to the geometry of the experiment in which the scattering sample is rotated round the deuteron beam line in order to change the scattering angle, though not significant, has been taken into account for the observed excitation energy calculation. Due to the heavy mass of the scatterer the change of the scattered neutron energy as a result of the kinematics of the scattering was also negligible.

A neutron group was accepted for the determination of excitation energy when reliably observed at all the scattering angles for which measurements were performed. The observed excitation energies were defined as the simple averages of the respective measured values with the uncertainties expressed as the deviation from the mean value. Up to approximately 7.9 MeV excitation energy 10 excitations were so identified in Bismuth 209 as summarized in Table (5.1). These excitation groups were all identified with the excitation energy information available for ^{208}Pb and ^{209}Bi (110). Each energy group

TABLE (5.1)

Observed excitation energies in Bismuth 209

Excitation level number	Excitation Energy (MeV)
1	2.6 ± 0.1
2	3.4 ± 0.1
3	4.2 ± 0.1
4	4.8 ± 0.1
5	5.5 ± 0.1
6	6.2 ± 0.1
7	6.8 ± 0.1
8	7.1 ± 0.1
9	7.4 ± 0.1
10	7.9 ± 0.1

corresponded to excitation levels of energies where the experimental resolution was not comparable with the expected detail of the ^{209}Bi structure. As a result of that most of the observed neutron groups were probably composites of several components.

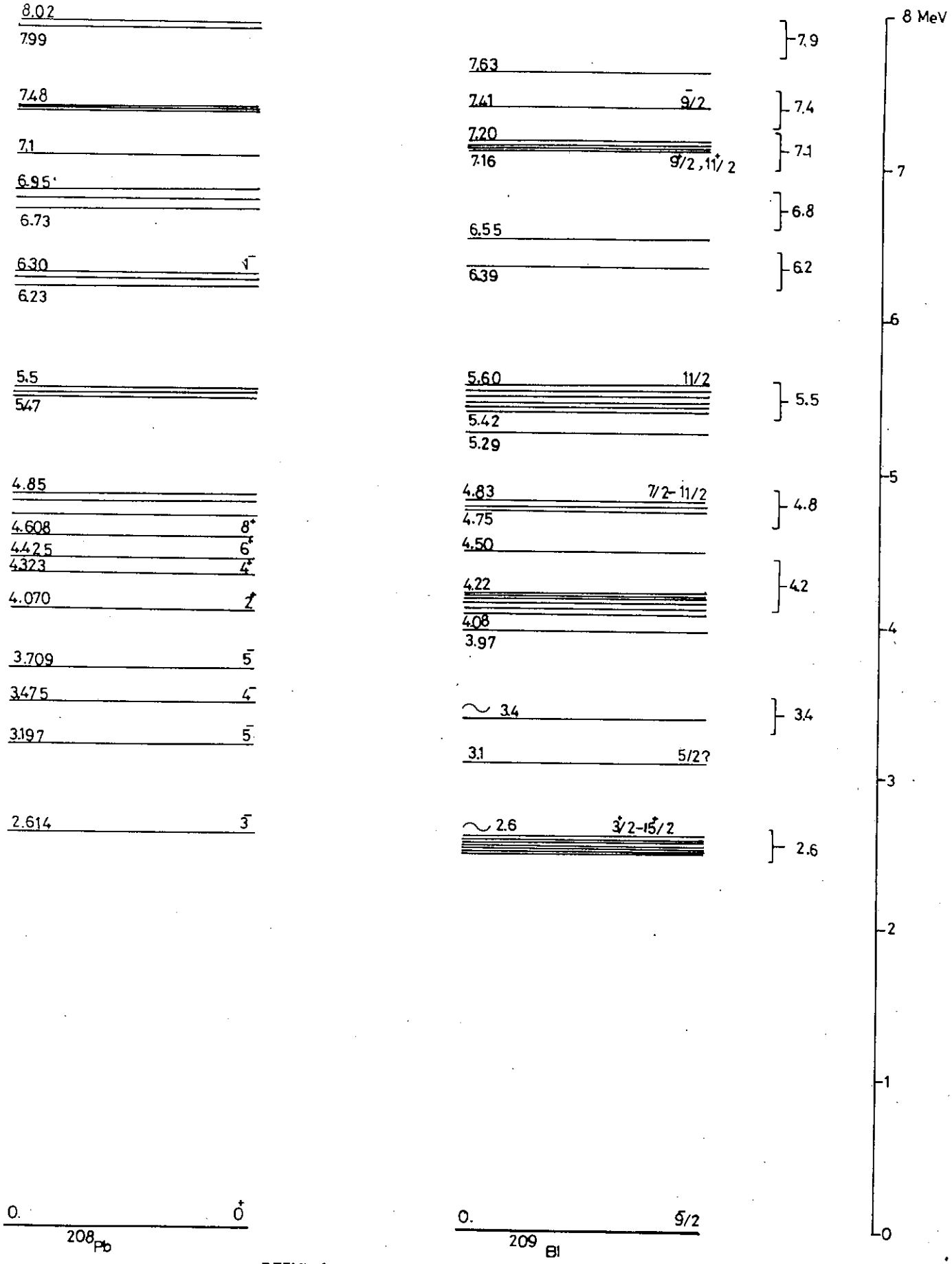

DETAIL IN REF (110)

Fig. 5.14.

In the time of flight spectra some structure was observed above the 7.9 MeV level. The uncertainty for these levels, however, was such that they could not reliably be analysed.

Table (5.1) shows that the observed excitation energies are, within the accuracy to which the energies can be determined, consistent with previously reported structure information as illustrated in Fig. (5.14).

5.3 Correction for Finite Geometry and Multiple Scattering in the Scattering Samples

In reducing data from a neutron time of flight scattering experiment to elastic and inelastic neutron scattering cross sections, using equation (5.4), three effects due to the finite size of the scattering sample must be taken into account: neutron attenuation in the sample, angular spread in single scattering, and multiple scattering.

Corrections for finite sample size effects in cylindrical samples have been attempted by several experimenters in the field of fast neutron scattering using either analytical or Monte Carlo methods. Analytical treatments of the multiple scattering problem have been given by Placzek[111] and Block and Jonker[112] and were later refined by Cox[113] and Kinney[108]. The difficulty involved in an analytical treatment is to estimate the validity of the necessary simplifying assumptions which may make this method less accurate than the Monte Carlo method. Despite this difficulty a comparative study by Velkley et al.[107] of Monte Carlo and analytical corrections has shown good agreement between these methods.

In this work a Monte Carlo Program MULTSCAT[109] was used to correct for finite sample size effects. The correction applied to the observed elastic cross section angular distribution is given by the expression:

$$\alpha = \frac{\Phi}{\bar{\Phi}} \cdot \frac{F}{\bar{F}} \cdot q \qquad (5.7)$$

The ratio, $\frac{\Phi}{\bar{\Phi}}$ is the correction for the anisotropy of the target neutrons, where Φ is the neutron flux from the target in the direction of the scatterer centre and $\bar{\Phi}$ is the mean neutron flux from the target within the first solid angle of the scatterer. For the isotropic $^{3}_{1}H(d,n)^{4}_{2}He$ reaction used in this work the ratio $\frac{\Phi}{\bar{\Phi}}$ is unity.

$\frac{F}{\bar{F}}$ is the flux attenuation correction factor and q is the correction for the loss of neutrons in the scatterer by non-elastic collisions. MULTSCAT also corrects the experimental angular distribution for the elastic neutron multiple scattering in the sample, the finite angular resolutions of the target scatterer and scatterer detector systems. The program involved an iterative process in which successively better approximations were sought.

In the Monte Carlo method the scattered neutrons are followed from collision to collision in the scattering sample.

To obtain good accuracy for the flux attenuation factor, $\frac{F}{\bar{F}}$ the calculations were performed by using at least five neutron groups each containing 2×10^{4} neutrons.

The correction q and the multiple scattering corrections were calculated by using three iterations each with 5×10^{3} neutrons. The number of neutrons used should be increased depending on the sample size.

The correction described above was performed for the Carbon (graphite) scattering sample employed to normalize cross sections measured in this work. The total cross section, total inelastic, and total capture cross sections required by the MULTSCAT code were taken from ref. (114). The Monte Carlo calculation showed that the effect of multiple scattering on the elastic scattering cross section is negligible for this sample. The magnitude of the flux attenuation factor amounts to 1.22 and is in agreement with the result of the analytical approach of W.E. Kinney, equation (5.6), to within 5%. However the multiple scattering factor was only 0.5%.

TABLE 5.2

Characteristics of the Scattering Samples

Element	Form	Density (gr/cm^3)	Abundance %	Dimensions (mm) Height	Diameter	Weight (gr)
^{209}Bi	Metallic Solid	10.25	100%	50.8	50.8	1007
^{12}C	Graphite	1.57	98.9%	50.0	50.0	154.8

Finite Sample Size Correction to the Differential Inelastic Cross Sections

The cross sections for the inelastic neutron groups derived from equation (5.4) had to be corrected for the effects of finite sample size. These corrections are the effect of multiple inelastic scattering in the sample, attenuation of the incident neutron flux due to the thickness of the sample and the effect of the angular spread resulting from the sample size and the geometry of the experiment.

A simple correction formula developed by Engelbrecht[115], for inelastic scattering from cylindrical scattering samples, was used to correct the inelastic data. In this correction process the inelastic scattering is assumed to be isotropic and elastic scattering taking place after an inelastic collision is neglected, while removal of inelastic neutrons due to further inelastic scattering or other absorptive processes are taken into account.

The multiple scattering correction estimated by the Engelbrecht formula was found to be negligible as expected.

The flux attenuation correction for the inelastic data was performed in the same manner as for the elastic cross section by the Monte Carlo Code (MULTSCAT).

One important effect which it seemed necessary to consider is the effect of angular spread on the inelastic scattering data. It should be noted that the scattering angle is not unique but covers a range of several degrees in this work, due to the finite solid angle subtended by the scatterer as seen from the target. The angular spreads amounted to ± 7.0 degrees throughout the whole angular range except 20 degrees. When the scattering measurement at 20 degrees was performed the target-scatterer geometry had to be modified by increasing target to scattering sample distance from approximately 19 cm to 28 Cm. The angular spread for this angle was therefore reduced to ± 5.1 degrees. As far as inelastic scattering is concerned the effect of the angular spread on the cross section is of no significance due to the shape of the inelastic scattering angular distribution which varies smoothly with the scattering angle. Fig. (5.15) shows a typical inelastic scattering angular distribution calculated for Bismuth 209 and for

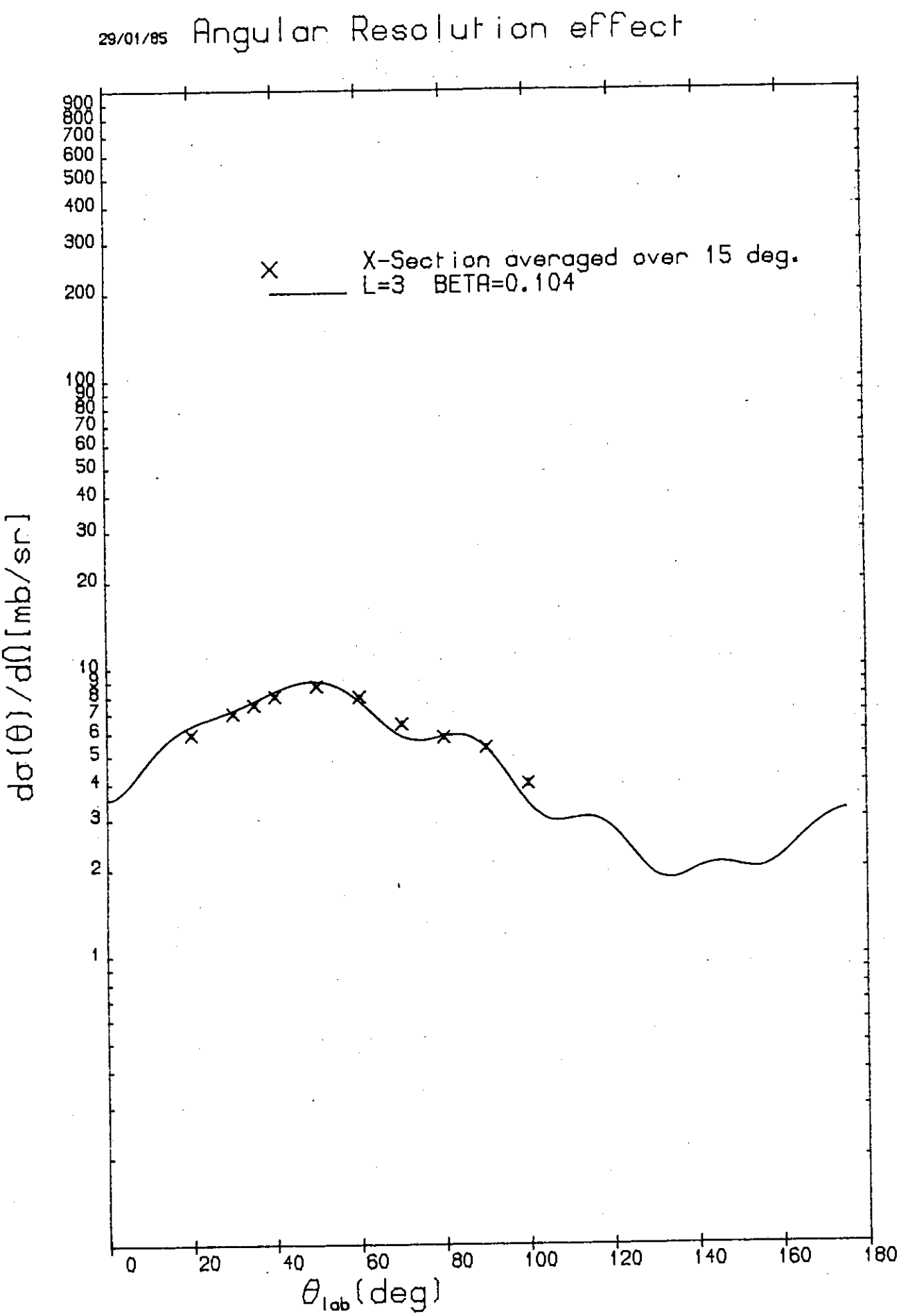
29/01/85 Angular Resolution effect
X-Section averaged over 15 deg.
L=3 BETA=0.104
dσ(θ)/dΩ [mb/sr]
θlab (deg)
900
800
700
600
500
400
300
200
100
90
80
70
60
50
40
30
20
10
9
8
7
6
5
4
3
2
1
0
20
40
60
80
100
120
140
160
180

Figure 5.15.

Q = 2.6 MeV using the DWBA calculation code DWUCK-4 (Chapter 6) The points in Fig. (5.15) are the averaged cross section over 15 degrees. It can be observed from the graph that the points resulting from averaging the cross section are still sufficiently close to the magnitude of the cross section given by the original curve and that no correction for finite angular spread need be considered.

Data Presentation

A) Bismuth Elastic Scattering Cross section.

Differential elastic scattering cross section data for Bismuth is presented in Fig. (5.16) and tabulated in Table 5.3.

The scattering sample dimensions are given in Table 5.2. Due to the relatively large sample size used in this work the elastic data had to be corrected for flux attenuation. Fig. (5.16) also shows the corrected elastic scattering cross section data.

The flux attenuation factor for the Bismuth sample was calculated by the Monte Carlo Code MULTSCAT using total cross sections, total inelastic cross sections and absorption cross sections given by Howerton[114]. The magnitude of the flux attenuation factor was 1.32 for neutrons of 14 MeV energy incident on the scatterer. Table 5.3 compares the uncorrected and corrected values of the elastic scattering cross section for Bismuth. The errors shown in Table 5.3 include the counting statistical error, background subtraction error, and Monte Carlo errors associated with the flux attenuation calculation for both Carbon and Bismuth samples, the 5% scaling error due to the

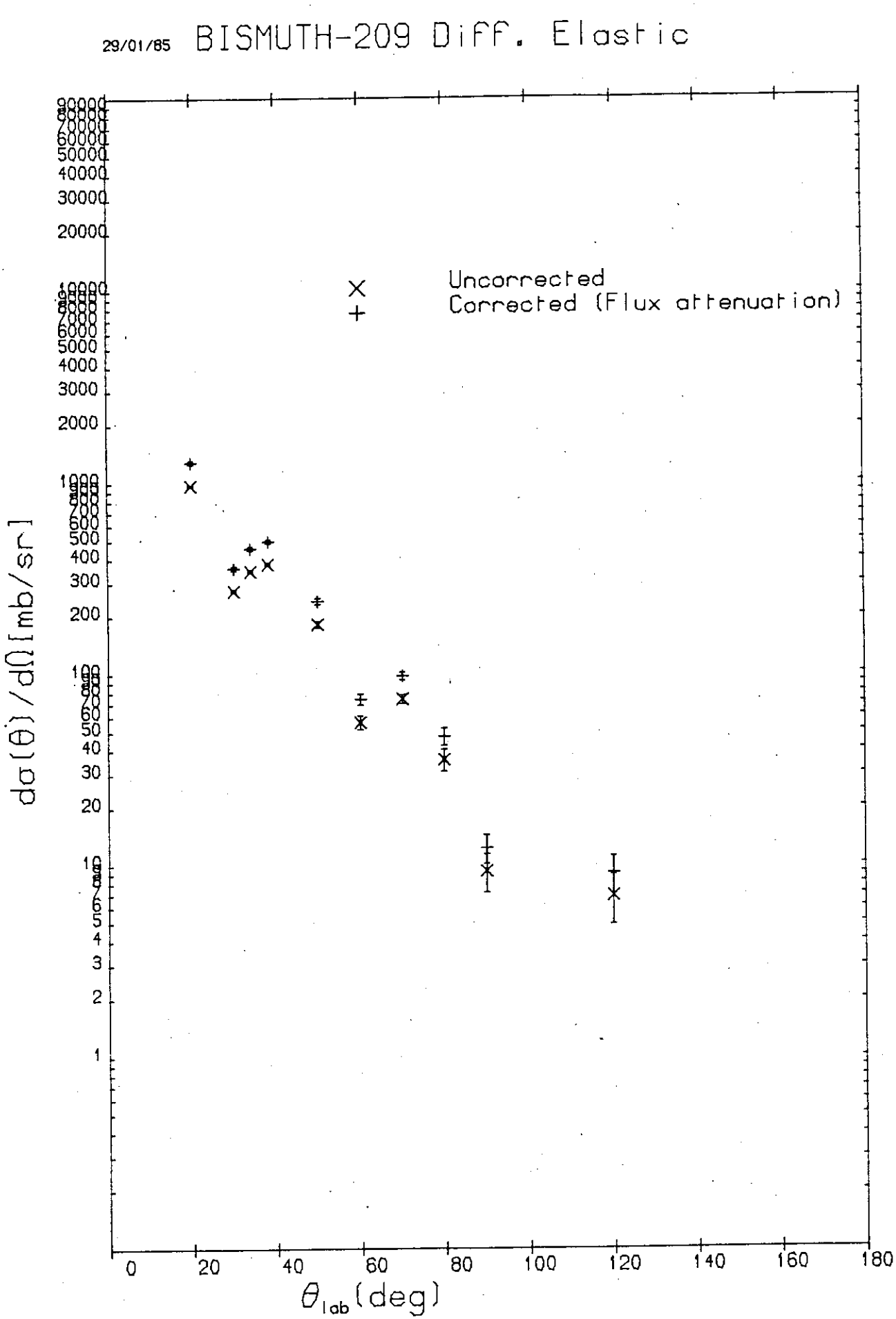
29/01/85 BISMUTH-209 Diff. Elastic
Uncorrected
Corrected (Flux attenuation)
dσ(θ)/dΩ [mb/sr]
θlab (deg)
0
20
40
60
80
100
120
140
160
180

Figure 5.16.

uncertainty of Carbon cross section and 3% error in the detector relative detection efficiency are also included in the tabulated elastic cross section data. These errors have been added quadratically to give the total error.

There are several previous reports in the literature utilizing 14 MeV neutrons for measuring the elastic scattering differential cross section for Bismuth. Fig. (5.17) illustrates the measurements of Stelson et al.[25], Kuijper et al.[30] and Matoba et al.[31] together with the present measurements. These data are in good agreement. The agreement is specially good between the data of Stelson et al., Matoha et al. and of this work. Some discrepancies are observed between the Kuijper et al. data and the rest of the distributions shown in Fig. (5.17), especially at backward angles where the Kuijper et al. data is too high. In Fig. (5.18) the differential elastic scattering cross section of 14.6 MeV neutrons measured by Cross and Jarvis[116] and also the elastic scattering cross section measured by Elliot[117] are compared with our data. The agreement between these three sets of data is reasonably good. There are, however, distinct discrepancies between the data of Cross and Jarvis and the other data at angles higher than about 80 degrees. Their data is generally less accurate and too large above 80 degrees. It is believed that too high a cross section in this region is due to contamination of elastic neutrons by those scattered from the low-excited states of Bismuth, Cross and Jarvis[116].

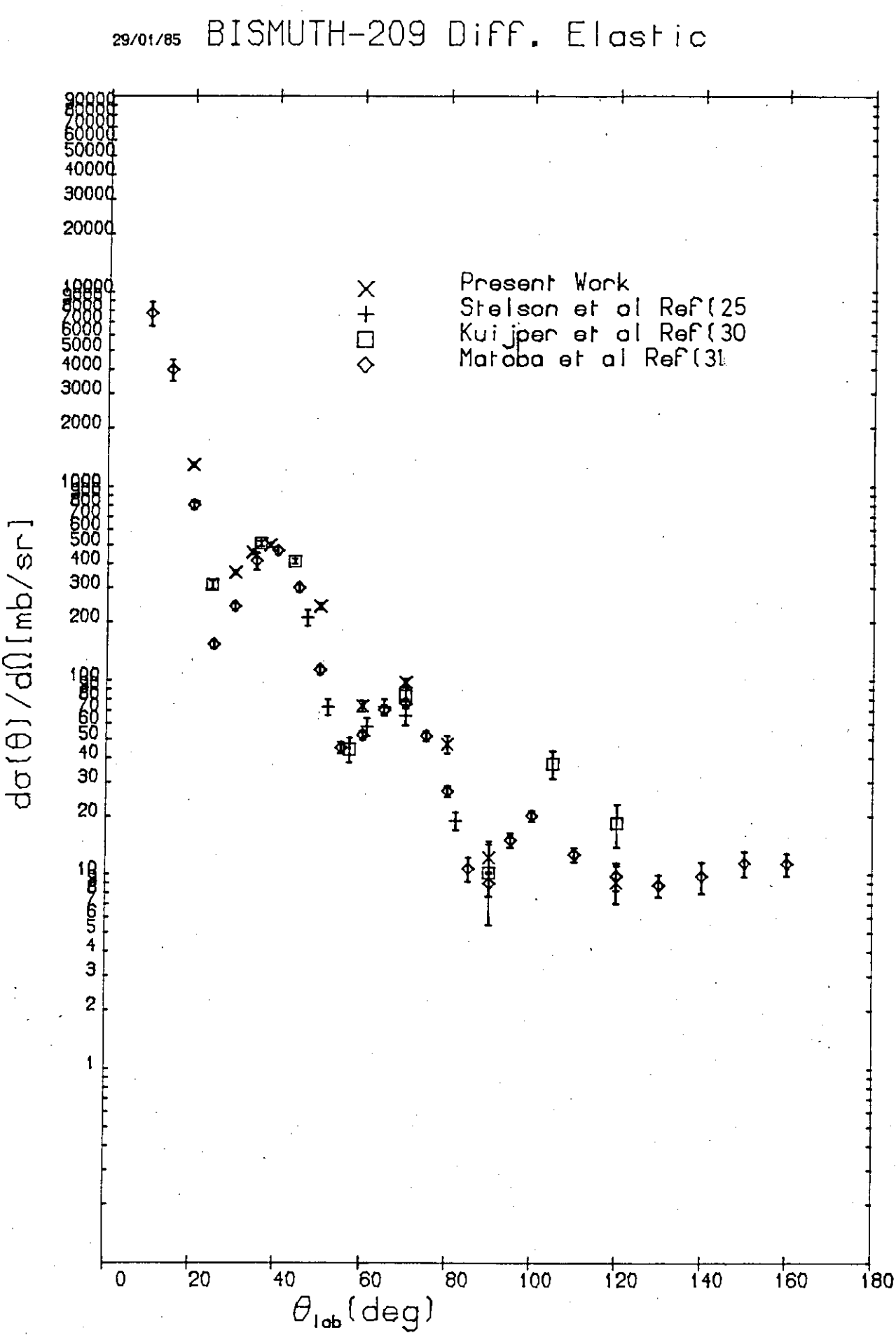
29/01/85 BISMUTH-209 Diff. Elastic
Present Work
Stelson et al Ref[25
Kuijper et al Ref[30
Matoba et al Ref[31
dσ(θ)/dΩ[mb/sr]
θlab(deg)

Figure 5.17.

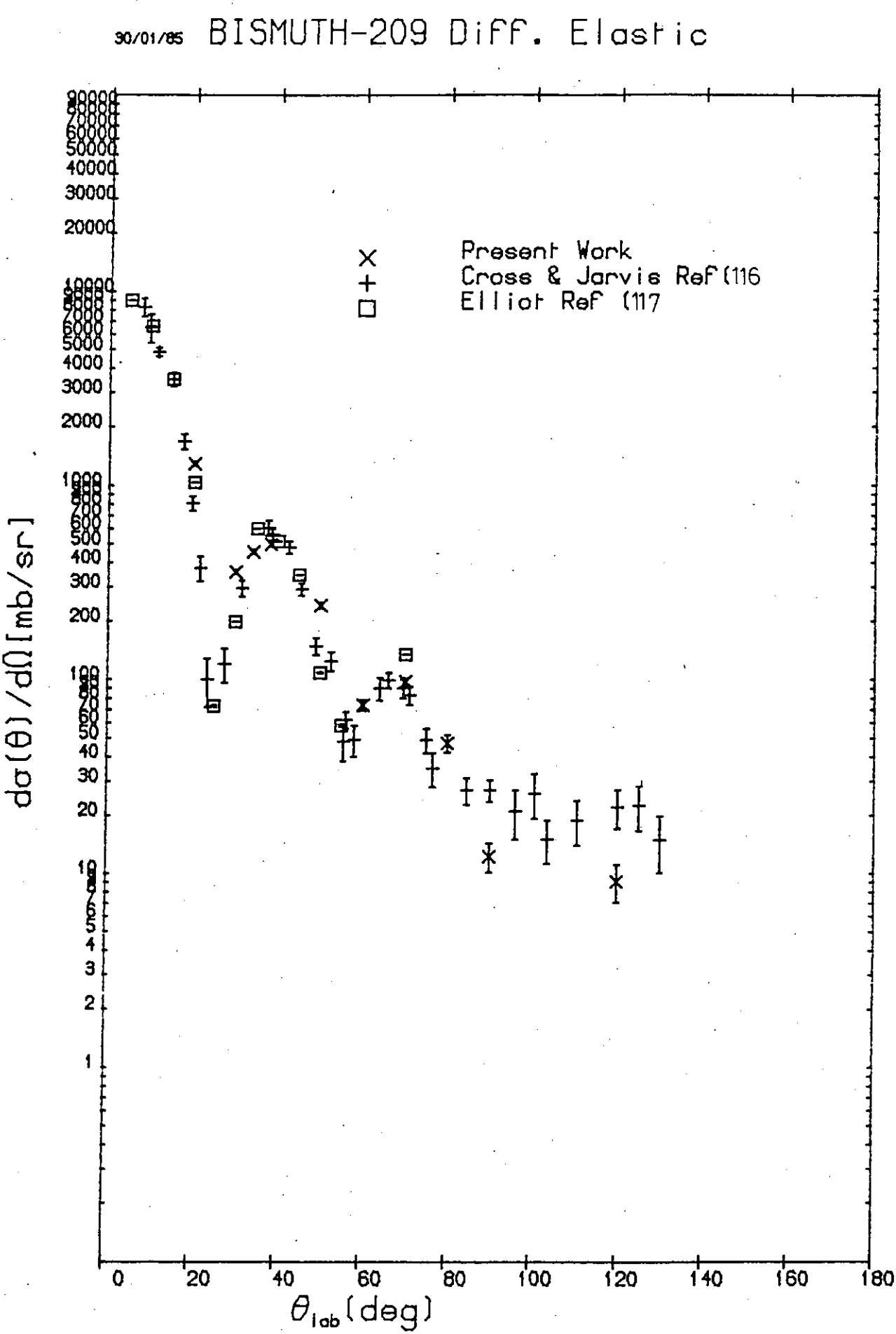
30/01/85 BISMUTH-209 Diff. Elastic
Present Work
Cross & Jarvis Ref (116
Elliot Ref (117
dσ(θ)/dΩ [mb/sr]
θlab (deg)
0
20
40
60
80
100
120
140
160
180

Figure 5.18.

TABLE 5.3

Differential Elastic Cross Section at 14.1 MeV

Lab. Angle	$(d\sigma/d\Omega)_{Lab}$ mb/sr Uncorrected	Corrected
20	976.9 ± 2	1289.5 ±29
30	271.08 ± 4	357.8 ± 9
34	346.0 ± 4	456.72 ±11
38.2	376.4 ± 4	496.8 ±12
50	181.75 ± 7	239.91 ± 9
60	55.89 ± 5	73.77 ± 5
70	73.95 ± 4	97.61 ± 5
80	35.7 ± 5	47.12 ± 5
90	9.27 ± 2	12.23 ± 2
120	6.86 ± 2	9.05 ± 2

B) Inelastic Scattering Cross Sections to ^{209}Bi Excited States

Differential inelastic scattering cross sections to 10 excited states of Bismuth have been measured up to an excitation energy of 7.9 MeV. Cross section data for these excited states are presented in Tables (5.4 - 5.13) and Figs. (5.22) - (5.30).

The errors shown in Tables 5.4 - 5.13 are the total error and include the counting statistical error, background subtraction error, Monte Carlo Correction errors associated with the flux attenuation calculation for both Carbon and Bismuth samples. The 5% cross section scaling error due to the uncertainty of Carbon cross section and 3% error associated with the detector relative efficiency are also included in the tabulated inelastic data. The scaling and the detector efficiency errors were a negligible source of error in most cases.

Previous measurements are available only for the 2.6 MeV, $\sim$ 4.2 MeV and $\sim$ 5.5 MeV states. There are three published measurements on the Bismuth excited states. Kuijper et al.[30] measured inelastic scattering cross sections to 2.6 MeV, 4.2 MeV and 5.5 MeV states of Bismuth. Stelson et al.[25], measured inelastic scattering cross sections to two excited states of Bismuth, 2.6 MeV and 4.2 MeV for only 6 angles. Matoba et al.[31] studied 2.6 MeV, $\sim$ 4.2 MeV and $\sim$ 5.8 MeV excited states in more detail. These available data, however, do not agree particularly well. A brief account of the extent to which the data of Matoba et al., Kuijper et al., and Stelson et al. agree with each other is given below.

Q = -2.6 MeV.

Fig. (5.19) illustrates the published data for this state. The data of Matoba et al. and Stelson et al. are within reasonable agreement

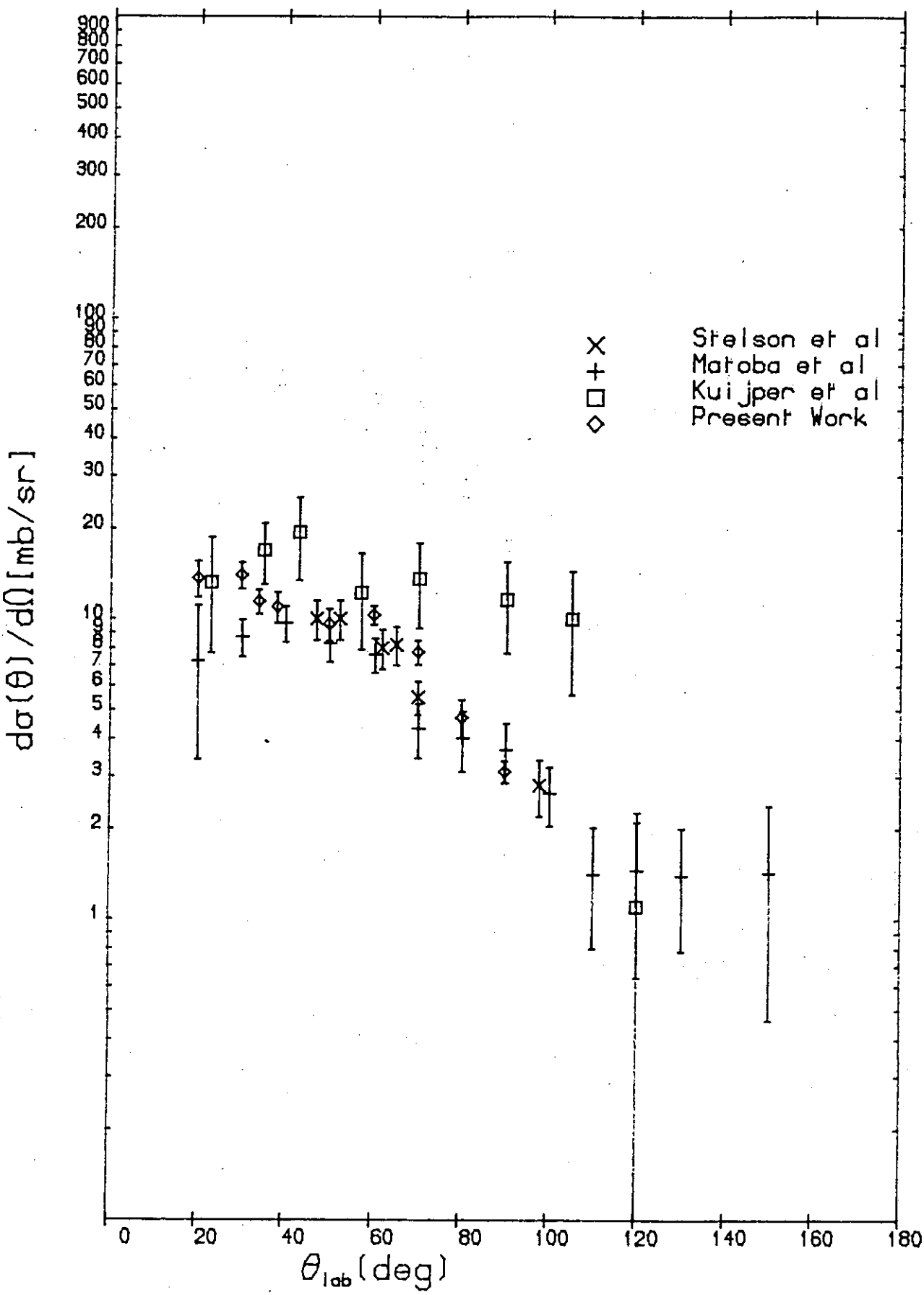
30/01/85 BISMUTH-209 Q=-2.6 MeV
Stelson et al
Matoba et al
Kuijper et al
Present Work
dσ(θ)/dΩ[mb/sr]
θlab(deg)

Figure 5.19

agreement in the angular range of 47 degrees to 98 degrees, to which the measurement of Stelson et al. is limited. Stelson et al. did not perform any measurement at more forward angles, where the measurement would be more difficult and normally results in less accuracy due to the increase of background. The accuracy of the data of Stelson et al. varies between about 15% at 47 degrees to 21% at 98 degrees scattering angle. The data of Matoba et al. for this state is generally more accurate than that of Stelson et al. Their accuracy amounts to approximately 2.5% to 14% for angles between 30 degrees to 150 degrees. Their data for 20 degrees, however, is very inaccurate, ± 53%. The measurements of Kuijper et al. are not only less accurate (accuracy ranges between 30% to 100%) but they also suggest a magnitude for the cross section more than twice as large as the other data for most of the angles they investigated. The present work presents the cross section for the 2.6 MeV excited state of ^{209}Bi in the angular range between 20 degrees and 90 degrees. The magnitude of our data is consistent with that of Matoba et al. and that of Stelson et al. The accuracy of our data varies between 8% and 14%.

At 20 degrees our data (accuracy 13%) is much more accurate than that of Matoba et al. Being consistent with the work of Matoba et al. and that of Stelson the result of this work therefore rejects the data of Kuijper as being too high.

Q = -4.2MeV.

There are three available measurements for the 4.2 MeV excited state of ^{209}Bi, Stelson et al.[25], Kuijper et al.[30] and Matoba et al.[31], Fig. (5.20). The data of this work is in agreement with

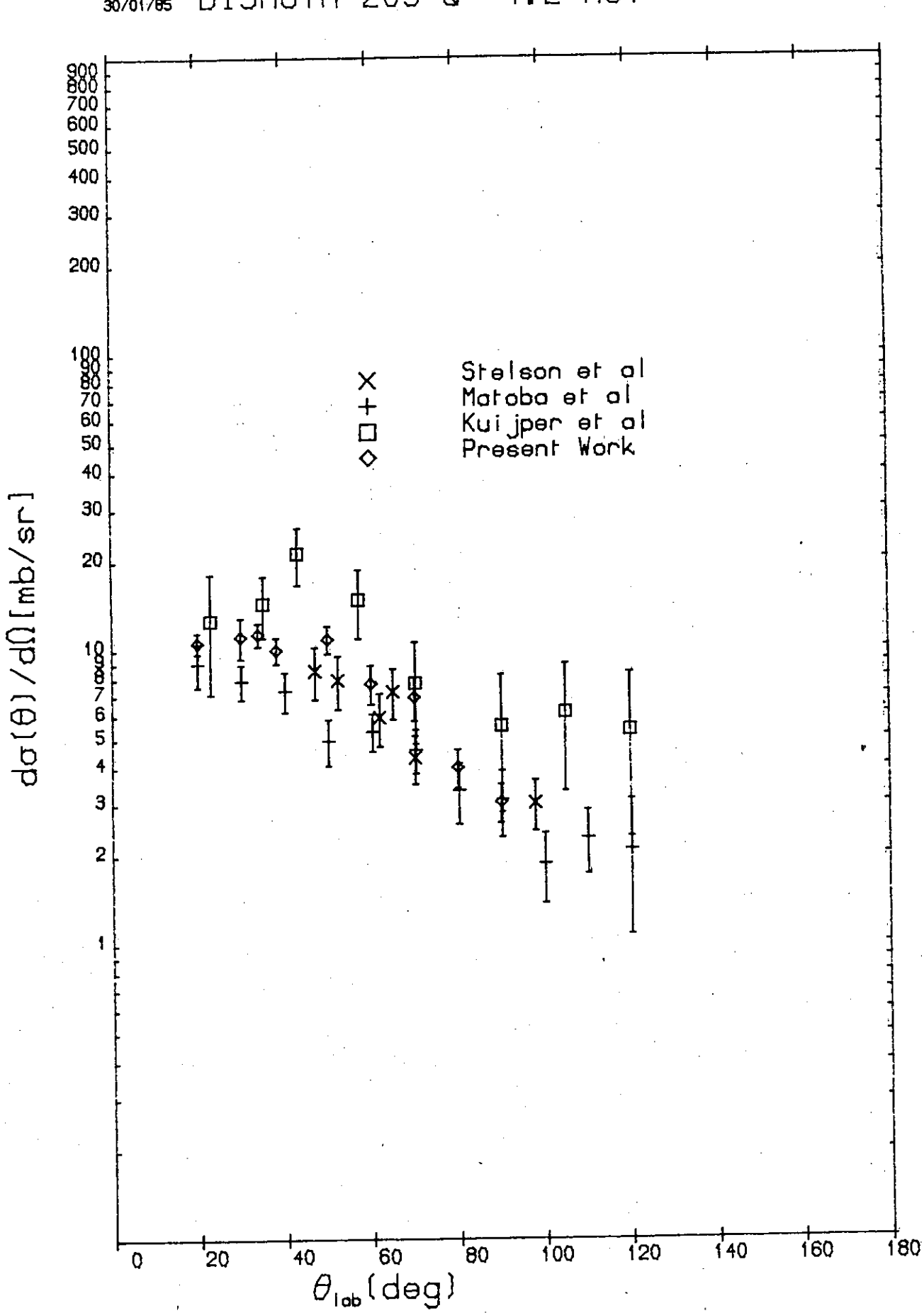
30/01/85 BISMUTH-209 Q=-4.2 MeV
Stelson et al
Matoba et al
Kuijper et al
Present Work
dσ(θ)/dΩ[mb/sr]
θlab(deg)

Figure 5.20.

the data of Matoba et al. and Stelson et al. This agreement is rather better for more backward angles. At more forward angles our data is slightly higher than that of Matoba et al. at 50 degrees, the measurement of Matoba et al. seems to be too low. It is inconsistent with our measurement and possibly with the measurements of Stelson et al. at 47 degrees and 52 degrees. There is close agreement at 20 degrees between our data and the data of Matoba et al. The data of Kuijper et al. is substantially higher than other measurements as shown in Fig. (5.20). It is also the less accurate set of measurements. The present measurements are considerably more accurate than any published data on the 4.2 MeV state and tend to reject the data of Kuijper et al. as too high and inaccurate.

Q = -5.5 MeV.

There are only two previous sets of measurements for the 5.5 MeV excited states performed by Matoba et al. and Kuijper et al.

The present measurements are in fair agreement with the measurements of Matoba et al, especially at angles above 40 degrees. For more forward angles the agreement is not particularly good. The present measurements show a tendency to higher cross sections than those of Matoba et al. at angles between 20 degrees to 40 degrees. Fig. (5. 21) demonstrates differences between the three sets of data. The data of Kuijper et al. are much higher than the other two sets, especially their measurement at 40 degrees scattering angle. The accuracy of our data is overall better than the accuracy of other measurements shown in Fig. (5.21). The present data are considerably more accurate than the measurements of Matoba et al. at 20 degrees scattering angle.

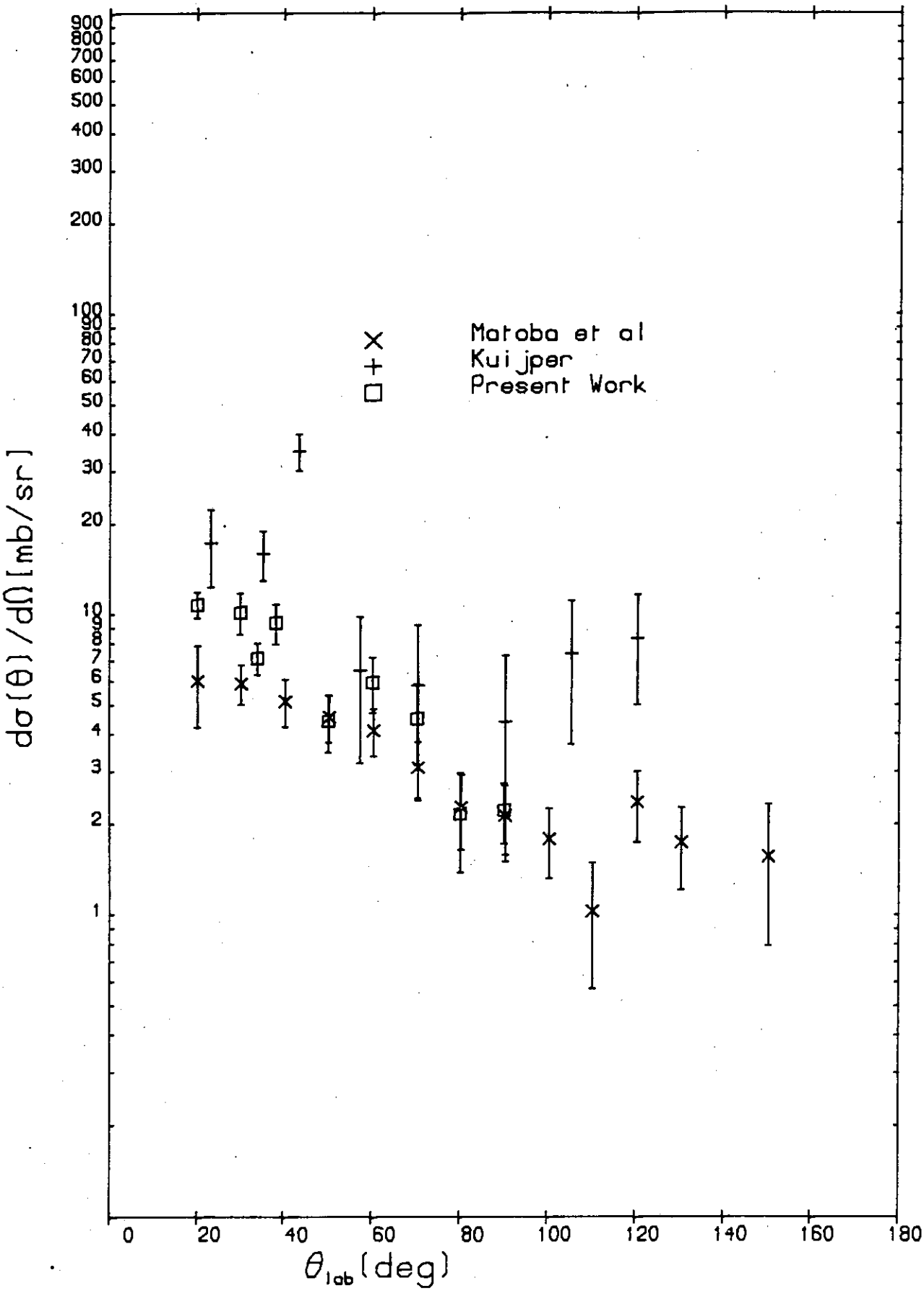
27/02/85 BISMUTH-209 Q=-5.5 MeV
Matoba et al
Kuijper
Present Work
dσ(θ)/dΩ[mb/sr]
θlab(deg)

Figure 5.21

TABLE 5.4

Differential inelastic cross section, Q = 2.6 MeV.

Lab. Angle (Degrees)	$(d\sigma/d\Omega)_{Lab.}$ (mb/sr) Uncorrected	Corrected
20	10.35 ± 1.7	13.66 ± 2.0
30	10.59 ± 1.2	13.97 ± 1.6
34	8.65 ± 0.8	11.41 ± 1.2
38.2	8.31 ± 0.9	10.96 ± 1.4
50	7.27 ± 1.0	9.60 ± 1.3
60	7.81 ± 0.5	10.30 ± 0.9
70	5.89 ± 0.6	7.77 ± 0.8
80	3.57 ± 0.6	4.71 ± 0.7
90	2.36 ± 0.2	3.11 ± 0.3

TABLE 5.5

Differential inelastic cross section, Q = -3.4 MeV..

Lab. Angle (Degrees)	$(d\sigma/d\Omega)_{Lab.}$ mb/sr.	
	Uncorrected	Corrected
20	3.64 ± 0.5	4.80 ± 0.7
30	4.04 ± 1.1	5.33 ± 1.3
34	1.78 ± 0.6	2.34 ± 0.7
38.2	3.12 ± 0.9	4.11 ± 1.0
50	2.10 ± 0.8	2.77 ± 0.9
60	2.20 ± 0.6	2.90 ± 0.7
70	1.0 ± 0.5	1.32 ± 0.5
80	1.69 ± 0.4	2.230± 0.5
90	0.76 ± 0.3	1.00 ± 0.3

TABLE 5.6

Differential inelastic cross section, Q = -4.2 MeV.

Lab. Angle (Degrees)	$(d\sigma/d\Omega)_{Lab.}$ mb/sr.	
	Uncorrected	Corrected
20	8.07 ± 0.6	10.6 ± 1.0
30	8.41 ± 1.6	11.10 ± 1.8
34	8.58 ± 0.8	11.32 ± 1.2
38.2	7.58 ± 0.8	10.00 ± 1.1
50	8.23 ± 1.0	10.86 ± 1.3
60	5.82 ± 1.0	7.68 ± 1.2
70	5.22 ± 1.0	6.89 ± 1.2
80	3.02 ± 0.5	3.98 ± 0.6
90	2.30 ± 0.4	3.03 ± 0.5

TABLE 5.7

Differential inelastic cross section, Q = -4.8 MeV.

Lab. Angle (Degrees)	$(d\sigma/d\Omega)_{Lab.}$ mb/sr.	
	Uncorrected	Corrected
20	3.98 ± 0.7	5.25 ± 0.8
30	5.42 ± 0.7	7.15 ± 0.9
34	3.21 ± 0.6	4.23 ± 0.7
38.2	3.10 ± 1.0	4.09 ± 1.1
50	3.37 ± 0.8	4.44 ± 0.9
60	1.94 ± 0.6	2.56 ± 0.6
70	2.30 ± 0.6	3.03 ± 0.6
80	1.89 ± 0.6	2.49 ± 0.7
90	1.26 ± 0.4	1.66 ± 0.4

TABLE 5.8

Differential inelastic cross section, Q = -5.5 MeV.

Lab. Angle (Degrees)	$(d\sigma/d\Omega)_{Lab.}$ mb/sr.	
	Uncorrected	Corrected
20	8.16 ± 0.8	10.77 ± 1.2
30	7.69 ± 1.5	10.15 ± 1.7
34	5.43 ± 0.7	7.16 ± 0.9
38.2	7.1 ± 1.3	9.37 ± 1.5
50	3.36 ± 0.9	4.43 ± 1.0
60	4.50 ± 1.2	5.94 ± 1.3
70	3.42 ± 1.3	4.51 ± 1.4
80	1.65 ± 0.7	2.17 ± 0.8
90	1.69 ± 0.5	2.23 ± 0.5

TABLE 5.9

Differential inelastic cross section, Q = -6.2 MeV.

Lab. Angle (Degrees)	$(d\sigma/d\Omega)_{Lab.}$ mb/sr.	
	Uncorrected	Corrected
20	2.93 ± 0.6	3.86 ± 0.7
30	3.03 ± 0.8	3.99 ± 0.9
34	2.50 ± 0.7	3.3 ± 0.7
38.2	5.39 ± 0.9	7.11 ± 1.0
50	3.04 ± 1.2	4.01 ± 1.2
60	1.38 ± 0.4	1.82 ± 0.5
70	3.03 ± 0.7	3.99 ± 0.8
80	1.46 ± 0.6	1.92 ± 0.6
90	1.04 ± 0.2	1.37 ± 0.2

TABLE 5.10

Differential inelastic cross section, Q = -6.8 MeV.

Lab. Angle (Degrees)	$(d\sigma/d\Omega)_{Lab.}$ mb/sr.	
	Uncorrected	Corrected
20	2.58 ± 0.6	3.40 ± 0.6
30	2.43 ± 0.7	3.20 ± 0.7
34	2.73 ± 0.6	3.60 ± 0.7
38.2	2.77 ± 1.1	3.65 ± 1.2
50	1.29 ± 0.5	1.70 ± 0.5
60	2.49 ± 0.9	3.28 ± 0.9
70	2.5 ± 0.7	3.3 ± 0.7
80	0.72 ± 0.1	0.95 ± 0.1
90	0.85 ± 0.2	1.12 ± 0.2

TABLE 5.11

Differential inelastic cross section, Q = - 7.1 MeV.

Lab. Angle (Degrees)	$(d\sigma/d\Omega)_{Lab.}$ mb/sr.	
	Uncorrected	Corrected
20	2.37 ± 0.8	3.12 ± 0.9
30	3.16 ± 0.6	4.17 ± 0.7
34	2.42 ± 0.7	3.19 ± 0.8
38.2	2.64 ± 0.8	3.48 ± 0.9
50	1.60 ± 0.7	2.11 ± 0.7
60	1.78 ± 0.9	2.34 ± 0.9
70	1.02 ± 0.4	1.34 ± 0.4
80	0.72 ± 0.3	0.95 ± 0.3
90	0.66 ± 0.2	0.87 ± 0.2

TABLE 5.12

Differential inelastic cross section, Q = -7.4 MeV.

Lab. Angle (Degrees)	$(d\sigma/d\Omega)_{Lab.}$ mb/sr.	
	Uncorrected	Corrected
20	2.21 ± 0.8	2.91 ± 0.8
30	3.17 ± 0.6	4.18 ± 0.7
34	2.33 ± 0.6	3.07 ± 0.7
38.2	1.5 ± 0.5	1.98 ± 0.5
50	1.89 ± 0.6	2.49 ± 0.6
60	0.97 ± 0.5	1.28 ± 0.5
70	1.93 ± 0.5	2.54 ± 0.5
80	2.12 ± 0.7	2.79 ± 0.7
90	1.28 ± 0.2	1.68 ± 0.2

TABLE 5.13

Differential inelastic cross section, Q = -7.9 MeV.

Lab. Angle (Degrees)	$(d\sigma/d\Omega)_{Lab.}$ mb/sr.	
	Uncorrected	Corrected
20	3.10 ± 0.7	4.09 ± 0.8
30	4.20 ± 0.9	5.54 ± 1.0
34	2.89 ± 0.5	3.81 ± 0.6
38.2	2.45 ± 1.4	3.23 ± 1.5
50	2.46 ± 0.6	3.24 ± 0.6
60	3.20 ± 0.7	4.22 ± 0.8
70	2.30 ± 1.0	3.03 ± 1.0
80	1.46 ± 0.7	1.92 ± 0.8
90	0.91 ± 0.4	1.11 ± 0.4

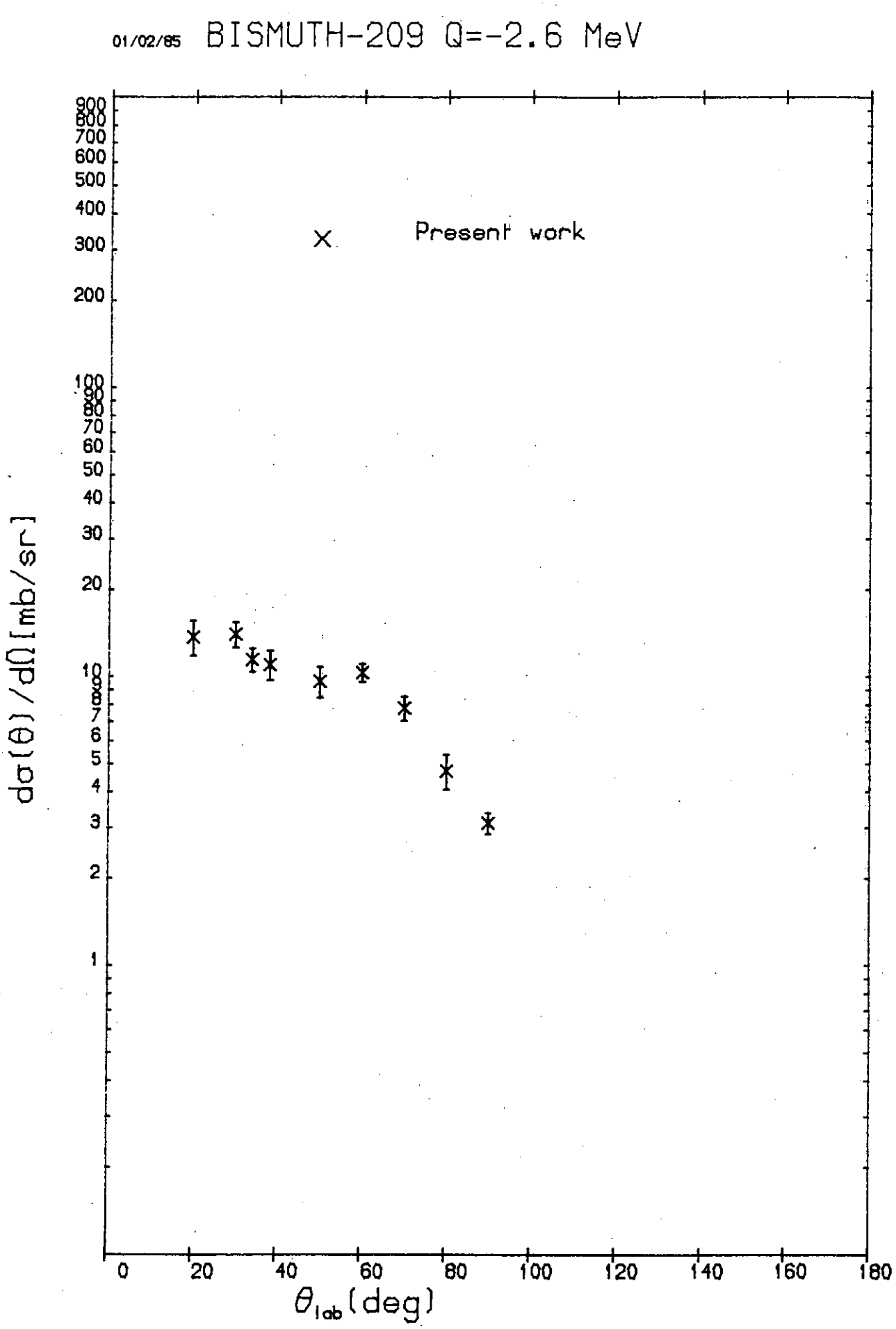
01/02/85 BISMUTH-209 Q=-2.6 MeV
Present work
dσ(θ)/dΩ[mb/sr]
θlab(deg)
900
800
700
600
500
400
300
200
100
90
80
70
60
50
40
30
20
10
8
7
6
5
4
3
2
1
0
20
40
60
80
100
120
140
160
180

Figure 5.22.

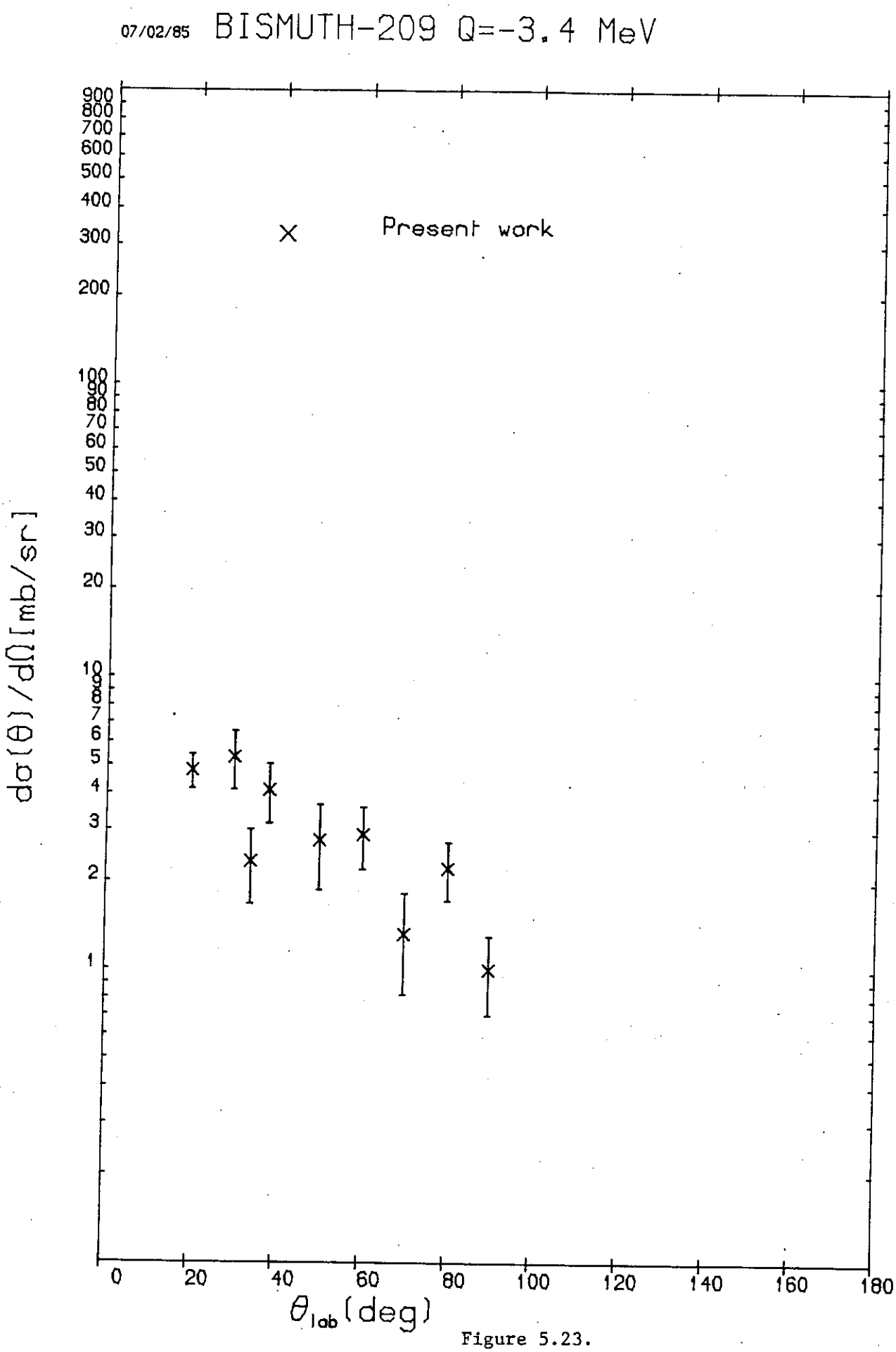
07/02/85 BISMUTH-209 Q=-3.4 MeV
Present work
dσ(θ)/dΩ[mb/sr]
θlab(deg)
900
800
700
600
500
400
300
200
100
90
80
70
60
50
40
30
20
10
9
8
7
6
5
4
3
2
1
0
20
40
60
80
100
120
140
160
180

Figure 5.23.

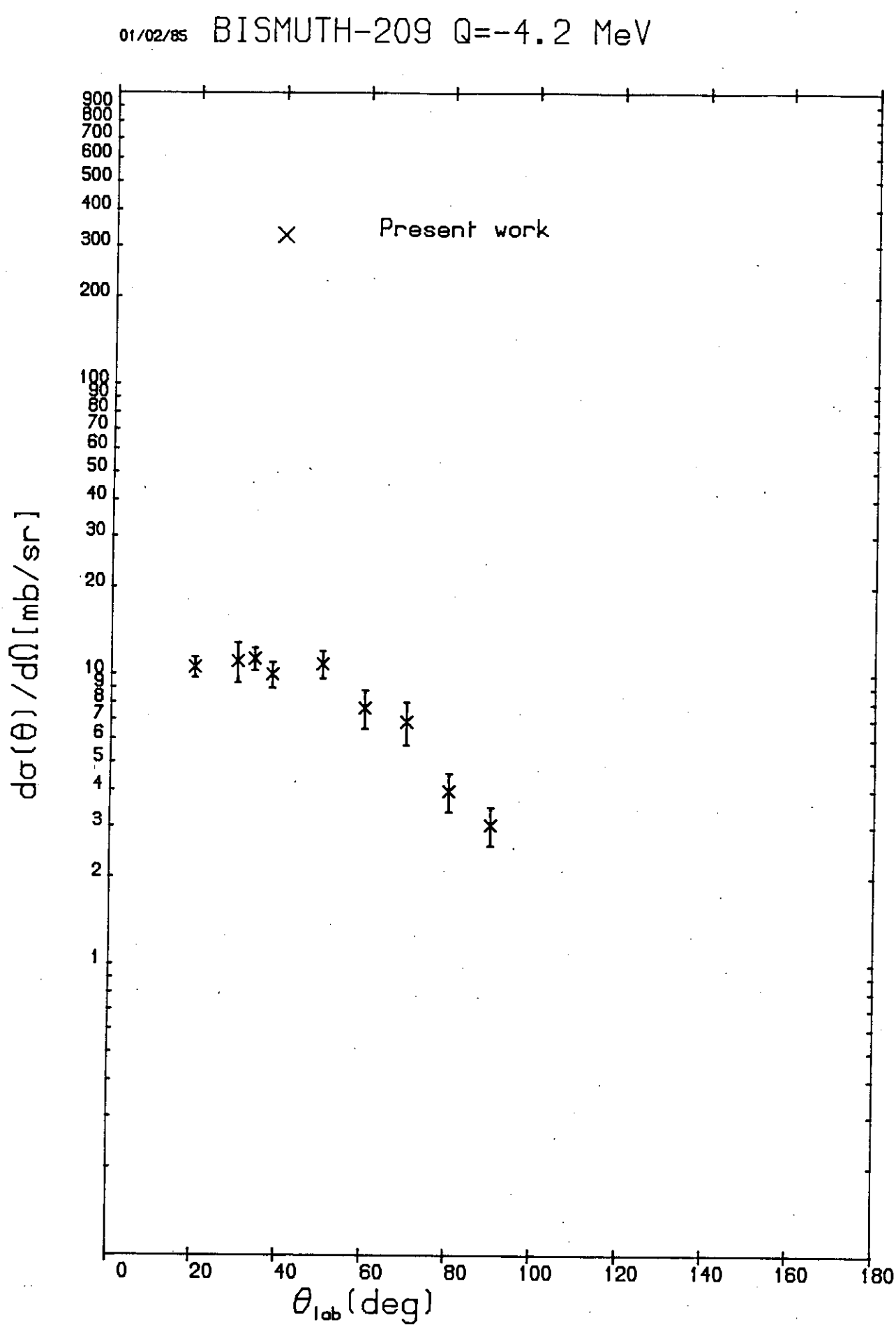
01/02/85 BISMUTH-209 Q=-4.2 MeV
Present work
dσ(θ)/dΩ[mb/sr]
θlab(deg)
900
800
700
600
500
400
300
200
100
90
80
70
60
50
40
30
20
10
9
8
7
6
5
4
3
2
1
0
20
40
60
80
100
120
140
160
180

Figure 5.24

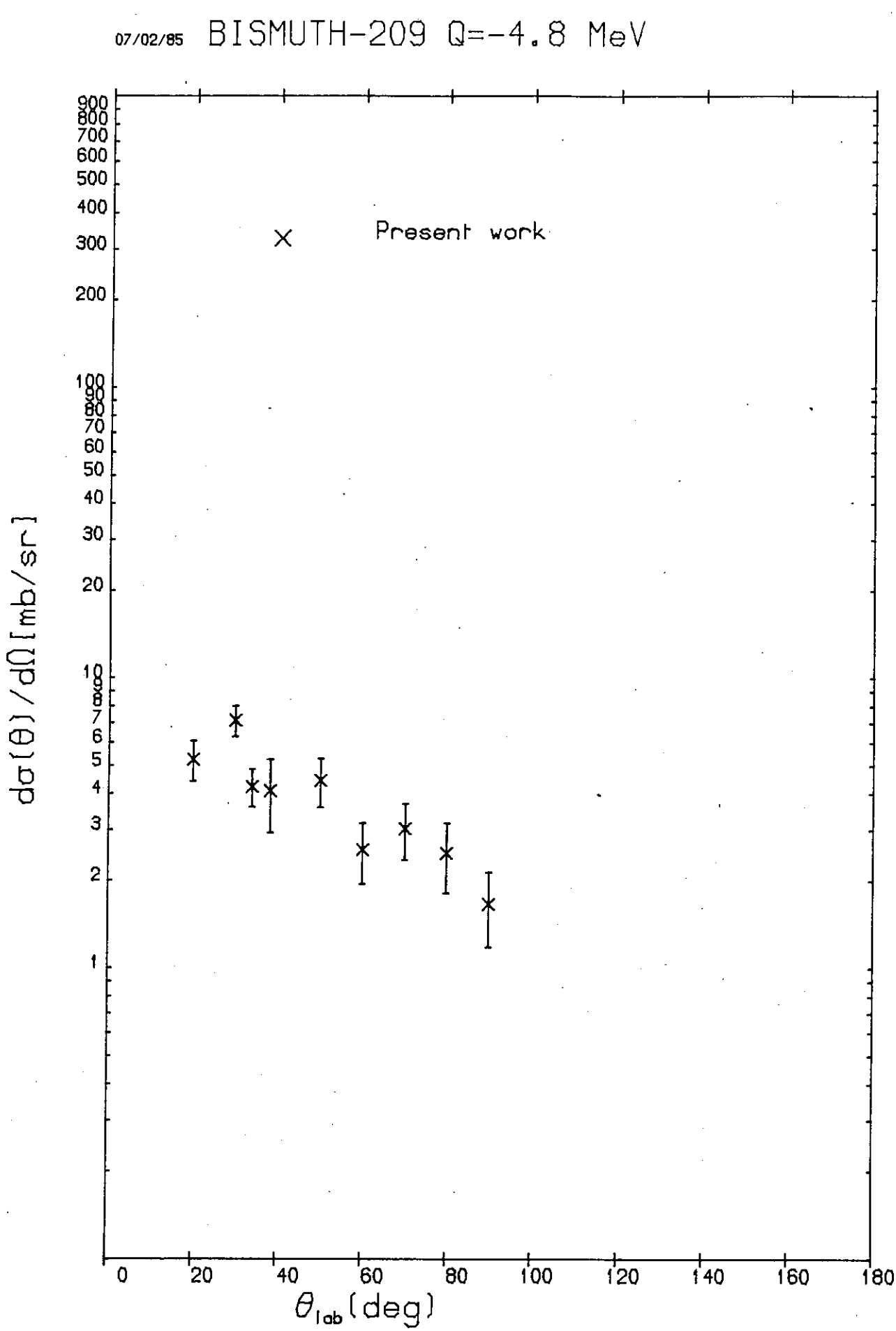
07/02/85 BISMUTH-209 Q=-4.8 MeV
Present work
dσ(θ)/dΩ[mb/sr]
θlab(deg)
900
800
700
600
500
400
300
200
100
90
80
70
60
50
40
30
20
10
9
8
7
6
5
4
3
2
1
0
20
40
60
80
100
120
140
160
180

Figure 5.25.

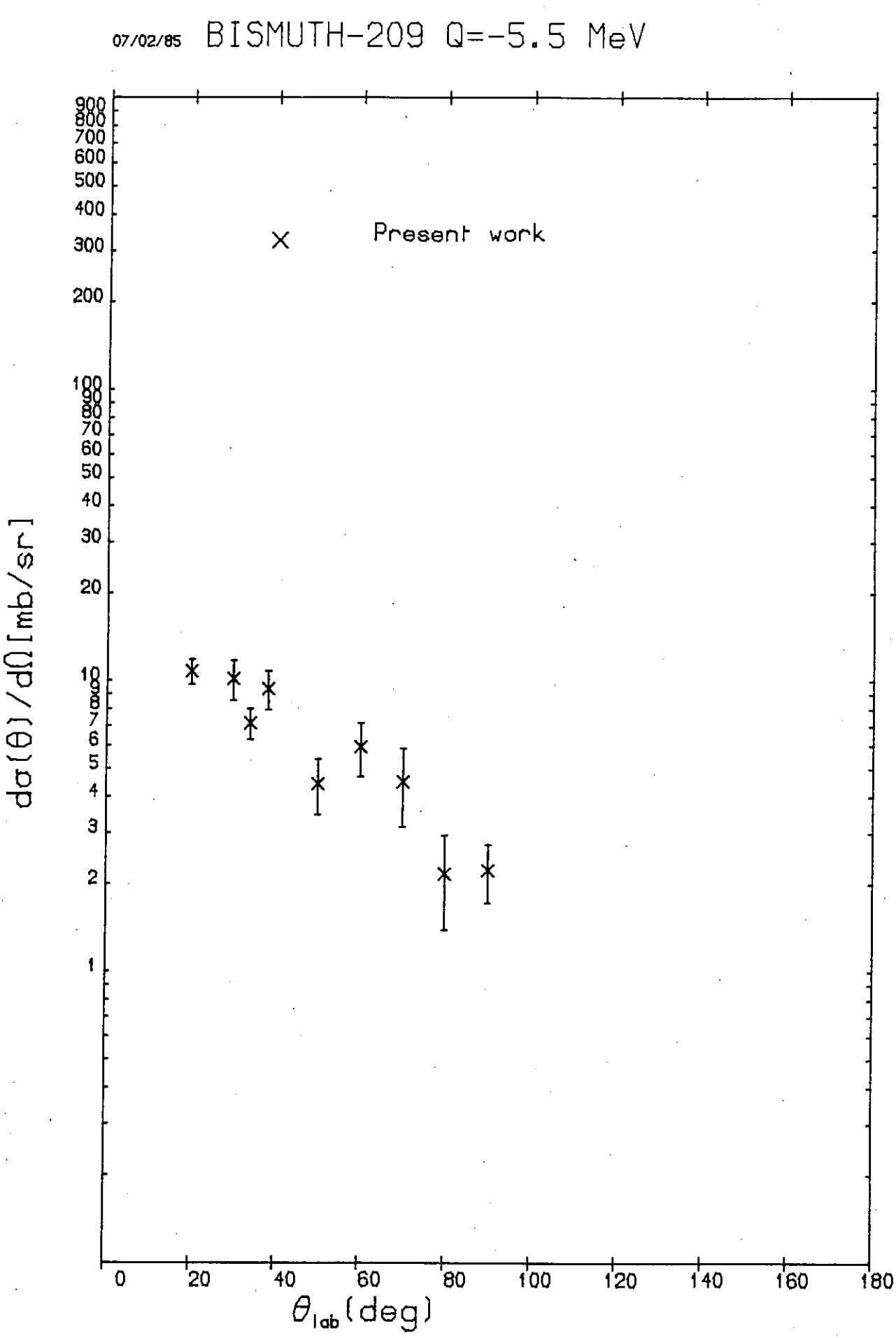
07/02/85 BISMUTH-209 Q=-5.5 MeV
Present work
dσ(θ)/dΩ[mb/sr]
θlab(deg)
900
800
700
600
500
400
300
200
100
90
80
70
60
50
40
30
20
10
9
8
7
6
5
4
3
2
1
0
20
40
60
80
100
120
140
160
180

Figure 5.26.

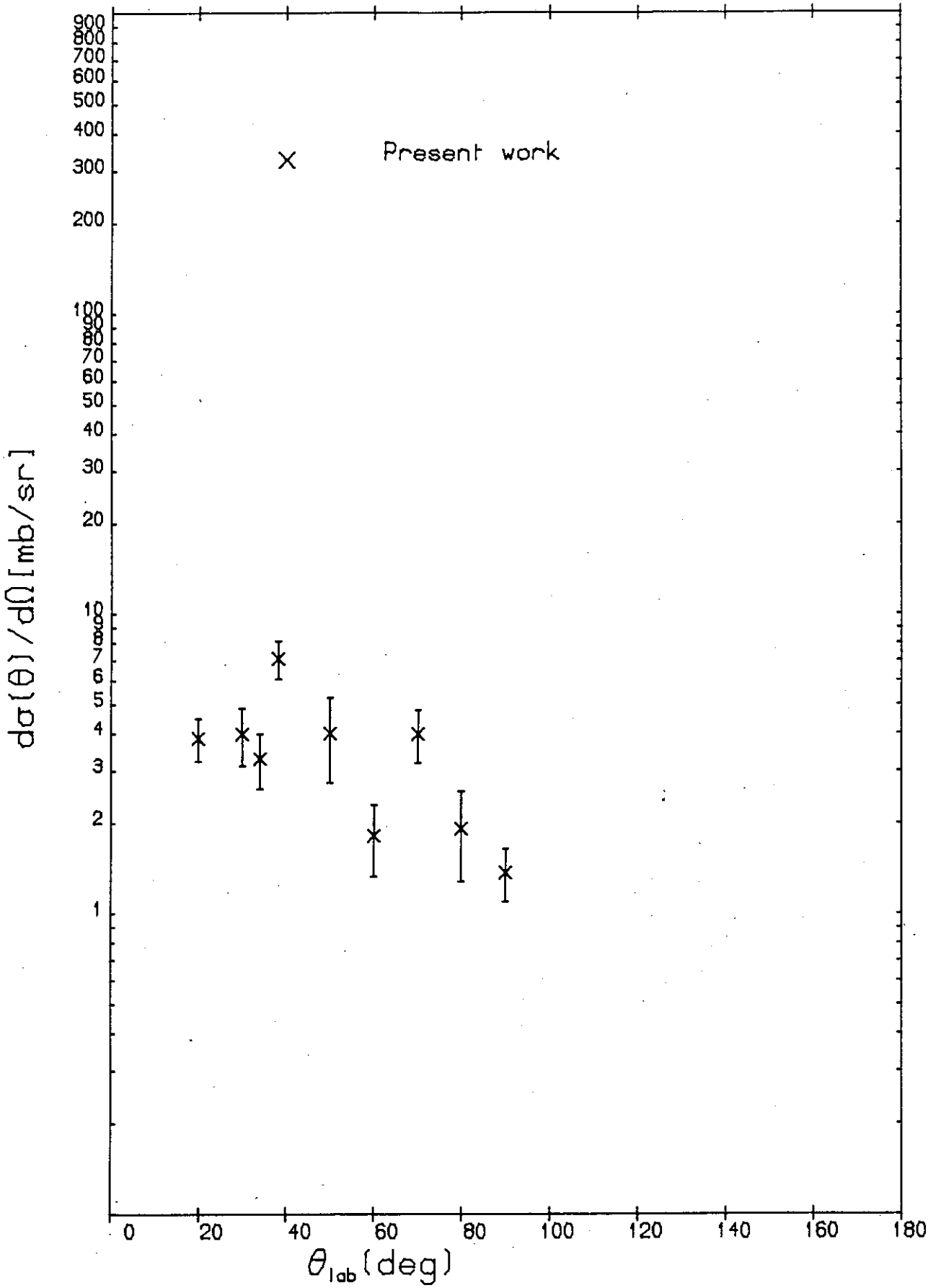
07/02/85 BISMUTH-209 Q=-6.2 MeV
Present work
dσ(θ)/dΩ[mb/sr]
θlab(deg)
900
800
700
600
500
400
300
200
100
90
80
70
60
50
40
30
20
10
9
8
7
6
5
4
3
2
1
0
20
40
60
80
100
120
140
160
180

Figure 5.27.

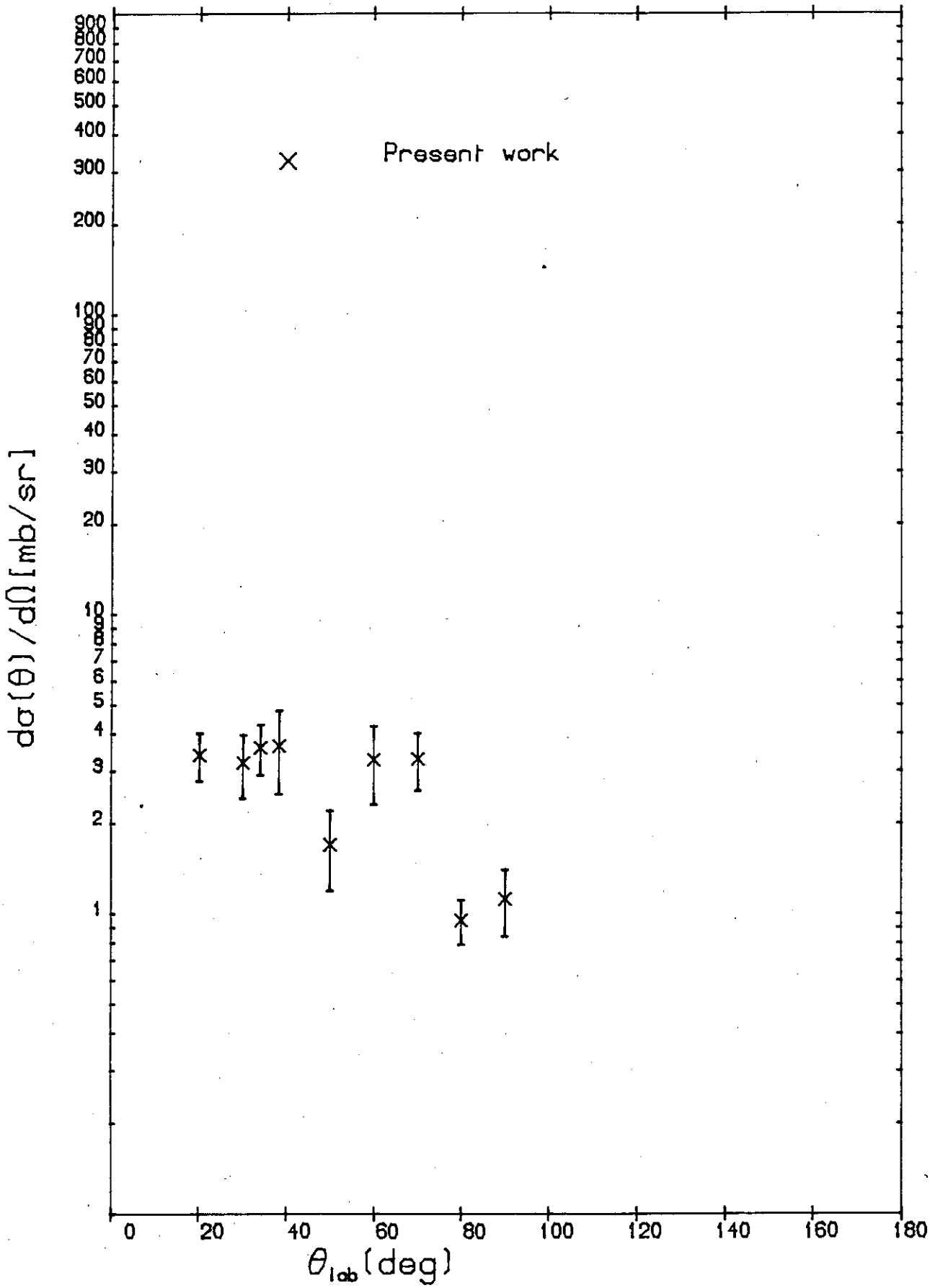
01/02/85 BISMUTH-209 Q=-6.8 MeV
Present work
dσ(θ)/dΩ[mb/sr]
θlab(deg)
900
800
700
600
500
400
300
200
100
90
80
70
60
50
40
30
20
10
9
8
7
6
5
4
3
2
1
0
20
40
60
80
100
120
140
160
180

Figure 5.28.

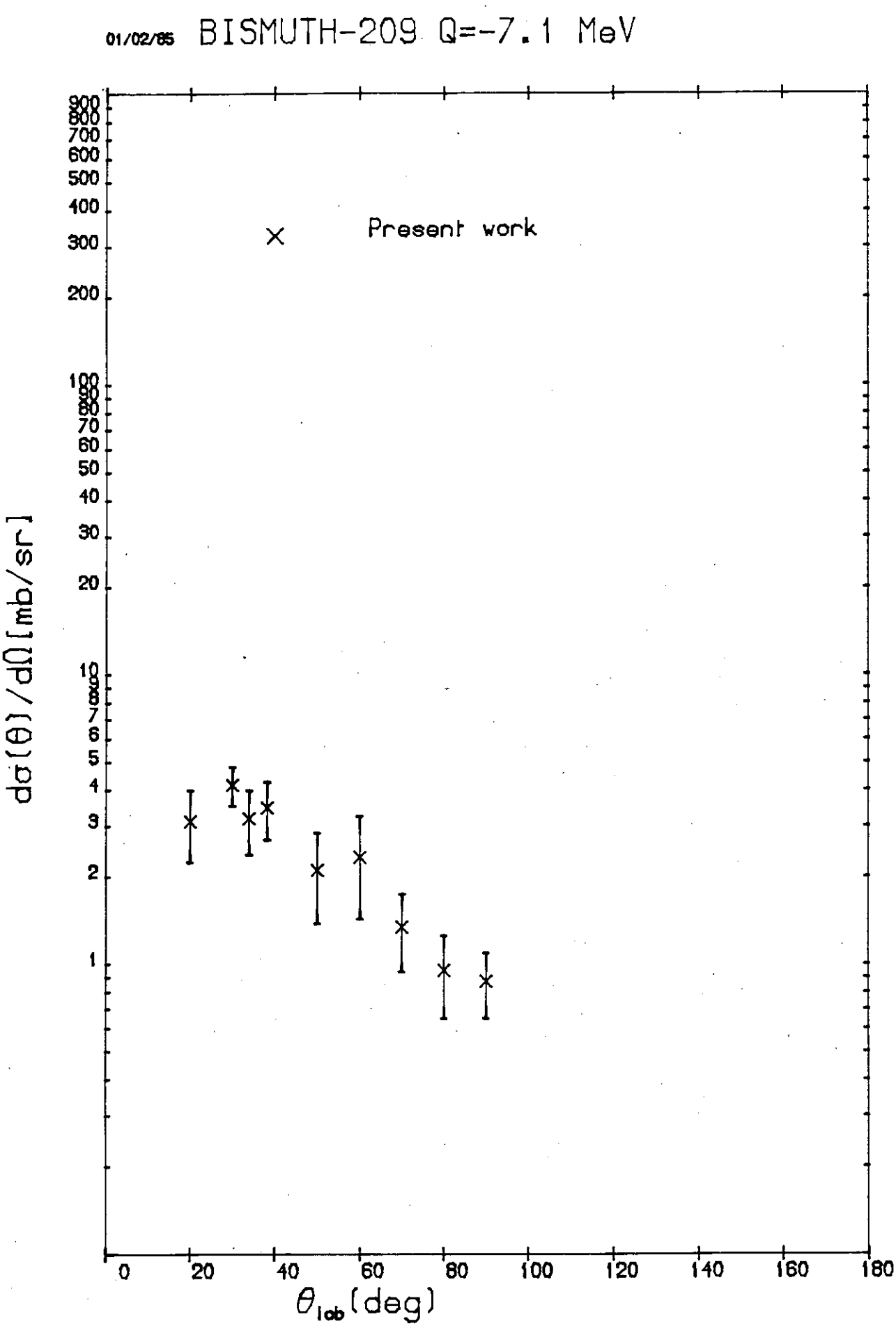
01/02/85 BISMUTH-209 Q=-7.1 MeV
Present work
dσ(θ)/dΩ[mb/sr]
θlab(deg)
900
800
700
600
500
400
300
200
100
90
80
70
60
50
40
30
20
10
8
7
6
5
4
3
2
1
0
20
40
60
80
100
120
140
160
180

Figure 5.29.

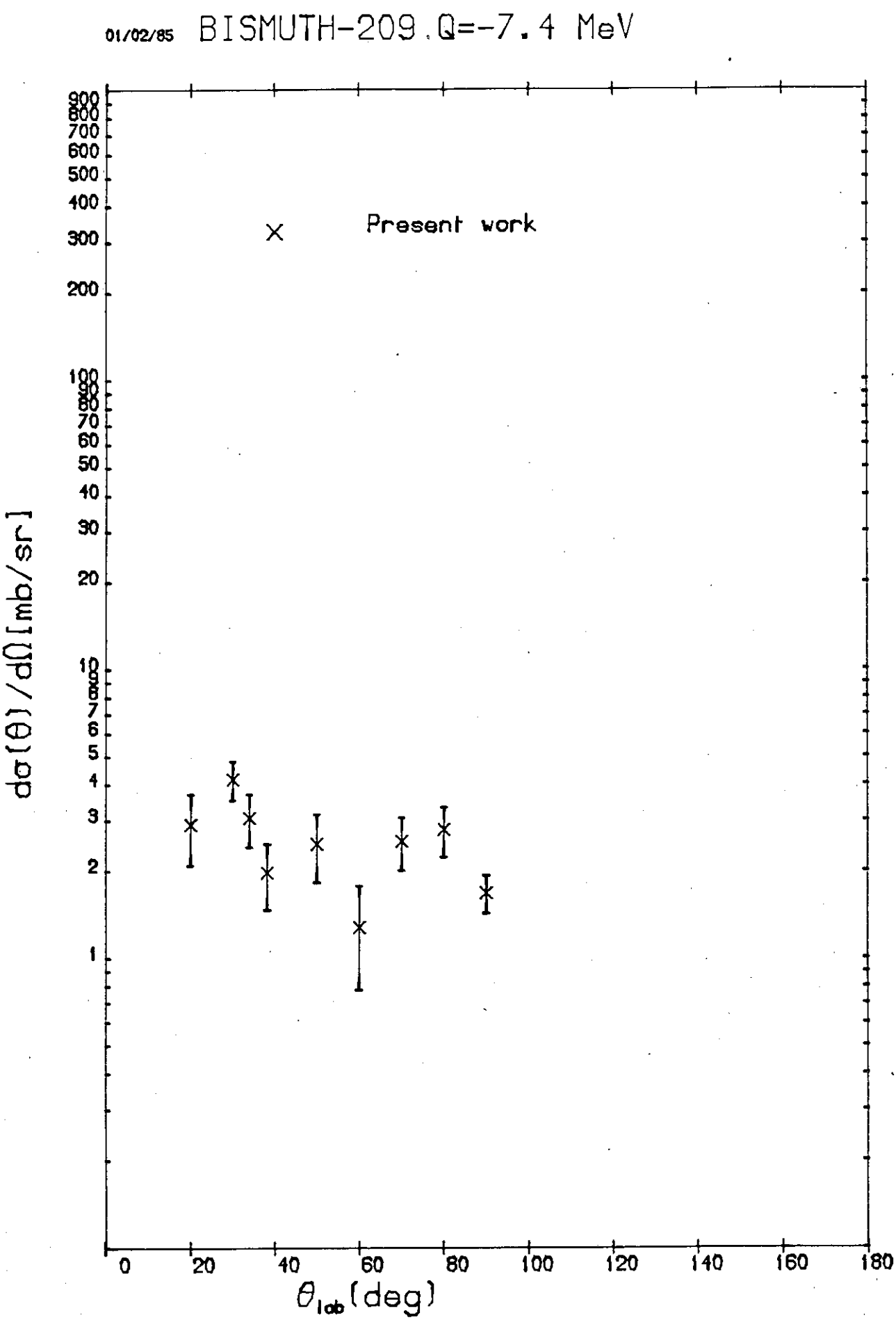
01/02/85 BISMUTH-209.Q=-7.4 MeV
Present work
dσ(θ)/dΩ[mb/sr]
θlab(deg)
0
20
40
60
80
100
120
140
160
180

Figure 5.30.

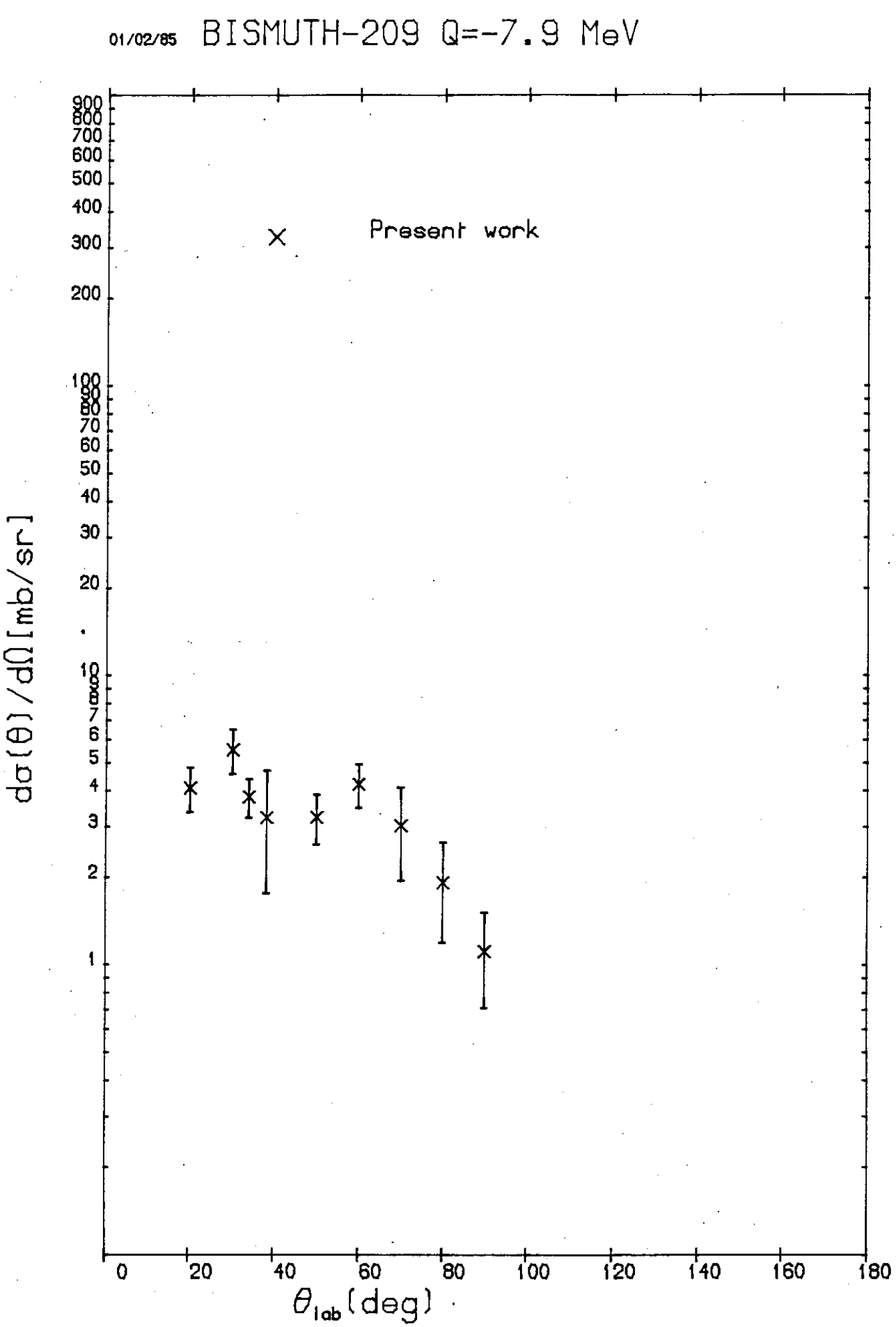
01/02/85 BISMUTH-209 Q=-7.9 MeV
Present work
dσ(θ)/dΩ[mb/sr]
θlab(deg)
900
800
700
600
500
400
300
200
100
90
80
70
60
50
40
30
20
10
8
7
6
5
4
3
2
1
0
20
40
60
80
100
120
140
160
180

Figure 5.31.

CHAPTER 6

SCATTERING MODEL CALCULATIONS

6.1 Introduction

The scattering of particles as a means to probe the structure of a target has been customary experimental practice since the early days of electron diffraction experiments in the 1920's. The experiments on nucleon scattering off nuclei in the early fifties were motivated along similar lines although in this case a curious feature, namely the broad resonances in the neutron scattering data[4], started off a new field of research - that is the use of the optical model to describe the scattering of the incident nucleon. Historically, the concept of the optical model was initiated by Bethe[118]. Fernberg et al. and later Feshbach et al. developed it to include an imaginary potential to explain absorption.

The absorption of light waves was explained by using a complex refractive index. Similarly an imaginary potential, in conjunction with a real potential, was needed to predict these broad scattering resonances[6,119,120].

Better resolution and an increase in the energy of the incident projectile, from the keV to MeV regions, made the scattering data look more promising of explanation by this model by the middle fifties and consequently the concept of the optical potential went through a gradual process of refinement. Attempts were being made to understand a complex many body scattering problem in terms of a one body potential, namely the optical potential. To be able to express a many body interaction in terms of an equivalent one body potential is appealing, not only

for its theoretical elegance but also because it provides a reasonably reliable and simple method of relating experimental data to theory. By 1964[121] it was established without doubt that the phenomenological optical potential needed three nuclear components, the real central, imaginary and the spin orbit potential, the last term arising from the coupling between the spin and the orbital angular momentum of the incident particle.

In 1968 Greenlees, Pyle and Tang, (GPT)[122] motivated by the work of Drell[123] suggested a microscopic model. The GPT model was used to analyse scattering data. Since 1968 the phenomenological and many body interaction approaches to the optical model have achieved a great deal of success. Calculations of various degrees of complexity for the potential from a many body point of view have been successfully made. To date the majority of neutron scattering data analyses have been made, using an optical model in which neutron cross sections and polarizations are calculated after solution of a time independent Schrödinger equation into which a complex interaction potential, the optical potential (OP), has been inserted. The real part is responsible mainly for direct or shape elastic scattering (Chapter 1) and the imaginary part accounts for all other processes where the incident neutron is absorbed to form a compound nucleus.

6.2 The Spherical Optical Model

It is convenient to write the complex spherical optical potential as the sum of real and imaginary parts, and to express each part as the product of a depth and a radial form factor:

$$U(r) = V f(r) + iWg(r) + V_{so} h(r) L\cdot\sigma \qquad (6.1)$$

The form factors f(r) and g(r) are chosen to have a maximum value of unity so that V and W are the depth of the real and imaginary parts of the potential. f(r) and h(r) form factors were introduced in Chapter 1 as Woods-Saxon and Thomas Fermi respectively:

$$f(r) = \{1 + \exp[(r - r_R A^{1/3})/a_R]\}^{-1} \tag{6.2}$$

and

$$h(r) = \left(\frac{\hbar}{m_\pi c}\right)^2 \cdot \frac{1}{r} \cdot \frac{d}{dr} \{1 + \exp[(r - r_s A^{1/3})a_s]\}^{-1} \tag{6.3}$$

The imaginary factor g(r), is usually given a surface peaked form. It is believed[124] that at low energy the absorption of the incoming nucleon occurs at the surface of the target nucleus. Convenient and widely used forms are the derivative Woods-Saxon and Gaussian radial dependence. The former will be used in the analysis presented here. It is

$$g(r) = 4a_I \frac{d}{dr} \{1 + \exp[(r - r_I A^{1/3}/a_I]\}^{-1} . \tag{6.4}$$

Solution of the Schrödinger equation with the potential given in (6.1) leads to the elements of the scattering matrix (S matrix) and from these elements the shape elastic, the total, integrated elastic, integrated absorption, differential shape elastic cross sections and differential polarizations can be calculated. In the energy domain of the present work both elastic and inelastic scattering occur through the direct nuclear reaction of the incident neutron with the target nucleus. The elastic scattering is therefore described by the spherical optical model, while the direct inelastic process is described using a deformed optical potential in the distorted wave Born Approximation (DWBA) calculations.

6.3 The Distorted Wave Theory of the Direct Excitation of Collective States - Extension to the Spherical Optical Model (O.M.)

The theoretical model with whose predictions the present measurements are compared is based upon the collective model of nuclear structure. The excitation of low lying collective nuclear states by a direct nuclear interaction has been known to be an important process in the scattering of medium energy alpha particles and proton scattering[24]. This process is also important for neutrons. It is known that fast neutrons can also strongly excite these collective states[25].

The collective nuclear model first proposed by Aage Bohr in 1952[125] has been found to be successful in accounting for the excited energy levels due to the collective motion of the nuclear surface. The collective nuclear model description has a wide range of validity. Such a description has been shown to be in good agreement with experiment for the excitation of quadrupole and octupole vibrations in even nuclei by the inelastic scattering of alpha particles and protons, and has been extended to "core excitation" in odd nuclei. The theory is based upon a natural extension of the optical model to include non-spherical potentials, or the coupling of odd nucleon to core vibrations in nuclei whose average shape is spherical. In a perturbation treatment the non-spherical parts of the potential are taken to induce inelastic scattering to these collective vibrational or rotational states. This is calculated in the Distorted Wave Born Approximation (DWBA), the spherical part of the potential giving rise to the elastic scattering described by the distorted waves. The parameters of this potential can then be determined by optical model analysis of the observed elastic

scattering; all that remains is the strength (or deformation) of the non-spherical part to be obtained by comparison with the experimental inelastic cross section.

The detailed formalism of the DWBA has been described elsewhere[22,126], so only the important features of this theory will be mentioned here.

The DWBA theory of the inelastic scattering $A(a, a')A'$ is based upon a transition amplitude of the form:

$$T_{fi} = \int dr\ \chi^{(-)*}(K_f,r)\ \langle A'|V|A\rangle\ \chi^{(+)}(K_i,r) \qquad (6.5)$$

in which K_i and K_f are the initial and final momentum of the scattering particle. In the scattering process the target nucleus is excited from state A to state A'. The differential cross section is proportional to $|T_{fi}|^2$, suitably averaged over the orientations of the nuclear and projectile spins. The functions $\chi^{(-)}(K_i,r)$ and $\chi^{(+)}(K_i,r)$ are the distorted waves which describe the relative motion (including the elastic scattering of the pair) before and after the inelastic collision. The superscript $(+)$ or $(-)$ denotes the usual outgoing or ingoing wave boundary conditions. The remaining factor in (6.5) is the matrix element of the interaction causing the inelastic event. It can be written as the product of a radial function and a spherical harmonic,

$$\langle A'|V|A\rangle = f_\ell(r)\ Y_\ell^m(\theta, \phi) \qquad (6.6)$$

where (r, θ, ϕ) are the coordinates of the projectile and ℓ, the angular momentum transfer between initial and final states. In equation (6.6), ℓ is determined by the spin of the state excited and the spin of the ground state (for odd nuclei), but the nuclear model chosen determines the radial shape $f_\ell(r)$ of the interaction. The deformed potential

model used here assumes that the potential strength depends only on the distance $(r - R)$ from the nuclear surface, the commonly used Woods-Saxon potential is of this form. The surface is then allowed to be non-spherical

$$R(\theta,\phi) = R_o\left[1 + \sum_{\ell m} \alpha_{\ell m} Y_\ell^m (\theta, \phi)\right] . \qquad (6.7)$$

The interaction V is then obtained by using equation (6.7) and expanding the optical potential to first order in $\alpha_{\ell m}$, the deformation parameter,

$$U(r-R) = U(r-R_o) - R_o\left[\sum_{\ell m} \alpha_{\ell m} Y_\ell^m(\theta, \phi)\right] \frac{d}{dr} U(r-R_o) \ \ldots \ (6.8)$$

The first term can be identified with the spherical optical potential needed to describe the observed elastic scattering, while the second term is the potential used in equations (6.5) and (6.6).

The distorted wave theory as just described briefly is then a first-order theory in two senses. The interaction (6.8) is expanded only to first order in the deformation parameters α and the transition amplitude (6.5) is itself only first order in V, and thus α. It has been demonstrated that this is a good approximation even for quite large deformation[25]. The validity of the DWBA for inelastic scattering from nuclei has been discussed by Perey and Satchler [127].

6.4 Optical Model Analysis

6.4.1 Analysis of the elastic scattering data.

The elastic scattering data were analysed by the optical model theory. The potential used was identical to that of (6.1), the real

part of the potential used a Woods-Saxon form factor (6.2), a surface peaked form factor was used for the imaginary potential (6.4) and a Thomas-Fermi form factor for spin orbit term (6.3),

$$U(r) = -V(e^{X}+1)^{-1} + 4a_I \cdot iW \frac{d}{dX'}(e^{X'}+1)^{-1} + \ell\cdot\sigma \left(\frac{\hbar}{m_\pi c}\right)^2 V_{so} \cdot \frac{1}{r}\frac{d}{dX}(e^{X}+1)^{-1} \qquad (6.90)$$

where: $X = (r - r_R A^{1/3})/a_R$ and $X' = (r - r_I A^{1/3})/a_I$. (6.10)

No attempt was made to search for a new set of parameters. 4 sets of published optical model parameters were used for the analysis of the elastic scattering data (Table 6.1). Parameter set 1 is the averaged parameters used by Stelson et al.[25] to analyse scattering of neutrons by a wide range of nuclear mass. Potential parameter set 2 is taken from an evaluation of neutron and gamma production cross section data for lead by Fu and Perey[128]. Parameters in set 3 are taken from an evaluation of neutron data for Bismuth reported in 1982 by Bersillon et al.[129]. While this work was being completed a new set of optical model parameters for lead in the energy range of 7 to 50 MeV became available by Finlay et al.[130]. These parameters are also tabulated in Table (6.1) as set 4.

In the choice of OM parameters extracted from elastic scattering data some care should be taken to avoid using parameters based on data contaminated with inelastic neutrons. Data on nuclei which have the smallest quadrupole excitation energy and therefore the most difficult to resolve experimentally have the largest distortion and hence the largest cross section for inelastic scattering.

TABLE 6.1 Optical Model Parameters used for Elastic and Inelastic Scattering Data Analysis.

	V_o (MeV)	r_R (fm)	a_R (fm)	W_D (MeV)	r_I (fm)	a_I (fm)	W_V (MeV)	r_V (fm)	a_V (fm)	V_{SO} (MeV)	r_{so} (fm)	a_{so} (fm)
Set 1 (Stelson et al.)	44.0	1.25	0.65	9.60	1.25	0.47	0.0	0.0	0.0	6.0	1.25	0.65
Set 2 (Fu & Perey)	43.50	1.25	0.65	9.56	1.25	0.47	0.0	0.0	0.0	6.0	1.25	0.65
Set 3 (Bersillon et al.)	42.34	1.265	0.65	6.26	1.235	0.50	1.12	1.235	0.5	5.5	1.08	0.60
Set 4 (Finlay et al.)	44.75	1.25	0.685	5.91	1.283	0.569	0.50	1.283	0.569	5.75	1.105	0.499

Finlay et al., ref. (130)

$V_V = 49.13 - 0.31E$
$r_R = 1.205$
$a_R = 0.685$

$W_V = -2.03+0.18E, \quad E > 11.20$
$r_I = 1.283$
$a_I = 0.569$

$V_{SO} = 5.75 \quad E < 50.0$
$r_{so} = 1.105$
$a_{so} = 0.499$

$W_D = 6.36-0.47(10.71-E), \quad 7.0 \leq E \leq 10.71$
$= 6.36-0.13(E-10.71), \quad 10.71 < E < 50.0$

Bersillon et al., ref. (129)

	r(fm)	a(fm)
$V = 45.45 - 0.22E$	1.265	0.65
$W = 2.2+ 0.47E \ (E \leq 10 \text{ MeV})$ $6.9-0.045E \ (E > 10 \text{ MeV})$	1.235	0.5
$W_V = 0.08E$	1.235	0.5
$V_{SO} = 5.5$	1.08	0.6

It seemed that Stelson et al.[25] have been conscious of the problem of the inelastic contamination when they proposed their average optical model potential parameters.

Figs. (6.1) - (6.4) present the comparison between the data and the optical model calculations of the angular distribution, using parameters of set 1 to set 4 respectively. The agreement between the calculations and the experiment are equally good for three sets of parameters (set 1, set 2, and set 4).

There is, however, a marked disagreement between the predicted cross section angular distribution by Bersillon et al.[129] parameters and the experimental data. These parameters produce angular distribution which is higher than the data over the whole angular range. Fig. (6.3) shows the extent to which the predicted angular distribution by Fu and Perey parameters (set 2) and that of Bersillon et al. differ.

The major difference between Finlay et al.'s optical model parameters and Stelson et al.'s parameters, as can be seen in Table 6.1, is the magnitude of the surface peaked Woods-Saxon imaginary potentials, although the Finlay et al. parameters have also an additional small volume type potential. These differences seem to have influenced the cross section angular distribution at only 25 degrees and beyond around 110 degrees.

6.4.2 Analysis of the inelastic scattering data.

The comparison made between the elastic scattering data of the present work and the optical model (OM) calculations based on the parameters of Table (6.1) in the previous section, showed that the Stelson et al. parameters and the Finlay et al. parameters are well

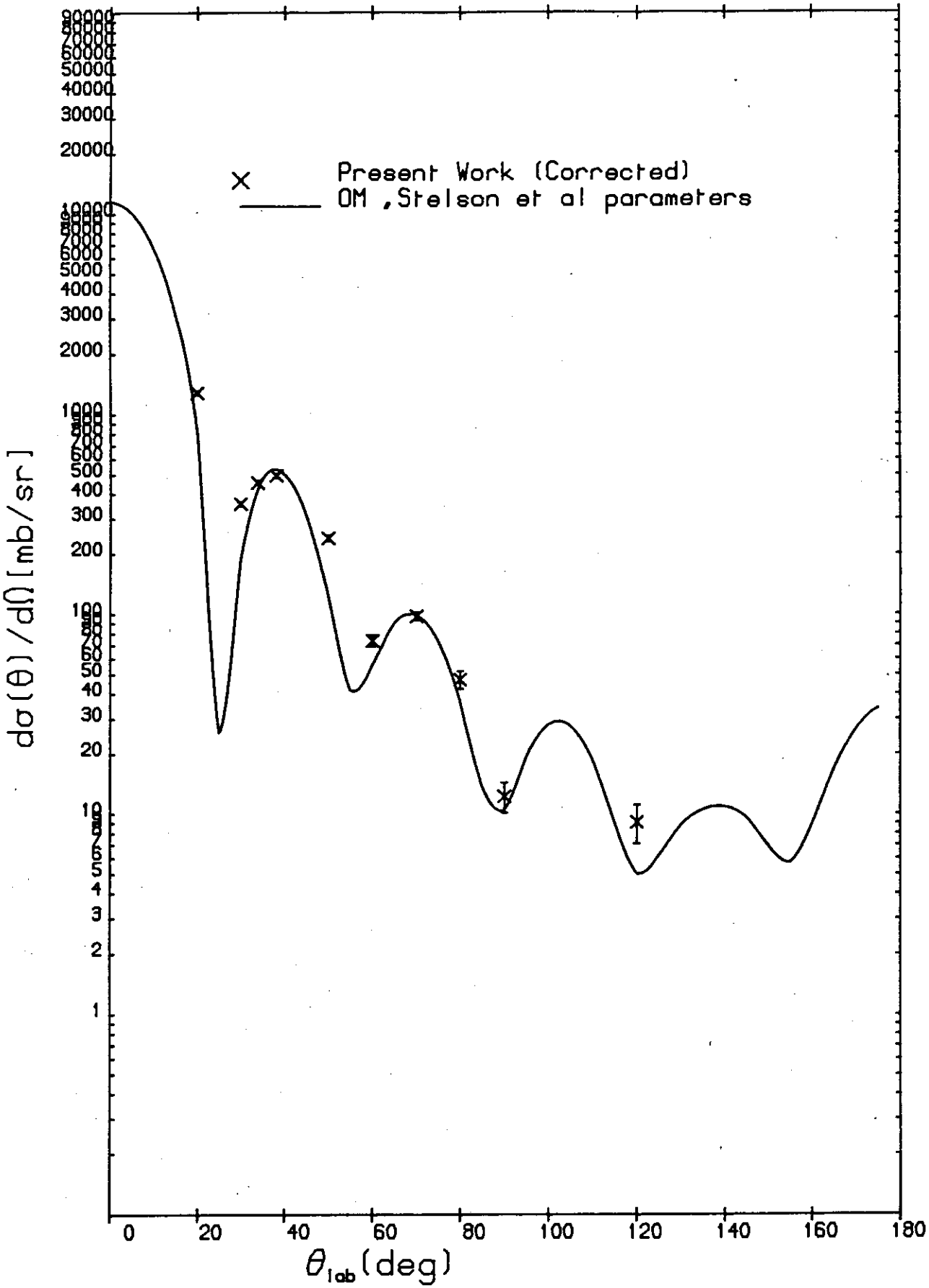
14/02/85 BISMUTH-209 Diff. Elastic
Present Work (Corrected)
OM , Stelson et al parameters
dσ(θ)/dΩ [mb/sr]
θlab (deg)
0
20
40
60
80
100
120
140
160
180

Figure 6.1.

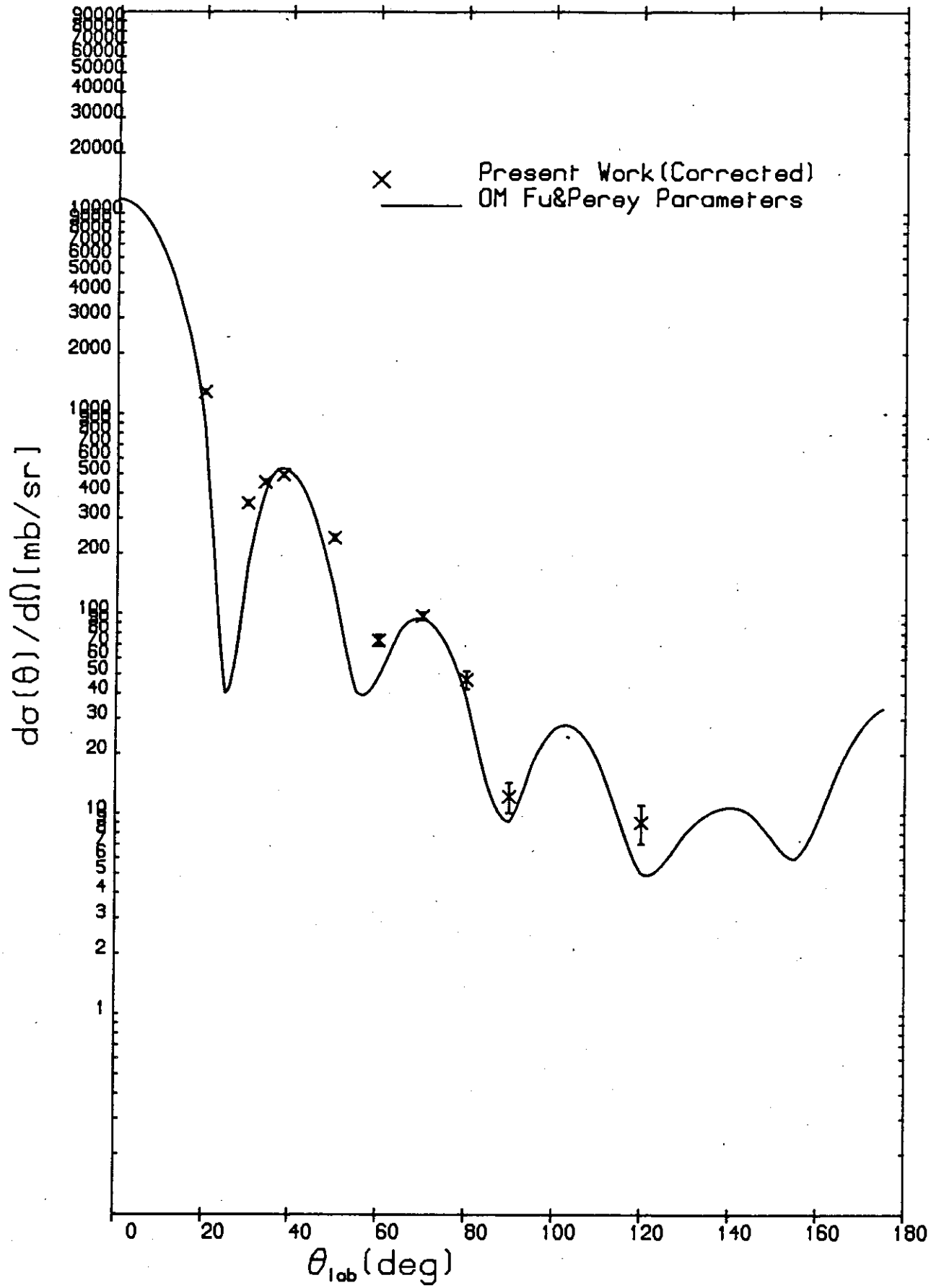
14/02/85 BISMUTH-209 Diff. Elastic
Present Work(Corrected)
OM Fu&Perey Parameters
dσ(θ)/dΩ[mb/sr]
θlab(deg)
0
20
40
60
80
100
120
140
160
180

Figure 6.2.

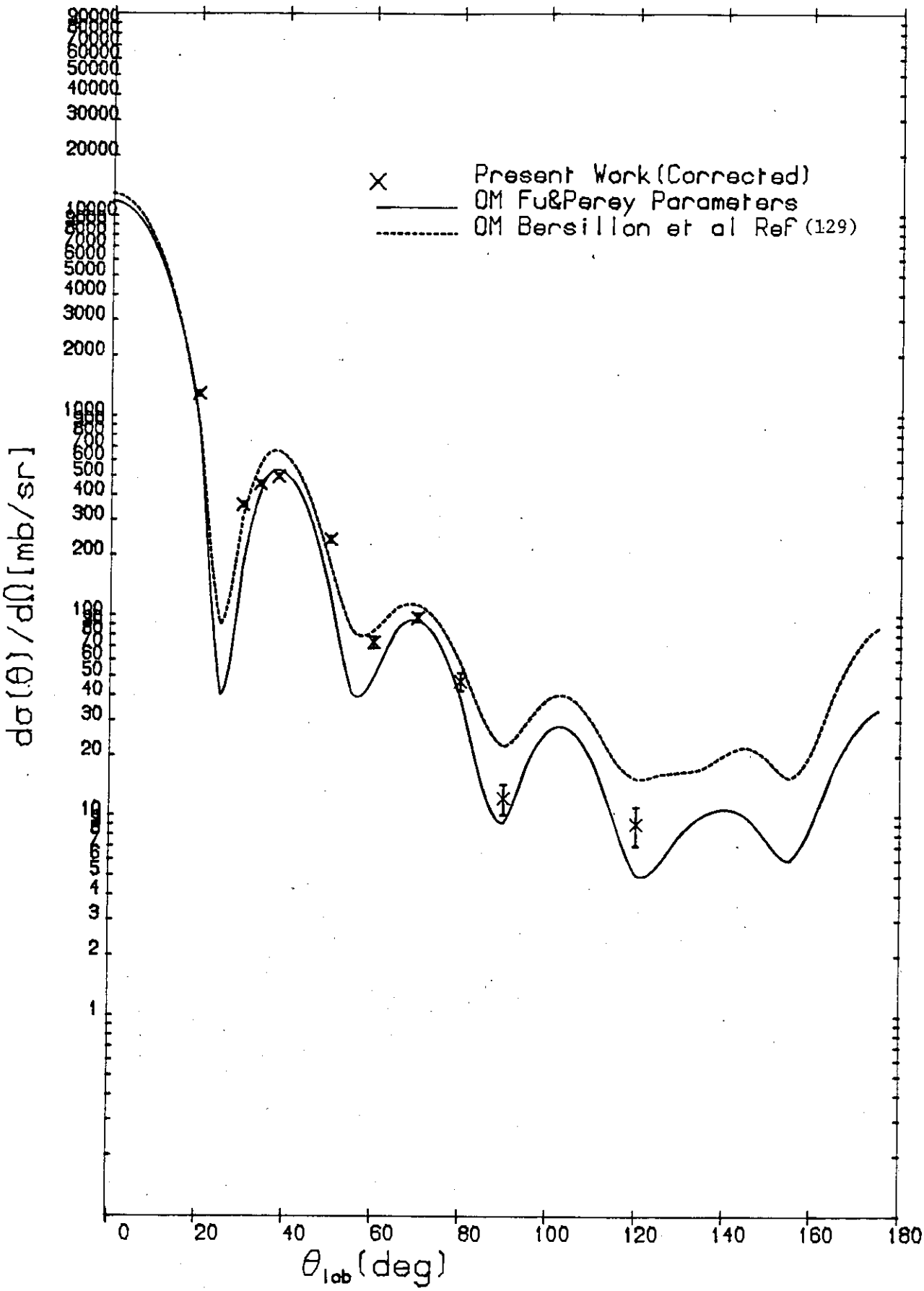
29/01/85 BISMUTH-209 Diff. Elastic
Present Work(Corrected)
OM Fu&Perey Parameters
OM Bersillon et al Ref(129)
dσ(θ)/dΩ[mb/sr]
θlab(deg)

Figure 6.3.

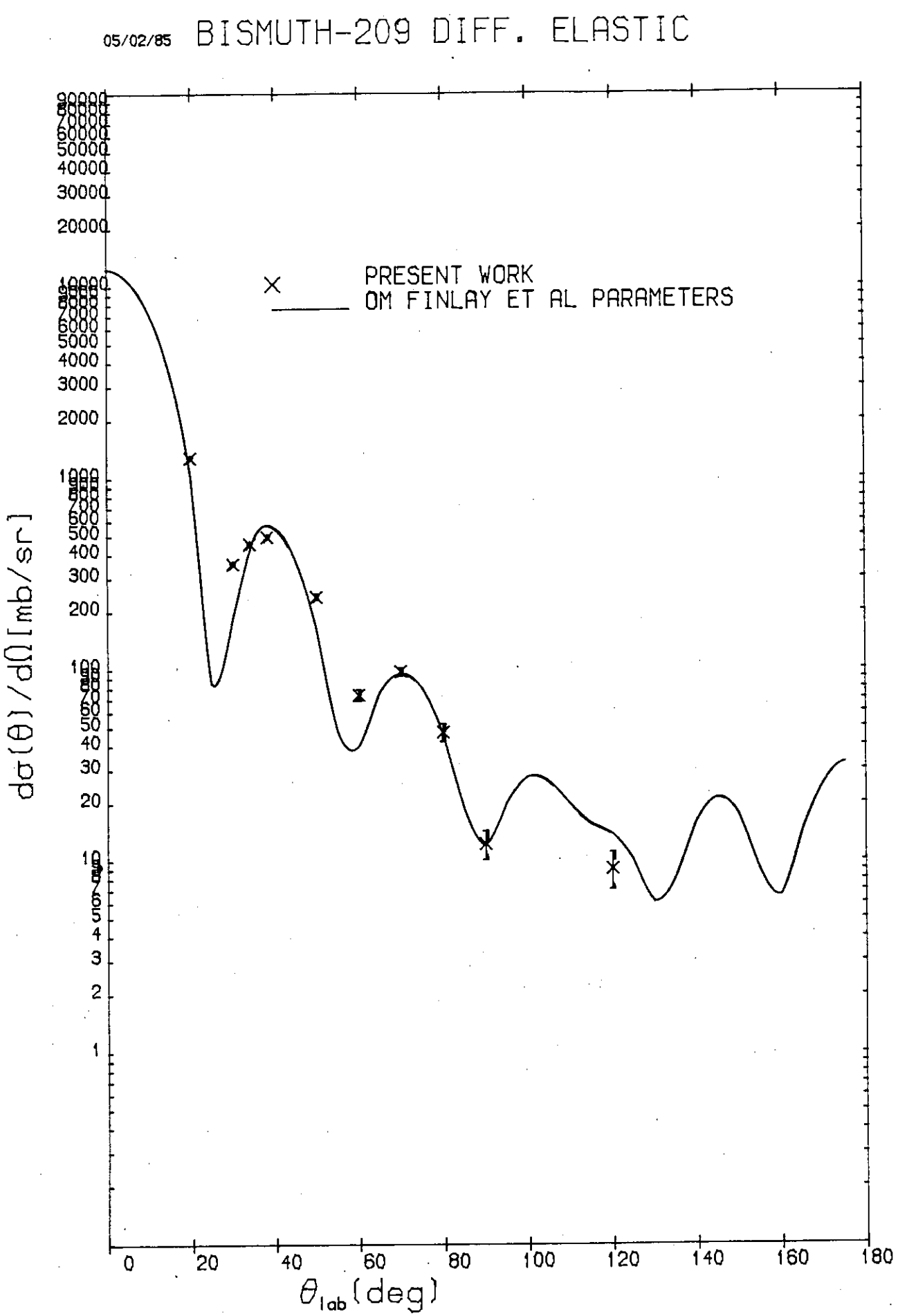
05/02/85 BISMUTH-209 DIFF. ELASTIC
PRESENT WORK
OM FINLAY ET AL PARAMETERS
dσ(θ)/dΩ[mb/sr]
θlab(deg)
0
20
40
60
80
100
120
140
160
180

Figure 6.4.

supported by our data.

Using these two sets of parameters, macroscopic collective model calculations were performed with the Distorted Wave Born Approximation (DWBA) Code DWUCK-4[35]. In the DWBA method the optical optential is made non-spherical to account for the collective motions (rotations or vibrations) of the nucleus. The non-spherical part of the potential induces inelastic events.

The shape of the inelastic angular distribution calculated by the DWBA method is determined by the angular momentum transfer ℓ. The magnitude of the cross section is proportional to β_ℓ^2, the deformation parameter, and can be found by normalizing the calculated curve to the experimental data points. The deformation parameter β_ℓ was calculated as follows:

$$\beta_\ell = \frac{1}{n} \sum_{i=1}^{n} \left[\frac{\sigma_{exp}(\theta_i)}{\sigma_{DWUCK}(\theta_i)} \right]^{\frac{1}{2}} \qquad (6.11)$$

where n is the number of experimental data points.

The vibrational excitation of the odd nucleus $^{209}_{83}Bi$ is interpreted as a coupling of the $h_{9/2}$ proton to the excited core of $^{208}_{82}Pb$[31,3]. The cross section of the resulting multiplet, not resolvable in neutron experiments, is then equal to that for the analogous collective excitation of $^{208}_{82}Pb$, enabling a comparison of β-values.

In order to establish the spin of each excited state where it is not known, the data were compared with seven different ℓ values ($\ell = 1$ to $\ell = 7$) angular distributions resulting from distorted wave calculations. A quantitative measure of the goodness of fit was then provided by χ^2 defined as:

$$\chi^2 = \sum_{i=1}^{n} \left[\frac{\sigma_{th}(\theta_i) - \sigma_{exp}(\theta_i)}{\Delta\sigma_{exp}(\theta_i)} \right]^2 \quad . \qquad (6.12)$$

6.4.3 Discussion of individual excitation levels

Q = -2.6 MeV

The excited state at 2.61 MeV in ^{208}Pb is reported as being a highly collective state[110]. The excitation at 2.6 MeV energy group has been taken by Stelson et al.[25] and Kuijper et al.[30] to be an $\ell = 3$ excitation. For pure $\ell = 3$ and $\ell = 5$ Figs. (6.5) and (6.6) show that the agreement between DWBA prediction and all the available data for 2.6 MeV excitation is only good for approximately the 40°-70° angular range. For angles smaller than $\sim 40^{\circ}$ the cross section for this level is underestimated and for angles beyond 70° the calculated cross section tends to be higher than the measurements reported by Stelson et al., Matoba et al. and the data of this work. Stelson et al. prediction of pure $\ell = 3$ for 2.6 MeV excitation is not decisive because, due to having too few data points, they could not observe the discrepancies between calculation and measurements at forward angles ($\theta < \sim 40$) and also for the same reason at backward angles. In addition, their deformation parameter produced in their publication for $\ell = 3$ appears to differ from our calculation by 40%.

Matoba et al. have interpreted the excitation group at 2.6 MeV as being due to the excitations of 2.615 MeV state ($\ell = 3^-$, $\beta_3 = 0.110$) and 3.198 MeV state ($\ell = 5^-$, $\beta_5 = 0.060$) in ^{208}Pb. However, in our experiment, both such states ought to be separated on grounds of better energy resolution. In addition, as a result of the small deformation of the state at 3.198 MeV ($\beta_5 = 0.060$) obtained by proton inelastic scattering

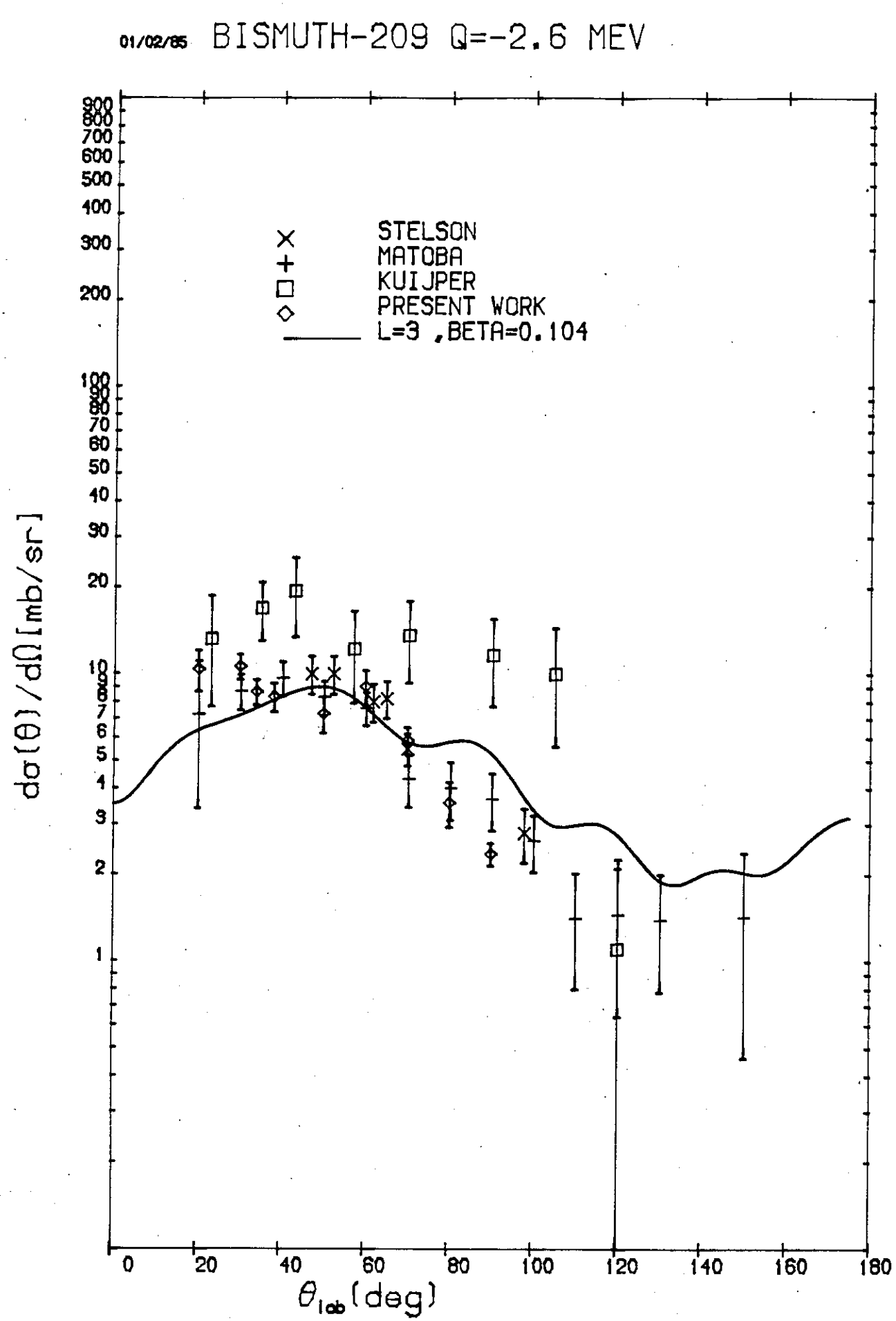
01/02/85 BISMUTH-209 Q=-2.6 MEV
STELSON
MATOBA
KUIJPER
PRESENT WORK
L=3 ,BETA=0.104
dσ(θ)/dΩ[mb/sr]
θlab(deg)
0
20
40
60
80
100
120
140
160
180

Figure 6.5.

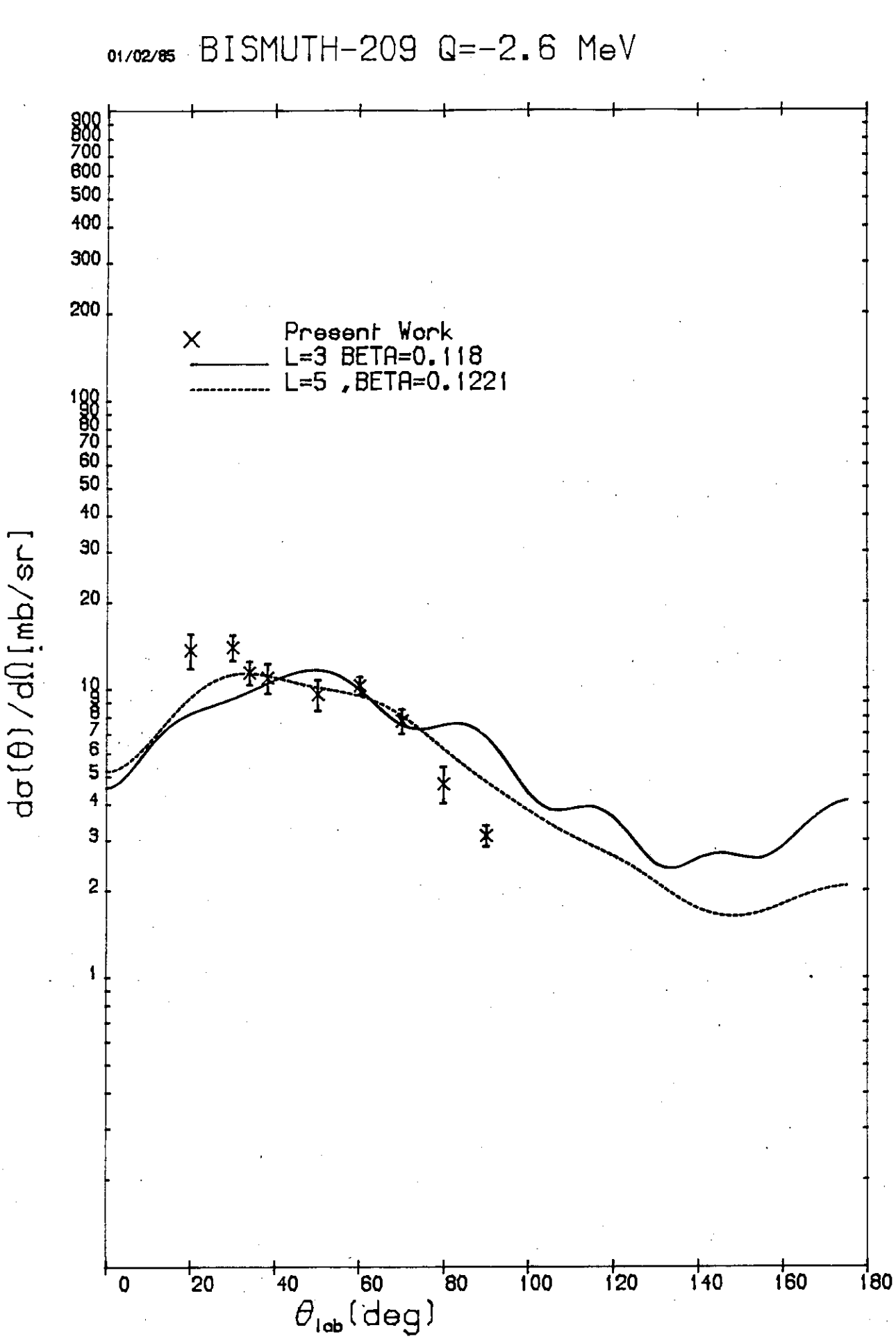
01/02/85 BISMUTH-209 Q=-2.6 MeV
Present Work
L=3 BETA=0.118
L=5 ,BETA=0.1221
dσ(θ)/dΩ[mb/sr]
θlab(deg)

Figure 6.6.

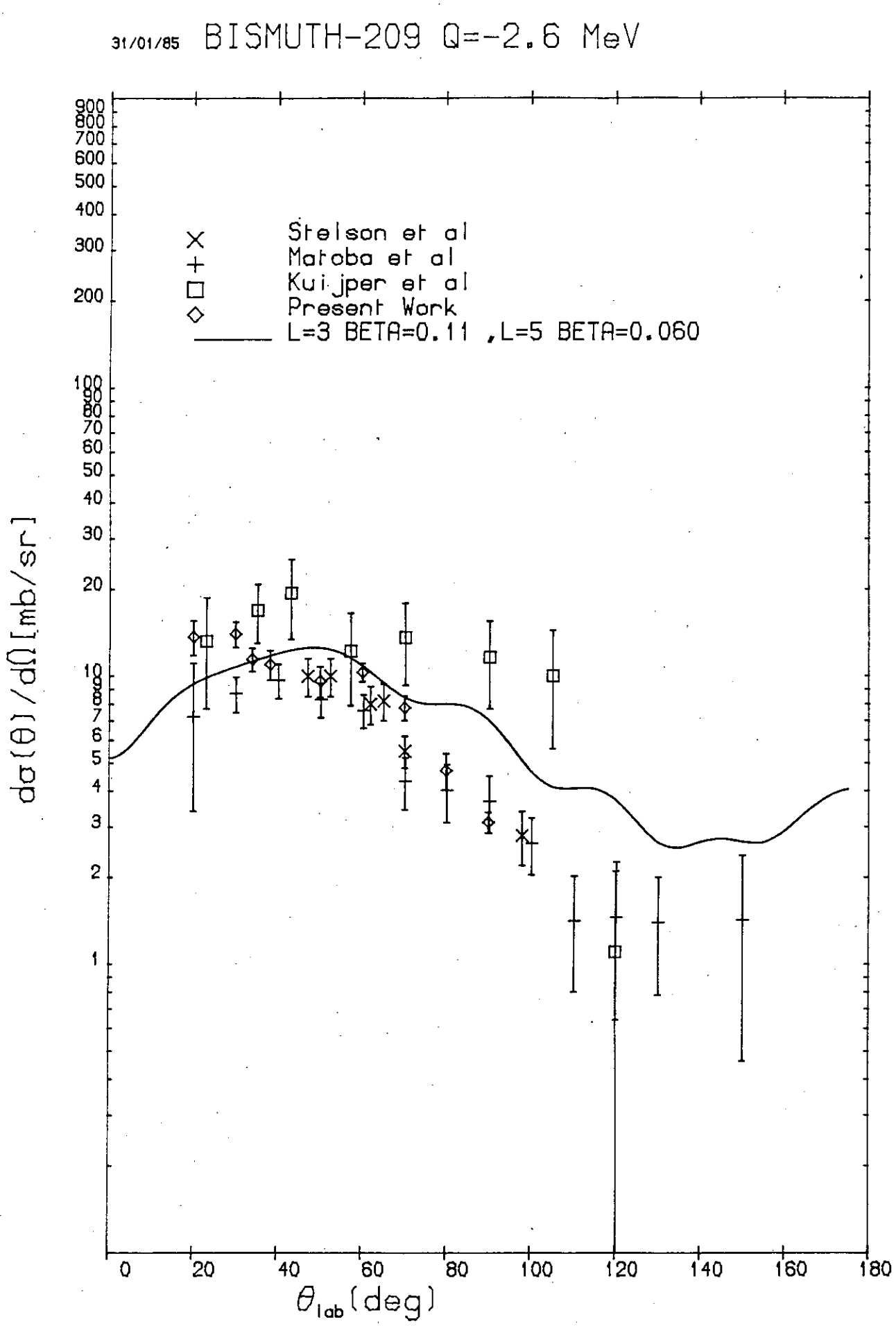
31/01/85 BISMUTH-209 Q=-2.6 MeV
Stelson et al
Matoba et al
Kuijper et al
Present Work
L=3 BETA=0.11 ,L=5 BETA=0.060
dσ(θ)/dΩ[mb/sr]
θlab(deg)

Figure 6.7.

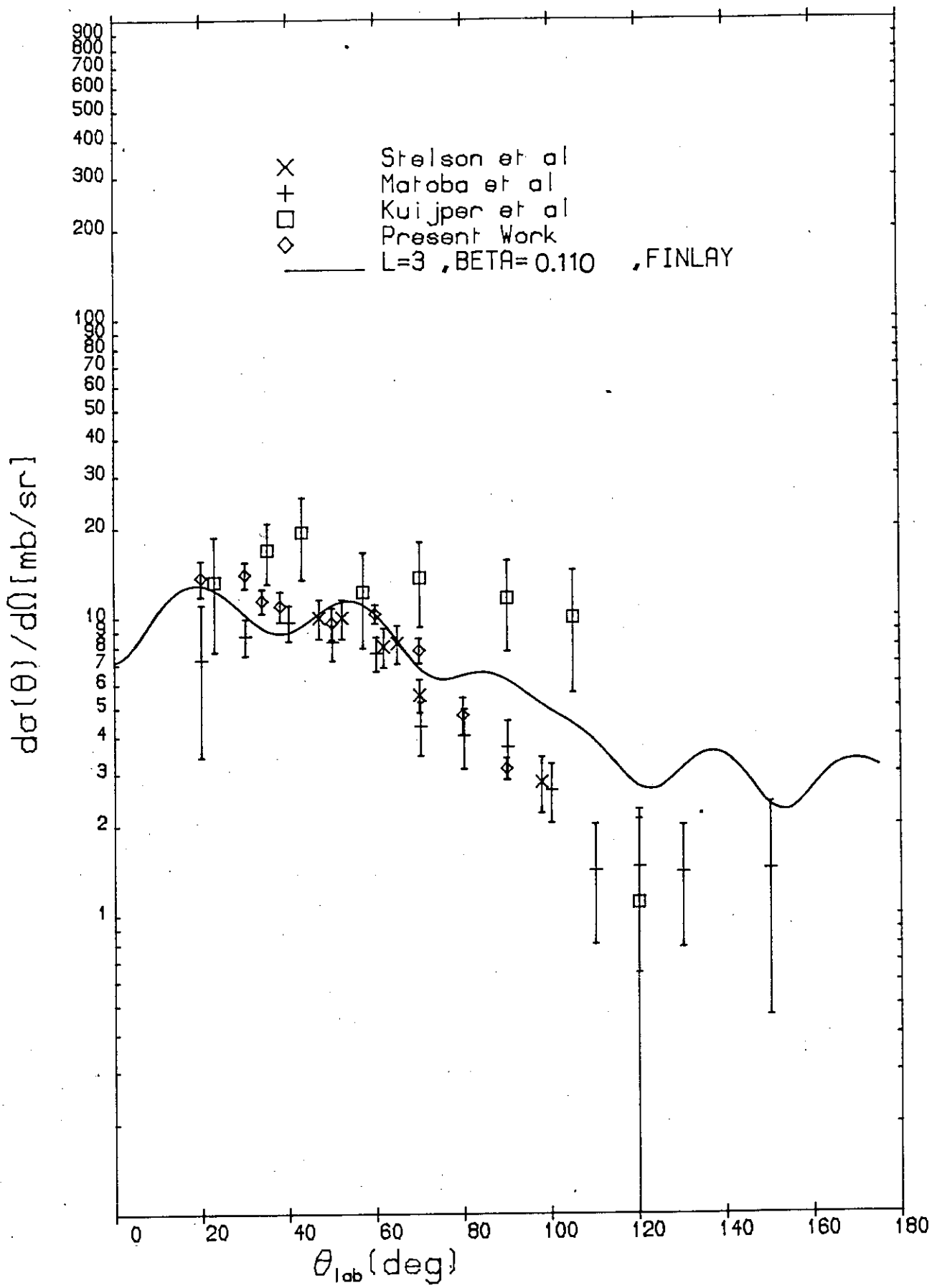
05/02/85 BISMUTH-209 Q=-2.6 MeV
Stelson et al
Matoba et al
Kuijper et al
Present Work
L=3 ,BETA= 0.110 ,FINLAY
dσ(θ)/dΩ[mb/sr]
θlab(deg)

Figure 6.8.

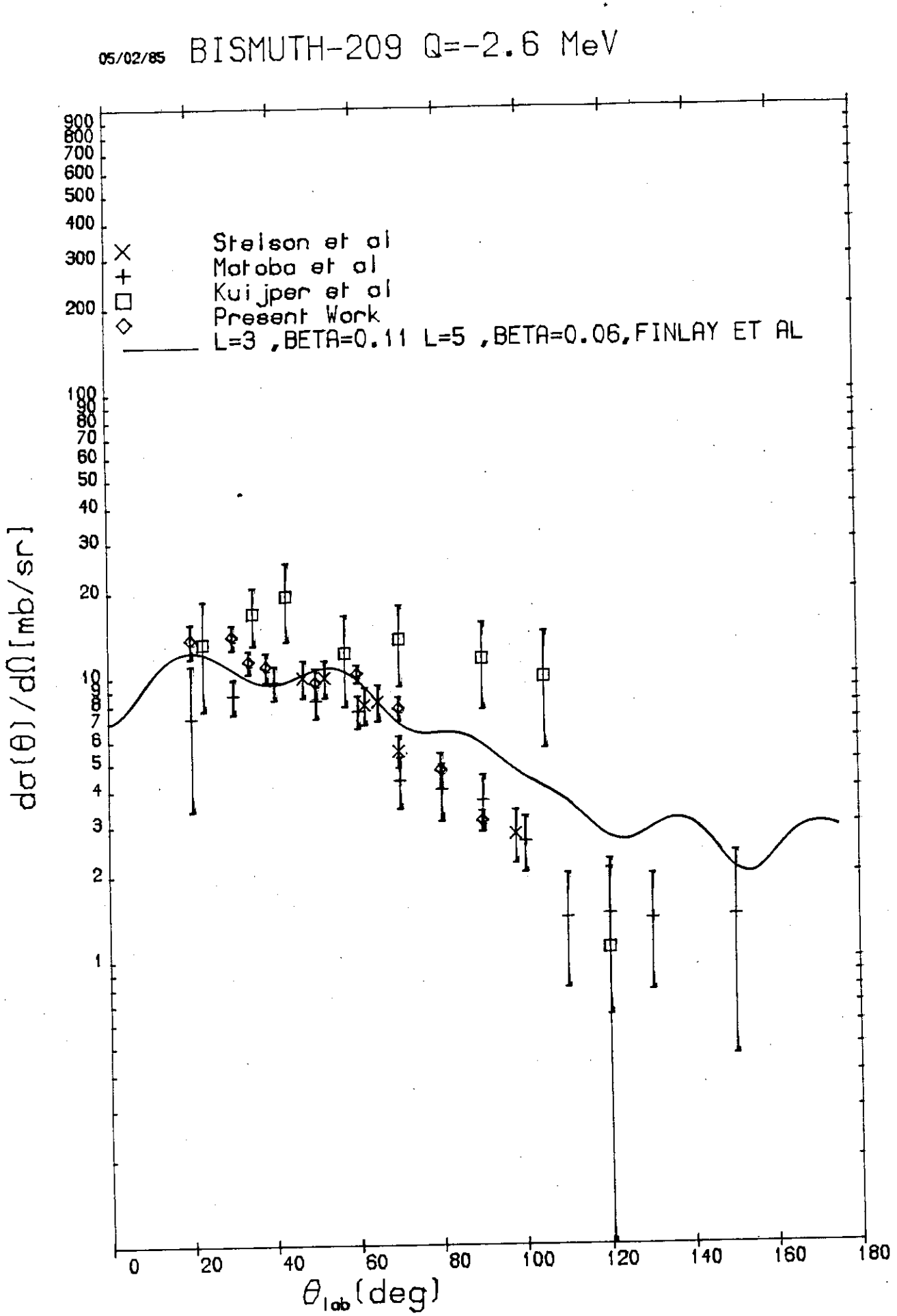
05/02/85 BISMUTH-209 Q=-2.6 MeV
Stelson et al
Matoba et al
Kuijper et al
Present Work
L=3 ,BETA=0.11 L=5 ,BETA=0.06,FINLAY ET AL
dσ(θ)/dΩ[mb/sr]
θlab(deg)

Figure 6.9

measurement, this state is not expected to make a significant contribution to the inelastic scattering process. To show this, the inelastic angular distribution due to both 2.615 MeV state ($\beta_3 = 0.110$) and 3.198 MeV state ($\beta_5 = 0.060$) was calculated using stelson et al. parameters. The fitting between experiment and theory did not improve, Fig. (6.7). Calculations using Finlay et al.'s optical model parameters with deformations ($\beta_3 = 0.110$) and ($\beta_3 = 0.110 + \beta_5 = 0.060$), Figs. (6.8) and (6.9), showed better agreement between the data and calculations particularly at forward angles. At 80 and 90 degrees the predicted values tend to be higher than the measurements.

The above discussion is strictly valid for the ^{208}Pb core, coupling of the 83rd proton to the ^{208}Pb core results in 7 states with spins from $^{3}/_{2}^{+}$ to $^{15}/_{2}^{+}$ around 2.6 MeV state in ^{209}Bi, which could account for the discrepancy between calculations based on ^{208}Pb core and 3 sets of available data in the backward angle region.

Q = - 3.4 MeV

No previous neutron scattering measurements have been reported for this excited state. This state can be identified with the state at around 3.4 MeV observed in neutron, alpha, and proton inelastic experiments in ^{208}Pb (110). An excitation state with $\tilde{\sim}$ 3.4 MeV energy has also been reported to have been observed in ^{209}Bi, based on the studies of (α, d) stripping reaction on ^{207}Pb, (α, t) reaction on ^{208}Pb, and (n,n'γ) reaction in ^{209}Bi.

The DWBA calculation for the 3.4 MeV energy group was performed with Finlay et al. and Stelson et al. OM parameters for $\ell = 1$ to $\ell = 7$ angular momentum transfer, Figs. (6.10) to (6.12). The present data clearly selects an even ℓ value for this excitation. The χ^2

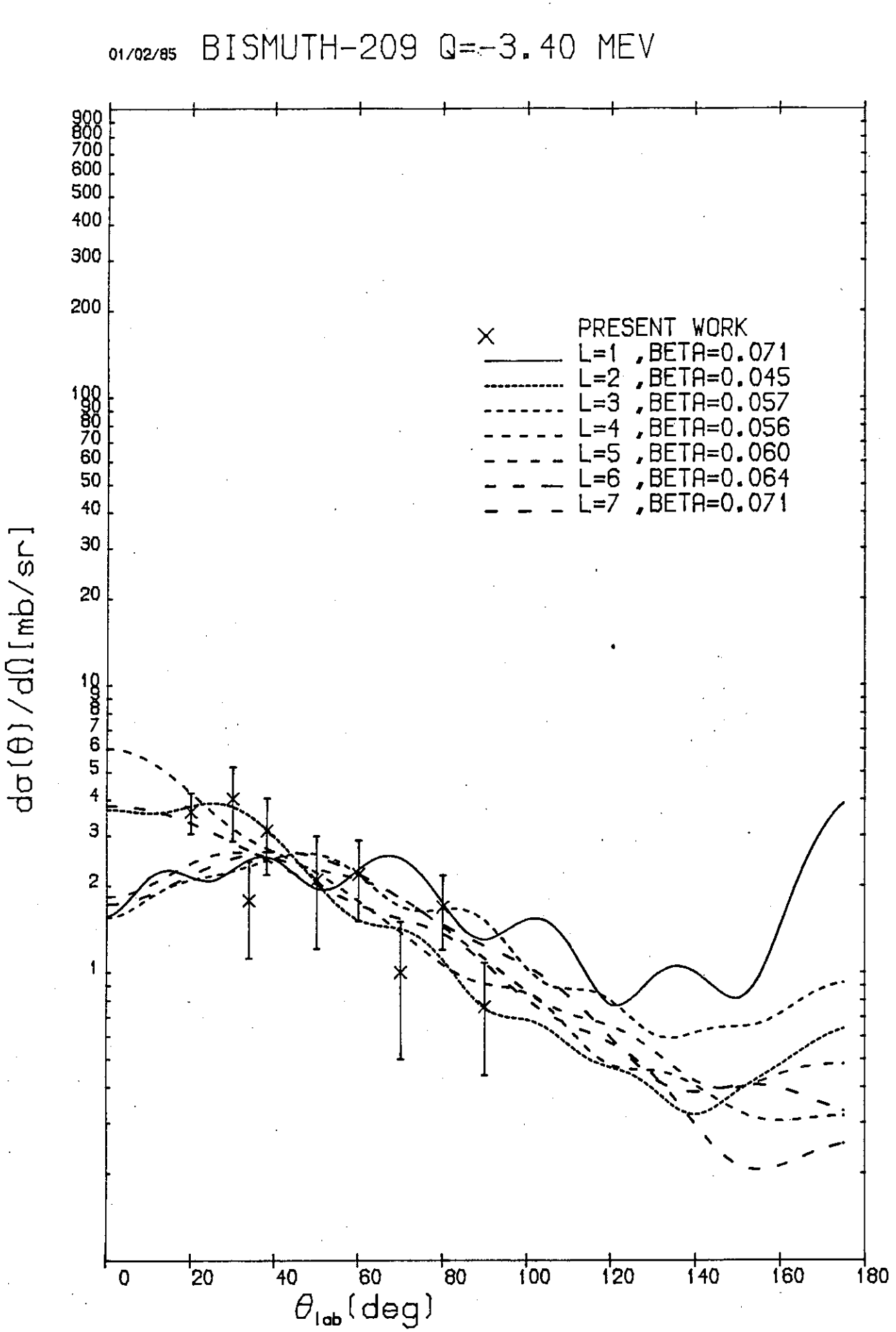
01/02/85 BISMUTH-209 Q=-3.40 MEV
PRESENT WORK
L=1 ,BETA=0.071
L=2 ,BETA=0.045
L=3 ,BETA=0.057
L=4 ,BETA=0.056
L=5 ,BETA=0.060
L=6 ,BETA=0.064
L=7 ,BETA=0.071
dσ(θ)/dΩ[mb/sr]
θlab(deg)

Figure 6.10.

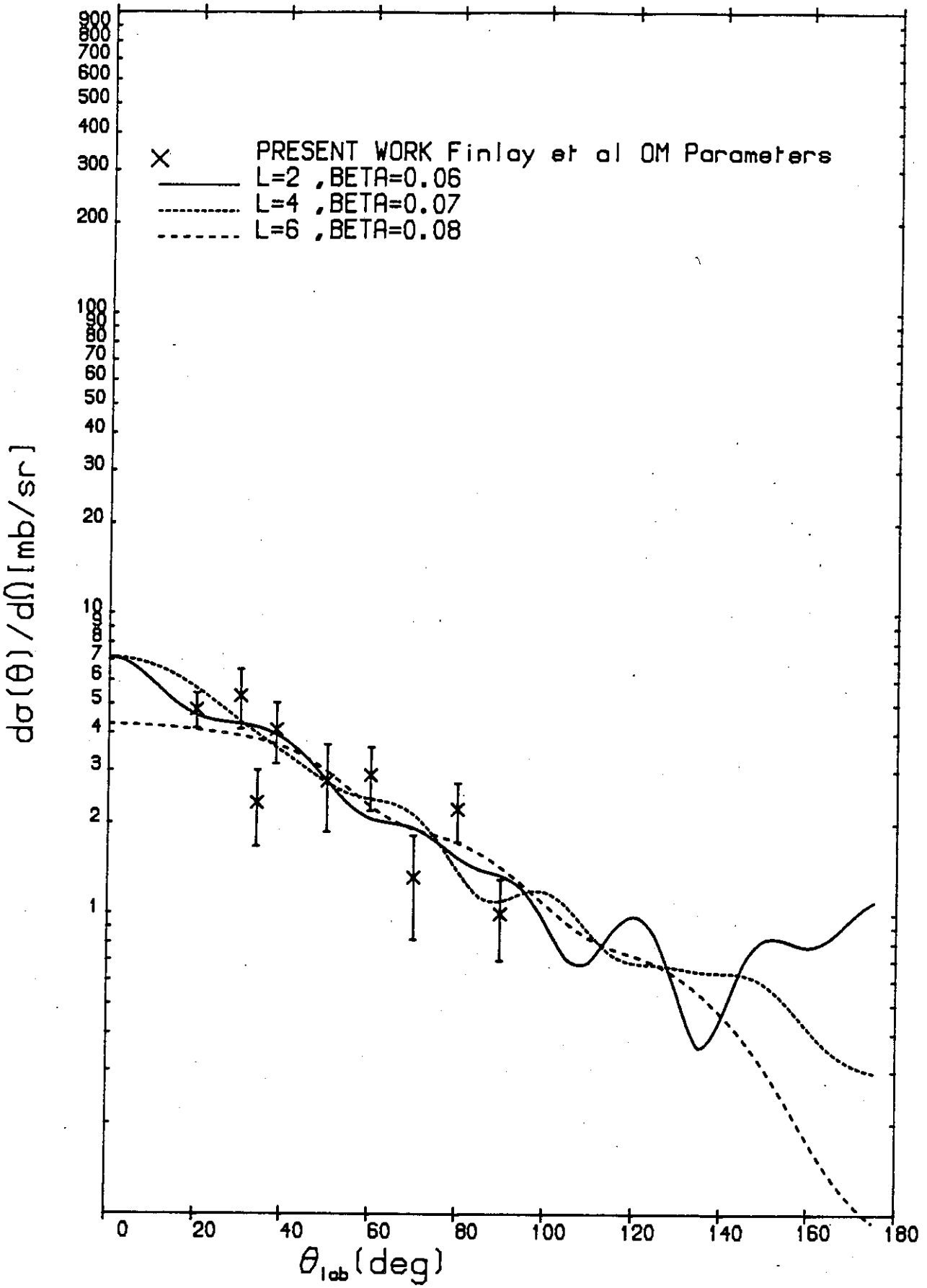
22/02/85 BISMUTH-209 Q=-3.4 MeV
PRESENT WORK Finlay et al OM Parameters
L=2 ,BETA=0.06
L=4 ,BETA=0.07
L=6 ,BETA=0.08
dσ(θ)/dΩ[mb/sr]
θlab(deg)
0
20
40
60
80
100
120
140
160
180

Figure 6.11.

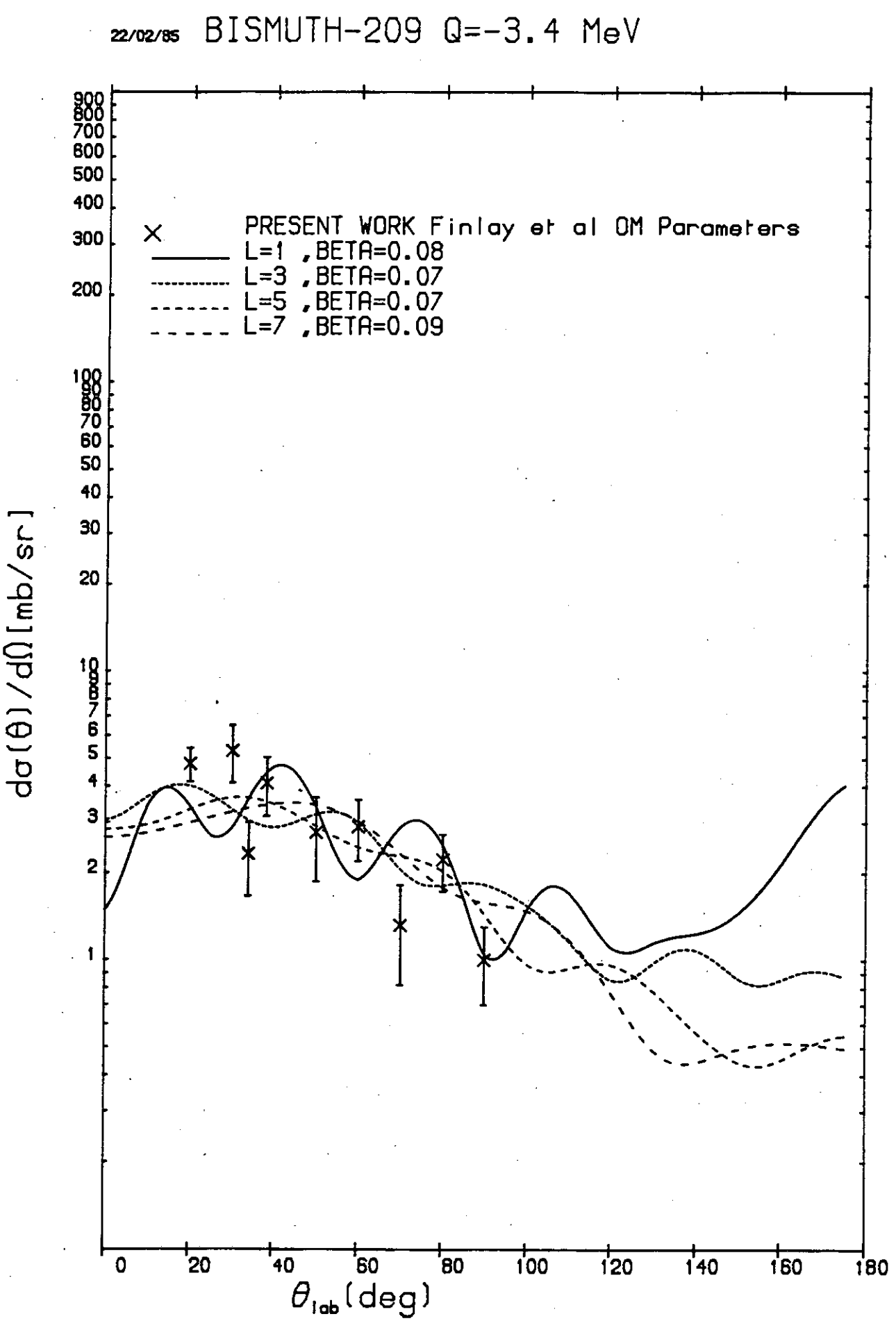
22/02/85 BISMUTH-209 Q=-3.4 MeV
PRESENT WORK Finlay et al OM Parameters
L=1 ,BETA=0.08
L=3 ,BETA=0.07
L=5 ,BETA=0.07
L=7 ,BETA=0.09
dσ(θ)/dΩ [mb/sr]
θlab (deg)

Figure 6.12.

values for each calculated curve, obtained with various ℓ values, were calculated in order to distinguish the favourite spin for this level. The reported spin for this excitation is 4 [110] and our data fits best with the $\ell = 4$ or $\ell = 6$ distribution, possibly $\ell = 6$ is the most favoured spin by our data, although the quality of fit differs little for the even ℓ values. Table (6.2) compares the ℓ values obtained with different sets of OM parameters (Table 6.1). It is worth pointing out that the Finlay et al. parameters result in a better fit to our data.

TABLE (6.2) - $Q_2 = -3.4$ MeV

Angular momentum transfer	Finlay et al. OM parameters	Stelson et al. OM parameters
1	3.0	4.2
2	1.6	1.8
3	2.0	3.5
4	1.6	1.4
5	2.0	2.2
6	1.4	1.3
7	2.6	2.7

Q = -4.2 MeV

On the basis of the level scheme of ^{208}Pb [110], the 4.2 MeV group is believed to be due to the excitation of a multiplet consisting of a 2^+ state at 4.086 MeV ($\beta_2 = 0.056$), 4^+ state at 4.323 MeV ($\beta_4 = 0.066$) and 6^+ state at 4.425 MeV ($\beta_6 = 0.066$). The 4.323 state is reported as being a collective state[110]. It is therefore not expected that

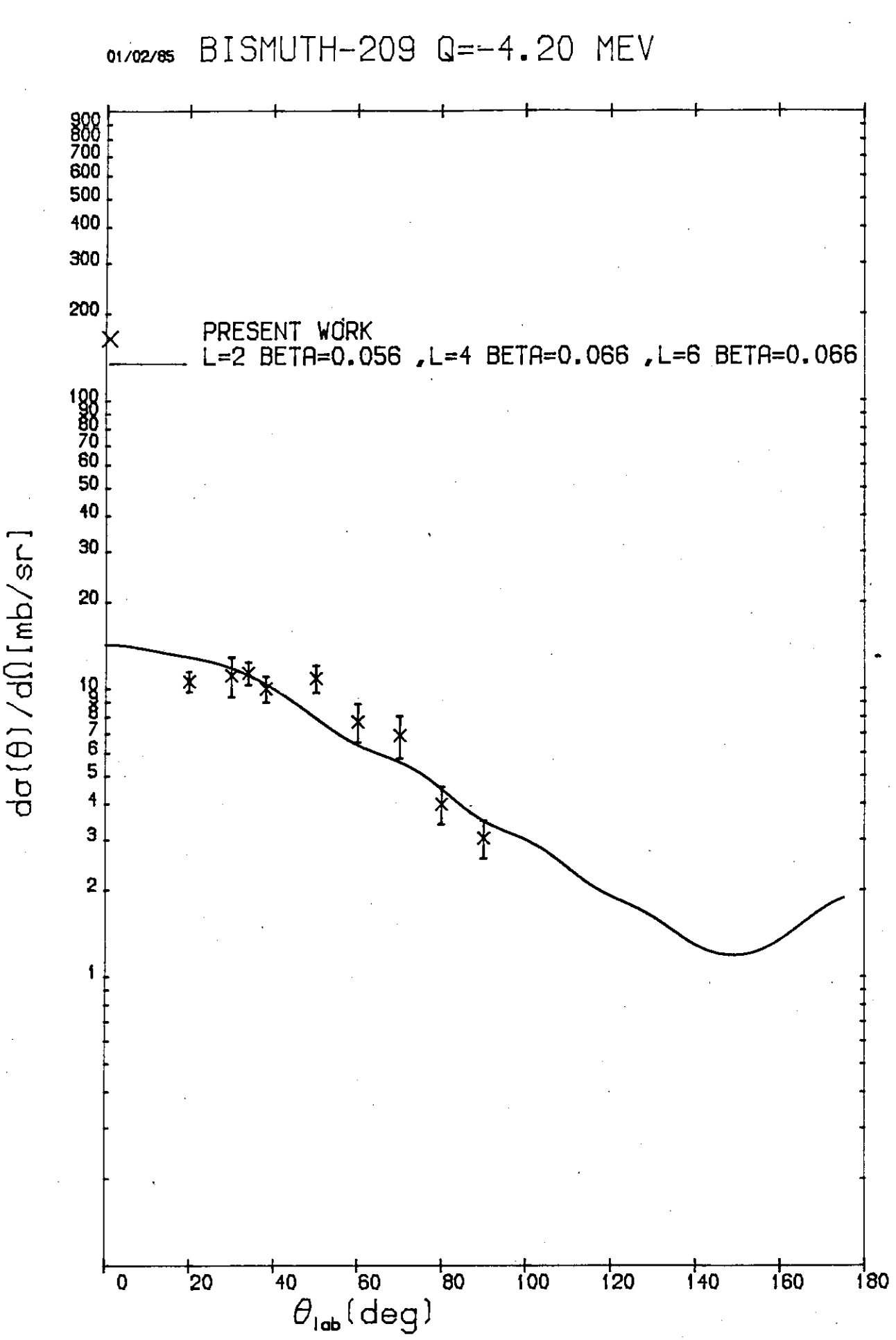
01/02/85 BISMUTH-209 Q=-4.20 MEV
PRESENT WORK
L=2 BETA=0.056 ,L=4 BETA=0.066 ,L=6 BETA=0.066
dσ(θ)/dΩ[mb/sr]
θlab(deg)
900
800
700
600
500
400
300
200
100
90
80
70
60
50
40
30
20
10
9
8
7
6
5
4
3
2
1
0
20
40
60
80
100
120
140
160
180

Figure 6.13.

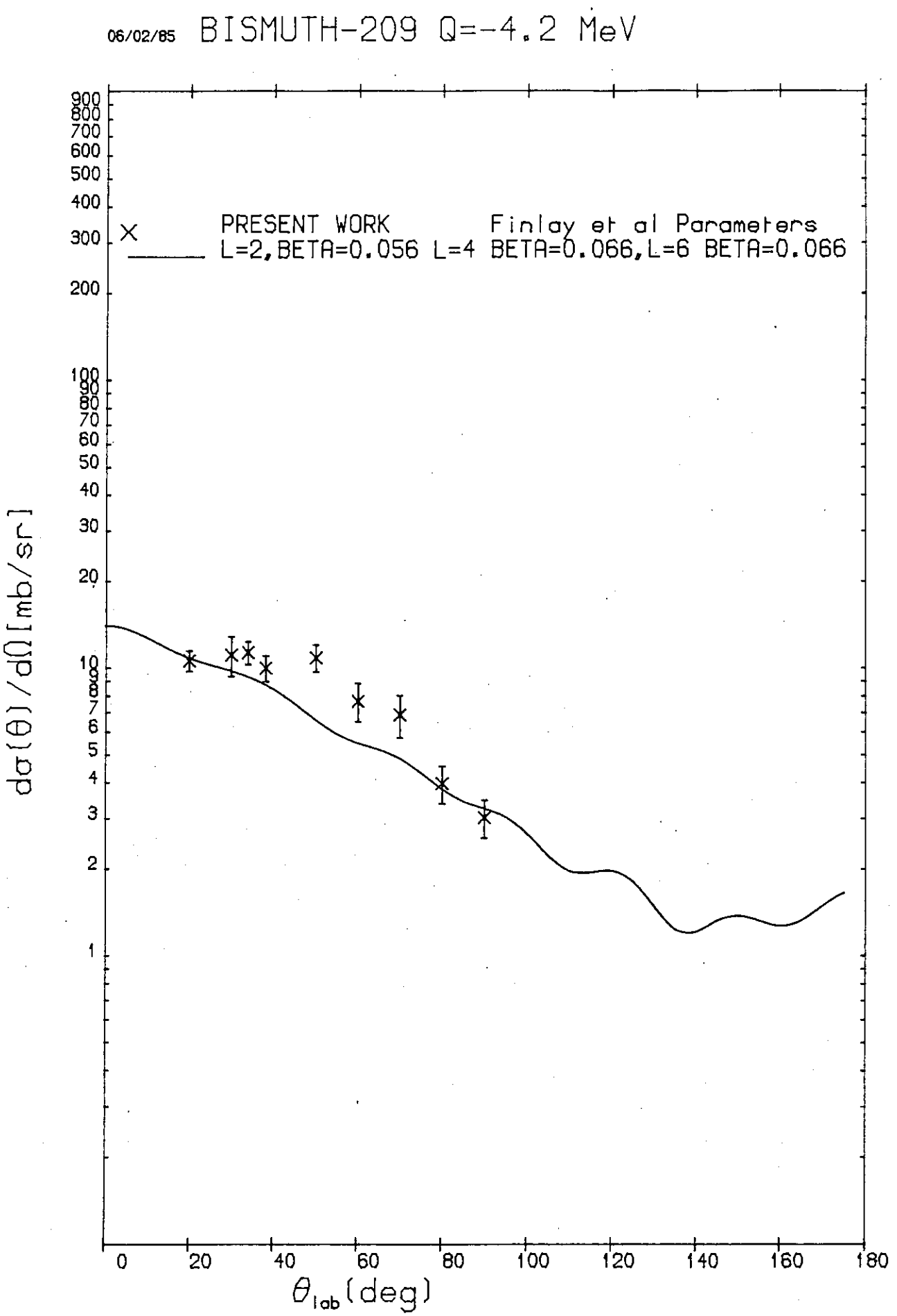
06/02/85 BISMUTH-209 Q=-4.2 MeV
PRESENT WORK
L=2, BETA=0.056
Finlay et al Parameters
L=4 BETA=0.066, L=6 BETA=0.066
dσ(θ)/dΩ [mb/sr]
θlab (deg)
0
20
40
60
80
100
120
140
160
180

Figure 6.14.

any pure ℓ value could describe the data satisfactorily.

An admixture of ($\ell = 2^+$, $\beta_2 = 0.056$), ($\ell = 4^+$, $\beta_4 = 0.066$) and ($\ell = 6^+$, $\beta_6 = 0.066$) can describe the data very well, particularly with the Stelson et al. parameters (Fig. 6.13). When the Finlay et al. OM parameters are used for the DWBA calculation, with the same admixture, it gave a cross section slightly lower than the data, particularly at forward angles, Fig. (6.14). It seemed, however, that a slight increase ($\simeq$ 10%) in the magnitude of the deformations can result in an equally good fit to data for the 4.2 MeV group with the Finlay et al. parameters.

Q = -4.8 MeV

The 4.8 MeV excitation level can be identified with the core excitation of ^{208}Pb at the same energy observed in proton inelastic scattering study[110]. The 4.8 MeV excitation energy has been reported by Bertrand and Lewis[131] when ^{209}Bi was excited by 62 MeV protons. The suggested spin for this energy group is 7^+ and 0. However, the calculated angular distributions for various ℓ values using Stelson et al. and Finlay et al. OM parameters are not so decisive and favour one of the four $\ell = 2$, $\ell = 4$, $\ell = 5$ and $\ell = 6$, depending on the optical parameters used for the calculations, Figs. (6.15) to (6.18). Table 6.3 demonstrates the values of χ^2 for each ℓ values for two sets of OM parameters.

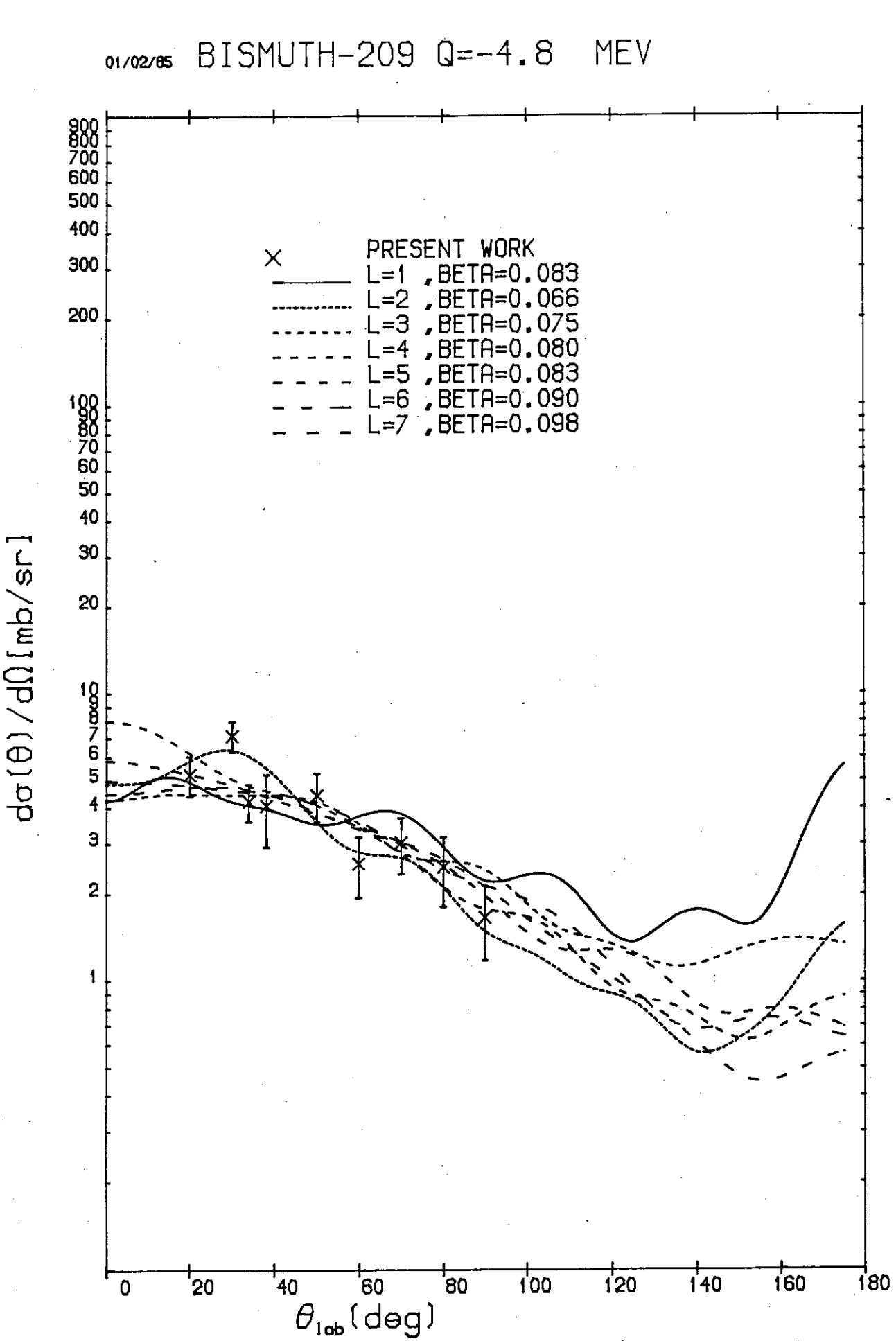
01/02/85 BISMUTH-209 Q=-4.8 MEV
PRESENT WORK
L=1 ,BETA=0.083
L=2 ,BETA=0.066
L=3 ,BETA=0.075
L=4 ,BETA=0.080
L=5 ,BETA=0.083
L=6 ,BETA=0.090
L=7 ,BETA=0.098
dσ(θ)/dΩ[mb/sr]
θlab(deg)
0
20
40
60
80
100
120
140
160
180

Figure 6.15.

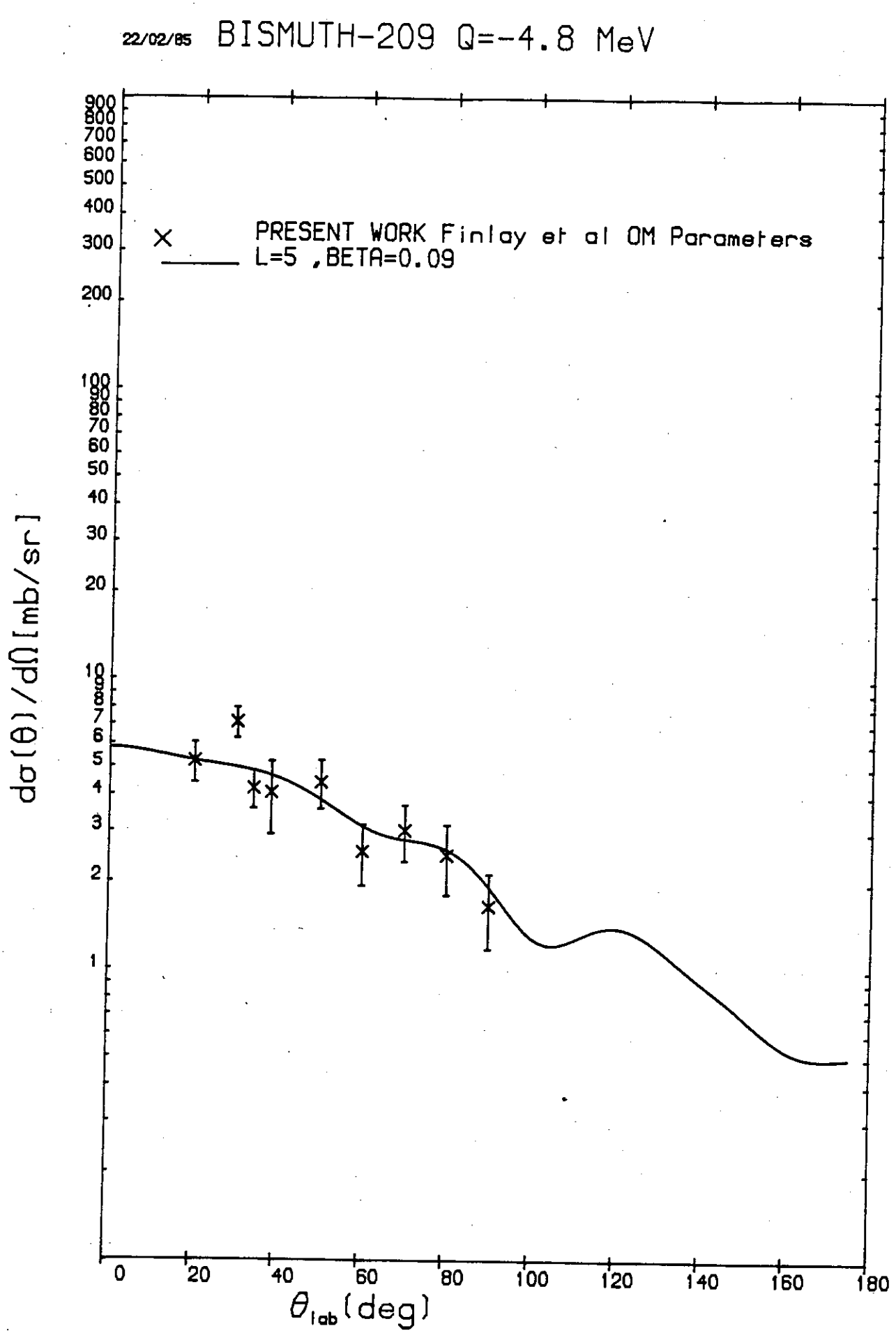
22/02/85 BISMUTH-209 Q=-4.8 MeV
PRESENT WORK Finlay et al OM Parameters
L=5 ,BETA=0.09
dσ(θ)/dΩ[mb/sr]
θlab(deg)
900
800
700
600
500
400
300
200
100
90
80
70
60
50
40
30
20
10
9
8
7
6
5
4
3
2
1
0
20
40
60
80
100
120
140
160
180

Figure 6.16.

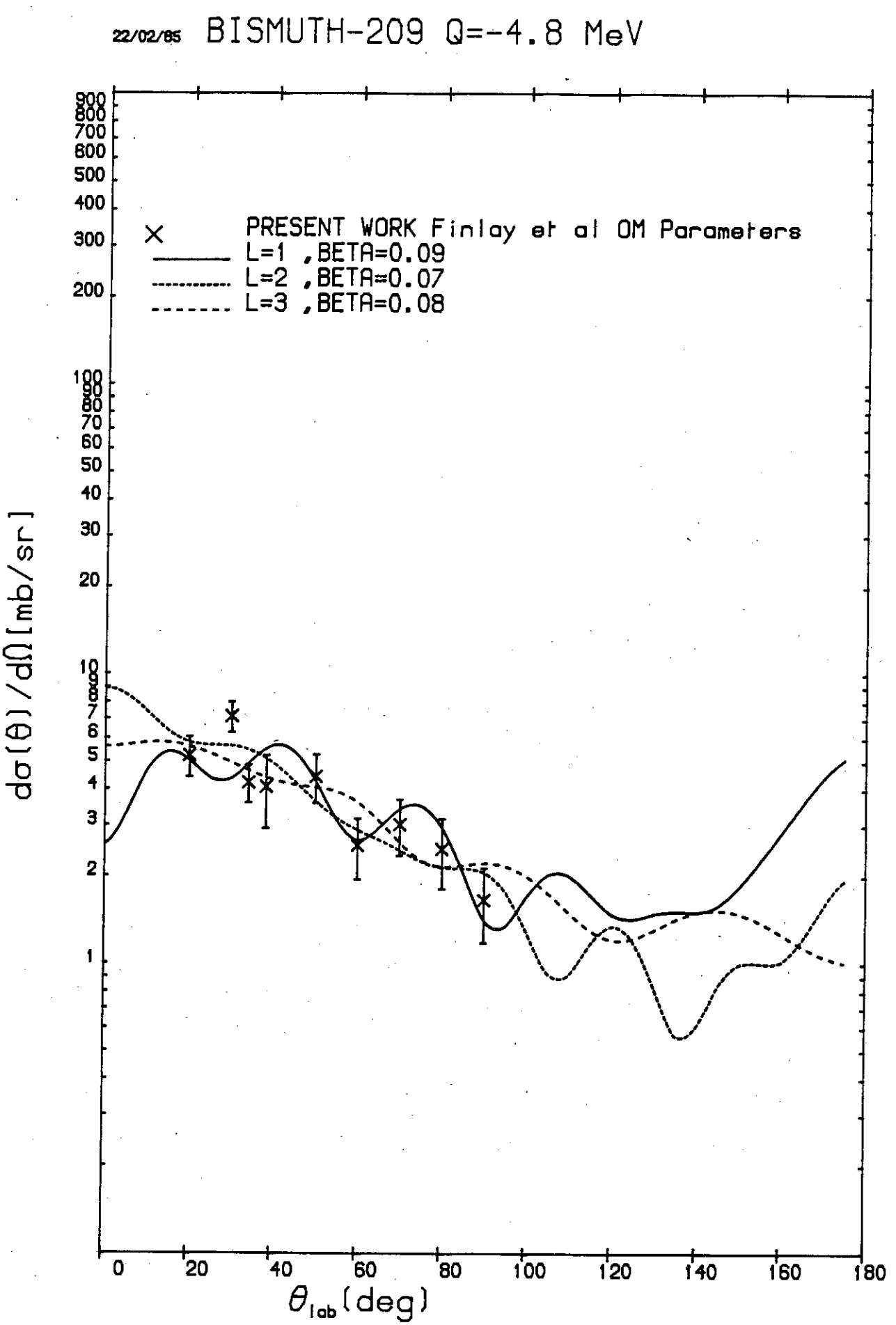
22/02/85 BISMUTH-209 Q=-4.8 MeV
PRESENT WORK Finlay et al OM Parameters
L=1 ,BETA=0.09
L=2 ,BETA=0.07
L=3 ,BETA=0.08
dσ(θ)/dΩ[mb/sr]
θlab(deg)

Figure 6.17.

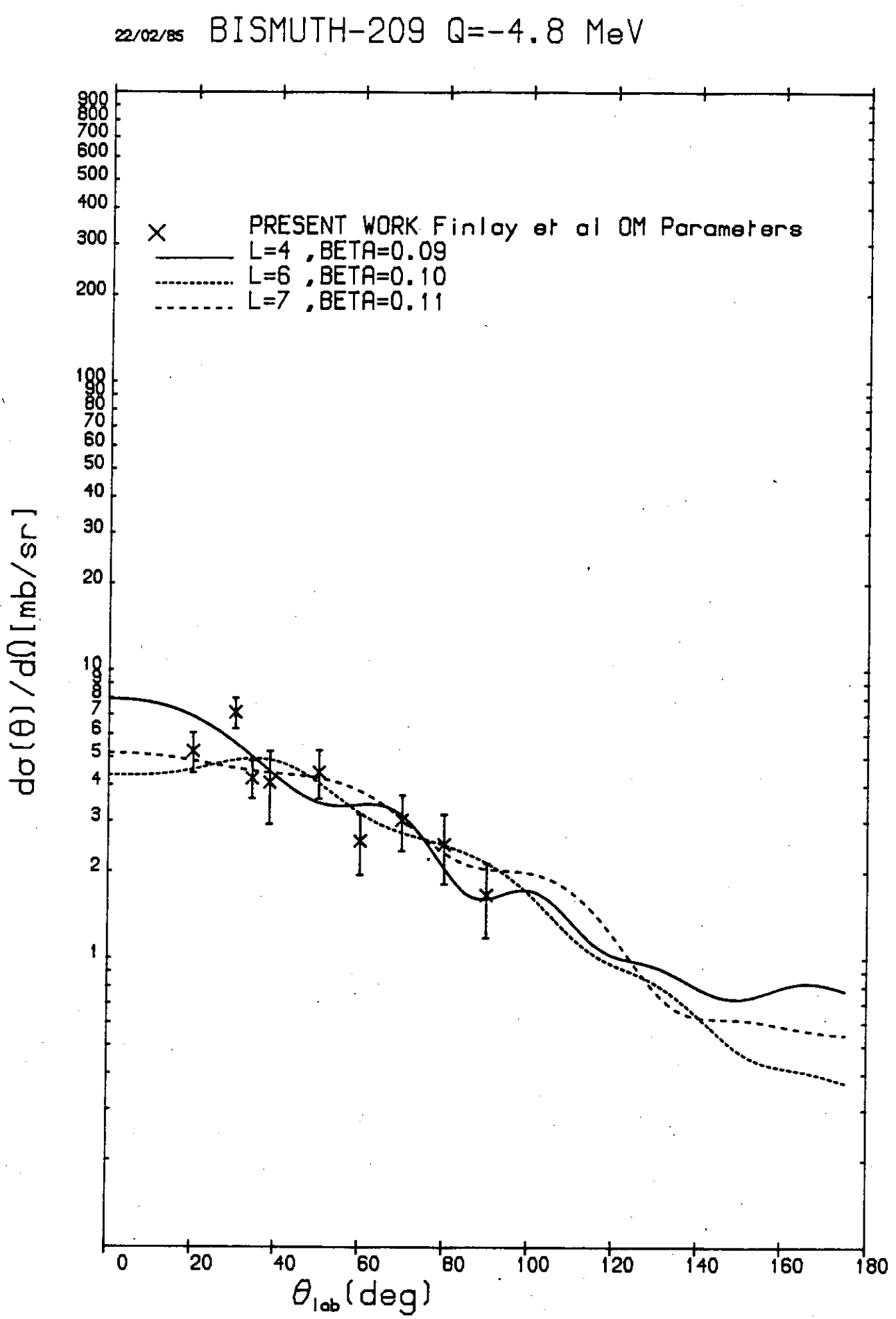
22/02/85 BISMUTH-209 Q=-4.8 MeV
PRESENT WORK Finlay et al OM Parameters
L=4 ,BETA=0.09
L=6 ,BETA=0.10
L=7 ,BETA=0.11
dσ(θ)/dΩ[mb/sr]
θlab(deg)
900
800
700
600
500
400
300
200
100
90
80
70
60
50
40
30
20
10
9
8
7
6
5
4
3
2
1
0
20
40
60
80
100
120
140
160
180

Figure 6.18.

TABLE 6.3 - Q = -4.8 MeV

Angular momentum transfar ℓ	χ^2 Finlay et al. OM Parameters	Stelson et al. OM Parameters
1	1.7	2.2
2	1.2	1.3
3	1.4	1.8
4	1.4	1.2
5	1.0	1.2
6	1.3	1.3
7	1.6	1.5

Q = - 5.5 MeV

The angular distribution for the 5.5 MeV energy group is shown in Fig. (6.19), for 7 ℓ transfers (ℓ = 1 to ℓ = 7) using the Stelson et al. OM parameters. An excitation level at 5.5 ± 0.3 MeV has been observed by Kuijper et al.[30], and at 5.8 MeV by Matoba et al.[31], both in 14 MeV neutron inelastic scattering studies. The suggested ℓ value by Kuijper et al. for this excitation group is ℓ = 2, whereas Matoba et al. have fitted their data with an ℓ = 3 angular momentum transfer.

The comparison of χ^2 obtained from fitting our data with 7 ℓ values for each set of OM parameters is presented in Table (6.4). Calculations based on Finlay et al. parameters tend to select ℓ = 4, however in the case of Stelson et al. parameters the choice is different and ℓ = 2 appears to be the most favoured ℓ value for this excitation group. From the density of levels at this energy it is

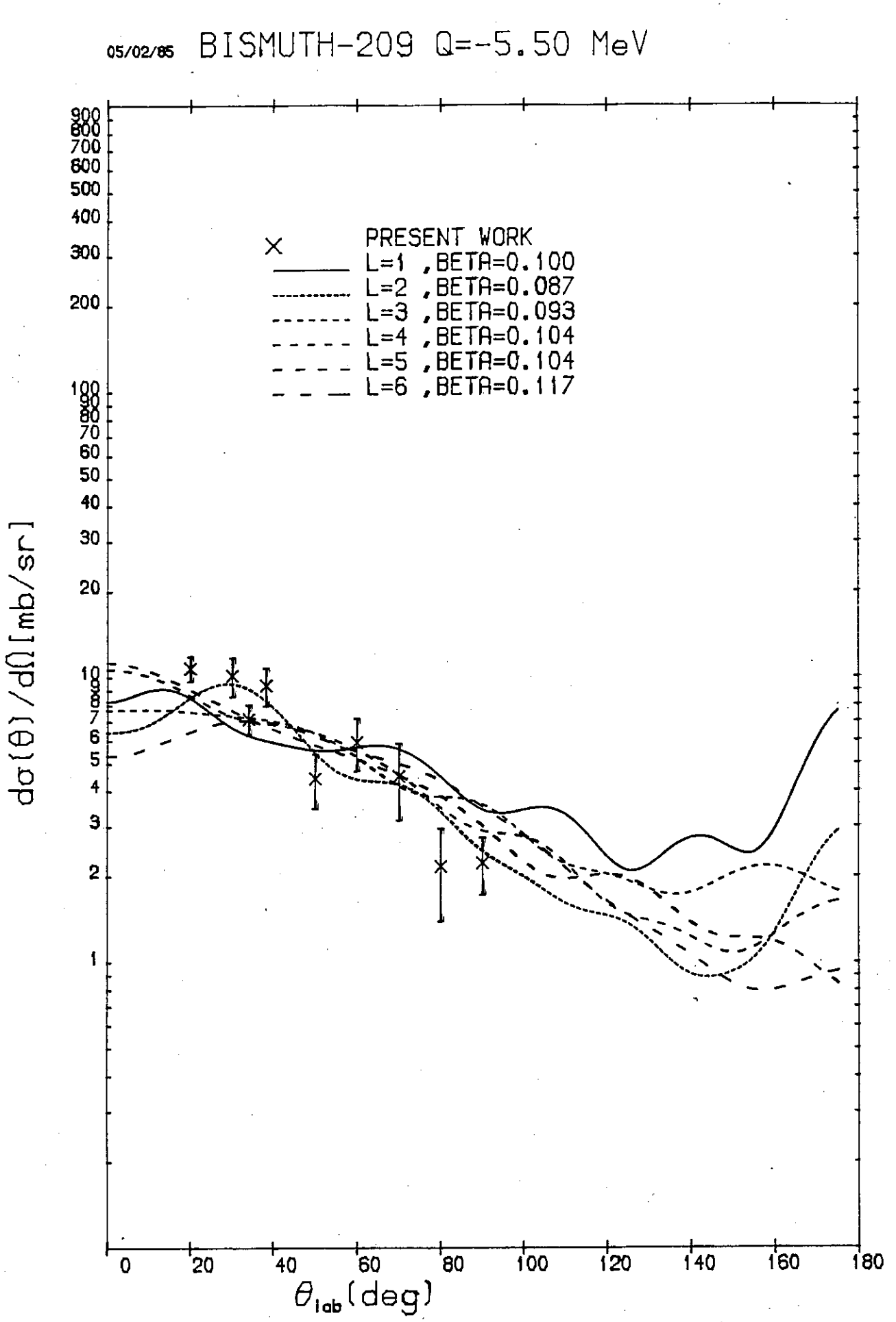
05/02/85 BISMUTH-209 Q=-5.50 MeV
PRESENT WORK
L=1 ,BETA=0.100
L=2 ,BETA=0.087
L=3 ,BETA=0.093
L=4 ,BETA=0.104
L=5 ,BETA=0.104
L=6 ,BETA=0.117
dσ(θ)/dΩ[mb/sr]
θlab(deg)
0
20
40
60
80
100
120
140
160
180

Figure 6.19.

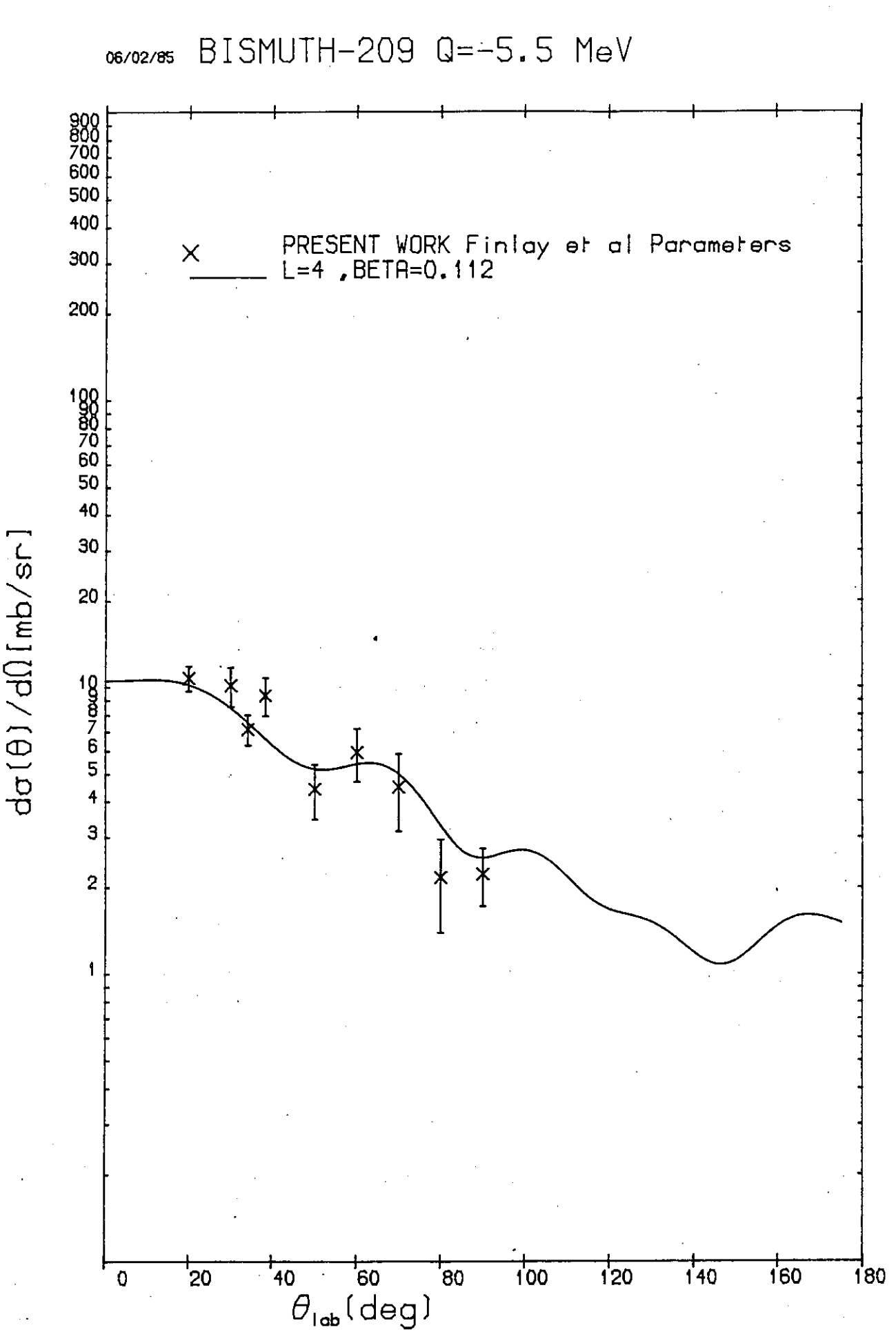
06/02/85 BISMUTH-209 Q=-5.5 MeV
PRESENT WORK Finlay et al Parameters
L=4 ,BETA=0.112
dσ(θ)/dΩ[mb/sr]
θlab(deg)
0
20
40
60
80
100
120
140
160
180

Figure 6.20.

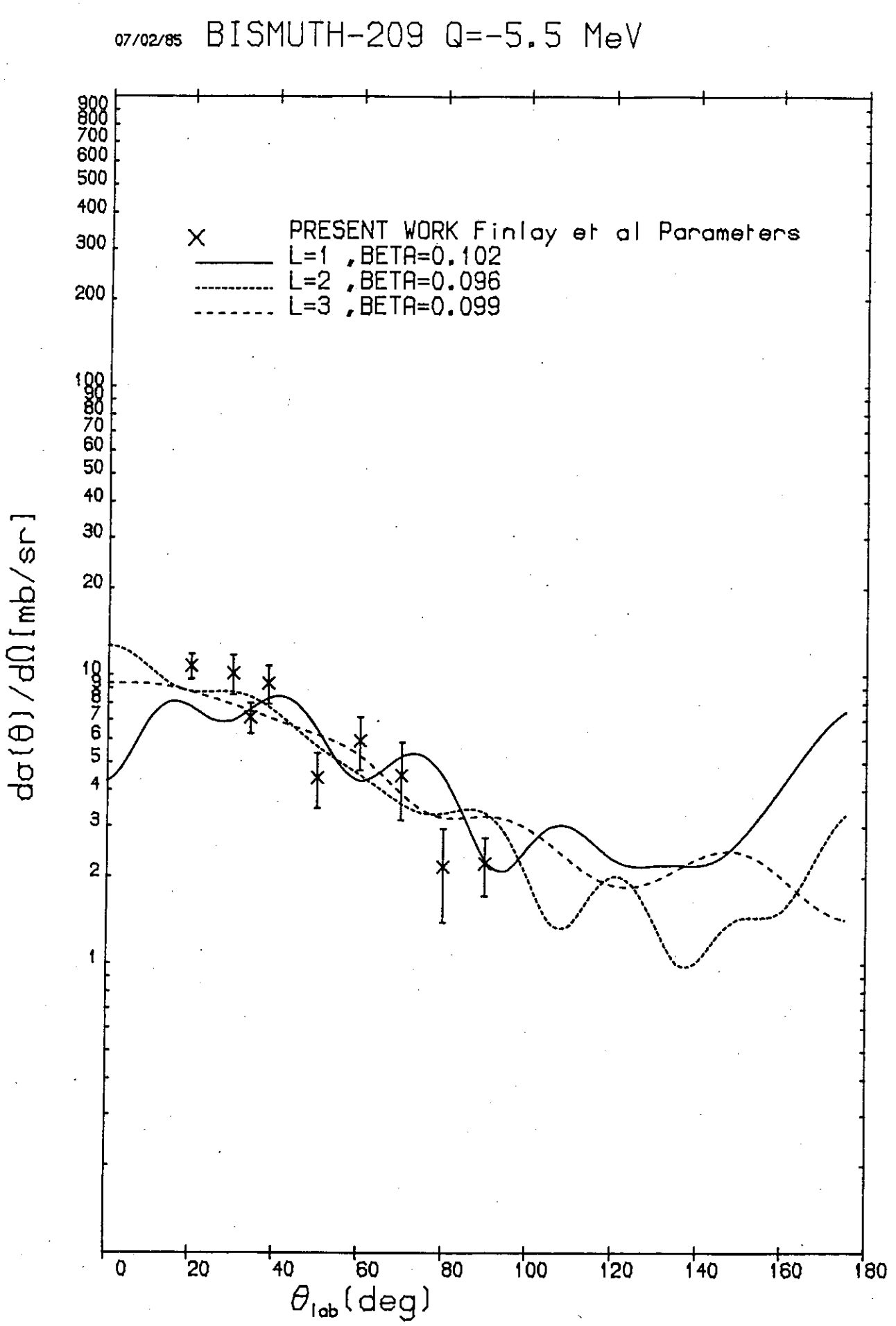
07/02/85 BISMUTH-209 Q=-5.5 MeV
PRESENT WORK Finlay et al Parameters
L=1 ,BETA=0.102
L=2 ,BETA=0.096
L=3 ,BETA=0.099
dσ(θ)/dΩ[mb/sr]
θlab(deg)

Figure 6.21.

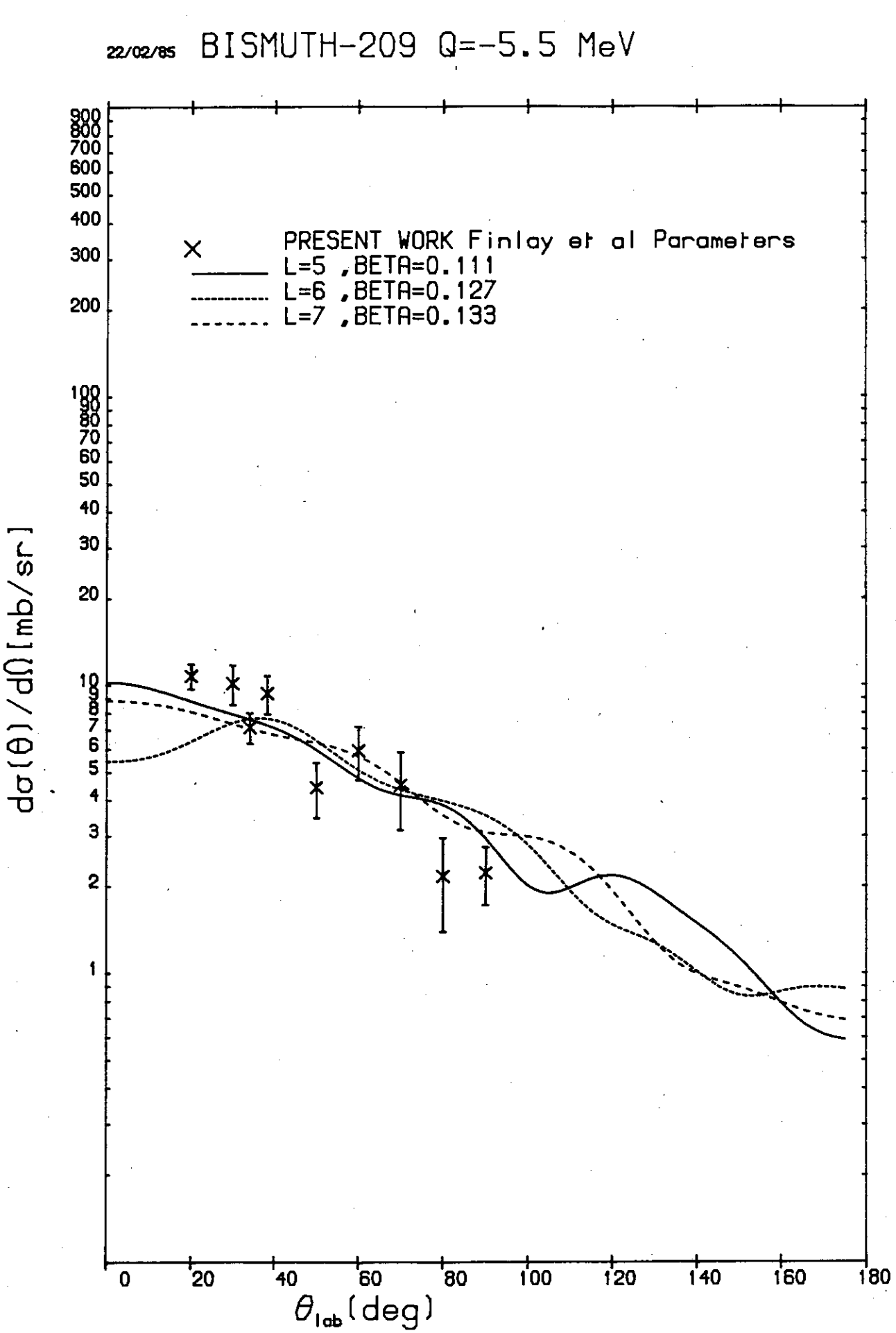
22/02/85 BISMUTH-209 Q=-5.5 MeV
PRESENT WORK Finlay et al Parameters
L=5 ,BETA=0.111
L=6 ,BETA=0.127
L=7 ,BETA=0.133
dσ(θ)/dΩ[mb/sr]
θlab(deg)

Figure 6.22.

quite likely that the 5.5 MeV group is a composite of a few states and that attributing a pure ℓ value to this excitation would not describe the data satisfactorily.

Fig. (6.20) shows the agreement between $\ell = 4$ distribution and the data. In Figs. (6.21) and (6.22) the DWBA calculations for 6 other ℓ values have been presented.

TABLE 6.4 - Q_2 - 5.5 MeV

Angular momentum transfer ℓ	χ^2 Finlay et al. parameters	Stelson et al. parameters
1	3.1	3.7
2	2.0	1.7
3	2.0	3.5
4	1.0	2.2
5	2.0	2.0
6	4.3	4.6
7	2.5	2.5

Q = - 6.2 MeV

There is no previous cross section measurement of the 6.2 MeV state. Kuijper et al.[30] observed by 14 MeV neutron scattering a state in ^{209}Bi with an energy of 6.4 ± 0.2 MeV. Their data, however, for this state were too uncertain to be analysed. The 6.2 MeV state has also been observed in electron inelastic scattering experiments[110].

The spin of this state is not established. It has been expressed with doubt that the 6.2 MeV state may have a spin of 2 [110], a spin of 1 also has been suggested[110].

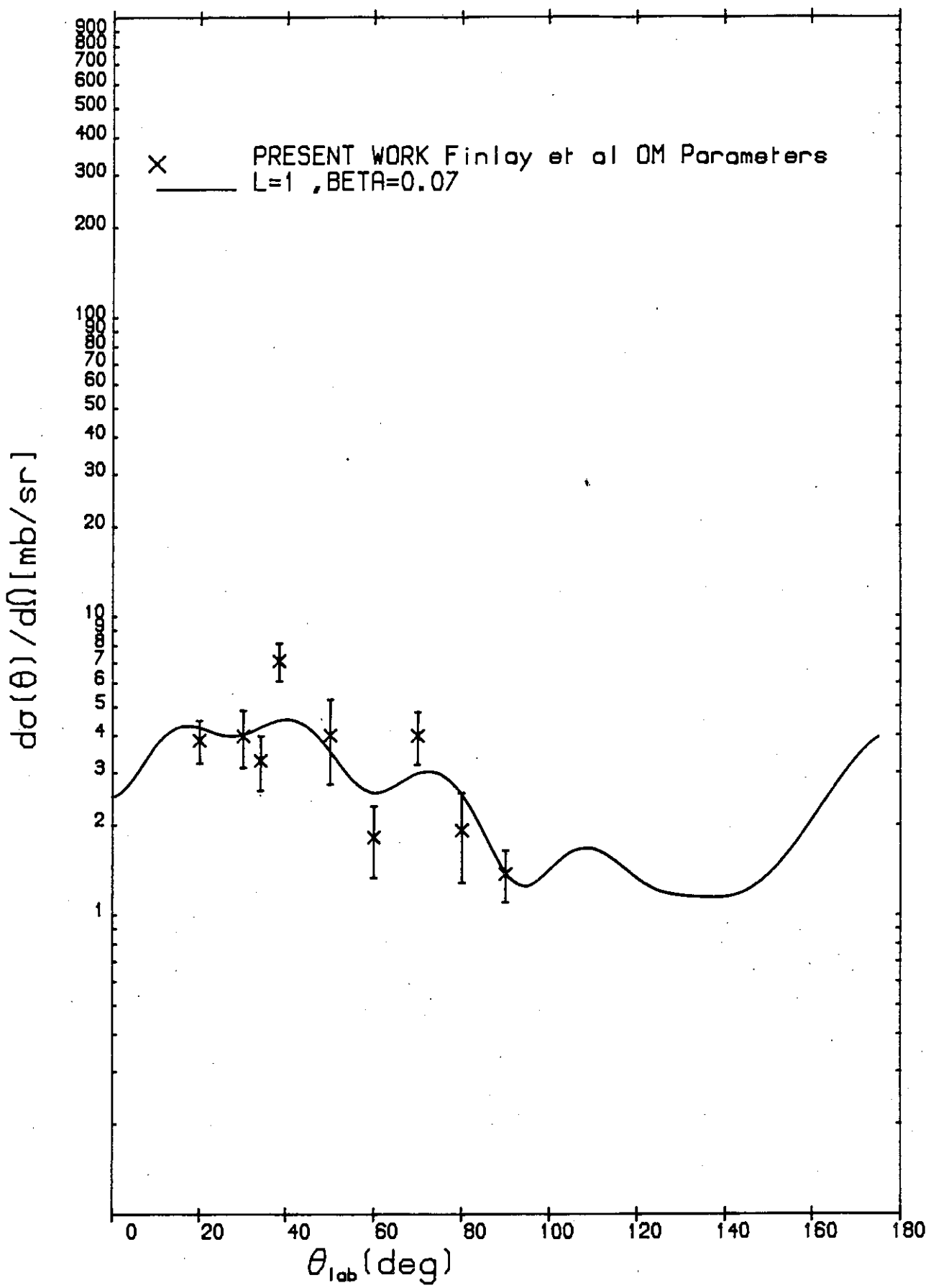
22/02/85 BISMUTH-209 Q=-6.2 MeV
PRESENT WORK Finlay et al OM Parameters
L=1 ,BETA=0.07
dσ(θ)/dΩ[mb/sr]
θlab(deg)
900
800
700
600
500
400
300
200
100
90
80
70
60
50
40
30
20
10
9
8
7
6
5
4
3
2
1
0
20
40
60
80
100
120
140
160
180

Figure 6.23.

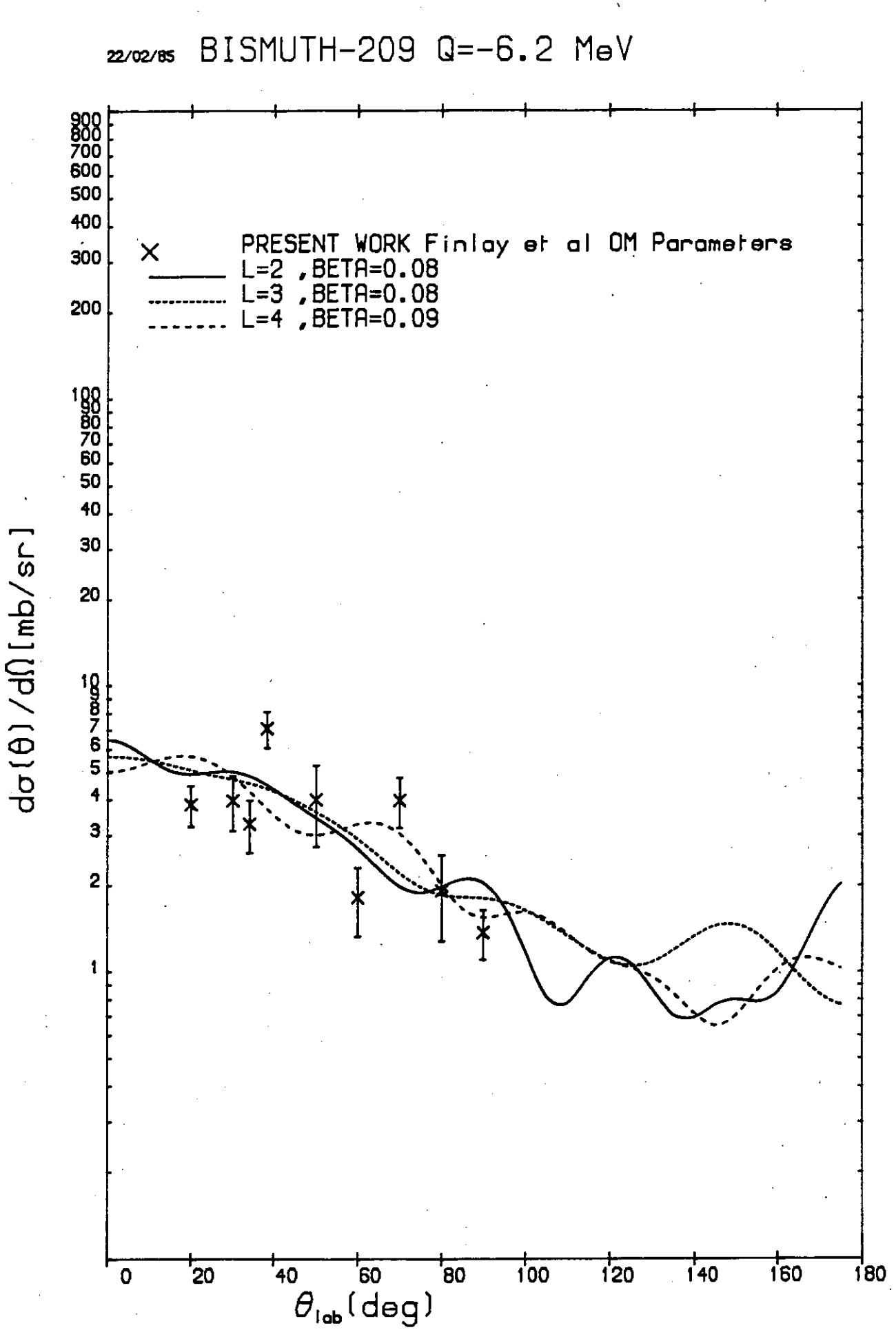
22/02/85 BISMUTH-209 Q=-6.2 MeV
PRESENT WORK Finlay et al OM Parameters
L=2 ,BETA=0.08
L=3 ,BETA=0.08
L=4 ,BETA=0.09
dσ(θ)/dΩ[mb/sr]
θlab(deg)

Figure 6.24.

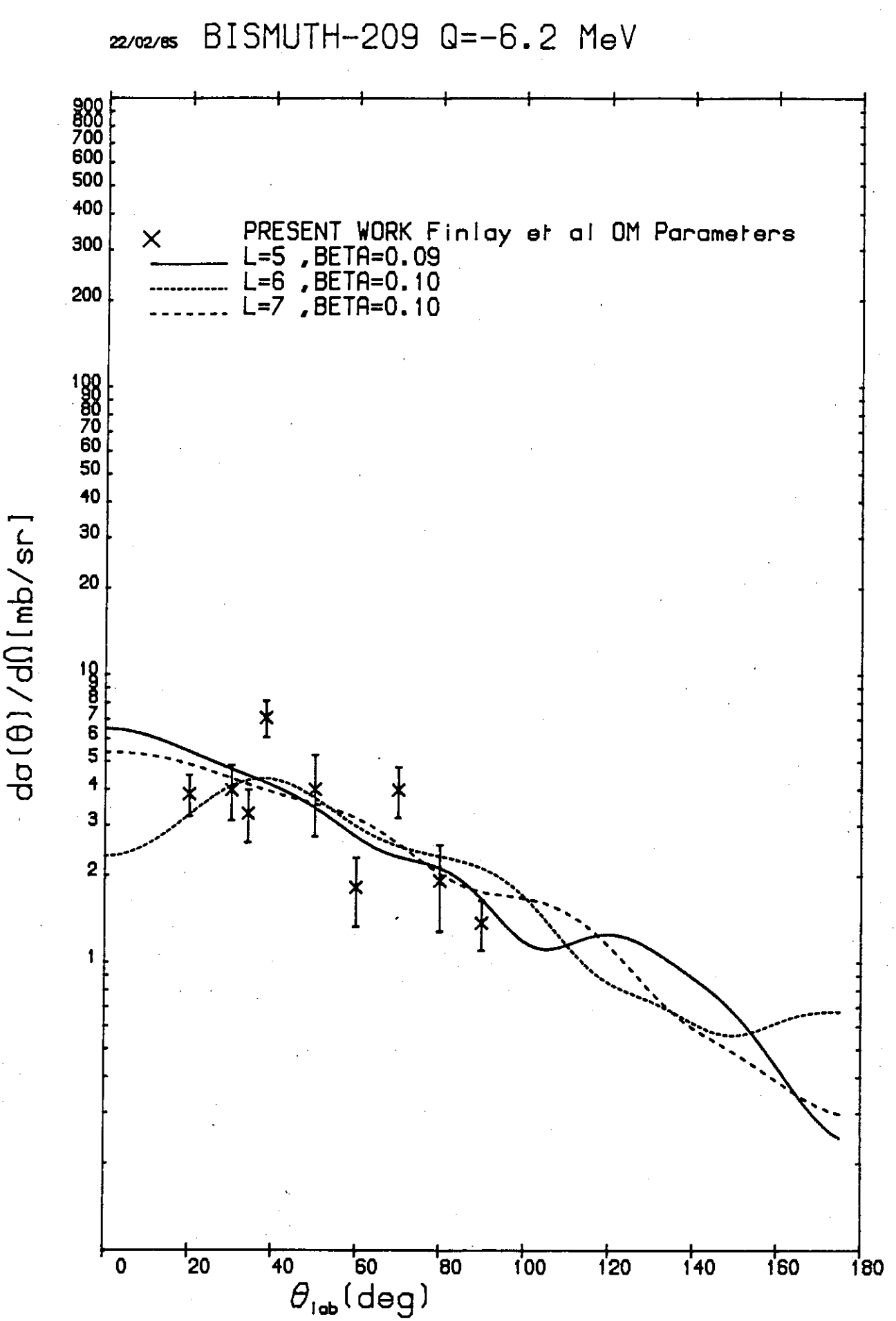
22/02/85 BISMUTH-209 Q=-6.2 MeV
PRESENT WORK Finlay et al OM Parameters
L=5 ,BETA=0.09
L=6 ,BETA=0.10
L=7 ,BETA=0.10
dσ(θ)/dΩ[mb/sr]
θlab(deg)

Figure 6.25.

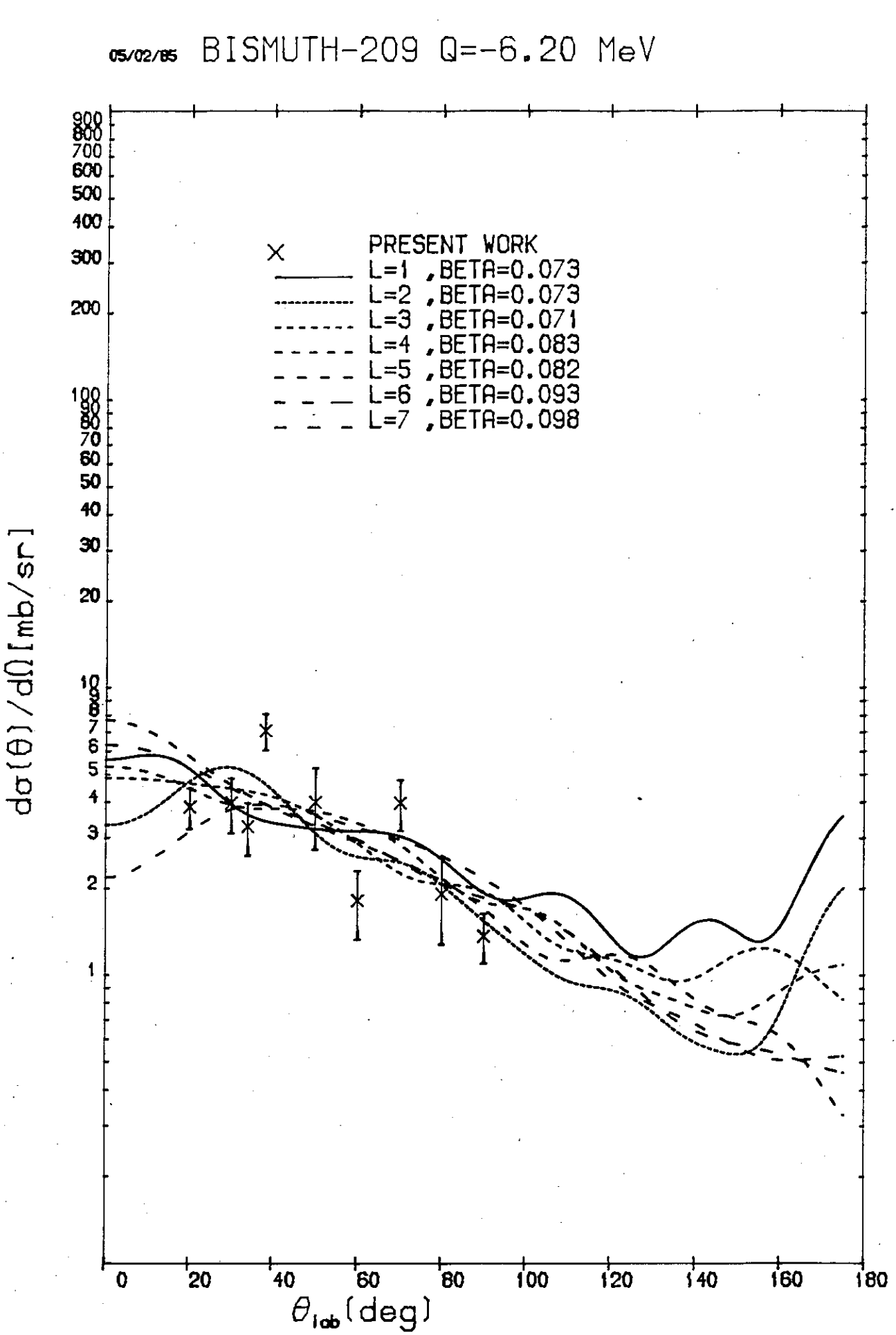
05/02/85 BISMUTH-209 Q=-6.20 MeV
PRESENT WORK
L=1 ,BETA=0.073
L=2 ,BETA=0.073
L=3 ,BETA=0.071
L=4 ,BETA=0.083
L=5 ,BETA=0.082
L=6 ,BETA=0.093
L=7 ,BETA=0.098
dσ(θ)/dΩ[mb/sr]
θlab[deg]

Figure 6.26.

The data of this experiment have been compared with angular distributions obtained by 7 angluar momentum transfer values ($\ell = 1$ to $\ell = 7$) for two sets of different OM parameters and the χ^2 values are tabulated in Table (6.5).

TABLE (6.5) Q = - 6.2 MeV

Angular momentum transfer ℓ	χ^2 Finlay et al. OM parameters	Stelson et al. OM parameters
1	1.5	3.6
2	3.6	2.7
3	3.1	3.0
4	3.9	3.0
5	3.1	3.5
6	3.1	3.6
7	3.0	3.4

In the case of the Finlay et al. parameters, the values of χ^2 have a rather strong tendency to suggest that $\ell = 1$ is preferred ℓ for our data, Figs. (6.23) to (6.25), whereas similar calculations using Stelson et al. OM parameters are in favour of supporting $\ell = 2$. Fig. (6.26) shows angular distributions based on Stelson et al. OM parameters.

Q = -6.8 MeV

The excitation group at 6.8 MeV is likely to be due to the excitation of a few states around 6.8 MeV observed by proton inelastic scattering in ^{208}Pb (110). There is not any suggested value for the spin of this state. It is most likely that the excitation at this energy

is a mixture of more than one spin.

Tabulated values of χ^2, Table (6.6) suggest preferred values of $\ell = 3$ and $\ell = 7$ supported by both sets of OM parameters, Figs. (6.27) (6.28) and (6.30), although in case of Finlay et al. parameters $\ell = 4$ is also a possibility, Fig. (6.29).

TABLE 6.6 Q = -6.8 MeV.

Angular momentum transfer ℓ	χ^2 Finlay et al. OM parameters	Stelson et al. OM parameters
1	5.8	5.2
2	3.7	3.3
3	2.5	3.1
4	2.7	4.3
5	3.3	3.4
6	5.9	7.8
7	2.8	3.1

Q = - 7.1 MeV

4 excited states with 7.168 MeV, 7.172 Mev, 7.179 MeV and 7.202 MeV energies have been reported previously for $^{209}Bi(110)$.

There is an indication that $\ell = 3$ could be the most favoured spin for our data on this energy group, Fig. (6.32), independent of OM parameters used, unlike the case for the two previous states at 6.2 MeV and 6.8 MeV. Table (6.7) shows the χ^2 values for various ℓ values, Figs. (6.31), (6.33) and (6.34) show the comparison between calculations and the data.

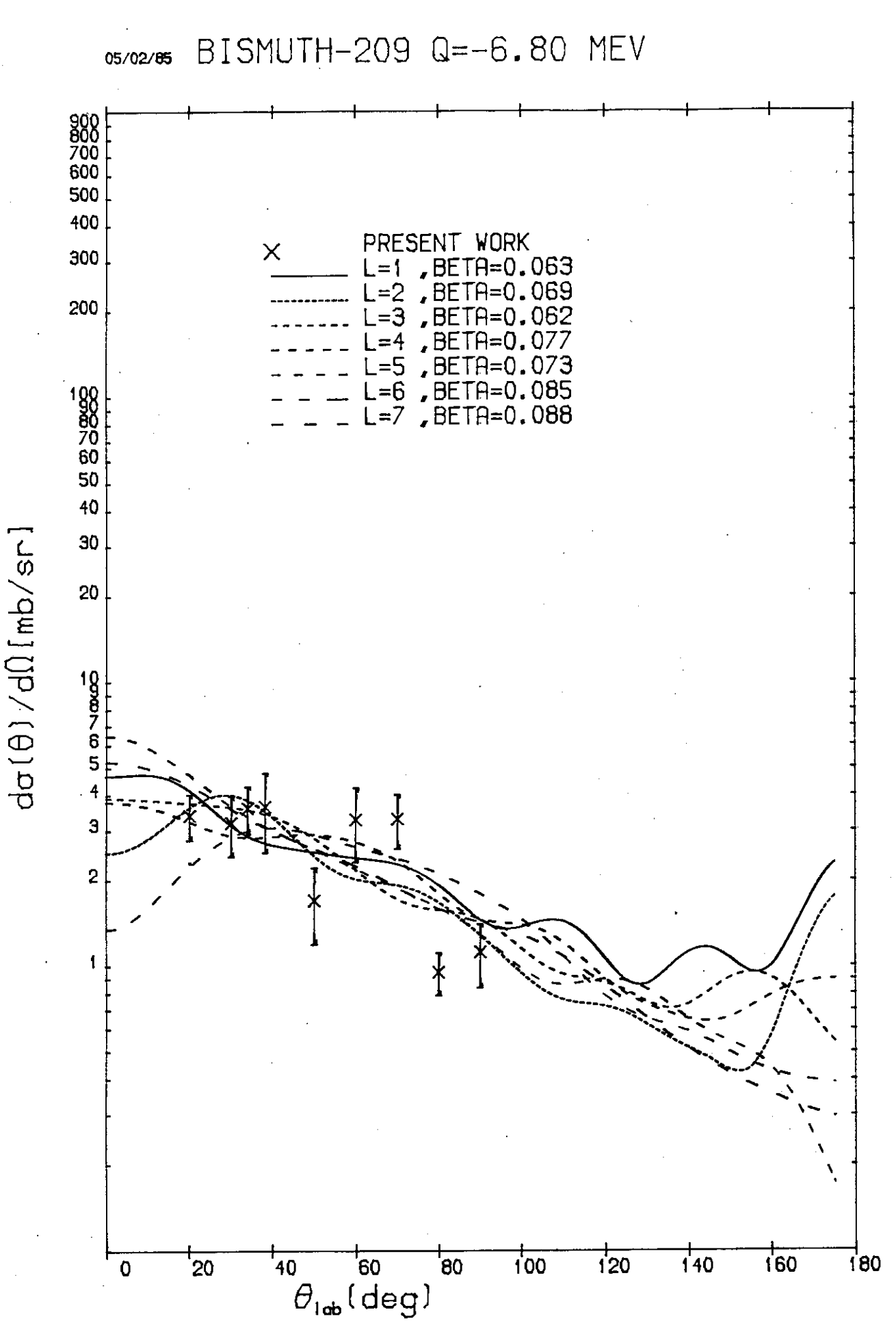
05/02/85 BISMUTH-209 Q=-6.80 MEV
PRESENT WORK
L=1 ,BETA=0.063
L=2 ,BETA=0.069
L=3 ,BETA=0.062
L=4 ,BETA=0.077
L=5 ,BETA=0.073
L=6 ,BETA=0.085
L=7 ,BETA=0.088
dσ(θ)/dΩ[mb/sr]
θlab[deg]
0
20
40
60
80
100
120
140
160
180

Figure 6.27.

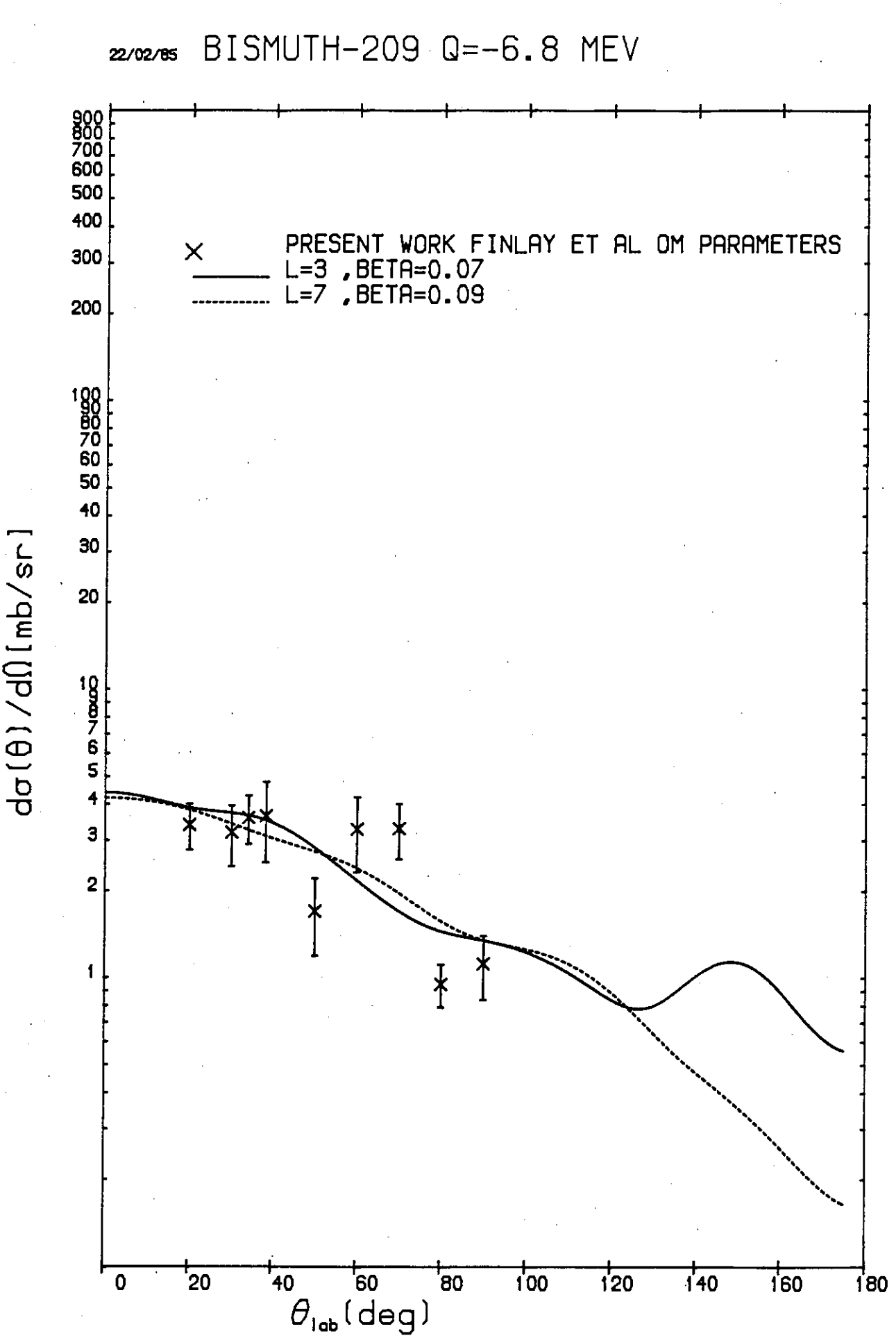
22/02/85 BISMUTH-209 Q=-6.8 MEV
PRESENT WORK FINLAY ET AL OM PARAMETERS
L=3 ,BETA=0.07
L=7 ,BETA=0.09
dσ(θ)/dΩ[mb/sr]
θlab(deg)
0
20
40
60
80
100
120
140
160
180

Figure 6.28.

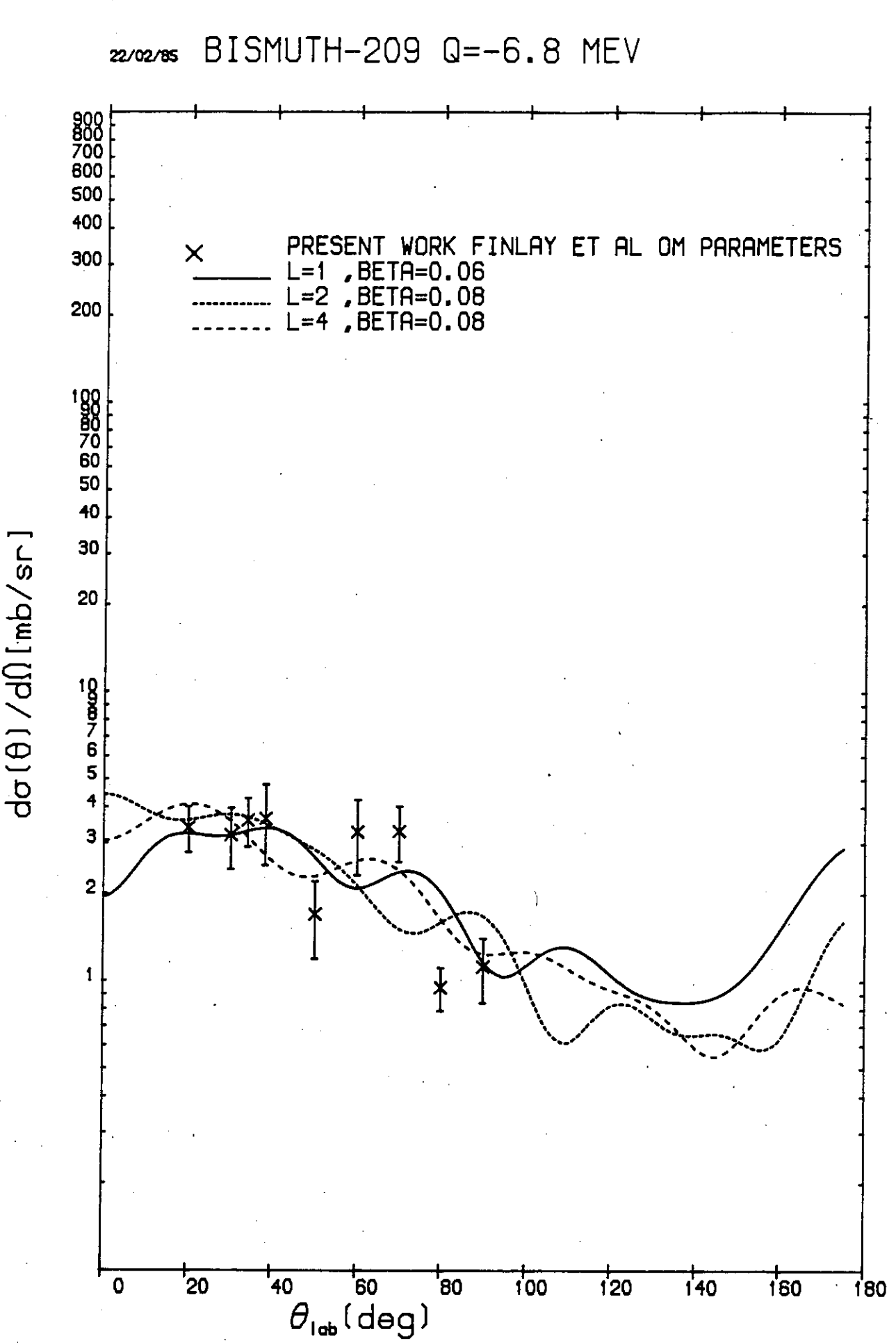
22/02/85 BISMUTH-209 Q=-6.8 MEV
PRESENT WORK FINLAY ET AL OM PARAMETERS
L=1 ,BETA=0.06
L=2 ,BETA=0.08
L=4 ,BETA=0.08
dσ(θ)/dΩ [mb/sr]
θlab (deg)

Figure 6.29.

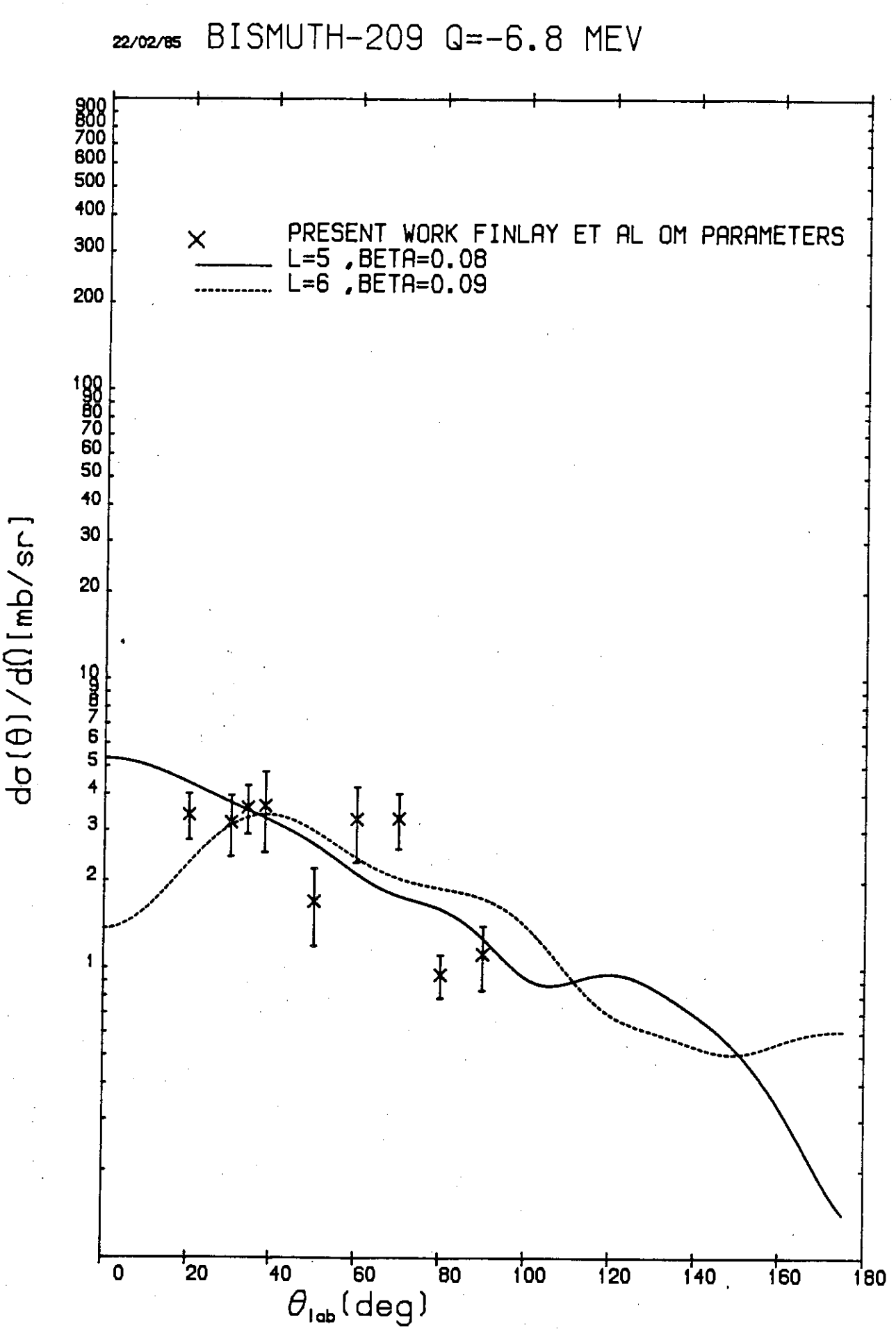
22/02/85 BISMUTH-209 Q=-6.8 MEV
PRESENT WORK FINLAY ET AL OM PARAMETERS
L=5 ,BETA=0.08
L=6 ,BETA=0.09
dσ(θ)/dΩ[mb/sr]
θlab(deg)

Figure 6.30.

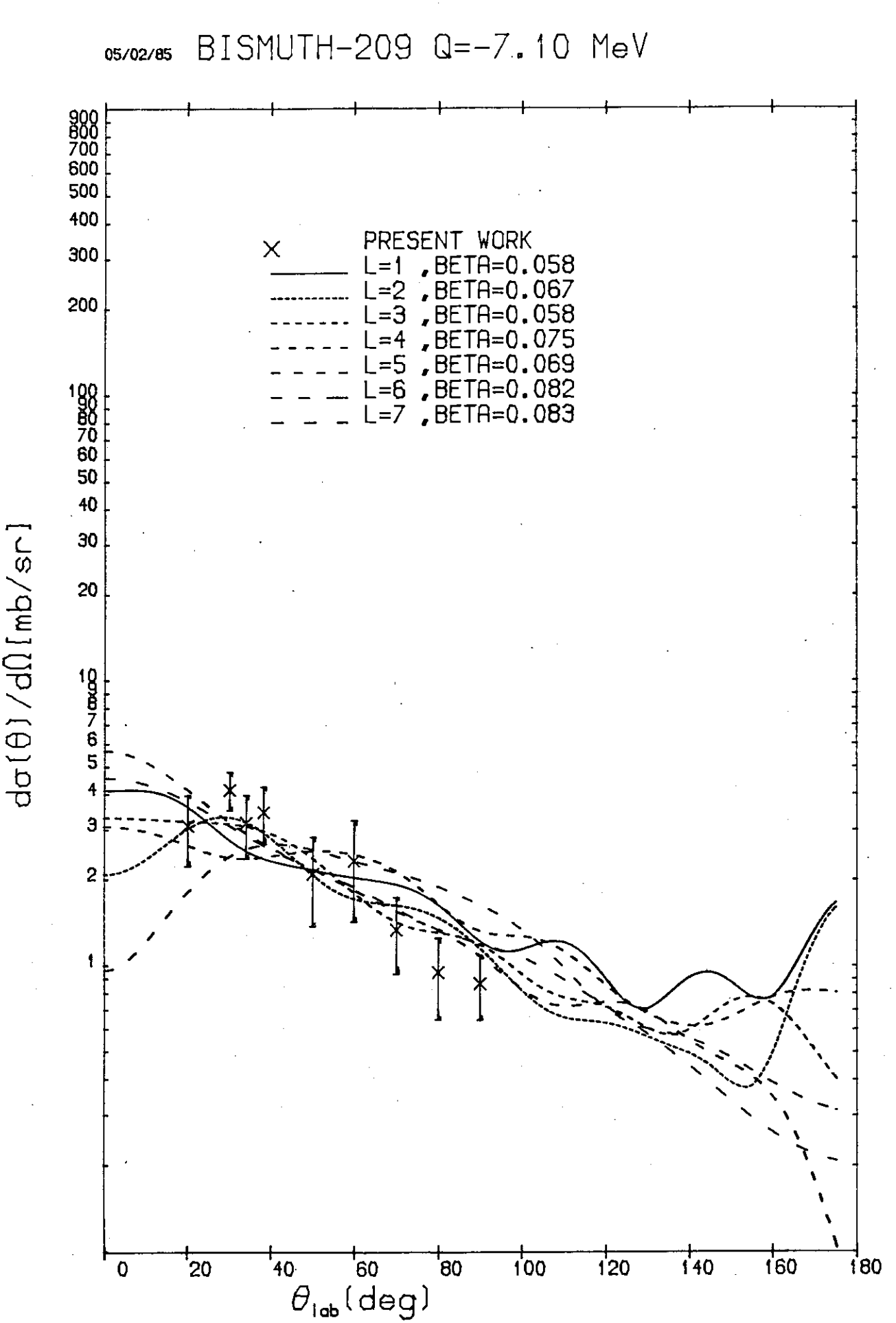
05/02/85 BISMUTH-209 Q=-7.10 MeV
PRESENT WORK
L=1 ,BETA=0.058
L=2 ,BETA=0.067
L=3 ,BETA=0.058
L=4 ,BETA=0.075
L=5 ,BETA=0.069
L=6 ,BETA=0.082
L=7 ,BETA=0.083
dσ(θ)/dΩ[mb/sr]
θlab(deg)

Figure 6.31.

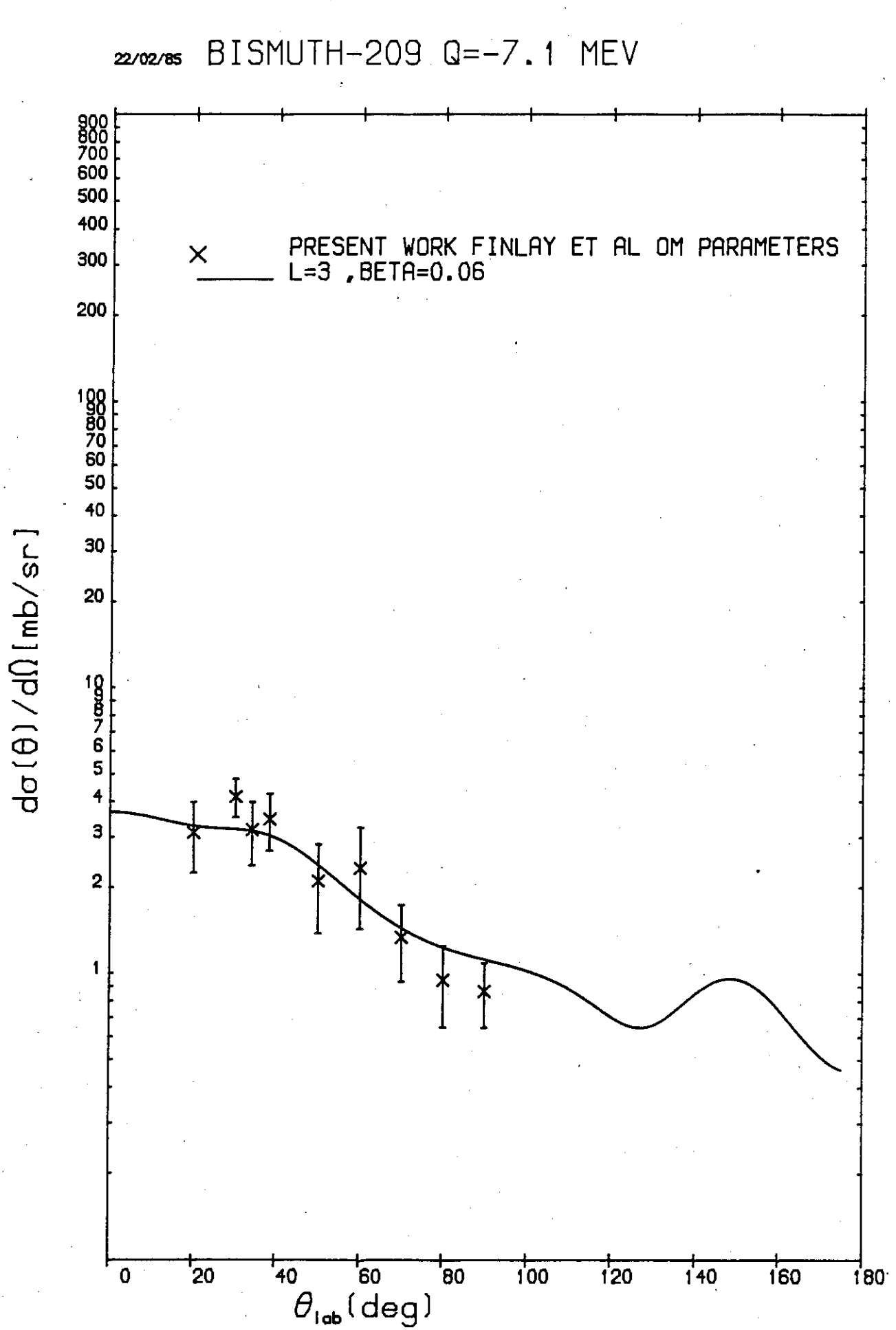
22/02/85 BISMUTH-209 Q=-7.1 MEV
PRESENT WORK FINLAY ET AL OM PARAMETERS
L=3 ,BETA=0.06
dσ(θ)/dΩ[mb/sr]
θlab(deg)
900
800
700
600
500
400
300
200
100
90
80
70
60
50
40
30
20
10
9
8
7
6
5
4
3
2
1
0
20
40
60
80
100
120
140
160
180

Figure 6.32.

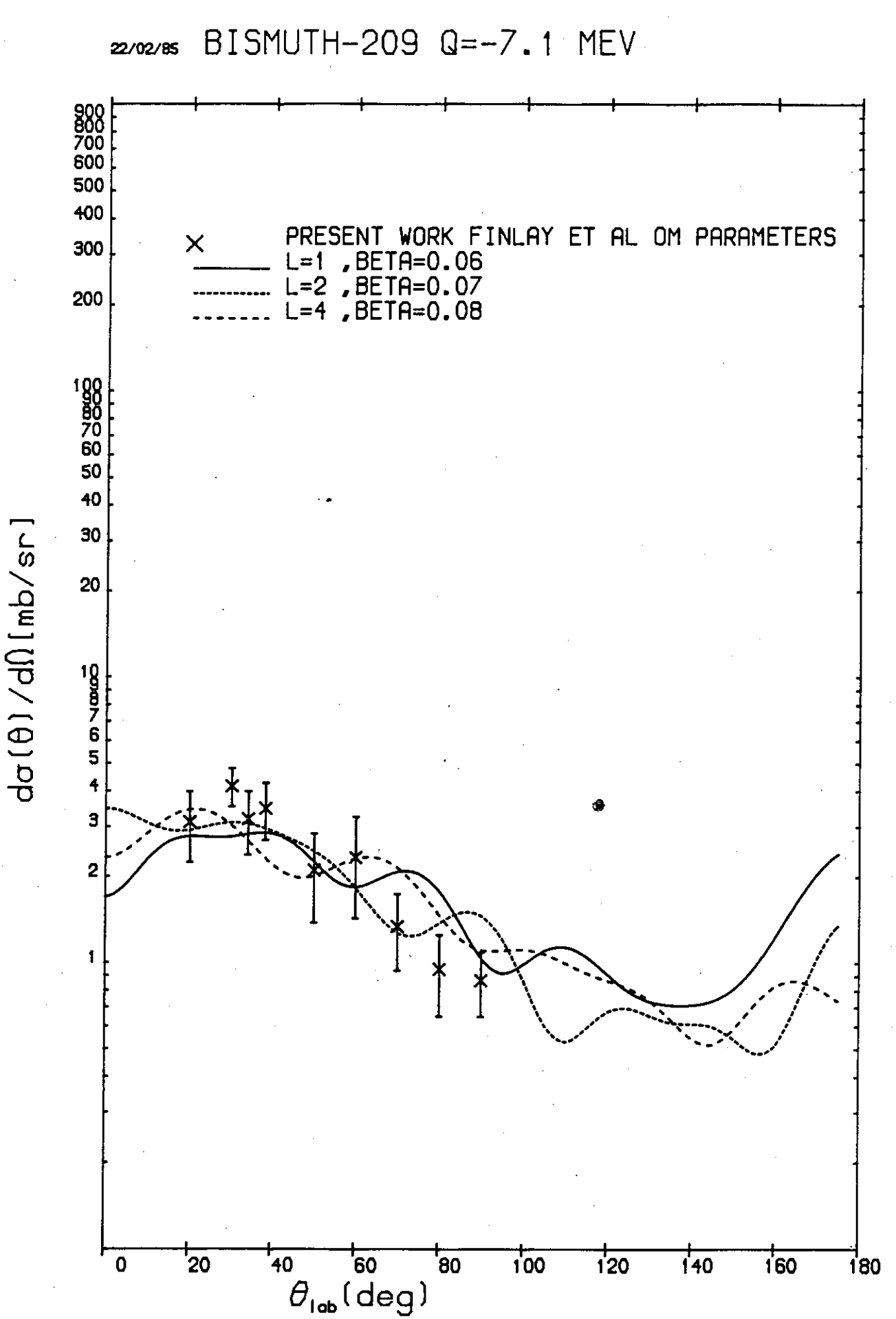
22/02/85 BISMUTH-209 Q=-7.1 MEV
PRESENT WORK FINLAY ET AL OM PARAMETERS
L=1 ,BETA=0.06
L=2 ,BETA=0.07
L=4 ,BETA=0.08
dσ(θ)/dΩ[mb/sr]
θlab(deg)

Figure 6.33.

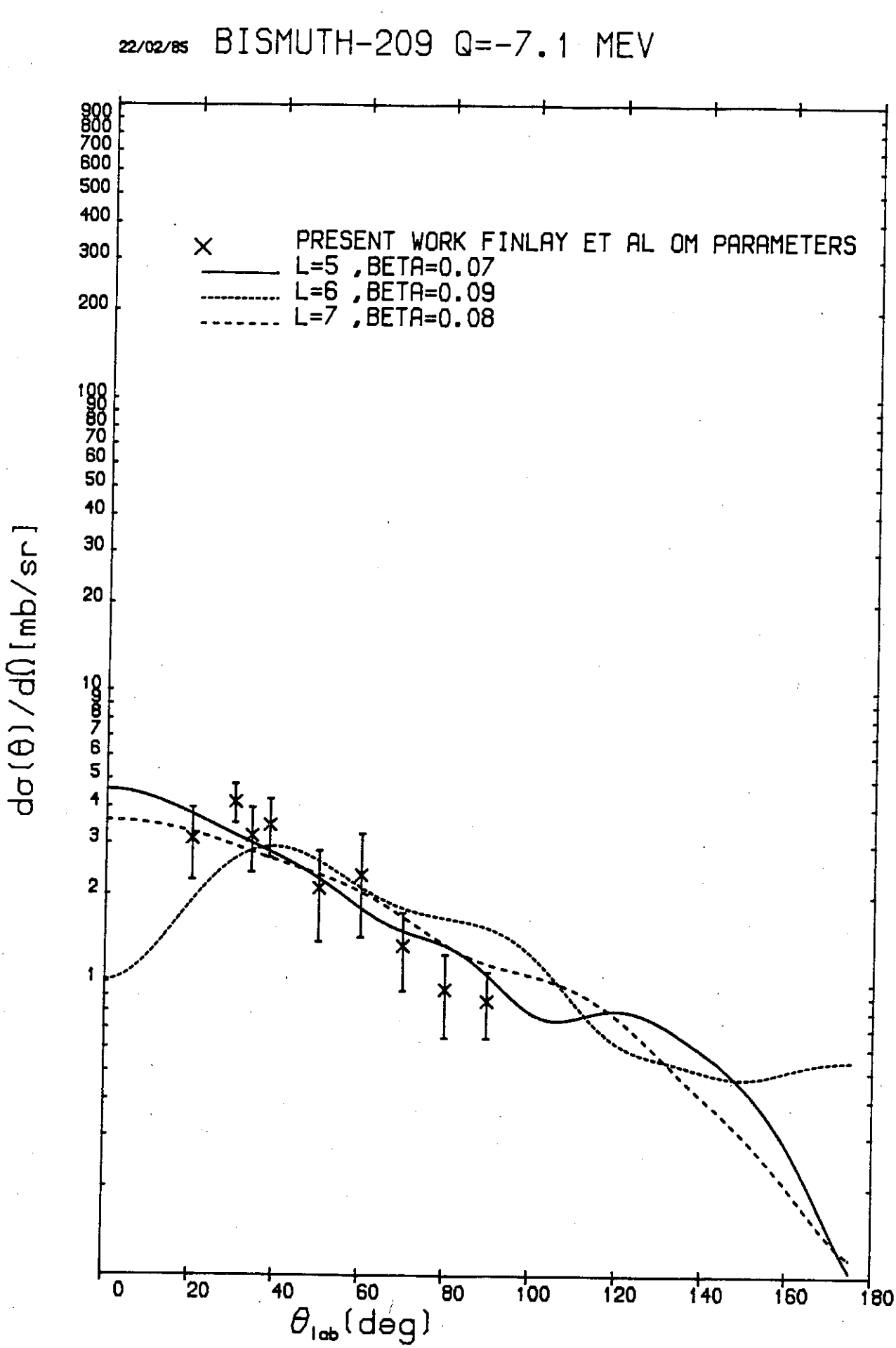
22/02/85 BISMUTH-209 Q=-7.1 MEV
PRESENT WORK FINLAY ET AL OM PARAMETERS
L=5 ,BETA=0.07
L=6 ,BETA=0.09
L=7 ,BETA=0.08
dσ(θ)/dΩ[mb/sr]
θlab(deg)

Figure 6.34.

TABLE (6.7) Q = - 7.1 MeV

Angular momentum transfer ℓ	χ^2 Finlay et al. OM parameters	Stelson et al. OM parameters
1	1.9	2.0
2	1.5	0.9
3	0.6	0.7
4	1.62	2.7
5	0.8	0.9
6	2.79	4.2
7	1.0	1.1

Q = -7.4 MeV

The 7.4 MeV group can be identified with an excitation energy of 7.416 MeV reported for ^{209}Bi (110). Kuijper et al. have also reported in their publication(30) the existence of an excited state in ^{209}Bi at 7.3 ± 0.3 MeV, though their data for this state was not analysed due to being uncertain at some angles. Fig. (6.35) shows DWBA calculation for $\ell = 1$ to $\ell = 7$ using Stelson et al. parameters. Figs. (6.36) - (6.38) show similar calculations with Finlay et al. OM parameters. It appears from the table of χ^2 values that $\ell = 1$, being indicated by both OM parameter sets, can possibly be the spin for 7.4 MeV excitation level.

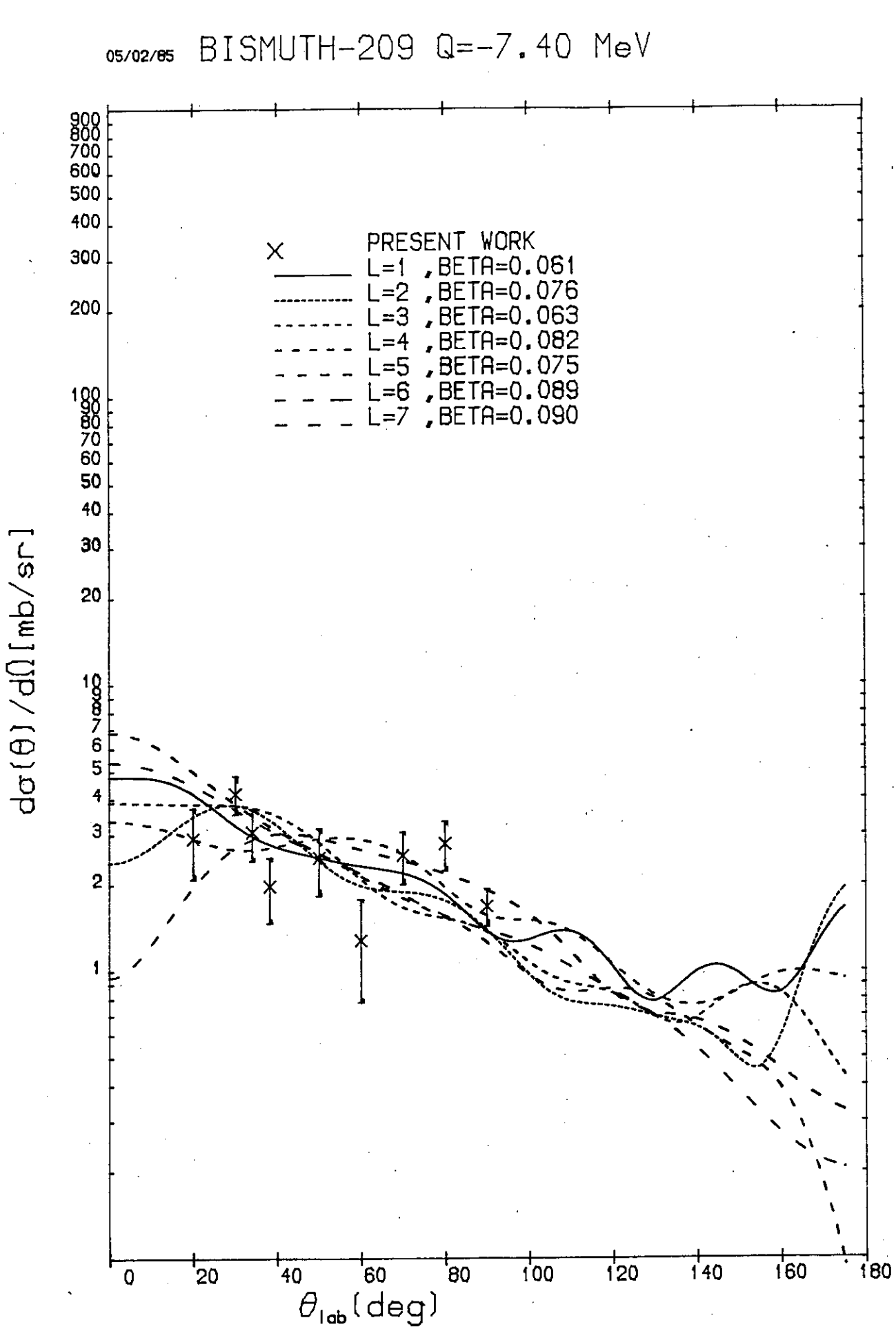
05/02/65 BISMUTH-209 Q=-7.40 MeV
PRESENT WORK
L=1 ,BETA=0.061
L=2 ,BETA=0.076
L=3 ,BETA=0.063
L=4 ,BETA=0.082
L=5 ,BETA=0.075
L=6 ,BETA=0.089
L=7 ,BETA=0.090
dσ(θ)/dΩ[mb/sr]
θlab(deg)

Figure 6.35.

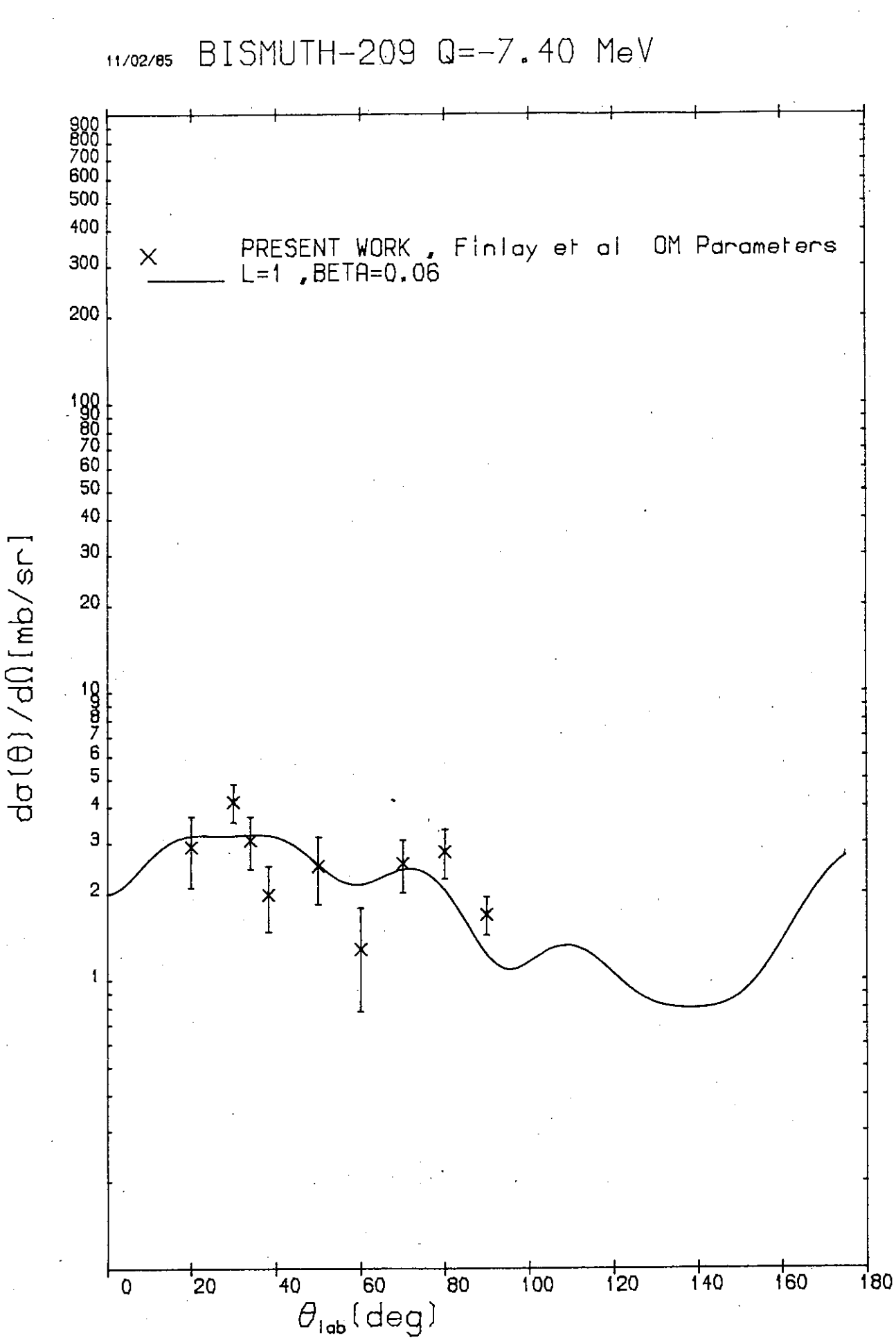
11/02/85 BISMUTH-209 Q=-7.40 MeV
PRESENT WORK , Finlay et al OM Parameters
L=1 ,BETA=0.06
dσ(θ)/dΩ[mb/sr]
θlab(deg)
900
800
700
600
500
400
300
200
100
90
80
70
60
50
40
30
20
10
9
8
7
6
5
4
3
2
1
0
20
40
60
80
100
120
140
160
180

Figure 6.36.

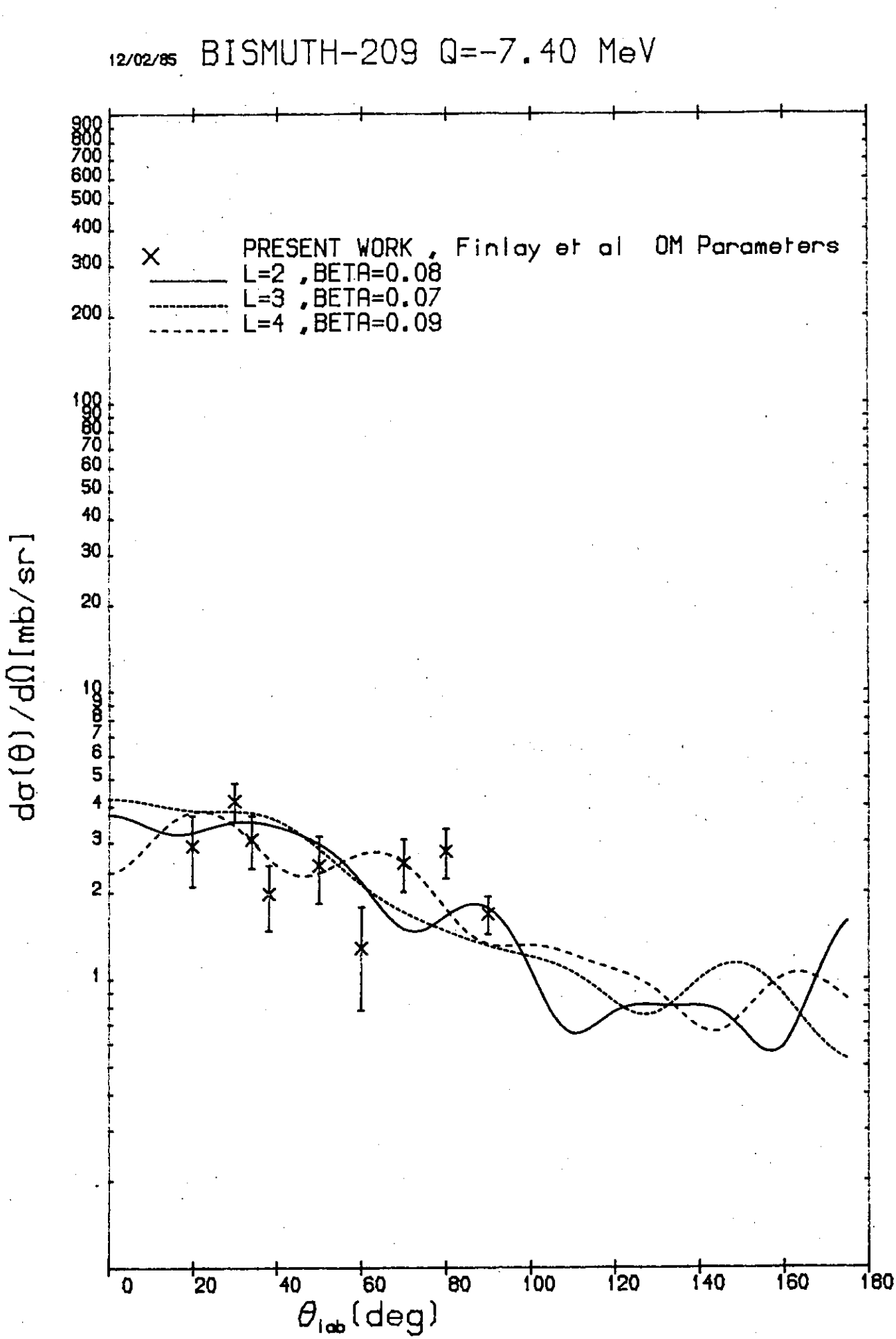
12/02/85 BISMUTH-209 Q=-7.40 MeV
PRESENT WORK , Finlay et al OM Parameters
L=2 ,BETA=0.08
L=3 ,BETA=0.07
L=4 ,BETA=0.09
dσ(θ)/dΩ[mb/sr]
θlab(deg)

Figure 6.37.

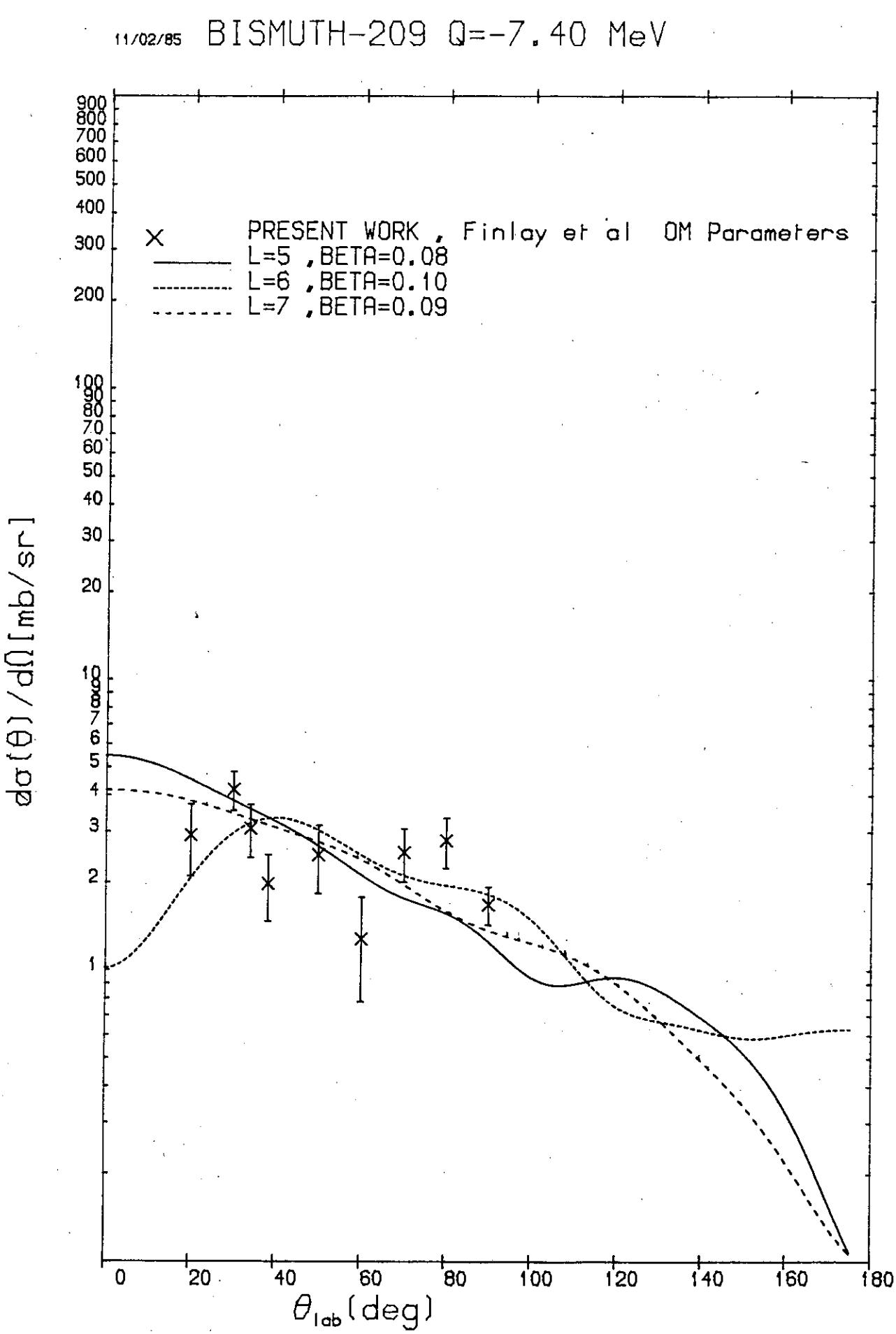
11/02/85 BISMUTH-209 Q=-7.40 MeV
PRESENT WORK , Finlay et al OM Parameters
L=5 ,BETA=0.08
L=6 ,BETA=0.10
L=7 ,BETA=0.09
dσ(θ)/dΩ [mb/sr]
θlab (deg)

Figure 6.38.

TABLE 6.8 Q = -7.4 MeV.

Angular momentum transfer ℓ	χ^2 Finlay et al. OM parameters	Stelson et al. OM parameters
1	1.7	1.7
2	2.4	1.8
3	3.0	2.7
4	2.0	2.4
5	2.6	2.8
6	2.4	2.4
7	2.2	2.3

Q = -7.9 MeV

An excitation energy equal to 7.99 MeV is known to exist in $^{208}_{Pb}$ (110). The spin for this state, however, is not known.

In Fig. (6.39) DWBA calculations of inelastic cross section angular distributions for $\ell = 1$ to $\ell = 7$ with Stelson et al. parameters are shown. χ^2 calculated on the b asis of these calculations and that of Finlay et al. indicate that $\ell = 1$ is favoured by the inelastic scattering at this energy group, Figs. (6.40) to (6.42).

TABLE (6.9) Q = -7.9 MeV

Angular momentum transfer ℓ	χ^2 Finlay et al. OM parameters	Stelson et al. OM parameters
1	1.0	1.1
2	2.2	1.4
3	1.4	1.4
4	0.8	1.7
5	1.5	2.0
6	2.7	3.0
7	0.9	1.4

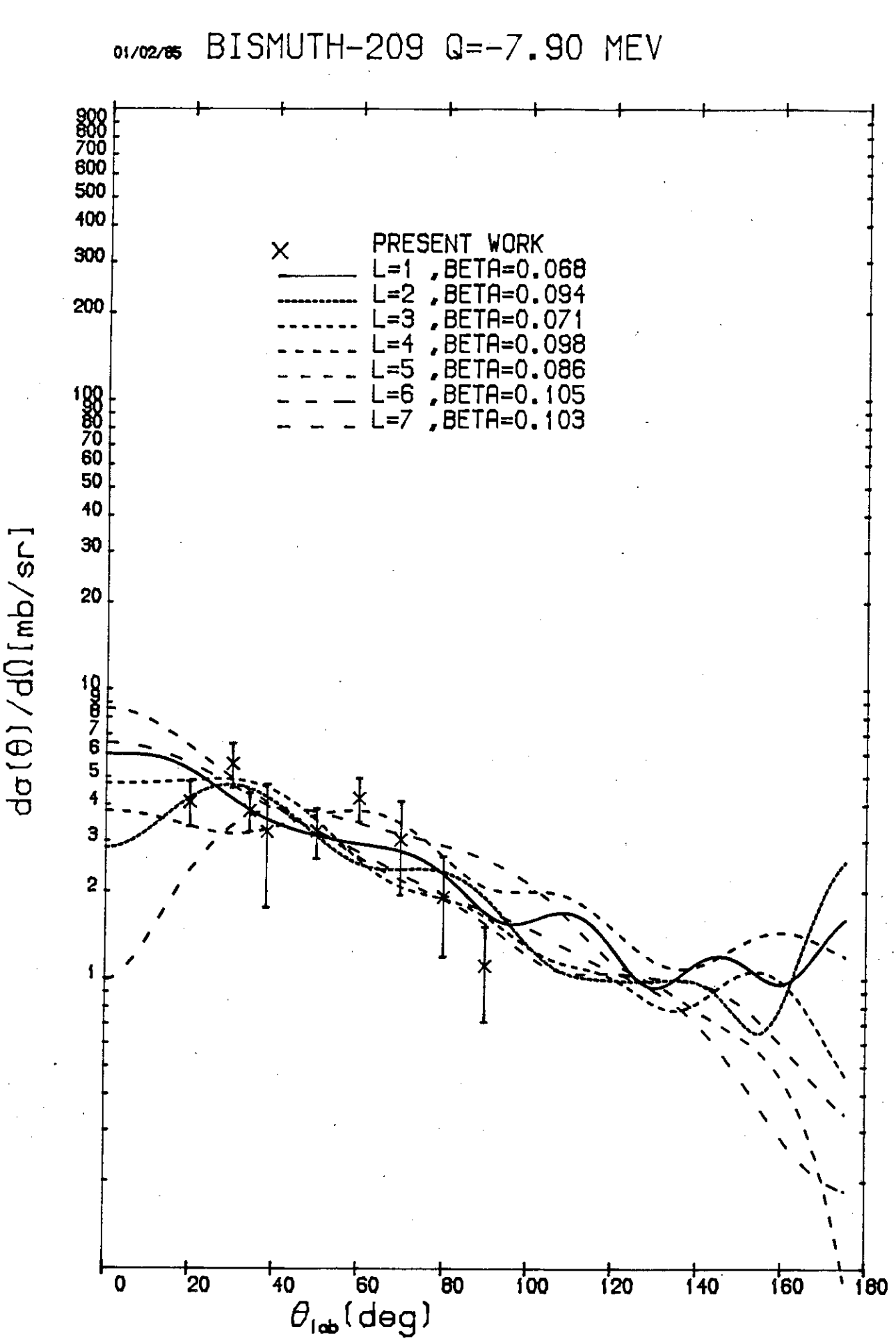
01/02/85 BISMUTH-209 Q=-7.90 MEV
PRESENT WORK
L=1 ,BETA=0.068
L=2 ,BETA=0.094
L=3 ,BETA=0.071
L=4 ,BETA=0.098
L=5 ,BETA=0.086
L=6 ,BETA=0.105
L=7 ,BETA=0.103
dσ(θ)/dΩ[mb/sr]
θlab(deg)

Figure 6.39.

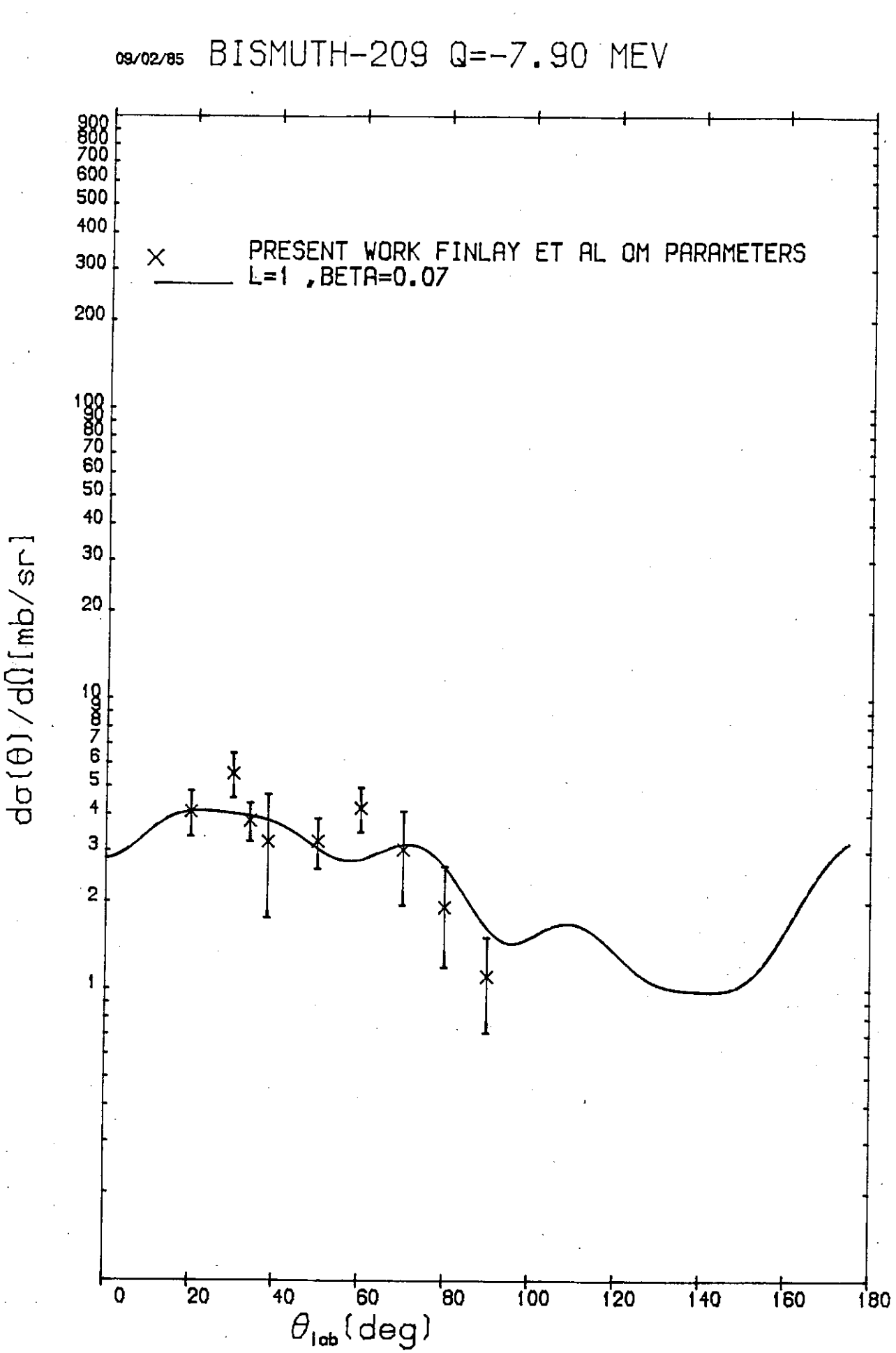
09/02/85 BISMUTH-209 Q=-7.90 MEV
PRESENT WORK FINLAY ET AL OM PARAMETERS
L=1 ,BETA=0.07
dσ(θ)/dΩ[mb/sr]
θlab(deg)
0
20
40
60
80
100
120
140
160
180

Figure 6.40.

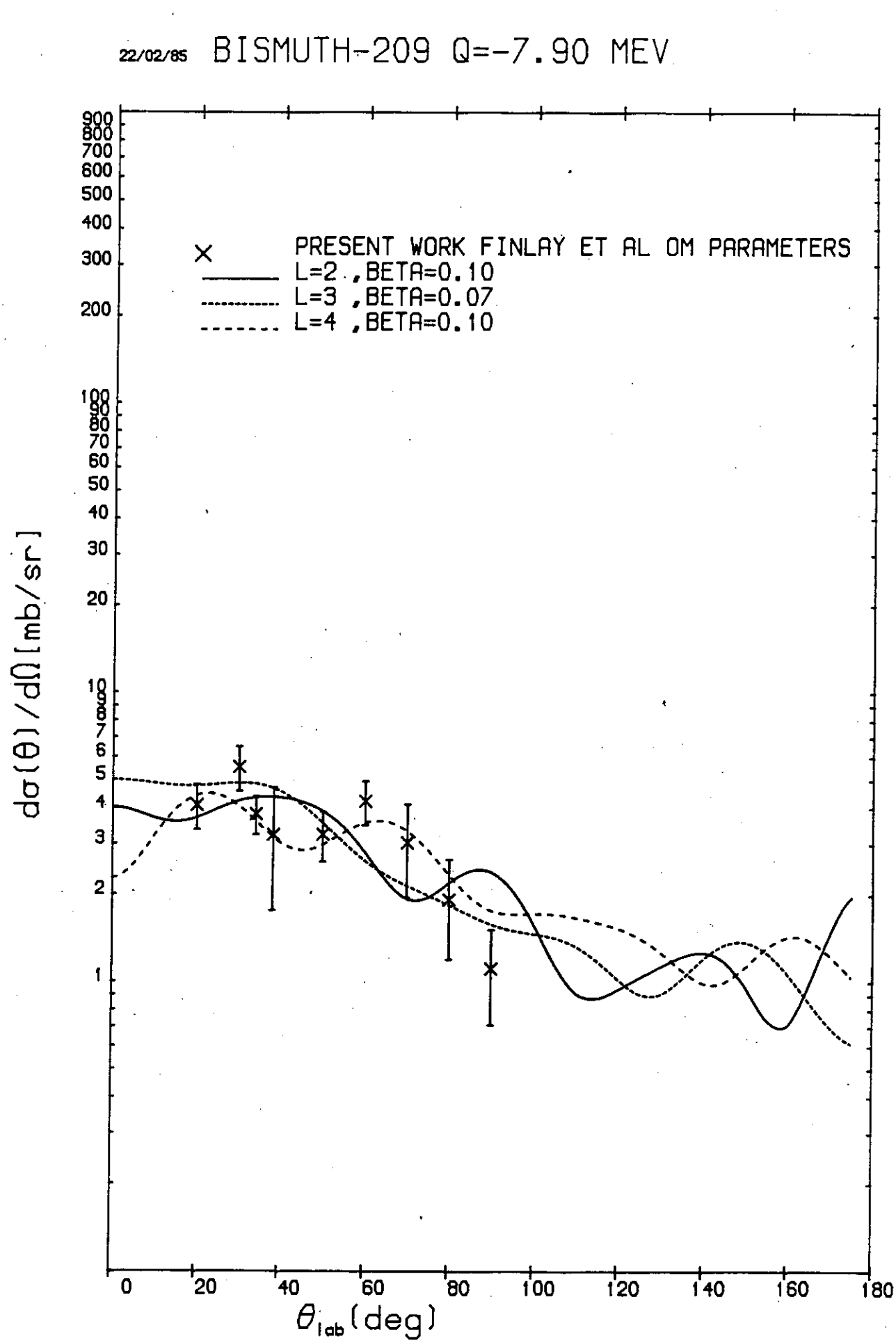
22/02/85 BISMUTH-209 Q=-7.90 MEV
PRESENT WORK FINLAY ET AL OM PARAMETERS
L=2 ,BETA=0.10
L=3 ,BETA=0.07
L=4 ,BETA=0.10
dσ(θ)/dΩ [mb/sr]
θlab (deg)

Figure 6.41.

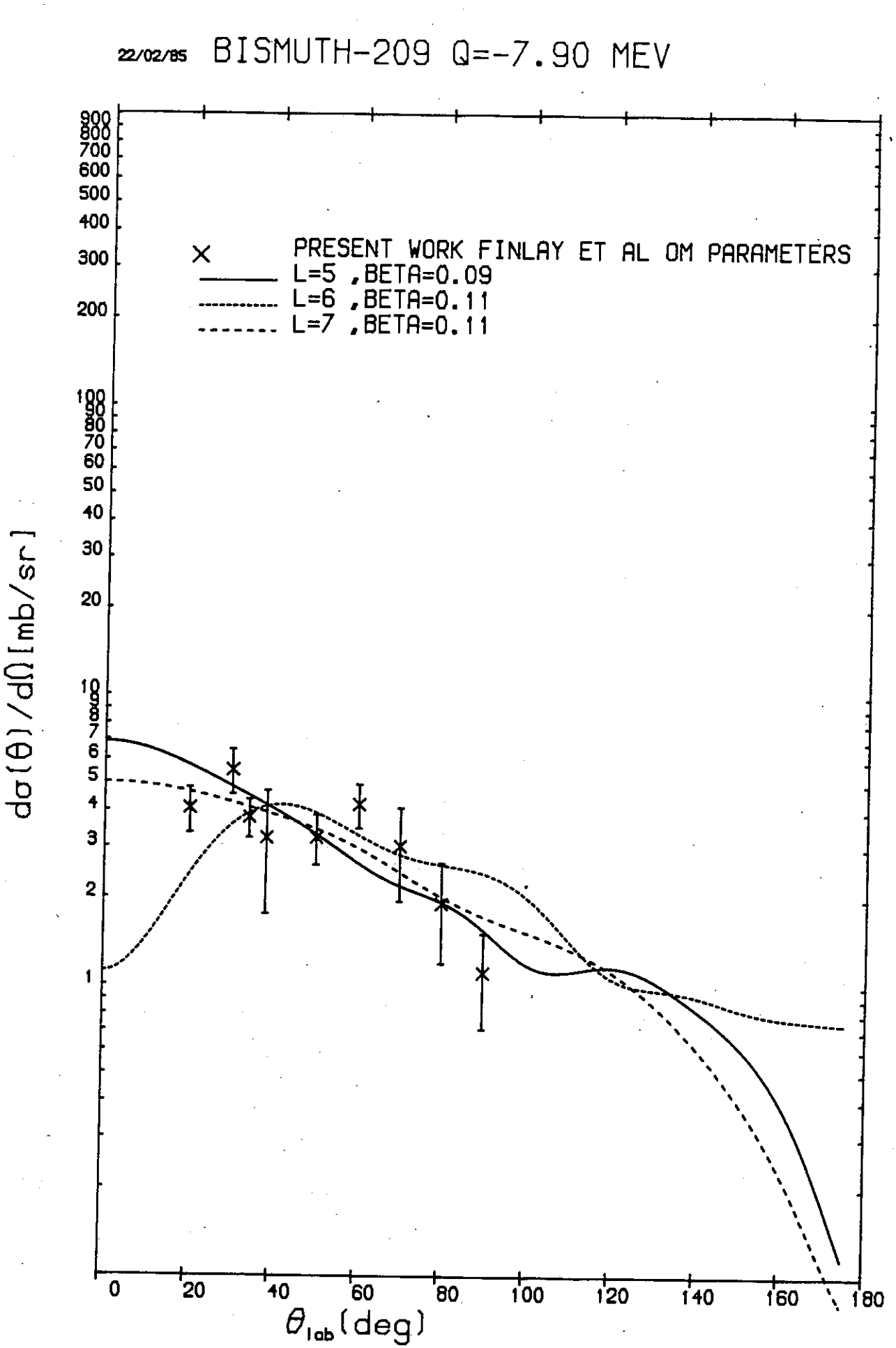
22/02/85 BISMUTH-209 Q=-7.90 MEV
PRESENT WORK FINLAY ET AL OM PARAMETERS
L=5 ,BETA=0.09
L=6 ,BETA=0.11
L=7 ,BETA=0.11
dσ(θ)/dΩ[mb/sr]
θlab(deg)

Figure 6.42.

CHAPTER 7

CONCLUSION

The central aim of this project was to develope and construct a fast neutron spectrometer with good energy resolution properties. This objective has been achieved by the construction of a high energy resolution associated particle time of flight spectrometer with approximately 300 keV energy resolution for 14 MeV neutrons.

This energy resolution achieved by the associated particle time of flight technique is comparable with recently reported energy resolution[130], utilizing a modern pulsed beam Scattering System. Such an energy resolution is adequate for most nuclei, in particular for light and medium weight nuclei with relatively well-separated energy levels.

Scattering measurements using the Spectrometer described above have been made on Bismuth-209 differential cross-sections. The measured elastic cross sections have been compared with previous measurements and show a good agreement with previous work. Inelastic scattering cross section measurements have been made for 10 excited states in Bismuth, with an excitation energy between 2.6 MeV to 7.9 MeV, seven of these states being states for which no previous neutron inelastic data exists. The measurement for the three previously studied states could also decisively confirm two of the three reported measurements, for 2.6 MeV and 4.2 MeV states and remove the existing discrepancies.

The inelastic data have been compared with deformed optical model calculations using the DWBA theory of direct reactions and the deformation parameters for the excited states deduced. Indication of the most probable

transition angular momentum change was deduced for each excited state. This comparison provides a good test for the theory of scattering through direct reaction.

Differential inelastic cross sections calculated with the DWBA theory were similar to the experimental data. However, in view of the complexity of the states in Bismuth, all of which could not realistically be resolved in neutron experiments, it was not possible to attribute a uniquely valued spin for the observed excited states.

REFERENCES

1. Walter Hauser and Herman Feshbach, Phys. Rev. 87 No.2 (1952) 366.
2. Kinney, W.E., Perey, F.G., Nucl. Sci. Eng. 40 (1970) 396.
3. G.R. Satchler, Introduction to Nuclear Reactions, Chapter 2, p.69. Macmillan Press Ltd. (1980).
4. H.H. Barschall, Phys. Rev. 86 (1952) 431.
5. M. Walt and H.H. Barschall, Phys. Rev. 93 (1954) 1062.
6. H. Feshbach, C.E. Porter and V.F. Weisskopf, Phys. Rev. 96 (1954) 448.
7. R.E. Le Levier and D.S. Saxon, Phys. Rev. 87 No. 1 (1952) 40.
8. R.D. Woods and D.S. Saxon, Phys. Rev. 95 (1954) 577.
9. F.A. McDonald and M.H. Hull, Jr., Phys. Rev. 143 (1966) 838.
10. R.H. Lemmer, T.A.J. Maris, Y.C. Tang, Nucl. Phys. 12 (1959) 619-624
11. F. Perey and B. Buck, Nucl. Phys. 32 (1962) 353-380.
12. D. Wilmore and P.E. Hodgson, Nucl. Phys. 55 (1964) 673-694.
13. F.D. Becchetti, Jr. and G.W. Greenlees, Phys. Rev. 182 No. 4 (1969) 1190.
14. J.P. Jeukenne, A. Lejeune and C. Mahaux, Phys. Lett. 25C (1976) 83.
15. J.P. Jeukenne, A. Lejeune and C. Mahaux, Phys. Rev. C15 No. 1 (1977) 10.
16. J.P. Jeukenne, A. Lejeune and C. Mahaux, Phys. Rev. C16 No. 1 (1977) 80.
17. F.A. Brieva and J.R. Rook, Nucl. Phys. A291 (1977) 299-317.
18. F.A. Brieva and J.R. Rook, Nucl. Phys. A297 (1978) 206.
19. F.A. Brieva and J.R. Rook, Nucl. Phys. A307 (1978) 493.
20. P.E. Hodgson, Ann. Rev. of Nucl. Phys. 20 (1970) 1-32.
21. T. Tamura, Rev. Mod. Phys. 37 No. 4 (1965) 679.
22. G.R. Satchler, Nucl. Phys. 55 (1963) 1-33.
23. B. Buck and P.E. Hodgson, Phi-. Mag. 6 (1961) 1371.
24. B. Buck, Phys. Rev. 130 (1963) 712.
25. P.H. Stelson, R.L. Robinson, H.J. Kim, J. Rapaport and G.R. Satchler, Nucl. Phys. 68 (1965) 97.

REFERENCES (Contd.)

26. M.D. Goldberg, Angular distribution in neutron induced reactions, Vol. 1, BNL400 (1962).

27. J.D. Anderson, C.C. Gardner, J.W. McClure, M.P. Nakada and C. Wang Phys. Rev. 111 (1958) 572.

28. C. Wang, J.D. Anderson, J.W. McClure, Nucl. Phys. 33 (1962) 680.

29. R.L. Clarke and W.G. Cross, Nucl. Phys. 53 (1964) 177-203.

30. P. Kuijper, J.C. Veefkind and C.C. Jonker, Nucl. Phys. A181 (1972) 545.

31. M. Matoba, M. Hyakutake, H. Tawara, K. Tsuji, Nucl. Phys. A204 (1973) 129.

32. J.W. Watson, F.J. Wilson, C.A. Miller, D.C. Wells, Nucl. Instr. Meth. 164 (1979) 129-141.

33. J. Rapaport, T.S. Cheema, D.E. Bainum, R.W. Finlay and J.D. Carlson, Nucl. Phys. A296 (1978) 95.

34. M.N. Erduran, Ph.D. Thesis (1984), University of Edinburgh.

35. P.D. Kunz, University of Colorado (Unpublished).

36. J.R. Dunning, G.B. Pegram, G.A. Fink, D.P. Mitchell and E. Segre, Phys. Rev. 48 (1935) 704.

37. L.W. Alvarez, Phys. Rev. 54 (1938) 609.

38. J.B. Marion and J.L. Fowler, Chapter 1C, Interscience. Mon. and Texts in Physics and Astron. 4, New York.

39. J.B. Marion and F.C. Young, Nuclear reaction analysis, graphs and tables, North Holland (1968).

40. D.C. Santry and R.D. Werner, Nucl. Instr. Meth. 188 (1981) 211.

41. M. Ahmad, Munir Ahmad and M. S. Chaudhary, Nucl. Instr, Meth. 126 (1975) 309.

42. P. Kuijper and D. Spaargaren, Nucl. Instr. Meth. 98 (1972) 173.

43. L. Ruby and R.B. Crawford, Nucl. Instr. Meth. 24 (1963) 413.

44. W. Whaling, Handbuch der Fysik, 34 (1958) 13.

45. Nuclear Enterprises Brochure No. 126, page 10.

46. M. Drosg, Nucl. Instr. Meth. 105 (1972) 573.

47. J.L. Fowler, J.A. Cookson, M. Hussain, R.B. Schwartz, M.T. Swinhoe, C. Wise and C.A. Uttley, Nucl. Instr. Meth. 175 (1980) 449.

REFERENCES (Contd.)

48. J.B. Marion and J.L. Fowler, Fast Neutron Physics Part I, Chap. IVF, 807. Interscience Mon. and Texts in Physics & Astron. 4, New York.

49. D.W. Glasgow, D.E. Velkley, J.D. Brandenberger, M.T. McEllistrem, H.J. Hennecke, D.V. Breitenbecher, Nucl. Instr. Meth. 114 (1974) 521.

50. D. Schlegel-Bickmann, G. Dietze and H. Schölermann, Nucl. Instr. Meth. 169 (1980) 517.

51. W.C. Parkinson, J.F. Petersen, R.H. Day, R.M. Polichar, P.F. Julien and D.C. DuPlantis, Nucl. Instr. and Meth. 119 (1974) 51.

52. D.A. Lind, R.F. Bentley, J.D. Carlson, S.D. Schery and C.D. Zafiratos, Nucl. Instr. and Meth. 130 (1975) 93.

53. M. Elfield, E.L. Miller, N.W. Reay, N.R. Stanton, M.A. Abolins, M.T. Lin, and K.W. Edwards, Nucl. Instr. and Meth. 100 (1972) 237.

54. A. Del Guerra, A. Giazotto, M.A. Giorgi, A. Stefanini, D.R. Botterill, D.W. Braben, D. Clarke and P.R. Norton, Nucl. Instr. and Meth. 135 (1976) 307.

55. G. Charpak, L. Dick and L. Feuvrais, Nucl. Instr. and Meth. 15 (1962) 323.

56. C. Ward, A. Berick, E. Tagliaferri and C. York, Nucl. Instr. and Meth. 30 (1964) 61.

57. L. Paoluzi and R. Visentin, Nucl. Instr. and Meth. 65 (1968) 345.

58.

59. D. Evers, E. Spindler, P. Konrad, K. Rudolph, W. Assmann, and P. Sperr, Nucl. Instr. and Meth. 124 (1975) 23.

60. W. Braunschweig, E. Königs, W. Sturm and Wallraff, Nucl. Instr. and Meth. 134 (1976) 261.

61. R.K. Bhowmik, R.R. Doering, L.E. Young, S.M. Austin, A. Galonsky and S.D. Schery, Nucl. Instr. and Meth. 143 (1977) 63.

62. C. Cernigoi, N. Grion, G. Pauli and B. Saitta, Nucl. Instr. and Meth. 144 (1977) 479.

63. C.D. Goodman, J. Rapaport, D.E. Bainum and C.E. Brient, Nucl. Instr. and Meth. 151 (1978) 125.

64. Y. Deschamps, E. Hourany, S. Kakigi, F. Reide and T.Yuasa, Nucl. Instr. and Meth. 155 (1978) 135.

65. H. Orihara and T. Murakami, Nucl. Instr. and Meth. 188 (1981) 15.

REFERENCES (Contd.)

66. C.D. Goodman, J. Rapaport, D.E. Bainum, M.B. Greenfield and C.A. Goulding, IEEE Trans. Nucl. Sci. Vol. NS-25, No. 1 February 1978.

67. Scintillator Catalogue, Nuclear Enterprises, Edinburgh.

68. J.R. Prescott and A.S. Rupaal, Can. J. Phys. 39 (1961) 221.

69. L.E. Beghian, S. Wilensky and W.R. Burrus, Nucl. Instr. and Meth. 35 (1965) 34.

70. R.B. Galloway and N.S. Wang (to be published).

71. J. D. Carlson, R.W. Finlay and D.E. Bainum, Nucl. Instr. and Meth. 147 (1977) 353.

72. NE224 Liquid Scintillator, Brochure No. 126, Nuclear Enterprises, Edinburgh.

73. RCA Technical Series PT-61 Photomultiplier Manual, page 34.

74. B. Leskovar and C.C. Lo, Nucl. Instr. and Meth. 123 (1975) 145.

75. D.A. Gedcke, and W.J. McDonald, Nucl. Instr. and Meth. 58 (1968) 253.

76. D.A. Gedcke and W.J. McDonald, Nucl. Instr. and Meth. 55 (1967) 377.

77. P.W. Nicholson, Nuclear Electronics (1974) 233-247, Wiley-Interscience Publication, London.

78. F.D. Brooks, Nucl. Instr. and Meth. 4 (1959) 151.

79. B. Sabbah and A. Suhami, Nucl. Instr. and Meth. 58 (1968) 102.

80. D.W. Jones, IEEE Trans. Nucl. Sci. NS15 No. 3 (1968) 491.

81. J.M. Adams and G. White, Nucl. Instr. and Meth. 156 (1978) 459.

82. T.K. Alexander, F.S. Goulding, Nucl. Instr. and Meth. 13 (1961) 244.

83. N.S. Wang, Private communication.

84. F.K. McNeil-Watson, Internal Report (unpublished).

85. A. Hall, Ph.D. Thesis, University of Edinburgh (1976).

86. G. Charpak, L. Dick and L. Feuvrais, Nucl. Instr. and Meth. 15 (1962) 323.

87. C. Ward, A. Berick, E. Tagliaferri and C. York, Nucl. Instr. and Meth. 30 (1964) 61.

88. L. Paoluzi and R. Visentin, Nucl. Instr. and Meth. 65 (1968) 345.

89. D. Evers, E. Spindler, P. Konrad, K. Rudolph, W. Assmann and P. Sperr, Nucl. Instr. and Meth. 124 (1975) 23.

90. B.E. Leshchenko, M.E. Gurtovoi, A.S. Kukhlenko and V.I. Strizhak, Sov. Jour. Nucl . Phys. 15 (1972) 5.

91. D.W. Glasgow, F.O. Purser, H. Hogue, J.C. Clement, K. Stelzer, G. Mack, J.R. Boyce, D.H. Epperson, S.G. Buccino, P.W. Lisowski, S.G. Glendinning, E.G. Bilpuch, H.W. Newson and C.R. Gould Nucl. Sci. Eng. 61 (1976) 521.

92. Fast Netron Physics, Marion and Fowler, Part I, Chap. IIB, Interscience Mon. & Texts in Physics and Astronomy 4, New York.

93. R.J. Schuttler, Efficiency of Organic Scintillators for Fast Neutrons ORNL-3888 (1966).

94. V.G. Zolotukhin and G.G. Doroshenko, Atom. Eng. 15 (1963) 194.

95. V.G. Zolotukhin and G.G. Doroshenko, Atom. Eng. 18 (1965) 287.

96. H. Grässler, K. Tesch, Nucl. Instr. and Meth. 10 (1961) 353.

97. R. Batchelor, W.B. Gilboy, J.B. Parker and J. H. Towle, Nucl. Instr. Meth. 13 (1961) 70.

98. J.B. Marion and G.N. Fowler, Fast Neutron Physics, Part II, p. 2209 Interscience Mon. & Texts in Physics & Astron. 4, New York.

99. A. Del Guerra, Nucl. Instr. Meths. 135 (1976) 337.

100. C.Y. Fu, F.G. Perey, Atomic Data and Nuclear Data Tables, Vol. 22, No. 3, Sept. 1978.

101. R. Madey, F.M. Waterman, A.R. Baldwin, J.M. Knudson, J.D. Carlson and Rapaport, Nucl. Instr. Meths. 151 (1978) 445.

102. E. Woye, W. Tornow, G. Mack, C.E. Floyd, P.P. Guss, K. Murphy, R.C. Byrd, S.A. Wender, R.L. Walter, T.B. Clegg and W. Wylie, Nucl. Phys. A394 (1983) 139.

103. F.B. Hildebrand 'Introduction to Numerical Analysis', McGraw-Hill Book Co. Inc. (1956) 295-302.

104. M. Matoba, M. Hyakutake, H. Yamamoto, A. Katase and M. Sonoda, Nucl. Instr. Meths. 94 (1971) 199.

105. N. Sasamoto, K. Koyama and S. Tanaka, Nucl. Instr. Meths. 125 (1975) 507.

106. E. Von Meerwall Computer Physics Communication 9 (1975) 117, CPC Program Library, Queen's University, Belfast, N.I.

107. D.E. Velkley, J.D. Brandenberger, D.W. Glasgow and M.T. McEllistrem, Nucl. Instr. Meths. 129 (1975) 231.

108. W.E. Kinney, Nucl. Instr. Meths. 83 (1970) 15.

109. 'MULTSCAT', B. Holmqvist, B. Gustavsson and T. Wielding, Arkiv. för Fysik 34 (1966) 481.

REFERENCES (Contd.)

110. Nuclear Data Sheets 22 (1977) 545.
Nuclear Data B5 (1971) 243.

111. G. Placzek, Phys. Rev. 72 (1947) 556.

112. J. Block and C.C. Jonker, Physica 18 (1952) 809.

113. S.A. Cox, Nucl. Instr. Meths. 56 (1967) 245.

114. R.J. Howerton, UCRL 5351 (1958).

115. C.A. Engelbrecht, Nucl. Instr. Meths. 80 (1970) 187.

116. W.G. Cross, R.G. Jarvis, Nucl. Phys. 15 (1960) 155.

117. J.O. Elliot, Phys. Rev. 101 (1956) 684.

118. H.A. Bethe, Phys. Rev. 47 (1935) 747.

119. H. Feshbach, Peaslee and Weisskopf, Phys. Rev. 71 (1947) 145.

120. S. Fernbach, R. Serber and T.B. Taylor, Phys. Rev. 75 (1949) 1352.

121. P.E. Hodgson, Ann. Rev. Nucl. Science 17 (1967) 1, Nuclear Reactions & Nuclear Structure, (Clarendon Press, Oxford, 1971).

122. G.W. Greenlees, G.J. Pyle and Y.C. Tang, Phys. Rev. 171 (1968) 1115.

123. S.D. Drell, Phys. Rev, 100 (1955) 97.

124. J.P. Delaroche, Ch. Lagrange, J. Salvy, Nuclear Theory in Neutron Nuclear Data Evaluation,[held at Trieste, 8-11 Dec. 1975.]

125. A. Bohr, K. Danske Vidensk. Slesk. Mat. Fys. Medd. 26 (1952) 14.

126. R.H. Bassel, G.R. Satchler, R.M. Drisko and E. Rost, Phys. Rev. 128 (1962) 2693.

127. F. Perey and G.R. Satchler, Phys. Lett. 5 (1963) 212.

128. C.Y. Fu, F.G. Perey, Atomic Data and Nuclear Data Tables 16 (1975) 409.

129. O. Bersillon, B. Caput, C.A. Philis, "Nuclear Data for Science and Technology", Proc. of the International Conference, 6-10 Sept. 1982, Antwerp.

130. R.W. Finlay, J.R.M. Annand, T.S. Cheema, J. Rapaport and F.S. Dietrich, Phys. Rev. C30 (1984) 796.

131. F.E. Bertrand and M.B. Lewis, Nucl. Phys. A168 (1971) 259.

ACKNOWLEDGEMENTS

I would like to express my sincere thanks to Dr. R.B. Galloway who suggested this project and who has given me such support and encouragement throughout the course of this work.

I would also like to thank Dr. D.G. Vass for his advice and consultation in some aspects of the work.

My warmest thanks are also due to both Mr. H.J. Napier for his technical assistance in maintaining the accelerator, and to Mr. G. Turnbull for his assistance in the earlier stages of this work.

My warmest thanks must go to Mustapha Erduran for many fruitful discussions and help during the course of this work.

To Mrs. Ray Chester for help and speedy typing of this thesis, my grateful thanks.

I wish to acknowledge partial financial support from Urmia University.

Last, but by no means least, I have to thank Miss Setsuko Wakabayashi for her considerable support throughout the entire period of study.